SILICON PHOTOSENSITIZATION AND LIGHT HARVESTING USING LANGMUIR BLODGETT MONOLAYERS

By: William Henry Banks (Msci)

Supervisor: Dr Lefteris Danos

This thesis is submitted for the degree of Doctor of Philosophy

Lancaster University Department of Chemistry

October 2022

Silicon Photosensitization and Light Harvesting Using Langmuir Blodgett Monolayers

Author: William H Banks Student ID: 38199149

Abstract

This thesis looks at potential modifications to silicon wafers to reduce the amount of material required to absorb light energy and increase electron hole pair generation.[1,2] To achieve this, the separation of the light absorption and electron hole pair generation is suggested so that the light absorbing component can be optimised independently. This is known as silicon photosensitization. To study this phenomenon light absorbing Langmuir Blodgett films were deposited onto silicon wafers and characterised using time resolved fluorescence techniques to estimate the light harvesting efficiency.

Organic absorbing structures which can perform light harvesting were investigated using mixed monolayers of 3,3'-Dioctadecyloxacarbocyanine Perchlorate (DiO) and 1,1'-Dioctadecyl-3,3,3',3'-Tetramethylindocarbocyanine Perchlorate (DiI) deposited on quartz glass slides in ratios of high donor (DiO) to low acceptor (DiI). Energy transfer was shown from DiO to DiI. An efficiency of 95% was calculated for a donor acceptor ratio of 1-1 and energy transfer was shown to occur up to the 100-1 ratio.

Triplet state energy transfer directly to silicon from a Langmuir Blodgett monolayer was then investigated. Langmuir Blodgett monolayers of a Rhenium (ReC18) and Ruthenium (RuC18) complex were both found to transfer energy to unmodified silicon wafer. Using inert stearic acid spacer between the emitting layers and the surface of silicon to alter the distance, the change in phosphorescence emission as a function of distance from the surface on silicon was observed.

Following on from this the photoluminescence of silicon wafers was studied. Tetraphenylporphyrin (TPP) was mixed in a 1-1 ratio with stearic acid and deposited on silicon passivated with aluminium oxide, the luminescence of silicon and TPP film was observed. Enhancement of the silicon luminescence was shown but was not repeatable. The TPP emission also showed reduction in intensity but enhancement of the lifetime.

This thesis provides examples of silicon photosensitization which can be applied directly on the top of silicon wafers and shows the potential for an ultrathin device using sensitization.

Pages: 240

Words: 57,070

Acknowledgments

This thesis would not have been possible without several people who have my lifelong gratitude for their help. I would like to thank my supervisor Dr Lefteris Danos for offering me this opportunity and going above and beyond for me throughout this process. I would additionally like to thank my secondary supervisor Dr Lorna Ashton for her kind help with my writing and encouragement over the years and Professor Jamshed Anwar for giving up his time to chair my panels. I would also like to thank Dr Mike Coogan without whose synthetic expertise this project would not have been possible and Dr Sara Baldock and Dr Nathan Halcovitch for their technical support.

Additionally, I would like to thank Professor Jeremy Frey and Dr Kathryn Toghill for reading this work and being a wonderful viva panel alongside my panel chair Dr John Hardy.

I would also like to thank all my friends and colleagues for their personal and professional support, in particular, Ben Wood, Dipen Pandya, Dr Tom Britten, Isobel Dixon-Wilkins, Dr Mateusz Jurczyński, Judy Jurczyńska, Dr Dhruv Trivedi, Dr Shahin Nikman, Dr Craig Armstrong, Dr Edward Dearden, Hannah Wesson, Dr Andrew McKendrick and My parents Suzanne and Nick Banks.

Finally, I would like to acknowledge and thank both the Lancaster University Department of Chemistry for funding this project and Lancaster University for further funding during the Covid 19 pandemic.

Author’s Declaration

I hereby declare that this thesis is my work and has not been submitted in substantially the same form for the award of a higher degree elsewhere. None of the work is published anywhere at time of submission.

Signed: William Henry Banks

Table of Contents

Acronyms

Acronym	Full name
AFM	Atomic force microscopy
CB	Conduction band
CFD	Constant fraction discriminator
DiI	1,1'-Dioctadecyl-3,3,3',3'-Tetramethylindocarbocyanine
DiO	3,3'-Dioctadecyloxacarbocyanine
DPPC	Dipalmitoylphosphatidylcholine
E%	Percentage energy transfer
ET	Energy transfer
FRET	Förster resonance energy transfer
FTIR	Fourier transform infrared spectroscopy
LB	Langmuir Blodgett
LHC	Light harvesting complex
N doped	Negative Doped
P doped	Positive doped
Re-C16	Rhenium bipyridine tricarbonyl pyridine-2-MethylHexadecoate
RU-C18	Ruthenium bipy 2,7 Bi Octadecanylamine bis Bipy
S0	Ground energy level of an absorbing molecule
S1	Fist energy level of the singlet state of an absorbing molecule
S2	Second energy level of the singlet state of an absorbing molecule
SPP	Surface plasmon polaritons
T1	First energy level of the Triplet state of a phosphorescent molecule
TAC	Time to amplitude converter
TCSPC	Time correlated single photon counting
VB	Valence band

Figures

Equations

Tables

1. Introduction

1.1 Motivation

1.1.1 The global energy challenge

The global demand for energy is increasing year on year. As such the demand for the current hegemonic fuels is increasing. According to the International energy agency the second highest rise in global energy demand occurred from 2020 to 2021, a rise of 4.6% across the world, this naturally entails the use of the most readily available source of energy, coal, oil and natural gas. As the development of previously undeveloped regions increases and the world recovers from an economic recession the use of natural gas and coal continues to rise as a cheap source of energy that most countries have access to. However, the demand for renewables is also increasing. The demand for renewables increased more than the decrease in the demand for oil in 2021.[1] The effect this has on the fight to keep the rise in global temperature below 1.5 ^{o}C can only be negative, however, increasing the uptake of renewables through a reduction in cost to make them competitive with coal and natural gas for developing economies may solve this issue.[3]

The place of the solar PV industry within the renewables sector cannot be disputed. The energy generated by solar PV grew by 18% in 2021 and accounted for approximately 15% of renewable energy generation showing it to be a reliable growth sector. Solar should in theory be the largest sector of renewables as the sun is an abundant resource available anywhere however it is eclipsed by wind in terms of percentage power generation.[1] Both solar and wind are the main drivers for the deployment of renewable energy around the world.

This project seeks to address the specific problems arising from the need for more widespread adoption of green energy technologies. Photovoltaics are now available on the consumer market. A reduction in price per unit that at least maintains the current efficiency without requiring more expensive material would undoubtedly increase uptake of this technology. This would require a maintenance of efficiency of around 20% conversion of incident light to current. It may also allow for a consumer design which reaches the theoretical limit of a single layer silicon solar cell (30%). To that end we will propose some ideas for future photosensitization platforms for silicon wafers which could be added to either a functionalised or a non-functionalised ultrathin silicon wafer, thus reducing the amount of silicon required by two orders of magnitude for a solar cell and therefore the overall cost. This project looks specifically at reducing the

thickness of silicon required by applying layers to the top of the silicon which absorb light instead of silicon and thus using light harvesting behaviour in those layers.

1.2 Current solar technologies and suggested improvements

1.2.1 The P/N junction silicon solar cell

Solar cells utilise what is known as a P/N junction in order to direct the flow of current from the generation of electron hole pairs. Silicon, as a semiconductor is able to generate electron hole pairs through the absorption of sunlight.

The photovoltaic (PV) process can be separated into two steps. The first step is absorption of light, and the second step is the creation of an electron hole pair. In the regular solar panel design bulk silicon both actions are handled by one component, the silicon semiconductor. The semiconductor is used for PV cells is silicon usually doped with electrons (negative carrier charge, n doped) or holes (positive carrier charge p doped). N doped semiconductor is suffused with atoms with an excess electron. This allows for there to be an excess of electrons in this semiconductor. Therefore, there will be electrons in the conduction band. The P doped materials contain atoms with fewer electrons than the silicon, therefore at the valence band has an excess of holes. When the N and P materials are attached the gradient pulls holes and electrons towards one another. This creates a neutral zone. Generation of electron hole pairs causes the electron to cross this zone from N to P and creates the photovoltaic current. (Figure 1.1)[4,5]

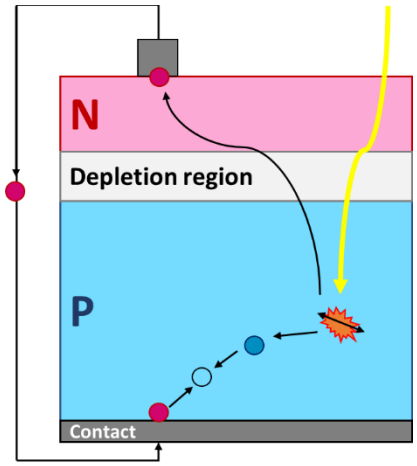

Figure 1.1: The P/N Junction in the context of a solar cell. The hole is extracted, the electron diffuses across the depletion region to recombine with the hole.

1.1.1. First generation

80% of the solar market is currently taken up by first generation solar cells. These are manufactured from crystalline silicon wafer doped to N and P silicon. These are the most efficient solar cells currently available on the market. Most of this is the cheaper polycrystalline which is made up of multiple silicon crystals melted together as opposed to single crystal cells. Single crystalline achieves around 22% Polycrystalline achieves around 15-18% efficiency and it currently takes around 4 years to recoup the costs of purchase and installation. These also have a higher production cost in terms of energy than second generation designs showing the need to scale back the amount of material used.[6]

1.1.2. Second and third generation

Second generation solar cells describe multiple ultrathin designs of solar cells designed to reduce the number of materials needed to create working solar cells. Thin films are deposited on large glass substrates or on flexible polymer support structures to make light flexible cells. Designs include different semiconducting materials such as cadmium telluride thin semiconductor layers. Cadmium telluride (CdTe) is a semiconductor with a band gap of 1.48 eV and can be used to create solar cells, these cells using a heteronjunction with Cadmium Suphide (CdS) to create a P/N junction. These cells are cheaper in the long term due to a 2 year payback time (compared to the 4 year payback time of crystalline silicon solar panels) as well as a lower production cost in terms of energy. However, Cadmium and Telluride are both toxic and carcinogenic, and although stable when in a lattice together, they pose risks such as pollution of the environment when the panels are disposed of at the end of their service life. Additionally they have a lower efficiency of around 11-15%.

Copper indium gallium and selenium (known as CIS or CGIS) thin films have also been used, this material is also a semiconductor with a bandgap of 1.1 eV which can be applied to glass or a flexible plastic backing making lightweight flexible panels, these again use a CdS heteronjunction and are cheaper but less efficient than conventional silicon solar cells.These second-generation thin film cells are a smaller share of the market than silicon wafer cells but are still under development.[6–86–8]

Third generation solar panels represent single or multi junction solar cells able to achieve higher efficiency and overcome the theoretical ~30% incident energy conversion efficiency limit of first- and second-generation solar cells. Multi junction solar cells have a high unit cost but have a much higher conversion efficiency. A multi junction cell uses multiple P/N junctions layered on top of one another. Each junction is made of a different material with a different bandgap, making each junction more sensitive to different wavelengths of light allowing these cells to be sensitive to more of the AM1.5 spectrum. The presence of multiple bandgaps reduces a loss called thermalization, where an electron is excited in excess energy of the bandgap and the excess energy is lost as heat.

An example of the different materials used in one cell are as gallium arsenide, indium gallium arsenide and indium gallium phosphide. Their applications are currently confined to space applications such as satellites as befits their high cost however their efficiency is high at 40-45%.[9]

It is also worth mentioning that most of the thinking around new generations of solar panels involves new semiconducting materials instead of improvements to existing materials. Other possible materials include using quantum dots (16% efficiency), using novel materials like perovskites (25% efficiency) or organic polymers as semiconductors (17% efficiency) and dye sensitised electrochemical cells (12% efficiency). These have not yet emerged as cheap and efficient solar cells but are the subject of research.[6]

1.1.3. Proposed sensitizing layers

Having enough silicon to absorb sufficient light to generate enough current creates expensive PV panels. A reduction in material would remedy this issue. In order to achieve this, a separation of the process of absorption and the process of electron hole pair generation is proposed. The semiconductor can be covered with an organic absorbing layer which transfer absorbed energy to the semiconductor, since this will be developed with a high absorption coefficient it has a much shallower absorption depth than bulk silicon. This energy can then be passed to silicon which would cause the splitting of an electron from a hole which allows the flow of current. Splitting the PV process allows for the use of very thin silicon. This is shown in Figure 1.2 .

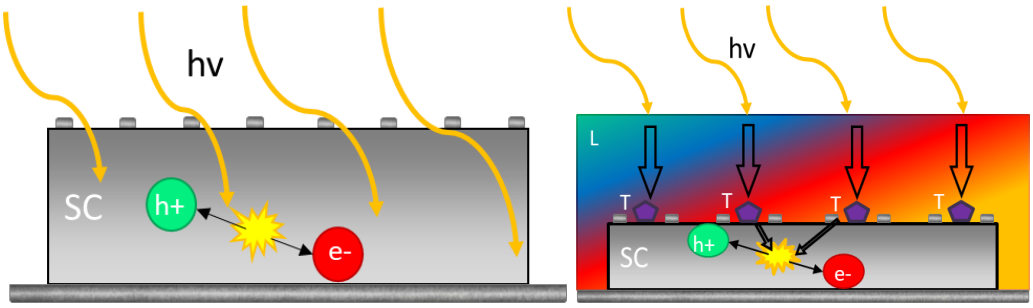

Figure 1.2 : (Left) A regular solar cell made of 150-400 µm thick bulk silicon. (Right) A thinner silicon solar cell using approximately 1 µm thick silicon with an absorbing layer applied to the top.

This presents a range of research questions; a broad range of absorbing wavelengths is needed in order to absorb a large proportion of the spectrum. As well as determining whether or not energy transfer would even occur between a sensitizer and a semiconductor or acceptor, these pairings need to have factors such as optimum transfer distance studied in order to facilitate efficient energy transfer as well as optimised ratio of donor to acceptor so that there are as few idle components as possible. The phenomenon to be investigated which is suggested to improve energy absorption is light harvesting.

1.3 Light harvesting

1.3.1 Photosynthesis and light harvesting

Light harvesting is a key component of photosynthesis.[10,11] This process involves pigments fixed in a protein structure which allows them to transfer the energy of excitation between one another. Energy can be forced towards a target molecule (in this case the reaction centre in the structure) and can be spatially directed to a target area.[11,12] The same concept may be used to inform the fabrication of a structure which allows this absorption of light and trapping of energy by transfer of excitation energy from one molecule to another in successively higher wavelengths ensuring that little energy is lost.[12] This is shown in Figure 1.3.

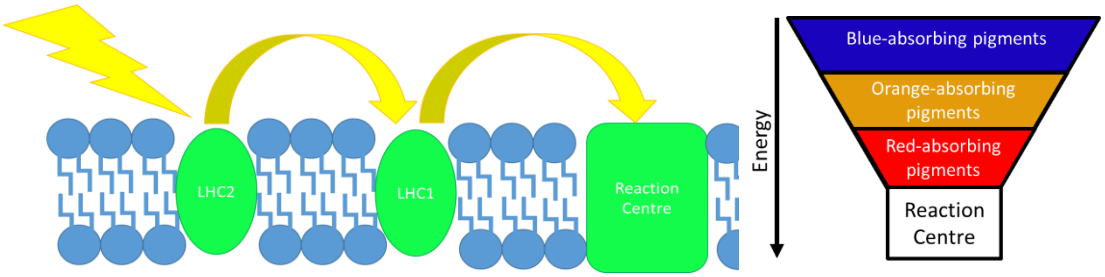

Figure 1.3: A schematic of a photosynthetic membrane which outlines the basic principles of photosynthesis showing how the energy from an absorbed photon moves in a nonradiative fashion from light harvesting complex 2 (LHC2) to light harvesting complex 2 (LHC1) to the target, the reaction centre. (Left) The absorbed energy moves from blue to orange to red pigments. (Right)

Photosynthetic light harvesting serves as inspiration for light harvesting devices. It should be noted this research is not concerned with replicating the complete action of photosynthesis itself which can split water and is a different area of research.[13]

There are different models of the organisation of the pigments in different photosynthetic organisms. The lake model describes the reaction centres completely surrounded by a continuous area of absorbing pigments. The puddle model describes each reaction centre surrounded by a group of pigments which are not connected as in the lake model. The two models are shown in Figure 1.4.

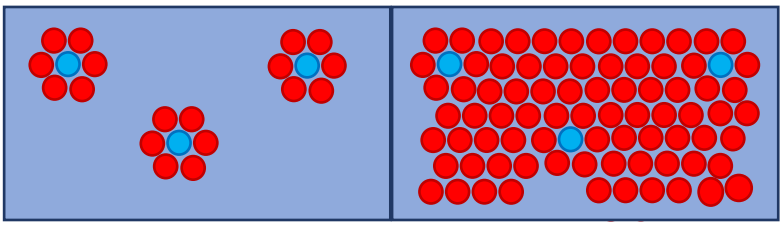

Figure 1.4: The Puddle model (left) and the Lake model (right) of pigment organization.

In the lake model the energy always finds its way to an available trap. This means that thin films are a good way to create an appropriation of this as it allows movement of the excitons to where they need to be no matter where in the structure they are absorbed. This takes place in the antenna system, fixed pigments move the excitation from higher to lower energy pigments, i.e., from a shorter to higher wavelength. There is also a

spatial aspect to the funnelling mechanism, meaning that the placement of the pigments within the structure ensures that energy is absorbed at any point.

1.3.2 Light harvesting for silicon.

The idea for the use of a film of sensitising molecules comes from Dexter[2]. This paper posits the idea of adding an organic absorbing layer that ends in a trap layer. This means the absorbing layer would perform the light absorption, the energy would then be moved to the trap molecules whose primary role would be to transfer energy to the silicon wafer extremely efficiently and therefore to bridge the gap between the absorber and the silicon.

Dexter specifically mentions the use of triplet excitons, the reason given is that they have very long diffusion length.[14] This is due to the forbidden nature of triplet excitons, giving the excited state a longer lifetime. A longer excited state lifetime gives it more opportunity to transfer to an acceptor.[2]

1.4 Literature review

1.4.1 Silicon sensitization

The primary goal of this thesis is to investigate the sensitization of silicon. Previous studies of silicon photosensitization have been carried out on energy transfer from various luminescent films to silicon substrates. These largely involve singlet dyes and will be discussed in this review. This is a first study in the use of rhenium and ruthenium triplet sensitization studied using time resolved methods.

Silicon sensitization is performed by separating the absorption of light from the generation of electron hole pairs using an absorbing layer. This concept of using an absorbing layer to achieve sensitization was first laid out by D.L. Dexter[2] who suggested that silicon wafers used for solar energy conversion will benefit from sensitization owing to its properties as an indirect bandgap semiconductor making it a poor absorber of light on its own. Separating the absorption of light from silicon using a layer with a much higher absorption coefficient can enhance the excitation rate of electron hole pairs in the silicon if energy transfer from the absorbing component is

highly efficient.[15] Splitting the PV process in this manner also allows for the use of very thin silicon.[2]

1.4.2 Use of triplet excitations in sensitizing

Dexter's paper specifically mentions the use of triplet excitons, the reason given is the long lifetime of triplet states makes movement of the excitation through the layer more likely as opposed to decay via singlet emission.[14] The excited state moves from molecule to molecule by energy transfer. Triplets move much further than a singlet due to their long lifetimes. This makes triplet states more likely to undergo energy transfer as they spend longer in the excited state than singlets and are far simpler to study by time resolved methods.[2]

Dexter also argues that a single photon absorption may produce two excitations if triplets are used. This is due to singlet exciton fission (SEF).[16] Singlets are higher energy than triplet states.[2] During SEF, a single singlet absorption and excited state results in two triplet excited states of lower energy than the parent singlet. If a triplet will transfer to silicon, then this would result in an effective doubling of the number of electron hole pairs as transfer of a single excited state to silicon produces a single electron hole pair. It is important to remember this is a multiplication in the number of excited states and not the amount of energy itself. This is the opposite of a well-studied phenomenon known as triplet-triplet annihilation (TTA).[17,18,19]

Triplet-triplet energy transfer in films has been studied extensively before. Regular triplet energy transfer occurs through Förster energy transfer but involves the exchange of electron spins as well as the energy. Dexter has performed work in the past to combine the Dexter and Förster energy transfer as a coulombic dipole-dipole interaction between two molecules.[20,21]

1.4.3 Examples of self-assembled sensitising layers

Klaus Lips and colleagues have published work on self-assembled and spin coated films.[22,23] Dye sensitized solar cells are the primary focus of the work, however the

work includes methods for silicon sensitization. Their work focuses on methods of adding layers of sensitizer inside or on top of silicon wafers. Earlier studies consisted of testing different sensitizers by forming sensitizing structures through industrial deposition methods and mechanical attachment solutions, such as using cuvettes affixed to a solar cell containing solutions of rubrene and Palladium porphyrin as an up-conversion unit to sensitise silicon. The palladium porphyrin acted as a sensitizer and the rubrene acted as an emitter. They claimed a 200 percent higher efficiency than previous up conversion devices using rare earth metals. Further work on characterization proves this to be a reliable upconverter.[22,23]

They later suggested the use of the same design of upconverter from dye sensitised solar cells to sensitise regular silicon wafer by installing them behind the wafer alongside a reflecting plate so that low wavelengths of infra-red light that passes through silicon is caught and reflected back at silicon in an upconverted state.[24]

Later chemically deposited nanostructures were suggested, tetracene interfaces were used to sensitise silicon being attached directly on top of the wafer and the energy level differences being probed. The tetracene was found to cause an overall reduction in photocurrent despite sensitising the silicon as light was blocked from coming in to the silicon by the tetracene, additionally the sensitization efficiency, despite using singlet exciton fission, was found to be low, only 8%. [25,26] Further work on metal organic frameworks yielded promising results for up conversion for sensitising perovskites.[27]

Other examples of work which explicitly expand on Dexter's ideas and study the sensitisation of silicon was introduced by Hayashi, Castner and Boyd[28] In their work, chemical vapour deposition was used to create lithium fluoride spacer layers in order to alter distance between the absorber/emitter layer from the semiconductor surface. They then used tetracene as an emitter. Gallium arsenide and silicon were tested as semiconductors. In the case of both silicon and gallium arsenide the rate of quenching decreased the further away from silicon the tetracene was deposited.[28] Examples of similar work completed around the same time showed similar results with different combinations of absorbing layers and semiconductors. Whitmore, Alivisatos and Harris[29] showed distance dependent transfer from Pyrazine layers to Gallium Arsenide using ammonia as a spacer.[29] The same behaviour of Pyrene spaced from (111)

Silicon wafer with Xe spacer was shown later by Alivisatos et al.[30] Similarly Sluch et al[31] used palmitic acid as an absorber/emitter and arachidonic acid as a spacer in Langmuir Blodgett films. They measured the distance dependence of the steady state emission intensity and fitted the results using a d^{-3} distance dependence for 100-300Å. Each paper mentioned so far was fitted with a d^{-3} distance dependence, however the adherence to the fitting varied. Hayashi, Castner and Boyd found a perfect adherence to the d^{-3} fitting, Sluch et al found a much lower level of quenching at a distance of approximately 25Å whereas Whitmore, Alivisatos and Harris found a higher level of quenching, showing that whilst at distances of over 100Å there is usually a high degree of agreement with the d^{-3} model, close to the surface of a semiconductor however there is deviation from the model between these three papers.

Recent research has shown a distance dependent phenomenon in similar structures. Moerland and Hoogenboom[32] used indium tin oxide (a semiconductor) as a quencher and tetraphenoxy-perylene diimide (TPD) as the absorbing layer and showed linear dependence of emission quenching. Quenching was observed at 0nm, 2nm and 5nm. However the rate of quenching began to plateau at 5nm and had almost completely plateaued at 10nm.[32]

The research lays out the basics of these investigations as using an inert spacer material to increase the distance between a sensitizing layer and a semiconductor, however they make use of chemical vapour deposition (CVD) and related methods. Compared to Langmuir Blodgett, CVD does not make as uniform a film as Langmuir Blodgett. They do not mention any cleaning techniques or microscopy measurements to confirm the uniformity or smoothness of the surface making it difficult to ascertain how accurate the distance measurements may be beyond the error they state.

Much of the work specifically on silicon sensitization up until 1998 has been covered in a review by Barnes, published in 1998.[33] The article covers much of the theoretical basis for energy transfer and effects of an interface on fluorescence emitters at very close distances.

1.4.4 Examples of synthetic light harvesting systems

Examples of attempts to mimic the light harvesting and water splitting of photosynthetic systems involved have been created. For instance, interconnected metal ions of ruthenium and osmium, connected by bridging or terminal ligands in so called dendrimer systems.[34] We argue that only the light harvesting step of photosynthesis needs to be re-created for silicon photosensitization as the electron transfer involved in photosynthesis is both complex and unnecessary. According to a review by Balzani et al[34] this causes energy to be moved around within these structures, the review also mentions similar structures incorporating porphyrins or organic absorbers.[34]
Energy transfer between layers of deposited material has been investigated using novel emitters, for example quantum dot systems have been extensively studied already. A review by Peng et al[35] summarizes much of the currently available work on quantum dots. They show the different methods of assembling layers. The methods of attachment covered are deposition of quantum dots onto functionalized silicon and metal surfaces. Using layer by layer deposition to build layers of quantum dots and Langmuir Blodgett techniques involving functionalised quantum dots. In particular the close packing created by Langmuir Blodgett was pointed to as being potentially useful to enhance interactions between the quantum dots owing to the closer distances allowing stronger energy transfer interactions.[36]

Förster resonance energy transfer has already been discovered between monolayers using these emitters. Yeltik et al[37] has published studies on layers of quantum dots. They include deposition on aluminium oxide on top of silicon oxide in order to create space between a quantum dot multilayer and the surface of the silicon itself. Quenching was measured as a function of the temperature of the sample. Hybrid nanostructures of multiple monolayer films were formed by spin coating wafers at 2000rpm. Film thickness was recorded by an ellipsometer. Time resolved measurements were performed between 520 and 610nm. As they reduced the distance from the film to the surface of silicon FRET became stronger, however reducing the temperature down to around 15^{o}C reduced the energy transfer to under 20%, whilst increasing it to 100^{o}C increased it to 50%. They also believe inter-dot resonance energy transfer was taking place allowing the charge to move throughout the film.[37]

In a later study[38] two different films of quantum dots, one absorbing at around 540nm and one absorbing around 630nm were deposited one on top of the other to funnel light energy from film to film towards the surface of silicon. Four different time resolved measurements were made of combinations of two-layer systems and two substrates. Either two layers of cadmium telluride green quantum dots with a radii of 1.29nm or CdTe red quantum dots with a radii of 1.86 nm, were deposited on either silicon wafer or cleaved quartz.[38] They found that the green quantum dots layer was quenched by the red quantum dots layer, and that the green layer was quenched by the silicon. The highest amount of quenching occurred when the green quantum dots and red quantum dots layers were deposited on silicon, showing 80% total energy transfer, this in, theory shows energy transfer from the top layer to the silicon.

A similar study by Nimmo et al[39] showed energy transfer to silicon from various sizes of quantum dots absorbing from 500 to 800nm whilst connected to silicon by alkyl chains. They found an energy transfer efficiency of over 90% occurring over the various sizes and composition of quantum dots.[39]
Subsequent experiments using differing sizes of quantum dots, which absorb and emit at progressively longer wavelengths, attached directly to silicon wafer which could channel energy from the excited states of the quantum dots down into the silicon via energy transfer, with non-radiative energy transfer being the dominant mode of transfer at close distances and resonance energy transfer becoming prevalent at longer distances. Colloidal nanocrystals of quantum dots showed quenching of fluorescence lifetime on silicon in comparison with control samples[39,40]

Other interesting work on quantum dots include the fashioning of silicon nanorods which are then covered in quantum dots, these can then be excited and studied. They found an increased reduction in the fluorescence lifetime compared to the same quantum dots deposited on flat silicon wafer. The increase in quenching was proportional to the increase in the surface area of the silicon owing to the introduction of the nanorods and was attributed to increased rates of both radiative and non-radiative energy transfer processes. Additionally, zinc sulphur and cadmium selenium quantum dots have been covalently grafted onto silicon wafer. Energy transfer to bulk silicon wafer from this layer was investigated and this work found both radiative and non-radiative energy transfer occurring with non-radiative energy transfer being the dominant mechanism of energy transfer to the silicon wafer.[41]

Finally, light harvesting has also been studied in similar concepts to what is being looked at in this project. Some studies have investigated triplet energy transfer and light harvesting structures in lanthanide complexes emitting in the Infra-red and near infra-red regions of the spectra. The aforementioned work was discussed in a review of the use of Lanthanides by Bünzli and Eliseeva (2010).[42] Crystalline structures of Europium, Terbium and up-converting Structures which used Gadolinium were discussed in their potential to be used on silicon wafer-based technology. When these up converting structures were applied to silicon an increase in energy conversion efficiency of up to 40% of absorbed light was found, however the absorbance of light was found to have a low coefficient. This may be a problem with using organometallic complexes as some which emit phosphorescence tend to have weak absorption coefficients and may underperform when compared to singlet emitting organic dye. Using multiple layers of material can increase total absorption of an absorbing layer but this both increases the cost of the layer, thus defeating the purpose of the absorbing layer. It would also sacrifice some energy transfer efficiency of the absorbing layer as it would give excited states a longer path to travel making losses through de-excitation pathways more likely.

1.4.5 The effect of metal surfaces on a monolayer of lanthanide complexes

Of interest is that decay is altered by modulation of the photonic mode density (PMD) by interference from an interface, this is what causes some of the changes in the lifetime of a sensitizer. However, non-radiative energy transfer is the predominant force and the focus of interest here. Emission is subject to external influences and energy transfer may alter the decay rate. The decay rate describes the probability of a group of emitters to decay from their excited state to the ground state. This is predicted as a group as it is not possible to predict the decay of a single molecule. When decay occurs, the energy released may not exclusively be as a photon.

In research, the method of introducing an interface at different distances from an emitter allows for studying the effect of changing the PMD through the introduction of the interface. The first demonstrations of this were carried out in the 1960s by Drexhage et al.[33,43] Other early examples include the proposal of models of how the

layer and the mirrors interact. Using the example of a Europium 3+ complex layer and a silver mirror. Morawitz[44] performed mathematical modelling supposing two separate systems of the mirror and the layer which interact with one another over a defined distance. In the model the mirror acts as a partial reflector. This means that reflected light may interfere with the emission of the complexes either constructively or destructively. Meaning that the signal either appears to have been reduced or increased. Förster resonance energy transfer (FRET) only occurs within a very close distance and according to the modelling FRET began around 500Å away from the surface.[44]

Drexhage[43] gives more details of the materials used. An Eu^{3+} Complex which absorbs in the ultraviolet region or around 200-300nm and emits light at 612nm with a high quantum yield was deposited on metal mirrors of silver using vapour deposition. The mirrors of silver were deposited on glass slides using vapour deposition. The theory explained and expanded on in this paper describes effects of the angle of the fluorescence as contributing to the constructive or destructive forces. This is somewhat controlled for as the orientation of a complex does not change after deposition during and experiment, although LB films may change their orientation over a long time. They again describe a random orientation, however they do not specify the assumed distribution of orientations and simply say their model does not favour one orientation over the other.[43] This also highlights an issue with some studies mentioned in this review, their use of steady state based methods to determine energy transfer is insufficient owing to fact that both orientation of the emitters on a sample relative to the excitation light and the amount of emitter deposited will affect the fluorescence intensity making it difficult to get an accurate measure of the energy transfer. This is a problem that time correlated single photon counting lifetime measurements solve as they are not affected by concentration and orientation.

The quenching of Eu^{3+} complexes by the silver mirrors followed the theoretical quenching, specifically that there was extreme destructive interference and quenching signified by a reduction in the emission of the film when compared (presumably) to a film of the complex not in the presence of a metal mirror (glass substrate). Both studies found that outside of the ranges of FRET there was destructive interference resulting in

a reduction of fluorescence and amplification of the signal from constructive interference. This is consistent with the theory described.[45]
The data shows important features, such as the expected oscillation, damping of the oscillation and quenching of emission near the surface. There are several features that influence this behaviour. The first which may influence quenching is the dipole orientation. Closer to the surface radiative decay stops and non-radiative decay takes over. Ishibashi et al[46] used tetraphenyl porphyrin on gold silver copper and aluminium surfaces to investigate this behaviour. When a molecule is wavelength/4 away from a surface distance dependence quenching begins to take effect, transferring energy from the dipole of the emitter to the substrate. In semiconductors this is considered a dipole-dipole transfer as a dipole within the substrate receives the energy.[46]

A further example of a Europium 3+ complex layer and a silver mirror, Morawitz[44] performed mathematical modelling supposing 2 separate systems of the mirror and the layer which interact with one another over a defined distance. In the model the mirror acts as a partial reflector. This means that reflected light may interfere with the emission of the complexes either constructively or destructively. Meaning that the signal either appears to have been reduced or increased. Förster resonance energy transfer (FRET) only occurs within a very close distance and according to the modelling FRET began around 500Å away from the surface.

They also had to consider the dipole orientation at this work, they assumed a distribution of the dipole orientation based on the weight factors of the dipole they came up with a distribution of 1/3 perpendicular to 2/3 parallel. This describes what they say is a random orientation, however it bears mention that in a Langmuir Blodgett film the orientation is often uniform. Meaning that if the complexes included long chain tails and polar head groups (which is not mentioned in this work) the complexes should all be in a similar orientation.[44]

The finding for all the silver mirrors matched the described theory, specifically that there was extreme destructive interference signified by a reduction in the emission of the film when compared (presumably) to a film of the complex not in the presence of a metal mirror. Both studies found that outside of the ranges of FRET there was still

quenching and even amplification of the signal. This is consistent with the theory described in the two research papers.[43]

However, a final paper by Chance, Prock and Sibley[47] expanded further, substituting "fatty acid layers" for cadmium arachidate and using a similar Eu 3+ complex performed the same experiment on silver gold and copper metal mirrors. They again found the same behaviour of constructive and destructive interface over 500Å away from the surface and quenching due to FRET closer to the surface.[48] In a separate paper published that same year they also undertook a more detailed study of the same Eu/Silver system at a longer distance and found good agreement with theoretical values at distances over 500Å, although they stated poor agreement at distances close to the mirror.[47]

Our research uses silicon wafer, which is a semiconductor as opposed to a conductor. It is possible that silicon may also act as a field of dipoles and can act in the same way as the metal mirrors mentioned in this research paper.

1.4.6 Spectroscopy and Langmuir Blodgett films of Rhenium and Ruthenium complexes

Rhenium Complexes have been investigated for their triplet exciton diffusion properties in previous research using single layer deposition methods. Rhenium complexes deposited in Langmuir Blodgett studies have ligands in common which enable deposition and excitation/emission. Most, if not all will involve some form of a bipyridine ligand and carbonyl groups, bipyridine based ligands may have added unsaturated chains to create hydrophobic regions of the complex. Additionally, the use of phenyl groups as an attachment point for longer chains is common, however the composition and configuration of these chains varies between studies. The same is true of the ruthenium complexes studied, most being based on an Ru^{2+} tris bipyridine head group.

Early examples like Li et al[49] studied films of an amphiphilic rhenium complex with and without complexation, both in solution and at the air water interface. They performed repeat compression-relaxation cycles up to a surface pressure of 25mN/m showing the

distance between the compression slope and the release slope produced during isotherm cycling widened suggesting increased film organization with increased compressions. They illuminated the complexes on the surface of water at 365nm and in solution and monitored for any changes in the isotherm after illumination.

Illumination produced changes suggesting in situ photoisomerization on the surface of the water and in solution. Of particular interest was the changes to the isotherm showing altered film forming properties. Evidence of photodimerization was shown by the disappearance of a 510nm MLCT absorption band. Illumination changed the area per molecule from 0.46nm^2 to 0.42nm^2 and compression every half hour showed a 0.38nm^2 molecular area which remained largely the same showing the film becoming viscous.[49]

Other studies have only focussed on study of the isotherms, in lieu of spectroscopic methods. An early example of this is by Yam et al,[50] three different ligands were synthesised to add to $ReCO_3$ to make 3 different complexes. Two separate solutions of three different $ReCO_3$ complexes were prepared and compressed into monolayers. Solutions were all slightly different concentrations; a compression speed of 150cm/min was used. The isotherms produced all show a liquid phase transition to a second gas phase on top of the regular isotherm. The molecular area did not change appreciably over repeated compressions and agreed with the theoretical value it showed a shift of the liquid phase to a lower molecular area suggesting the formation of a very highly organised film. They were all compressed to different constant pressure for deposition, and transfer ratios were reported to be close to unity, the samples were then used for second harmonic generation experiments.[50]

Synthesis of complexes containing complex ring structures for Langmuir Blodgett is also possible. Zhang et al[51] synthesised several examples of a Rhenium complex using aromatic rings in addition to saturated organic tails. Addition of the rings makes the complexes bulkier overall and act as the saturated tails which make the complex amphiphilic and therefore suited to floating on the surface of water. Ruthenium complexes were made using the same ligands, the ligands were varied by attaching a C18 saturated hydrocarbon tail at two different points on the ligand and experimenting with how this effected the rhenium and ruthenium complexes.[51] The Rhenium complex

showed a very intense absorption spectra in the 256-307nm band.[51] Compression isotherms for the complexes showed common behaviour for a large organometallic complex, the initial lift off region being followed by a liquid phase which does not transition to the solid phase. No deposition was recorded in this paper however they studied the second harmonic signal properties and found this to indicate good film forming properties.

In the same year even larger complexes were tested, Hwi et al[52] published a short communication in which a very large ligand was synthesised containing two C60 Buckminsterfullerenes as well as eight carboxyl groups and four $C_{17}H_{35}$ chain groups. They showed how the surface morphology of the films was affected by different compression pressures. The group had begun looking into using these for solar energy conversion.[52]

A later example of bulkier rhenium tricarbonyl complex films is Joo et al.[53] They use similar complexes to the ones in Fernandez-Moreira et al[54] but with very bulky chain groups with carboxylic acid groups and five membered rings. These showed a different isotherm, exhibiting a well-defined gas, liquid, and solid phase. One of these complexes is already used in DSSCs but could not be successfully compressed into a Langmuir film. They found that it could form “tubes” and micelles if it was over-compressed, this suggests that it is actually very good for Langmuir as it behaves more like “classical” Langmuir molecules. They also found that the shorter chain molecule formed a much better film, suggesting that the closer proximity of the head group to the water and the shorter chain length stops the films breaking down because of the molecules repelling each other.[53] A particular area of interest to us is the spectroscopy of such complexes and their transitions. Rhenium tricarbonyl complexes have characteristic spectral features, these have been described in many research papers before and have been assigned electronic transitions. A full explanation of MLCT can be found in the theory chapter.

Rhenium and Ruthenium spectroscopy has been extensively investigated, an early example is from Wrington and Morse[55] who undertook synthesis of various rhenium tricarbonyl 1,10 phenanthroline complexes and showed the absorption and fluorescence behaviour that defines these complexes. They show a sharp peak around

300 which is assigned to *d* to *π** MLCT and a broader peak close to 400nm which is assigned to *n* to *π** and *π* to *π** transitions within the ligands. This was one of the first examples of a phosphorescent Rhenium complex which absorbed and emitted light at room temperature and at 77^{o}k (-196^{o}C) which caused a down shifting of the emission by around 75nm. The provide additional commentary on the sensitivity of the complexes to their environment, showing the effects of solvent polarity, causing a shift to higher energy absorption, on the spectrum.

Differences in the ligands such as variants of the bipyridine ligands and phenyl ligands added to the complex, differences in solvent polarity, deposition into films and attachment to comparatively large nanoparticles. Studies of different ligands on similar complexes within one paper is common; An example of another similar Ruthenium complex was in Zhang et al[51], this being a rhenium with two bipyridine groups and 4 different variations of a third ligand with C18 chains attached.

They found the same high energy absorptions, intra ligand *π-π** transitions and Low energy *d/π* (Rhe) - *π** (diamine) MLCT mixed with *π-π** transitions which are expected from rhenium complexes at 256-307nm and 356-398nm respectively. They performed basic isotherm study in this case, performing single compressions and reporting this. However, this work did show that the modifications to the ligand caused all but one of the Rhenium complexes to be viable, showing that ligand design is an important factor.[56]

Complexes like the one used here have also been synthesised for energy transfer applications. Rhenium bipyridine tricarbonyl complexes with different long chain ligands for attachment were synthesised by Li et al.[57] All of the complexes showed extremely similar absorbance spectra to the complex shown here. A high peak from 250-320nm and a smaller broader peak from 350-400nm. This is consistent with work done previously to this by Yam et al[58], Coe et al[59] and Rajkumar et al [60], who all synthesised Rhenium Bipyridine tricarbonyl complexes with a variant of a Pyridium ligand. all showed a similar pattern of strong absorption at approximately 250-320nm and smaller shoulders around 350nm. However, Coe et al[59] and Yam et al[58] both observed absorption at approximately 400nm.[58–60]

Of interest is Yam et al[58] in this study Langmuir Blodgett films of the complexes were created. Included in this study was the deposition of multilayers of complex on glass from one layer to ten layers. The aim in depositing multiple layers was as a method to study the quality of deposited layers, stating that the linearity observed shows that each layer deposited increased the intensity of the absorption by the same amount. They also observe a shift in the spectra when changing one of ligands between three variant ligands.[58]

Phosphorescence spectra were also recorded for several complexes. The spectra all showed the same broad spectra and the peak for each one was approximately 550nm.[57,60] The only exception was Coogan et al[61] showed some shifts from 550nm when the complex was dissolved in water and hexane compared to acetonitrile. Water and hexane caused a shift down to approximately 520nm, this being consistent with previous work showing that solvent polarity causes shifts to higher energies. This is because the splitting of the d orbitals of the metal and thus the difference between the t_{2g} and the ligand π^* orbital becomes smaller or larger depending on the environment.[55,61] This shows that rhenium tricarbonyl complexes have a characteristic fluorescence which is only disturbed by changes in the nature of the solvent. It is therefore not unreasonable to expect a shift when they are deposited into films.

Light absorption improvement for dye sensitised solar cells has been attempted using ruthenium complexes. This is not impossible as Langmuir films of ruthenium complexes have been studied for their electronic properties before.[52,62] Dye sensitised solar cells were created by Graitzel and O'Regan,[63] and use oxidation and reduction of a solution. Electrochemical rhenium LB films have been studied, however they have been shown not to improve performance on dye sensitised solar cells.[64]

The ReC18 complex used in this study was synthesised in Fernandez-Moreira et al[42] synthesised for us by one of the authors on this paper Mike Coogan. The complex was one of a series of complexes created to be taken up by cell membranes, as such was created with a long chain tail group and polar head group. Whilst not perhaps making

the molecule fully amphiphilic does mean that it is given to forming a monolayer on water and therefore could be used with the Langmuir Blodgett technique. This is similar to the series of carbocyanine dyes we have studied as they too were originally synthesised as membrane tracers for confocal microscopy.[42]

Ruthenium is extensively studied in the context of thin films and energy transfer. Examples of energy transfer in ruthenium complexes in the solid phase already exist. Odobel et al [65]Showed shifted emission spectra for the osmium complex used, and using time resolved techniques were able to resolve a very short lived ruthenium emission, having been quenched by the osmium complexes.[65]

They found evidence of energy transfer and were able however to calculate the exact distance between the ruthenium and osmium complexes. One issue this may have been a practical one. Namely that the quenching distance to a semiconductor was not established, therefore whether this matrix would work as a coating in practice is yet to be seen.

However, examples of Langmuir studies do also exist and were published before this work. Okamoto et al[66] studied the effect on chirality, something which we have heretofore not considered in our research. They used ruthenium and osmium dpp3 complexes, these do not have the saturated hydrocarbon tail however they did create isotherms when they mixed two enantiomers of this complex in two different solutions in a 1:3 ratio of ruthenium complex to stearic acid. They created mixed films or alternately layered films spaced with stearic acid. They found chirality effects for the energy transfer and the way the complexes pack. This has not been considered by us yet, however we have so far been assuming no effect of chirality. Since this could be an entire project in of itself, we may not have chance to study this. However it is something important to consider when trying to analyse results and is a feature of columbic interactions.[67]

Ruthenium complexes using ring structures with an attached hydrocarbon tail group have also been synthesised and characterised, in terms of Langmuir Blodgett in other

research papers. These complexes behave in a manner similar to simpler amphiphiles compared to other emitting molecules. They also find H and J aggregate formation; this could indicate similar problems to using carbocyanine dyes in that any spectral properties that are found to be undesirable because of the changes to lifetime properties or absorption and emission range. The MLCT bands were found to be down shifted in this work when J aggregation occurred.[68,69]

One thing that this research has brought up is the fact that if a large range of the spectrum is to be absorbed then different complexes of each heavy metal must be investigated, the reason for this being that different ligands applied to the same metal ion centre causes shifts in absorption and emission spectra. Indeed a colour change was observed in a film of Biphosphate complexes showing the need for a large variety of complexes to be studied.[69,70]

In all rhenium and ruthenium complexes are both well studied and have been shown to be versatile. They have been shown to form Langmuir films readily and have a distinct isotherm shape that is extremely different to a classical isotherm. There has been shown to be variation between the molecular areas, shown to be between 25-145Å^2 with the majority around 60-80Å^2 for rhenium complexes [50,51,53,58], and between 30 to 90Å^2 for ruthenium complexes.[70,71] It is difficult to draw comparisons between studies however as many studies show different complexes. All show a similar range of absorption that covers the ultraviolet and blue end of the visible spectrum.

1.4.7 History of cyanine dyes.

Cyanine dyes are a well-studied class of dyes that have existed for over a century and are part of a family of dyes known as methine and polyene dyes.[72] First discovered in 1856 and christened cyanine dye after the blue colour it exhibited. In the intervening years many analogues would be developed and by 1922 the dyes were the subject of research into their viability as sensitisers in silver-based photography, showing their potential to act as enhancers of light absorption, they would go on to play a role in the development of colour photography.[72] The advent of polymer-based fibres gave cyanine dyes a role in the textile industry as incredibly fast dyes for polyester-based

fibres (fastness referring to the resistance to dyes running from fabrics). Research on cyanine dyes shifted focus to optical data storage in the 1980s.[72] Today cyanine dyes are used as labelling agents in the study of cells using fluorescence microscopy. They are favoured for their ability to bind to many different components of cells such a membranes, DNA and various proteins with various colours, allowing differential staining of different components of a cell with relative ease.[72]

1.4.8 Steady state spectra of thin films of cyanine dyes

An example of thin film work using 3,3'-Dioctadecyloxacarbocyanine (DiO) is seen in the works of Danos, Greef and Markvart.[73] This work was primarily on films of DiO mixed with stearic acid and expands upon work done on the aggregation studies of DiO and control thereof by Beismanns, Van Der Aurweraer and Schriver in 1990.[74] By adding a saturated chain carboxylic acid in a mixed solution with DiO and depositing it as a film the amount and type of aggregation can be controlled. The effect on the absorption spectra of this aggregation manifests in an increase in the intensity of the peak assigned to the aggregates (465nm) in comparison to the peak assigned to the monomer (480nm).[73] This information is useful in determining the presence of aggregation and also shows that there is precedent for the mixture of DiO with co-molecules which can result in changes to the tendency for aggregation.

The fluorescence of DiO in solution follows the mirror image rule and shows a single strong peak at around 520nm with a smaller hump at a higher wavelength of 570nm. The shape and location of the peak are characteristic of the small stokes shift of a singlet emission, this also gives the dye extremely good overlap with itself, which plays a positive role in exciton diffusion. When deposited into a film the mirror image rule no longer applies. Between two and three emission peaks can be seen which do not follow this rule and significant red shifts to lower energy states can occur. Fang et al[75] show this behaviour with mixing of the dyes in different ratios, this shows the range of spectra which may be created when the aggregation is controlled by the addition of stearic acid, each peak representing emissions from different aggregation species within the films.

DiO has been shown to readily form aggregates with multiple emission peaks, DiI however does not show the same alteration of the emission spectra. This is due to the

fact that DiO has multiple modes of aggregation, able to form dimers (two molecules) trimers (three molecules) and higher order aggregates consisting of multiple molecules.

Pure DiO was deposited by Chakraborty et al[76], to study control of the aggregation effects. In this study two subphases were used, Millipore water and a laponite dispersion in Millipore water. The DiO was deposited using chloroform. The dye was deposited onto a quartz plate in a hydrophilic fashion. Changes in the concentration of laponite related to broadening of the spectra and observed blue and red shifting of the two peaks of DiO. Blue shifting is attributed to the formation of H aggregates, the red shifts to the potential formation of a unique type of hybrid aggregate in the presence of the laponite, however increasing the laponite concentration controlled the aggregation. Similar studies of the same dye have shown the presence of J aggregate formation, suggesting that aggregation can be controlled by altering the subphase. This may have the advantage of still allowing the deposition of immobilised pure films of dye.[76,77] Aggregation control is important to consider in Langmuir Blodgett studies, especially in the case of monolayers of spectroscopically active molecules, aggregation will have an effect on the results.

Debnath et al[50] has also studied aggregation of cyanine dyes and showed an example of the fluorescence changes in DiI.[78] In this study DiI J aggregate formation was achieved and the degree of aggregation was controlled. Similarly, to other studies and to the methods used here, ultrapure water was used and similarly to Chakraborty, high volumes of less concentrated solutions are used. Mole fractions of DiI to stearic acid were created of 0.1-1 to 1-1 showing only small changes in the molecular area compared to the pure DiI isotherm. Depositions were performed on a cleaned quartz surface for spectroscopic characterisation.[78] Debnath et al[78] showed fluorescence maxima shifts to a higher wavelength occur, the absorption spectrum does not show any change. However they report controllable aggregations.[78]

By studying the excess molecular area and Gibbs free energy of the film, calculated in Matlab, they were able to ascertain the most stable ratio. This ended up being around a mole fraction of 0.4, they were able to relate this to changes in the absorption and fluorescence spectra which revealed how the rate and type of aggregation can be controlled by varying the ratio of stearic acid to dye molecule. They were able to use

FTIR to study the way the head groups were interacting with the stearic acid being used as a spacer which confirmed the mechanism by which aggregation was controlled.[78]

1.4.9 Thin Films of cyanine dyes in sensitization

The cyanine dyes shown in this study form films readily and exhibit high absorption coefficients. This group of four dyes has overlapping shifted absorption and fluorescence spectra, making donor acceptor energy transfer possible which makes them ideal for use in a donor acceptor framework.[79] Sensitization means that the absorption of light energy occurs separately to the silicon wafer which allows for the use of very thin silicon wafer. To develop a light harvesting structure, improving the absorption range of individual dye layers must be achieved which would enable absorption of as much of the electromagnetic spectrum as possible. A solution to this issue is to introduce dyes which cover much of the solar spectrum and can undergo energy transfer with other dyes within the film.

As far back as 1965 the use of cyanine dyes has been suggested for sensitisation. Whilst not specifically referred to as cyanine dye, two papers by Kuhn[80,81] discuss the use of dyes in detail. The paper "*Versuche zur herstellung einfacher organisierter systeme von molekülen"* (Attempts to produce simple, organized systems of molecules) published in 1965 discusses the uses of organized systems of sequential molecules deposited using the Langmuir Blodgett technique which may sensitise a surface by energy transfer. They discuss the appropriate way to deposit sequential layers, comparing a hydrophobic and hydrophilic single orientation method and the "traditional" alternating orientation that LB can produce. This study also performs some early energy transfer work with cyanine dyes, using three different dyes and discusses using the pairs of dyes with inert spacers to determine the distances at which energy transfer will occur.[80]

Kuhn expands upon this idea further in a review of several concepts[81] which states that using a layer of J aggregated sensitizers can take advantage of the properties of a J aggregate, for instance highly efficient excitonic diffusion through the layer, this facilitates efficient transfer as excited states will be able to seek out an "exit point" to

transfer to the next layer, diminishing losses through radiative and non-radiative de-excitation.[81]

Use of cyanine dyes as a molecular ruler is reported by Kuhn and Mobius[82] which is an early example of the use of cyanine dyes energy transfer. They describe the formation of “sandwich aggregates” and how the formation of these aggregates changes the patterns of absorption and fluorescence. In particular that aggregate formation tends to result in formation of maximal absorbance peaks at shorter wavelengths (higher energy) and maximal emission peaks at longer wavelengths (lower energy). This will be extremely relevant to the data collected in this study. Recent studies on the exact dyes being used in this study have shown similar transitions.[82]

Use of light harvesting based on photosynthetic principles requires research into both energy transfer from such structures to silicon and into the structures themselves.[11,83] Mixed films would allow the creation of light harvesting structures which requires research into their donor acceptor behaviour within a thin film. Light harvesting behaviour is a phenomenon seen in photosynthesis where it has over 90% efficiency of energy collection from sunlight.[12] More recent examples of this work were performed with cyanine dyes by Danos et al[73,84], including 3,3'-Dioctadecyloxacarbocyanine (DiO). In Danos, Greef and Markvart[73] DiO was deposited on increasingly thicker multilayers of stearic acid. It was found that the fluorescence intensity dropped the closer the deposition of the dye layer was to the surface of silicon. The drop-in fluorescence intensity suggests that energy transfer to silicon wafers from dye layers will occur, but that transfer becomes weaker with distance therefore cyanine dyes could be used in a light harvesting structure if used as part of a light harvesting structure with efficient exciton diffusion.

Ellipsometry was used to ascertain the thickness of the stearic acid monolayers, using the same refractive index as the silicon wafer’s oxide.[73] Optical spectra were obtained by excitation with a Xenon arc lamp. They found a high degree of control for the stearic acid monolayers and found that if quenching increased then the layers were closer to silicon. Further research by this group showed that there were some effects from aggregation, they performed similar experiments with mixed monolayers of stearic acid and DiO in order to control the amount of aggregation.[73]

Decay curves were measured as well, eliminating the problem of emission intensities depending on the amount of emitter, they found that the properties of the excitation and emission can depend on the concentration of dye in the monolayer. Monomer emission was found at molecular ratio of 1-100 Dye-Fatty acid. Significant quenching still occurred below 10nm with respect to silicon wafers. A Förster radius of 5nm was estimated.[73,84] This work is important to consider for two reasons, it is a good example of the usage of carbocyanine dyes for silicon sensitization and shows that the dyes used in this study can be used as part of a sensitizing structure. Additionally, some aspects of this work have been replicated by in this thesis and some of the methodology was used to study triplet emitting molecules in order to observe differences between the behaviour of the emitters and to optimise them for a light harvesting structure.

Energy transfer between molecules in separate layers has been studied in carbocyanine dyes. Meng et al[85] studied the use of carbocyanine dyes. They sandwiched a cyanine layer between polymer donors and C60 buckminsterfullerene acceptors and found energy transfer from the dye to the C60 efficiencies of 10% creating a reasonable organic solar cell showing how carbocyanine dyes can be used to enhance some of the properties of solar power generation.[85] Other examples from groups in the field claim to already have taken some of this research to develop solar technologies, Sinin et al[86] sensitized etched silicon with nanowires and alternate layers of DiO and DiI they saw increased charge trapping with both these layers on silicon, however they do not seem to have actually studied the energy transfer between the two dyes. Both of these papers show that energy transfer from cyanine dyes to an acceptor is possible, it therefore stands to reason that a pair or a set of cyanine dyes would exhibit energy transfer behaviour if the theoretical conditions of overlap between the absorption of one dye and fluorescence of another is met. Additionally, whilst Sinin et al[86] never directly observed the energy transfer to silicon nanowires by means of observing the effects on the fluorescence emission of the cyanine dyes, they did find evidence of the presence of cyanine dyes transferring energy to incredibly small amounts of silicon. They showed the accumulation of charge carriers in the silicon nanowires to be higher compared to uncoated nanowires when sensitized with alternating DiO and DiI layers, suggesting sensitization by energy transfer.[86]

Challenges with this research include the fact that simpler methods of deposition such as spin coating are used, and no fine control is exerted over the distances between the dyes or the surface of the silicon nanowires meaning no effort to discern the optimum structure is being made. This is not intra layer transfer either, and inter layer transfer has been shown several times over using other emitters.[38] This does however prove the concept that adding dyes to the surface of silicon may increase the number of charge carriers.

1.4.10 In situ studies of films on the Langmuir Trough

Dietmar Mobius[87] has been involved in several Langmuir Blodgett projects studying the air water interface interactions of films. In the case of these studies a customised trough was fabricated including a reflectance spectrometer built from several different parts. In this case the light was separated into two different light traps, allowing for reference and sample areas. They observed porphyrin dyes, they found linear correlation between amount of light reflected and dye concentration and were able to take reflection spectra of dyes on the surface of water of very high quality.[87]

IR spectroscopy is often carried out on films of fatty acids in order to elucidate their conformations. For instance, in a study of the head/tail arrangement of a Langmuir film of the surfactant Dipalmitoylphosphatidylcholine (DPPC) by Ma and Allen[88], peak shifts were observed in different environments when the film was compressed to different surface pressures, indicative of conformational changes as the film becomes more and more organised.[88]

Similar examples of infrared measurements at the air water interface have been recorded. The IRRAS, or infrared reflections-absorption spectroscopy system from Rutgers University is an example of another purpose-built device described by Mandelson and Flach.[89] Similar methods have been demonstrated before such as the in-situ FTIR investigation of Langmuir monolayers of octadecanoic acid and octadecanol which were performed.[90]

1.4.11 Surface characterization using AFM

Atomic force microscopy is used to create topographical measurements of microscopic structures in films. J aggregates have been measured using AFM, Porkhorov et al[91] visualised stripe and leaf J aggregate morphologies on J aggregate carbocyanine dye films. 3,30-di(g-sulfopropyl)-4,40,5,50-dibenzo-9-ethylthia- carbocyanine betaine pyridinium was dissolved in water. They do not specify how deposition occurred. They show several raised structures on the surface of the mica taking the form of very well-defined rectangles, or of leaf like structures which overlap. These are presumably the aggregates. The tip used was “several nanometres” in diameter and 220-300kHz frequency. No other properties of the tip were given. These structures give us something to look for in our work, allowing us to visually confirm the presence of J-aggregates as well as using the AFM to potentially figure out how they have formed.[91]

J aggregates can form in different structures, ladder, and brickwork, which can be observed using AFM. Papers have shown ladder aggregates to appear on an AFM image as lines aggregates to appear as leaf shapes. Since these are known. [91,92] Other papers on thin films have shown some problems with AFM on thin films. Magonov et al[93] discusses the difference in measuring thin films using constant contact mode. They created films of a “$C_{60}H_{122}$” using spin coating onto freshly cleaved graphite In this case this creates “shearing force” which may cause a broken tip.[93] Increasing the temperature caused the film to become more pliable, in this case using a lower tapping force caused the tip to stick in the film, presumably because exposure to other points of attraction on the molecule makes the tip more likely to stick to the film or because the tip is able to move into the films and get caught. AFM on stearic acid films is not uncommon, studying the effect of variables on film morphology has been attempted before.[93]

1.4.12 Examples of lateral energy transfer

Some examples of energy transfer within a monolayer have been reported. Sakomura has performed two pieces of research very similar to what has been performed in this thesis.[94,95] However, there are key differences. They tested ratios of donor to acceptor from 50-1 up to 2000-1 donor to acceptor and dyes which covered a high energy end of the spectrum which arguably is not where silicon wafers struggle to absorb light. Additionally, both works use only emission intensity in order to calculate the energy

transfer which can be affected by the concentration of dye on a surface. However, they do two things which we wish to emulate in this study. They determine how energy transfer is occurring from a donor to an acceptor laterally and show light harvesting behaviour of an exciton moving through multiple donors to a single acceptor.

The premise of the first paper by Sakomura et al[94] is that there have been multiple attempts at using energy transfer systems for light harvesting prior to this research being carried out and that these often utilise multilayer systems to improve light absorption, however they make the argument that the density of the antenna molecules is not high enough in these systems meaning that any given area there needs to be a high concentration of donor dye. In this case the cyanine dye N, N7-dioctadecyloxacyanine (Cy), is used a s a donor and a perylene derivative is used as an acceptor.

The solution proposed to this is to find aggregates that undergo efficient energy transfer. They provide rationale for choosing a cyanine aggregate as it acts as an efficient donor with a broad fluorescence spectrum which provide high donor, acceptor overlap.

The method is very similar to the one in this study with key differences. They still had ratios of donor to acceptor up to 100 to 1. However, they also added a fatty acid, octadecane, in the same ratio to acceptor as the donor. Therefore, for every molecule of donor there would be a molecule of octadecane. This they said was to act as a spacer and claimed it does not contribute to molecular area, but they do not elaborate on this point. They deposited additional ratios up to 2000-1. They found that energy transfer occurred in the very high molecular ratio samples and the low molecular ratio samples, however in the case of 20-1 and 50-1 the transfer was significantly lower. This is attributed to the presence of aggregates in the film as the predominant bands measured were the dimer and higher aggregate bands of the fluorescence. They did not present energy transfer efficiencies but rather tried to ascertain when the “antenna effect” of all donors being quenched by a single acceptor would take place. This was found to be at the lowest ratio in both cases, 250:1 donor to acceptor.[94]

Further study was published by Sakomura et al[95] where Cy was tested as a donor/acceptor pair with viologen as the acceptor in much the same way as before. Of note in both of these studies is the isotherms.

1.4.13 Light harvesting porphyrin systems

Porphyrins feature in a number of reviews into light harvesting, an area which encompasses a wide range of different approaches. According to a review by Balzani et al[34] research into analogues of the photosynthetic mechanism includes examples of attempts to copy the photosynthetic electron transfer mechanism (which is involves oxidation of a donor and reduction of an acceptor, differentiating it from non-radiative energy transfer), such as metal ions of ruthenium and osmium connected by bridging or terminal ligands in so called dendrimer systems, and similar structures incorporating porphyrins or organic absorbers all of which cause absorbed light energy to be moved within these structures.[34] Whilst electron transfer is different to NRET and not the objective of this study it does show that porphyrins are capable of emulating part of the photosynthetic process.

Hansen et al[96] states that light harvesting relies on heavily π conjugated systems, to that end bridging ligands were used to look at the non-radiative triplet energy transfer between porphyrin and anthracene complexes and showed that porphyrins with a ruthenium metal centre extended the lifetime of anthracene ligands attached to the complex from 20µs to 600µs. This shows that porphyrins have worked as an sensitizer that enhanced fluorescence emission which could form the basis of a light harvesting sturucture.[96] However this area of research has been mainly focussed on electron transfer, which involves the oxidation and reduction of donor and acceptors as opposed to energy transfer which does not involve the movement of electrons between donor and acceptor.[96]

1.4.14 Langmuir Films of porphyrins

Dietmar Mobius undertook studies[87] using a customised trough with a built-in reflectance spectrometer. The light from the illumination source was separated into two different light traps, allowing for separate reference and sample areas. They observed monolayers of TPP with attached C18 saturated chains mixed with methyl arachidate

(AME) fatty acid and tetra- sodium-mesotetra-(4-sulfonatophenyl) porphine (12-hydrate) (TSPP) mixed with AME and showed a linear correlation between the amount of light reflected and the dye concentration in the monolayer from the reflection spectra.[87]

This shows that modified porphyrins can be prepared into very stable monolayers and allow deposition into films with the expected changes in photophysical behaviour. Further study by Zhang et al[97] revealed that aggregation of porphyrins occurs and can be controlled. Mixed monolayers of stearic acid and TPP which was modified to have an additional C18 unsaturated chain and methyl groups attached to it were studied using a Langmuir trough. The presence of stearic acid caused aggregation which was confirmed using UV-visible spectroscopy and infra-red spectroscopy. This shows the great controllability of porphyrin aggregation as it only occurred upon the addition of stearic acid to the film.[97]

However, porphyrins have shown to form visible aggregates even without the introduction of fatty acids into the monolayer. Togashi et al[98] showed aggregation occurring in amphiphilic porphyrins with saturated C-12 chains added. Investigation using fluorescence lifetime microscopy (FLIM) was employed and showed the formation of islands. This is a strength of this work over the work of others, the formation of aggregates is usually inferred from changes in the spectra or the isotherm which could be attributed to other things. Direct observation of samples negates this and confirms aggregate formation is related to changes in the isotherms and spectra.[98]

Biswas et al[99] studied J aggregation of the porphyrin 5,10,15,20-Tetrakis(4-sulfonatophenyl) porphyrin (TSPP). They found formation of aggregates using alterations in the pH of the subphase and the addition of a polymer to force the dyes together produced similar spectroscopic shifts in the absorption peak around 440nm and a markedly shorter emission lifetime, showing a 64% reduction in lifetime from 6.4ns to 2.2ns. This suggests that aggregation is something which may reduce the emission lifetime and make the porphyrin a poor sensitizer unless properly controlled, however they do not make mention of how the quantum yield changes or if it does at all therefore it may only make the porphyrin difficult to study fir sensitization purposes which shows a need for different methods of detecting sensitization.[99]

1.4.15 Tetraphenylporphyrin Langmuir Blodgett films

Tetraphenylporphyrin (TPP) is not a naturally amphiphilic molecule and therefore needed to be stabilised at the air water interface. A common method of stabilization of the monolayer is mixing in molecular ratios with molecules known to form very stable films.

An early example is a paper by Bull and Bulkowski.[100] TPP had zinc, copper, cobalt, magnesium and nickel respectively in the +2 redox state inserted. These were then mixed with stearic acid in a 1-1 molar ratio and deposited on a Langmuir trough which yielded incredibly small molecular areas with respect to their expected molecular area. The addition of the stearic acid reduced the molecular area by approximately 20$Å^2$ and broadened the absorption spectra. No aggregation was observed and stable films were achieved.[100]

Films of unmodified TPP have been shown to be very sensitive to the deposition procedure, Mansur et al[101] showed that even the “spreading method” could have an effect on the orientation of TPP molecules on the monolayer, and observation of the absorption in the soret bands showed aggregation differences. This was tested by varying the speed of spreading, however in the work itself the flow rate of spreading is not quantified in vol/unit time. They instead quantify it as “one shot”, presumably the entire 200µl at once, “one drop” per second and “one drop” per five seconds.[101] This is a somewhat unscientific measurement as it is impossible to repeat, the size of the drop depends on the specific syringe and the movement of the syringe, they did not use the scale on the syringe to estimate the amount of material in a drop. Nevertheless, it does show that the formation of a monolayer by the pure porphyrin depends on this spreading method, with slower spreading allowing a much more stable monolayer. These films have been shown to be sensitive to pH changes as the hydrogen in the centre of the ring can be oxidised or reduced the pH of the environment. This shows the porphyrins to be somewhat problematic to work with without stabilizing the molecules in the Langmuir monolayer.[101]

It was additionally found that the metal added to the centre affects the film forming properties. Li et al[102] created multiple films of porphyrins. Tetraphenylporphyrin with chlorine terminated phenyls was used and terbium or gadolinium were inserted into the porphyrin ring. Stearic acid was used again as a monolayer stabilising agent. Mixing TPP with stearic acid in a 1-1 ratio gave the isotherms a smooth curve with no defined features as opposed to the expected appearance of an isotherm with a gas, liquid, and solid phase. The porphyrins deposited on their own showed multiple area where the rate of increase in surface pressure suddenly decreased, resulting in a hump in the isotherm.

Despite the two molecules having roughly the same molecular perimeter differences in the molecular area between different metals are recorded. They posit that the metal influences the way the stearic acid is able to interact with the porphyrin and the positioning of the Phenyl groups, in the case of the gadolinium it allowed the phenyl groups to rotate in the presence of the stearic acid, thus causing a change in the orientation of the complexes. The changes in the complex conformation were measured using infra-red spectroscopy and AFM as well as in situ polarised spectroscopy. This is an extremely strong method of detection for orientation as the S and P polarised light absorbs differently for different molecular orientations. Additionally, the infra-red spectroscopy identifies the changes in conformation which both can be tied back to the observations made on the microscopy images.[102]

1.4.16 Non-Langmuir Thin films of Tetraphenylporphyrin and other porphyrins

Functional deposition using non-Langmuir Blodgett thin film deposition methods have been demonstrated for various porphyrins and, showed them to be a versatile and robust tool for functional deposition. This is important to consider as when moving from the research phase to real world application, Langmuir Blodgett or Langmuir Schafer films are not usually used on large scale production. For instance Tetraphenyl porphyrin mixed with polymers and deposited onto carbon nanotubes has been researched in the context of glucose detection.[103]

TPP has also been shown to thermally evaporate using chemical vapour deposition and this offered a high level of control over the thickness and level of film annealing was varied. This paper shows an absorption spectrum a maximum peak shifted down

to 380nm.[104] In particular the optical band gap has been shown to be affected by the deposition of porphyrins into a thin film using chemical vapour deposition.[105] This has been shown to be because of the formation of crystalline structures during evaporation and treatment with solvent.[106] This is analogous to the aggregation shown in the Langmuir films.

Porphyrins function as a large ligand and can have metal ions inserted into the centre of their ring and this will modify the absorption and emission wavelengths of a porphyrin. When deposited into a film similar optical shifts are shown as in other thin film methods. In the case of Tetraphenyl porphyrin for instance, a large absorption peak with a shoulder at around 450nm is present alongside a smaller peak at 440nm when the TPP is deposited into a film. The process of annealing a non-Langmuir film into crystalline structures was shown to increase the intensity of the peak at 440nm, suggesting that this process is evidence of aggregation.[107]Additionally the attachment of Protoporphyrin IX to silicon has been shown to result in quenching of the fluorescence by silicon wafer, therefore the effect of the presence of porphyrin layers on the silicon wafer itself should be tested.[108]

1.4.17 Conclusion of literature review

There is a large body of work containing various approaches to utilising inspiration from photosynthesis for solar energy conversion. We argue that only the light harvesting need be imitated. The steps to imitate light harvesting are laid out from previous works and it is therefore an important step in the process to find sensitizers that will transfer energy to silicon wafer from a thin layer with extremely high efficiency. There is a strong body of evidence using distance dependence measurements on metal mirrors to observe the effect of these surfaces on the emission of light, most importantly at short distances quenching occurs, the pattern of reductions and increases in theoretically predictable ways. Similarly, there are examples of distance dependence work on silicon wafer using inert spacer created with non-monolayer methods such as spin coating and chemical vapour deposition and there are few examples of up conversion, those that do exist having low efficiency. Investigation of this behaviour with therefore not investigated complexes using the Langmuir Blodgett technique is therefore an important area of research. Rhenium and ruthenium complexes have been studied in Langmuir films before and have shown to form films which have been readily characterised showing their potential for this area. Similar complexes have been

investigated in relation to metal mirrors such as films of gold silver and copper. It is entirely possible that silicon wafer may act in a similar manner. Therefore, it is important that monolayers of these complexes be investigated in such a manner so as to eliminate problems with previous studies by forming a single highly organised monolayers of emitter which can be studied using a method which does not exhibit issues associated with steady state based methods of determining the rate of energy transfer.

Cyanine dyes have been shown to be effective at forming Langmuir films and a large body of work on the aggregation of these dyes in films has been written. Much is known about the way these molecules interact at the air water interface. There is also work on the absorption and fluorescence spectra of these dyes in thin films showing that changes to the spectra can be assigned to differences in the way the dyes are interacting in the films compared to the solutions.[73,78] Additionally, they have been shown to have the ability to sensitise silicon wafers showing that they already have the potential to be used as part of a light harvesting structure.[73] A large body of work on the microscopy and characterization of these films adds to the ability for interpretation of the films in multiple ways as well as attempting some novel techniques based on in situ characterization of previous Langmuir films.

Lateral and inter layer energy transfer has been shown between dyes in the cyanine family of dyes however the characterization of such has used comparatively simplistic methods. These studies rely on a reduction in the steady state fluorescence of the donor molecule. They show little characterization of the quality of the films produced which limits interpretations of the role that this and the formation of structures as a result of deposition into a solid monolayer may play in the energy transfer pairs.[95]

Considering their potential in creating a light harvesting structure that can sensitize silicon, this chapter intends to take a dye which has been extensively characterised and has been shown to sensitize silicon readily and pair it with an acceptor from the same family of dyes to measure lateral energy transfer within a Langmuir film which should aid in the development of our understanding of the phenomenon.

The literature shows porphyrins to be strong candidates for light harvesting. There have been multiple example of structures combing porphyrin and heavy metal ions which have demonstrated electron transfer and enhancement of fluorescence due to the presence of a porphyrin. Additionally, they have already been successfully attached to silicon wafer which resulted in a distance dependent quenching of the fluorescence emission of protoporphyrin IX.[108] They have also been studied in the context of thin films and Langmuir Blodgett films. In particular TPP has shown to be very flexible with regards to the addition of chains and the insertion of metal ions allowing them to serve in a variety of roles and will form films given the correct conditions. TPP has been shown to form aggregates which can be controlled using pH and mixed monolayers with stearic acid creating incredibly stable films. TPP an excellent candidate for silicon sensitization however the next step in this research is not only to investigate the quenching of the sensitizer but also to investigate the direct effect on silicon wafer. In order to observe the increased or decreased generation of electron hole pairs in the silicon wafer.

1.5 Thesis objectives

Using these ideas of light harvesting and the use of an organic thin film this thesis endeavours to show 3 modes of silicon photosensitization using Langmuir Blodgett films to deposit monolayers onto the surface of silicon wafer. Photosensitization will be shown using steady state and time resolved spectroscopic characterisation techniques and the relative strengths and weaknesses of each sensitizer will be discussed in detail. I will also show an example of light harvesting behaviour within a Langmuir Blodgett film using a known sensitizer of silicon.

2. Theory

2.1 Photophysics

2.1.1 Properties of light

Light is described as being simultaneously a stream of particles, which are known as photons, and an electromagnetic wave. The difference enables descriptions of the different ways light interacts with matter. A wave of light is described by the equation below.

$$\lambda v = c$$

Equation 2.1: The relationship of the speed of light to the wavelength and frequency of light.

Wavelength (λ) is the distance between the crest of two waves, this is measured in nm. Frequency (*v*) is the number of waves in a second and is measured in Hertz (Hz). *c* is the speed of light, ~3 x 10^8 m s^{-1}, this value is constant. The difference in wavelength and frequency is highlighted in Figure 2.1.

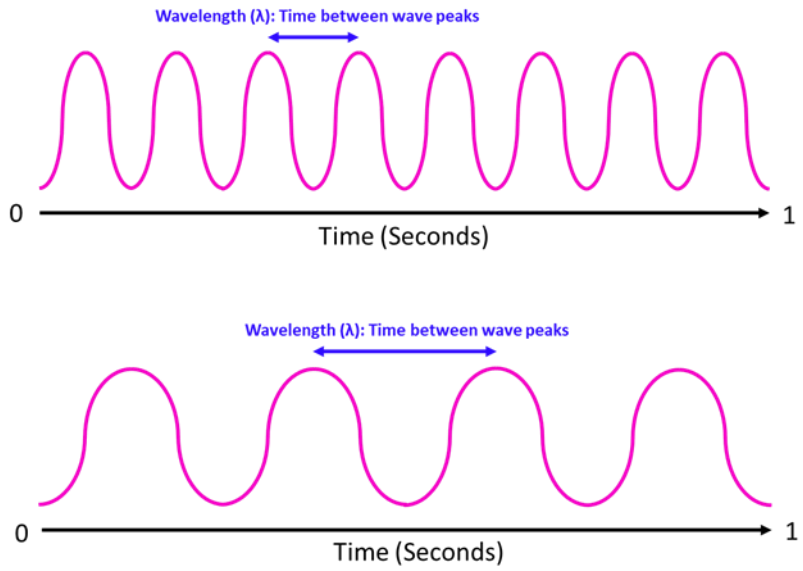

Figure 2.1: Two waves of light over a period of time. This demonstrates wavelength and wavenumber. Wavelength (λ) is given in nanometres and describes the distance between the waves. This also shows frequency (*v*) which is the number of waves per unit time.

Light can be quantified in terms of the energy of a photon. This is important as light will only be absorbed at certain energies by light absorbing molecules and materials. Light energy (*E*) is related to frequency by Planck's equation where h= 6.626 x 10^{-34}J s is Planck's constant

$$E = hv$$

Equation 2.2: The relationship of energy of a photon to Planck's constant and frequency

This can be used to describe energy of radiation with wavelengths from 100m (Radio waves) down to 0.0001nm (Gamma rays). However, the area that describes light is the region from 350nm to 800nm which encompasses the visible spectrum of light. Additionally, research into solar energy will be concerned with the 200-350nm region of ultraviolet radiation and the 800-1000nm region of the infra-red spectrum.

2.1.2 Absorption and emission processes.

Absorption and Fluorescence can be most easily explained using a Jablonski Diagram.

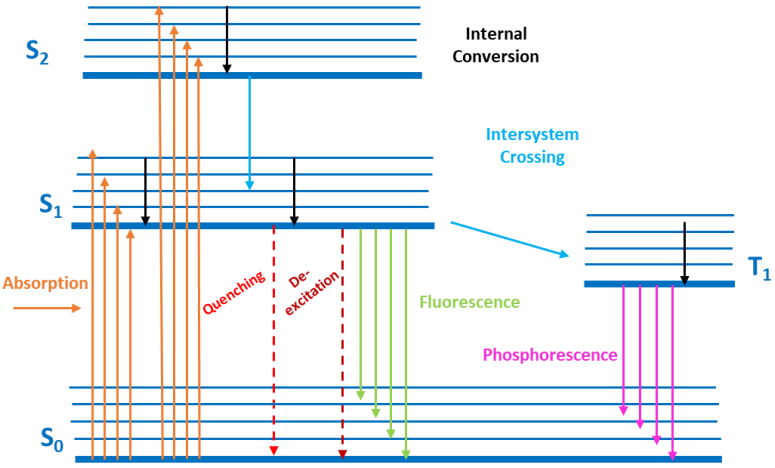

Figure 2.2: Jablonski diagram showing the routes to absorption and fluorescence after the absorption of energy by electrons. Absorption occurs (10^{-15} s) exciting an electron to the first of second Singlet state (S_1 or S_2). The excited electron then undergoes internal conversion to the bottom of the S_1 state (10^{-10}s). The electron then de-excites through a number of mechanisms resulting in emission of a photon or heat energy. The time taken to quench, de-excite, fluoresce, or phosphoresce depends on the rates of those processes, specific to the molecule. De-excitation occurs to a vibrational level in the S_0.

According to Figure 2.2 electrons are excited by the absorption of electromagnetic energy. In this thesis the wavelength of light being used is in the visible range of 300-800nm. When in their ground state the electrons will reside somewhere in the S_0 energy level. Depending on the ambient temperature they may be found in the low vibrational levels, excitation occurs from the lowest energy level of the molecule in it's ground state (referred to as S_0), to any of the vibrational levels in the excited states (referred to as the S_2 or S_1 state). Internal conversion must then occur to de-excite the electron down to the lowest vibrational level in the S_1 excited state. Fluorescence (at most times) can only occur from the S_1 state. Therefore, if excitation has occurred to the S_2 state the electrons can drop from the S_2 to the S_1 state by a de-excitation process where the excess energy is lost as heat, this is known as internal conversion.

Due to this and the aforementioned-internal conversion occurring within the S_1 level, a shift will occur when the fluorescence is emitted. Due to the loss in energy by heat of the electron, the emission will most likely be at a lower energy than the energy of the

absorption which gives rise to a stokes shift. The vibrational energy levels will be between the S_0 and S_1 energy levels giving rise to the mirror image rule, whereby the fluorescence spectrum will appear as the absorption spectrum reversed.[109,110]

2.1.3 The Beer Lambert law and molar absorption coefficient

The Beer Lambert Law gives a definition of absorbance.

$$A(\lambda) = log \frac{I_\lambda^0}{I_\lambda} = \varepsilon(\lambda) lc$$

Equation 2.3: The Beer Lambert law showing the relationship between absorbance *A*, the molar absorption coefficient ***ε***, path length *l* and sample concentration *c* and it's relationship to the incident and transmitted light.

Absorbance (*A*) is a measure of light blocked by a sample, this includes light absorbed and light reflected from a sample. Transmitted light (I_λ) is the amount of light transmitted through a sample. The incident light (I^0_λ) is the sum of the transmitted light (I_λ), the absorbed light (*A*), and reflected and scattered light (*R*). Absorbance can be calculated using the incident and transmitted light. Equation 2.3 shows *A* being equal to the *log* of the incident light divided by the transmitted light which is how absorbance is calculated by a spectrometer.

The absorbance can also be used to calculate the path length and concentration of a sample using the second term, $A = \varepsilon(\lambda)\, l\, c$, where *l* is path length in cm, *c* is concentration in moles per dm^3 and ***ε*** is the molar absorption coefficient with units of L mol^{-1} cm^{-1}. Typical values are in the order of thousands. The molar absorption coefficient can change depending on the medium the measurements are being taken in. Solvent polarity is often a factor here.

When a series of different known concentrations are measured, a Beer Lambert plot can be constructed. Taking the gradient of the line gives the molar absorption coefficient which can then be used to calculate the concentration of an unknown

solution. The molar absorption coefficient is specific to the solvent, container and wavelength used to calculate it.[111,109]

2.1.4 Quantum yield

Emission of light can be characterised in terms of its quantum yield (*Φ*). The quantum yield describes the ratio of de-excitations that result in the emission of a photon to the total number of de-excitations. This is calculated using the radiative and non radiative de-excitation rates.

$$\Phi = \frac{Kr}{Kr + Knr}$$

Equation 2.4: Calculation of the quantum yield (*Φ)* from the excited state decay radiative (*Kr*) and non-radiative rates (*Knr*).

Equation 2.4 shows the relationship between the quantum yield and the rates of radiative and non-radiative decay from the excited state. *Kr* describes radiative decay rate, meaning the number of decays that result in the emission of a photon per unit of time (seconds). *Knr* describes the non-radiative decay rate, meaning the number of decays that do not result in the emission of a photon. The quantum yield is the rate of radiative decay divided by the total rate of decay. The fluorescence lifetime is the reciprocal of the total decay rate.

$$\tau = \frac{1}{(Kr + Knr)}$$

Equation 2.5: Calculation of the fluorescence lifetime (***τ***) from the radiative (*Kr*) and non-radiative rates (*Knr*).

This gives the average time spent in the excited state and considers the non-radiative decay processes. The lifetime without any non-radiative processes is called the natural lifetime.

$$\tau_n = \frac{1}{Kr}$$

Equation 2.6: Calculation of the natural lifetime (τ_n) from the Radiative decay rate relationship between the lifetime and the radiative decay rate is shown as follows.

a

$$Kr = \frac{1}{\tau_n}$$

b

$$Kr + Knr = \frac{1}{\tau}$$

c

$$\Phi = \frac{{}^{1}/_{\tau_n}}{{}^{1}/_{\tau}}$$

d

$$\frac{1}{\tau_n} = \Phi\left(\frac{1}{\tau}\right)$$

e

$$\tau_n = {}^{\tau}/_{\Phi}$$

Equation 2.7: This shows the relationship between the quantum yield and lifetimes. And between the two different lifetimes.

2.1.5 Metal Ligand Charge Transfer

Metal to ligand charge transfer (MLCT) occurs when an electron from the outermost occupied orbital of the metal centre of a complex moves to the unoccupied antibonding π orbitals of the ligands during light absorption. This occurs due to the overlap or hybridization of the separate shells into new orbital systems created by the dative covalent bonds and is more likely to happen as transitions within the d orbital are forbidden.

When complexes are formed, the ligands are not attached to it by covalent bonds as in an organic molecule. They form dative covalent bonds. The metal ion will typically be in a positive oxidation state which leaves some of the outer orbitals empty. Instead of accepting a single electron a pair of electrons from a non-bonding ligand orbital are donated into empty metal orbitals. This creates overlap between the orbitals of the ligand and the metal, making it possible for electrons to move between the metal and the ligand or vice versa. The electronic structure of both ions is shown in Figure 2.3.

Re 74 (+1)

1S 2			
2S 2	2P 6		
3S 2	3P 6	3D 10	
4S 2	4P 6	4D 10	4F14
5S 2	5P 6	5D 4	5F 0
6S 2	6P 0	6D 0	

Ru 42 (+2)

1S 2			
2S 2	2P 6		
3S 2	3P 6	3D 10	
4S 2	4P 6	4D 6	4F0
5S 0	5P 0	5D 0	5F 0

Figure 2.3: The electronic structure of the rhenium and ruthenium ions showing the number of electrons in each orbital. the rhenium is in the first oxidation state and the ruthenium is in the second oxidation state.

Since the coordination number of both complexes is six (creating an octahedral complex) this means that six lone pairs from the ligands are donated to the metal ions, the coordination number is determined by the amount of space available around the metal ion. The unoccupied orbitals will be hybridised into a new coordinate bonding orbital which will accept the lone pairs. In the case of the rhenium, it is the unoccupied *5f* orbitals and the ruthenium the unoccupied *4f* orbitals.

The presence of the ligands raises the energy of and then splits the degenerate *d* orbitals into the e_g and t_{2g} orbitals. This splitting pattern creates two higher energy e_g and three lower energy t_{2g} orbitals. This orbital configuration is caused by the octahedral complexation. Other arrangements such as tetrahedral (a coordination number of four) will create different splitting patterns however they are not considered in this work.

The crystal field strength of the complex determines the energetic distance between the sets of orbitals. MLCT will not occur if the splitting does not raise the e_g to a higher energy than the ligand orbitals. In this case the ligand orbitals are lower in energy than the e_g orbitals. The paired electrons in the t_{2g} orbitals will be excited by the absorption of light energy. However, since moving into the e_g orbital is forbidden the excited

electrons will move into the π* orbital of a ligand. In the case of both complexes, it is a bipyridine ligand. The movement of electrons is shown in Figure 2.4.

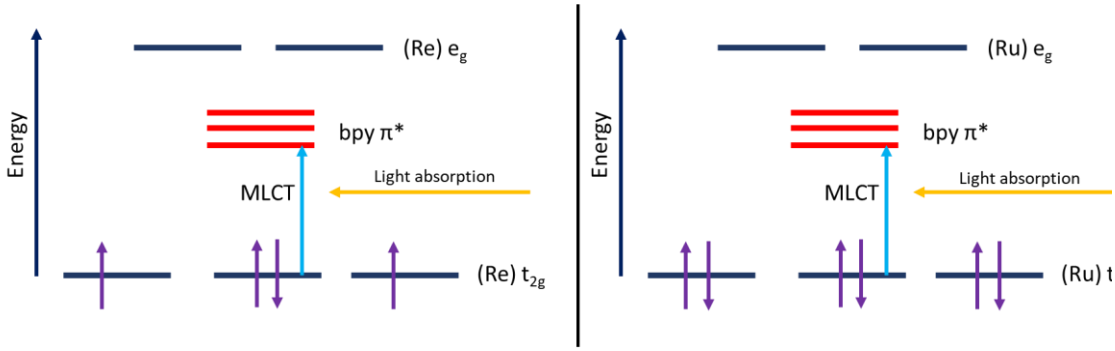

Figure 2.4: Shows the energy levels and movement of electrons in the rhenium and ruthenium complexes. MLCT occurs from the t_{2g} to the π^* orbitals. The π^* orbitals are much lower in energy than the e_g orbitals.

The splitting of the degenerate *d* orbitals into two sets of separate orbitals allows the movement of electrons from the t_2g to the e_g orbital, however the electrons are more likely to undergo MLCT which is a lower energy transition and not a forbidden transition as may be the case where a high spin complex would not allow promotion of an electron due to pairing rules. High spin complexes have unpaired electrons in high energy orbitals. Low spin complexes only have paired electrons in low energy orbitals which means that there are unoccupied orbitals for excited electrons to move into.

Electrons move to the nearby completely unoccupied orbitals of the ligand in a complex, as a result it will join the delocalised electrons and move freely across the aromatic rings, resulting in it remaining in the excited state for much longer than a singlet compound, which results in a longer emission lifetime. Once in the excited state spin orbit coupling between the metal and ligand allows intersystem crossing to occur in the ligand orbitals resulting in the triplet state. However, since other de-excitation pathways are available the entire complex can be thought of as luminescent as both singlet, triplet and non-radiative pathways are available.[110,112]

2.1.6 Organic dye absorption

In organic compounds the movement of electrons is from the bonding orbitals to the antibonding orbitals. Highest occupied molecular orbital (HOMO) electrons reside in the highest molecular orbital. This is furthest from the nucleus and therefore has the lowest energy attraction to their nucleus. These electrons are referred to as the valence electrons. Excitation moves them to the lowest unoccupied molecular orbital (LUMO). The exact transition depends on the availability of the transition. The lowest energy and therefore most likely transitions are the lowest energy n (nonbonding orbital) to π* or if there are no nonbonding orbitals a π to π* transition, occasionally transitions take place involving the n to sigma or σ to σ*. Transitions can be assigned to an excitation band in the absorption spectrum. A precondition of a transition's ability to occur is the spin of the electron. If the orbital the electron would be occupying is already occupied by an electron of the same spin that electron will instead move to an orbital of higher energy.[113]

2.1.7 Silicon wafer absorption

Semiconductors are defined by the arrangement of their electrons. Electrons may exist in two states: valence band (VB) and conduction band (CB). The VB electrons are close to their nuclei and have not absorbed any external heat or light energy. Excited state electrons have absorbed light or heat energy allowing them to move away from their nucleus into the CB. In semiconductors as opposed to conductors the energy gap between the VB and CB is large enough that the absorption of energy is needed for an electron to move from the top of the valence band to the bottom of the conduction band to allow conduction. This energy is known as the bandgap.

Silicon has what is known as an indirect band gap. The indirect bandgap is formed when the minimum of the VB and the maximum of the CB have different values of *k* (vector of electron momentum). Electrons may pass between bands with the same value of *k*, this is an allowed transition across what is known as a direct band gap. Passing between directly from the top of a valence band to the bottom of a conduction band with different values of *k* is not possible as conservation of momentum is not possible which creates an indirect bandgap. This drastically lowers the probability of a transition between the valence and conduction band in indirect band gap

semiconductors like silicon. This creates a very low absorption coefficient which results in a need for more material to absorb sufficient light.[114]

2.1.8 Aggregates

Dyes on a liquid subphase will self-associate, Van-Der-Waals forces pull the dyes together. They form well defined configurations, J bands which are shown by red shifts of the absorption spectrum and H bands evidenced by blue shifts of the absorption spectrum. The names stand for hipsochromic (H) referring to the name of the shift and Jelly (J) referring to the name of the researcher who coined the term. H aggregates are arranged in a parallel orientation and J aggregates are arranged in a head-to-tail orientation. The displacement of electrons by their repulsion from one another causes splitting of the S_1 and S_2 energy levels. Relative to the monomer this makes the S_2 higher and the S_1 lower.The geometry of the aggregate governs the most likely transitions. H aggregates will transition to the S_2 state causing a blue shift and J aggregates will transition to the S_1 state causing a red shift.[115]

2.2 Emission process variables

The emission process can be affected by processes which provide an alternative pathway to de-excitation. The use of this pathway is determined by how likely it is to occur compared to the likelihood of the de-excitation occurring by fluorescence. The most common de-excitation pathways which compete with fluorescence are non-radiative de-excitation. Non radiative de-excitation occurs when the excited fluorophore collides with another molecule, either of solvent or another fluorophore. The energy is transferred as heat to the second molecule allowing de-excitation without radiating energy. Hence this is non radiative de excitation.[116]

2.2.1 Quenching

The process described above is known as collisional quenching. Other components of a solution may cause fluorescence quenching. Dissolved oxygen is the most common quencher and is present in any solution that is prepared in air. The mechanism by which oxygen de-excites fluorescence is still theoretically speculated on. Interactions between the magnetic fields of oxygen and the fluorophore may trigger intersystem crossing to a triplet state. This is much more likely to be quenched by collisional

quenching within the solution. Therefore, no fluorescence or phosphorescence can be observed. To mitigate this, measurements can be taken in degassed solutions, either by bubbling inert gasses such as nitrogen through them or by methods such as freeze pump and thaw. Other collisional quenchers can be removed. For example, amines may be present in some solvents as stabilizers however this is mitigated by buying HPLC/Spectroscopic grade solvents.

Collisional quenching can be calculated by the Stern Volmer equation.

$$\frac{F_0}{F} = 1 + k_q \tau_0 [Q] = 1 + K_D [Q]$$

Equation 2.8: The Stern Volmer equation

Where F is the quenched fluorescence intensity and F_0 the unquenched fluorescence intensity. kq represents the quenching constant and Q the concentration of the quencher. $\boldsymbol{\tau_0}$ represents the lifetime of the fluorophore in the absence of the quencher. k_D is the Stern Volmer quenching constant and is equal to $k_D = k_q \tau_0$. Plotting F_0/F versus [Q] can give information on the kind of quenching that is occurring.

Static quenching is the second most common type of quenching. This occurs when a complex has formed between quencher and fluorophore, making emission of fluorescence impossible. In this case the rate of quenching can be defined simply as the concentration of the complex versus the total concentration of the components of said complex. Quenching may also be a combination of the two models of quenching.[110]

2.2.2 Triplet states

Triplet states are an alteration to the standard pattern of absorption and fluorescence. They are characterised by much larger stokes shifts than in singlet states and by a much longer emission lifetime than singlet states, typically by a factor of 10^4 (Figure 2.5). Triplet states arise owing to a conversion of the spin of the excited electron to the

opposite spin. This introduces difficulty as this is a forbidden transition. Intersystem crossing often depends on the transition involved initially and on the presence of components which enable spin-orbit coupling of the magnetic moments, like heavy atoms.

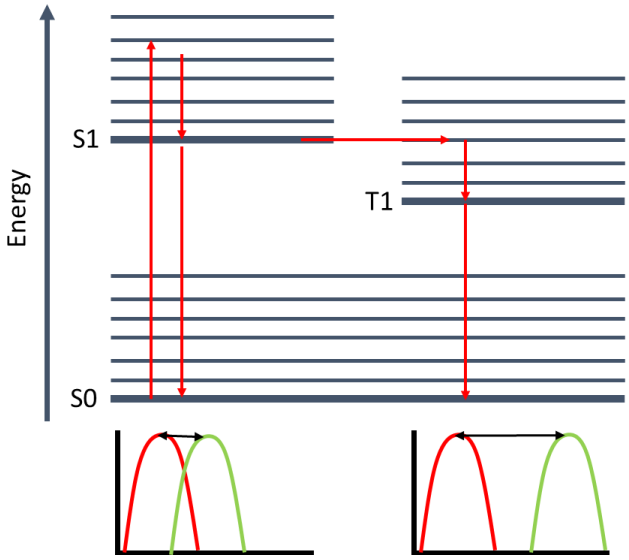

Figure 2.5: Showing the difference between the singlet and triplet stokes shifts. The lower energy of the triplet state compared to the singlet state corresponds to a larger stokes shift.

Triplets more commonly de-excite non-radiatively than radiatively. This is owing to their staying in the excited state for much longer due to the forbidden nature of the transition, thus opening them up to more collisions with solvent molecules. For this reason, phosphorescence is often more intense and longer lasting in solid or rigid media where collisional quenching is not possible.[110]

2.2.3 Energy transfer

Resonance energy transfer, also known as Förster resonance energy transfer (FRET) is the method by which an excited state moves from one molecule to another without the emission of any particles or waves, this is shown in Figure 2.6.

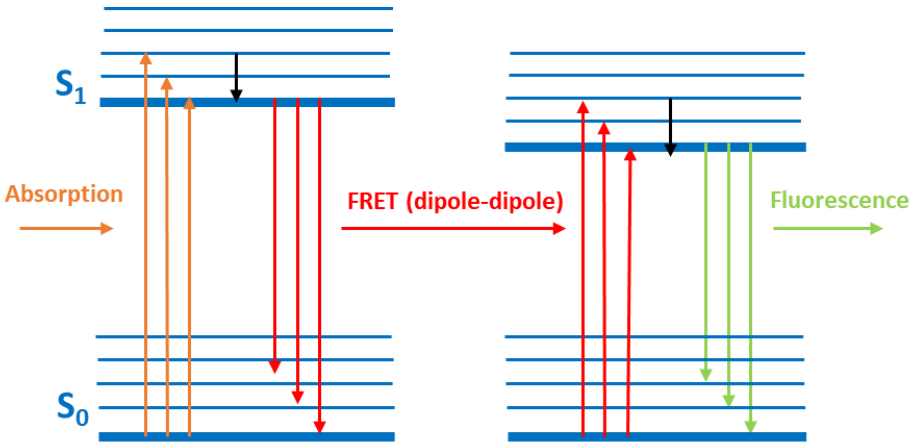

Figure 2.6: A Jablonski diagram showing energy moving from molecule to molecule. A photon is absorbed by the donor (left), the excited state relaxes to the bottom of S1. Non-radiative de-excitation takes place and the energy from the excited state is transferred to the acceptor (right) causing excitation and then de-excitation of the acceptor by emission of a photon.

Figure 2.6 shows a Jablonski diagram of the energy transfer process. The photon coming in has energy slightly higher than the energy of the gap between the S_0 and S_1 bands. The photon is absorbed, and the electron is promoted to one of the vibrational levels of S_1. Vibrational relaxation will then allow the electron to lose some of the excitation energy by radiating heat. Once it reaches the lowest level of the S_1 energy level energy can be lost by emission in the form of another photon. However, in the case of resonance energy transfer energy moves from one molecule to another by dipole-dipole interactions, provided that the gap between energy levels of the acceptor is slightly lower than that of the donor. The same processes may then occur in the acceptor.

As the electron de-excites from the excited state back to the ground state the energy gained during excitation is not lost as emission of a photon or heat as has been described above. It is instead passed from the higher energy donor to the lower energy acceptor by dipole-dipole interactions between the electrons. This can be measured by looking at the amount of quenching which occurs when a donor and acceptor are paired up. This pairing is a coulombic dipole-dipole interaction of two molecules.

There are several conditions that must be satisfied before this is possible. The donor, the molecule which absorbs the initial excitation, must be in resonance with the acceptor, the molecule which will accept the energy. For the molecules to be in resonance there must be some overlap between the fluorescence spectrum of the donor and the absorption spectrum of the acceptor. It would therefore be possible that light emitted from the donor would be able to be absorbed by the acceptor. However, when two such molecules are within a certain distance FRET will take place. Resonance energy transfer can be thought of as two electrons connected by a rod, when one electron moves away from its HOMO orbital, thus creating a dipole, the other must move too. This push and pull behaviour is what drives nonradiative energy transfer.

The closer two molecules are to one another the stronger the level of coupling and therefore the more efficient the transfer. This gives rise to the Förster radius, a number which is unique to each pair of donors and acceptors and governed in part by the fluorescence lifetime of the donor (τ_D). This value is not thought to be much affected by the nature of the solvent, however anything that quenches the donor fluorescence may prevent energy transfer from happening. The Förster distance describes the distance at which FRET is 50% efficient. The rate of energy transfer (k_T) is given by the following relationship.

$$k_T(r) = \frac{1}{\tau_D}\left(\frac{R_0}{r}\right)^6$$

Equation 2.9: The transfer rate (k_T) at a distance between a donor and a acceptor (r) is calculated using the lifetime of the donor (τ_D) and the ratio of distance between donor and acceptor (r) to Förster distance (R_0) to the power of six.

Where the rate of transfer is dependent upon the distance between a donor and an acceptor. This shows the transfer will be equal to the donor decay rate when the function of R_0/r is equal to 1, i.e., when the molecules are at the Förster distance.

If the spectral properties and the quantum yield of the donor are known the R_0 can be calculated for a donor acceptor pair.

$$R_0 = 0.211(k^2 n^{-4} Q_D J(\lambda))^{1/6}$$

Equation 2.10 : The calculation of R_0 using known values. k^2 is the orientation factor, describing the orientation of the donor and the acceptor relative to one another, it is is equal to 2/3 for isotropic distribution. n is the refractive index of the medium the transfer takes place in (usually solvent). Q_D is the quantum yield of the donor. J is the overlap integral of the donor and acceptor; the integral of the overlapping curves of the donor fluorescence spectrum and the acceptor absorption spectrum.

Once R_0 is known the transfer efficiency can then be calculated using the above equation, decay rates can tell us what the likely result is. A higher decay rate versus a low transfer rate shows a very inefficient energy transfer, likewise a lower decay rate than transfer rate would suggest high efficiency energy transfer. This information can be easily measured from samples and can be used to calculate the energy transfer efficiency.

$$E = \frac{k_T(r)}{\tau_D^{-1} + k_T(r)}$$

Equation 2.11: The transfer efficiency (E) is the ratio of the transfer rate ($k_T(r)$) to the total de-excitation rate. ($\tau_D^{-1} + k_T(r)$)

Since the transfer rate is also related to distance and Förster radius the efficiency can also be calculated at every distance between the donor and the acceptor if the R_0 is known.

$$E = \frac{R_0^6}{R_0^6 + r^6}$$

Equation 2.12: the R_0 value to the power of six divided by the sum of R_0 to the power six and the distance between the donor and the acceptor (r) to the power six to calculate the energy transfer efficiency.

The relationship between distance and energy transfer efficiency can therefore be plotted as a function of Efficiency versus the ratio of r to R_0 or as a function of E versus r.

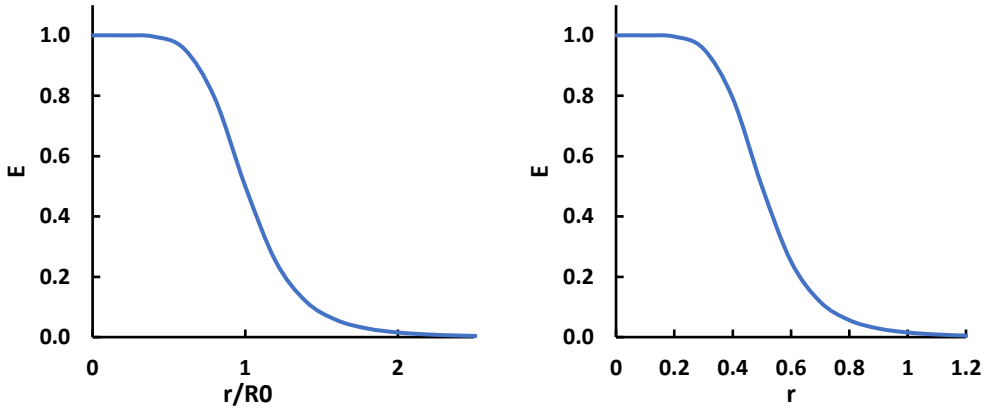

Figure 2.7: Two plots of Equation 12 where the Value of R_0 is equal to 0.5. Values of r were plotted from 0 to 2 (for this example they are arbitrary numbers with no distance units.) The ratio of r to R_0 versus E is shown alongside the value of r vs E to demonstrate that R_0 is the value at which E is equal to 0.5.

The graphs show that at a distance of r=0.5 the energy transfer efficiency is 0.5, i.e., 50%. As the distance approaches zero the rate of increase in the efficiency of energy

transfer approaches very close to 1 until reducing the distance further can no longer increase the efficiency of energy transfer. Similarly, as the distance approaches and passes 1 the efficiency of energy transfer decreases at a slower rate until it becomes 0 after 1.2. This shows how the measurement of distance becomes unreliable at very short or very long donor-acceptor distances. This is typically defined as above or below half of the R_0, so in the above example below 0.25 and above 0.75.

Equation 2.13: Calculating the energy transfer using the lifetime of the donor fluorescence or the intensity of donor fluorescence ($_D$) in the presence of the acceptor ($_{DA}$).

This does not however give a practical method for measuring energy transfer. Broadly speaking there are two methods of measuring energy transfer using spectroscopic methods. By using reduction of donor intensity (*F*) in steady state measurements in the presence of the acceptor compared to the absence of the acceptor. Or by the reduction of the lifetime (τ) of the donor in the presence of an acceptor when compared to the absence of the acceptor.

$$E = 1 - \frac{\tau_{DA}}{\tau_D} \qquad E = 1 - \frac{F_{DA}}{F_D}$$

It is possible to use enhancement of acceptor fluorescence to measure energy transfer; however, in this study and in most studies these methods are not used. The reason being that due to non-radiative losses in the acceptor such as de-excitation or reabsorption and exciton diffusion it can be difficult to measure the amount of energy transferred accurately.

On top of this the actual change in fluorescence will typically be very small making errors very likely and therefore making it difficult to get a definitive reading on the amount of energy transferred to the acceptor.

A problem which is universal to these methods is that they assume that the donor and acceptor are at a fixed distance, making the measurement of energy transfer in solution or viscous materials difficult. However, in this study transfer of the dyes to a solid surface in Langmuir Blodgett films solves this problem.[110]

2.2.4 Emitter interface Model

The emitter and the interface can be thought of as being made up of two faces of dipoles, one representing the emitter and the other representing the interface. Excitation of one will cause oscillation of the dipole of the excited molecule. Though dipole-dipole interaction the second row of dipoles will also oscillate. In the case of an emitter interface model the dipoles are in a fixed orientation.

The emitter being “in phase” with the surface results in dipoles being driven by the presence of the interface which enhances the emission rate of the emitter. Similarly, being out of phase will inhibit the emission. The presence of the interface provides additional paths of the light to take other than being absorbed. For instance, it may be reflected back away from both the emitter and the interface. As the distance between the emitter and the surface of an interface is varied the strength of the interface-emitter dipole-dipole interactions vary, closer to the surface will result in much stronger coupling and therefore much stronger interactions, this usually occurs within 15 nm.

Surface plasmon polaritons (SPP) are coupled dipoles from both the surface and the emitter, the oscillation of the dipoles creates charges at the interface.
There are three orientations of the emitter dipole with respect to the acceptor surface. The dipole may be perpendicular to the surface. Or it may be parallel to the surface in phase or parallel to the surface out of phase. The first case gives P polarized and the second and third case gives S polarized radiation.[33]

The relationship of the strength of the interaction to the distance depends on the arrangement of the dipoles. If the dipoles are arranged in lines the dependence is d^{-5}. A sheet of acceptors gives d^{-4}. And bulk transfer like in the case of silicon wafers shows a

d^{-3} dependence. Conservation of momentum must also occur alongside the transfer. This is achieved in three different ways. From the creation of an exciton in the bulk, from the creation of an exciton in the surface above the bulk. Or from components in the near field providing momentum.[33]

2.2.5 Time resolved decays fitting

Time resolved spectroscopy involves using a pulse of light, usually from a laser, to excite a sample. The resulting fluorescence lifetime is then measured by counting the time to detect the first photon. The pulse must be a short as possible so as to not interfere with the measurement. A longer pulse will influence the slope of the decay and therefore artificially increase the lifetime of the sample.

The lifetime is plotted as *log I (t)* vs *t* where *I* Is intensity measured in number of photons counted and *t* is time, usually in nanoseconds or microseconds. The slope of the graph should be equal to 1/lifetime. However, this is only theoretical and relies on several of the experimental conditions being perfect. The pulse would be have to be perfect with no interference with the slope.

From the initial population of excited fluorophores (*n0*) the sample decays at a rate which is equal to the sum of the radiative and non-radiative decay rate. The decay rate at any time can be calculated by Equation 2.14.

$$\frac{dn(t)}{dt} = (knr + kr)n(t)$$

Equation 2.14: the rate of decay Where *knr* and *kr* are the nonradiative and radiative decay rates and *n(t)* is the number of excited fluorophores at time *(t)*.

This gives the same result as dividing the change in number of excited states by the change in time. The observed intensity is proportional to the number of excited states. Therefore, it can be expressed in terms of either.

$$nt = n0\exp\left(-t/\tau\right)$$

$$nI = I0\exp\left(-t/\tau\right)$$

Equation 2.15: Number of excited fluorophores.

Therefore, the decay lifetime ($\boldsymbol{\tau}$) is the inverse of the total decay rate.

$$\tau = (knr + kr)^{-1} = \frac{1}{(knr + kr)}$$

Equation 2.16: The relation of the lifetime to the decay rate.

These equations are all true for single exponential decays. A single exponential decay is one where there is only one species of fluorophore present that can influence the average lifetime. The lifetime is defined as the average time that a fluorophore stays in the excited state. There is a population of excited molecules, each has their own lifetime therefore an average could be calculated. However, the same is not true for multi exponential decays. Multi exponential decays arise when there are multiple different fluorescent species in the same sample that are excited by the Excitation source. When log photon counts vs time shows a linear decay, this indicates a likely single exponential. Multiple different slopes or a sharp curve within a decay indicates the presence of more than one species decaying at different rates.

Analysis of these curves makes use of a method called non-linear least squares to find a lifetime that best fits the data. Most samples will have more than one average lifetime due to a variety of effects that may create another fluorescent species. The equation must account for several variables. It must disregard the starting intensity as different species will have differing absorption coefficients. Multi Exponential decays are calculated as a sum of the individual decays present in a sample. The decay times and the amplitudes of the individual components are considered.

$$I(t) = \Sigma a_i \exp\left(-{}^{t}/_{\tau_i}\right)$$

Equation 2.17: Showing the amplitude and lifetime of each component at time ($t > 0$),

Amplitude; the distance from the crest to the trough of a wave, is described as a pre-exponential factor, i.e., it is not included in the exponential function and instead the exponential function is multiplied by it. Each component has a decay time represented by τ. This is represented at a time t=0. The meaning of alpha can be different depending on the fluorophore being studied and can rely on the absorption of a sample (i.e., it's concentration, path length, absorption coefficient, quantum yields).

The value of amplitude (α) determines the fraction that each fluorophore contributes to the total lifetime.

$$f_i = \frac{\alpha_i \tau_i}{\Sigma_j \alpha_j \tau_j}$$

Equation 2.18: Shows the calculation of the fraction of a component

Where α_i and τ_i represent the lifetime and amplitude for a single component; and $\Sigma\ \alpha_j\ \tau_j$. f_i and represent the sum of amplitudes and lifetimes of all components. The term $\alpha_i\ \tau_i$ can be used to calculate the average lifetime of a sample, hence the fractional intensity of each component can also be used to calculate average lifetime ($\bar{\tau}$).

$$\bar{\tau} = \frac{\Sigma(\alpha_i \tau_i^2)}{\Sigma \alpha_j \tau_j} = \Sigma f_i \tau_i$$

Equation 2.19: the average lifetime calculated using the fractional intensity of each component.

However, in practical terms the lifetime is calculated from the lifetimes of multiple (usually up to 10,000) single photons from the sample. Therefore, the area under the curve of the decay needs to be integrated to calculate the lifetime. However, the multiple components of a multi exponential lifetime must be considered therefore the equation used in this case is different.

$$\int_0^\infty I(t)dt = a_1\tau_1 + a_2\tau_2$$

Equation 2.20: Showing the relationship between the area under the decay curve and the amplitude and lifetime of each fractional component of a sample.

This considers the amplitude and lifetime of each component to estimate an average lifetime for the complete sample and also allows for the number of components to be calculated and for each component to have their lifetime and amplitude scrutinised.[110]

2.3 The Langmuir Blodgett technique

2.3.1 Historical development of the technique

The Langmuir Blodgett (LB) technique as it is known today is a combination of the techniques developed by Irving Langmuir and then further developed by Katharine Blodgett.[117,118] The early observation of the effects of amphiphiles on water was

recorded by Benjamin Franklin in 1773[119] who observed a calming effect from oil dropped onto a pond. Knowledge of this was used to develop the first trough used to control the spread of a monolayer, which was devised by Agnes Pockels.[120] Pockels used a homemade trough to contain water and controlled the spread of a monolayer using a handheld barrier and a balance to show phase change. This was published in 1891 in letters by Lord Raleigh to the Royal Society.[121]

Development of what would become the modern technique is credited to Irving Langmuir, who published a comprehensive study of van der Waals interactions between various fatty acids on the surface of water in 1917.[122,123] He was able to determine the importance of van der Waals forces and polar interactions in the ability of a molecule to form a monolayer on a liquid subphase. He used the isotherm data to determine the orientation of the molecules in the monolayer as standing upright. Later, Katharine Blodgett working at General Electric alongside Langmuir, led to the development of a deposition method which would become the Langmuir Blodgett technique.[124,125] A historical account was written by Greene.[120,126]

2.3.2 Langmuir monolayer and the LB technique

Formation of a Langmuir monolayer is achieved by amphiphilic molecules that are trapped at the air/water interface, the part of a body of water that meets the air. Amphiphiles; which have a hydrophilic polar region, are able to dissolve in water and also have a hydrophobic non-polar region preventing it from fully dissolving. They are commonly used to form monolayers.[127] An example is stearic acid ($C_{18}H_{36}O_2$). (Figure 2.8)

Figure 2.8: An example of an amphiphile such as stearic acid. Note the long hydrophobic tail, making up the hydrophobic part of the molecule and the COOH region making up the hydrophilic part of the molecule. ($C_{18}H_{36}O_2$)

For monolayer formation to be successful the aliphatic balance of the molecule, which describes the ratio of hydrophobic and hydrophilic areas, must be thermodynamically favourable to the formation of a monolayer which means a significantly hydrophilic portion, known as the head group and a sufficiently large hydrophobic portion known as the tail group has to be present in the molecule. This factor is important to the formation of a film however is not the only thing which affects the compressibility of the molecule. Other factors, such as the size and shape of the molecule, the exact position and number of hydrophilic/hydrophobic regions will influence monolayer formation.[120]

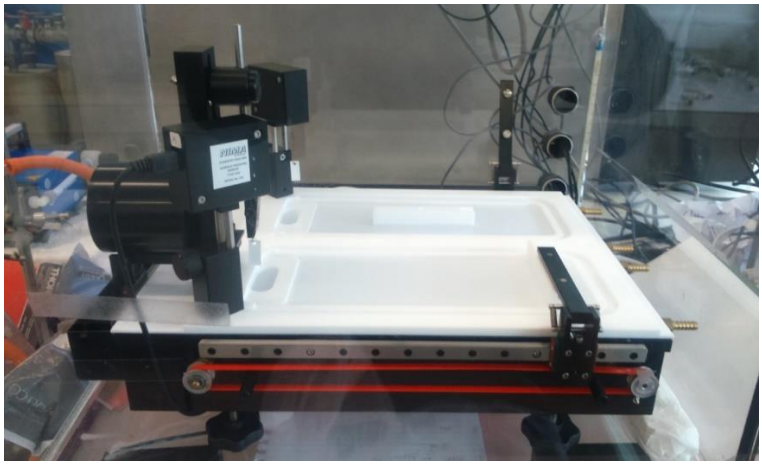

Figure 2.9: The Nima technologies trough used throughout this project, compression occurs from the right-hand side only, the troughs can be compressed and dipped independently.

The LB technique is a thin film fabrication method for deposition onto solid substrates from a Langmuir monolayer. The technique allows fine control of sample preparation as one molecule thick layers can be deposited one layer at a time. Variables such as the surface pressure, dipper speed at which a layer is deposited, and the orientation and aggregation of a film can all be controlled using this method.

The method requires an LB trough. These troughs are typically constructed using milled Polytetrafluoroethylene (PTFE) plastic. PTFE is hydrophobic, which makes the troughs easier to empty after use. It is unreactive allowing for cleaning using aggressive solvents such as chloroform and preventing reactions with film forming materials deposited or ions in the subphase. Troughs may feature wells for dipping solid substrates which are either milled directly into the PTFE or can be detachable. The trough and well must be filled with a liquid (usually water) referred to as the subphase. Material in solution such as stearic acid can be added on the surface of water using volatile solvents which will evaporate at room temperature. Barriers sweep the surface to compress the monolayer and are usually made of interchangeable materials such as PTFE or coated metals. In this thesis all work was carried out exclusively using PTFE blocks mounted on metal brackets. An example of a trough is shown in Figure 2.9. This trough is a variant of the Nima 611D trough, which employs two troughs milled into the same sheet of PTFE each with its own balance and

independent surface tension measurement, removable dipping wells and a dipping arm which can move between the trough allowing for multiple different films to be deposited without cleaning the trough.

The monolayer goes through three phases described in Figure 2.10. A gas phase of no association, a liquid phase of loose association and a solid phase where the film has formed. The changes in the monolayer are reflected in the rate of surface pressure increase versus surface area per molecule shown in the isotherm.

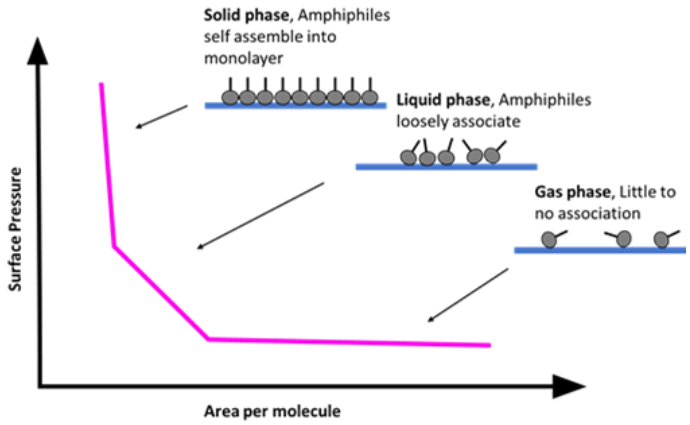

Figure 2.10: Schematic of a pressure-area isotherm showing the 3 phases of compression of a Langmuir Blodgett film. The gas phase is represented by the most shallow increase followed by the liquid and solid phase showing steeper and distinct phases.

2.3.3 Surface tension and measuring surface pressure.

In a body of liquid, every molecule is constantly undergoing intermolecular interactions with the other molecules surrounding it, for example water molecules hydrogen bond to one another in a body of water. When a molecule moves to the surface of a body of liquid it is in contact with the air and the body of liquid and there are no longer forces acting upon a molecule from the air side. This creates a smaller number of interactions between molecules at the surface which creates surface tension.

Surface pressure is what is measured during the use of the Langmuir Blodgett technique and refers to the reduction in surface tension by the presence of the Langmuir layer of molecules. Wilhelmy plates measure this change as shown in Figure 2.11, the surface tension of the water pulls the plate down into the water. As layers are compressed surface tension reduces causing the plates to move up and out of the water. By measuring the difference in surface tension, the Wilhelmy plate tensiometer allows for measurement of the surface pressure in millinewtons per metre (mN/m).[128]

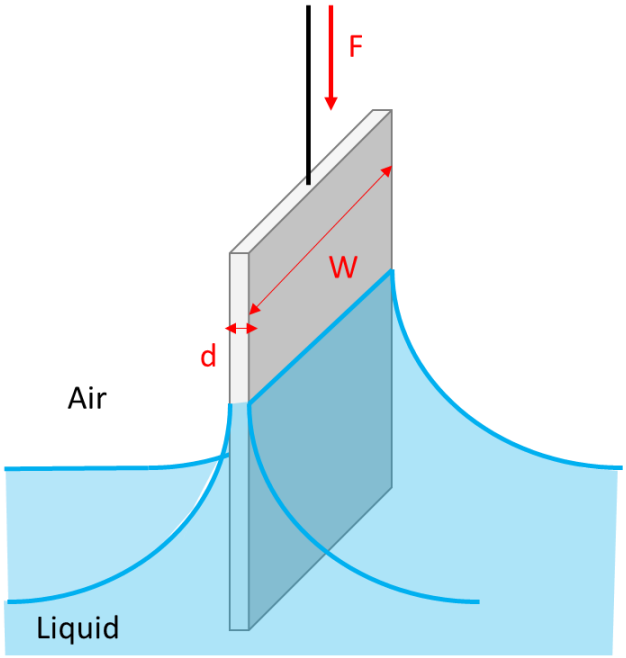

Figure 2.11: Surface pressure measurement with a Wilhelmy plate suspended from a balance. The width (*W*) and thickness (*d*) of the plate are used to calculate the plate perimeter. The force acting on the plate (*F*) is measured by the balance.

$$Surface\ Tension = \frac{Force}{Plate\ Perimeter}$$

Equation 2.21: Measurement of surface tension by a Wilhelmy plate.

$$Surface\ pressure = Pure\ subphase\ surface\ tension - Subphase\ \&\ film\ surface\ tension$$

Equation 2.22: Calculation of surface pressure using the change in surface tension

Wilhemy plates can be made from a range of materials but in this work the plates were made using a reel of Grade 1 filter paper. Once plates included with the trough where no longer available new ones were cut from a long ribbon of filter paper to an approximate length of 23.5 mm. The weight was approximately 19 mg. The trough was calibrated using the built-in calibration function in the software and a 100 mg weight supplied hung from the balances using a small pan.

The plates were cleaned before use by washing in chloroform to remove oil and dried under a nitrogen stream to blow off excess dust. They would then be attached to the tough and left to pre-soak in the water for over half an hour before use. During this time, the surface of the water was cleaned using a vacuum pump and PTFE nozzle to vacuum the surface of the water. A “blank” surface tension of below 0.5 mN/m was considered acceptable for a “clean” water surface.

2.3.4 Isotherm interpretation

Molecular area refers to the area that each molecule takes up on the surface of water when the film is in the solid state. Extrapolating the solid phase down to zero surface pressure allows calculation of the molecular area. (Figure 2.12)

This requires the area of the trough, or rather the change in area as measured during compression, to be converted to the change in area per molecule. This calculation (Equation 2.23) uses molecular weight, concentration in moles per litre and volume deposited in litres to calculate the number of molecules deposited.

$$Area\ per\ molecule\ (\text{Å}^2) = \left(\frac{Area\ (\text{Å}^2)}{(Conc\ (\text{mol.L}^{-1}) \times Vol\ (\text{L}) \times (6.022 \times 10^{23} \text{mol}^{-1})} \right)$$

Equation 2.23: Calculation of the area per molecule using the trough area and known concentration, volume and Avogadro's number.

The area per molecule in Angstroms squared is calculated by dividing the area in Angstroms squared by the total number of molecules calculated using the concentration and volume. This gives a graph of area per molecule versus pressure. Extrapolating down to a pressure of zero gives the molecular area, or A_0, of the Langmuir monolayer. This is the area a single molecule in the film occupies. An example isotherm for stearic acid is shown in Figure 2.12.[120]

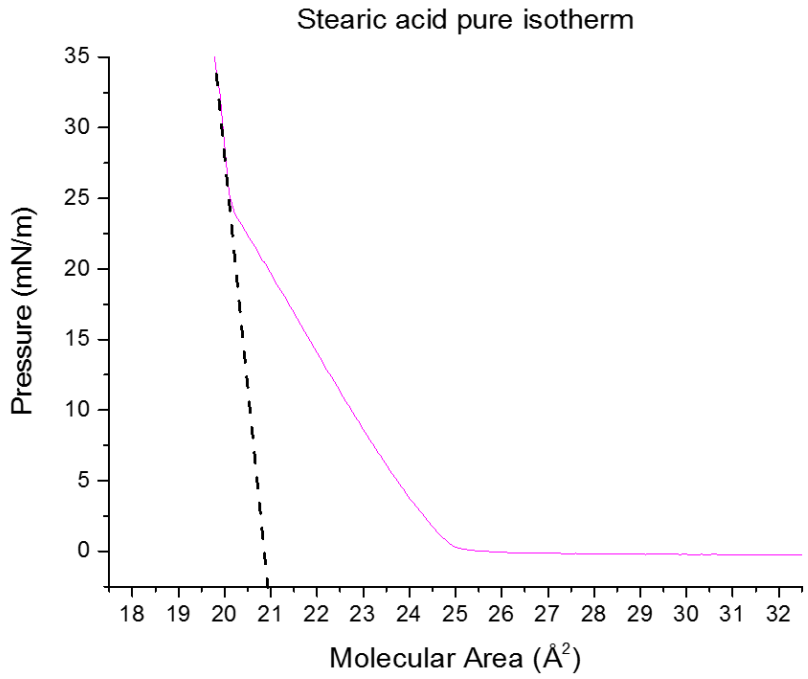

Figure 2.12: Stearic acid produces the classical isotherm showing the three well defined regions, the gas, liquid and solid. The dotted line extrapolates the solid phase down to Pressure = 0 to find the molecular area of stearic acid (21Å^2). The gas phase, where no interaction takes place. The liquid phase where weak interaction begins and the solid phase where the film becomes a well organised solid structure.

The molecular area is influenced by the size of the molecules and the way in which they interact with one another. Since repulsion or attraction between the molecules can raise or lower the surface pressure, this will influence the value of the molecular area. For instance, using counter ions in the subphase to crosslink fatty acid molecules will often pull them closer together resulting in a smaller molecular area. Other effects such as the temperature may also raise or lower the molecular area slightly. Molecular shape and orientation may also influence how the molecules pack on the surface and therefore their molecular area. For instance, a molecule standing up may appear having a smaller molecular area than a molecule laying down as a smaller cross section is being measured.

Measuring the change in surface pressure against the monolayer area compressed allows assumptions to be made about the orientation of the molecules on the surface of water. Each isotherm can have three phases as shown in Figure 2.10. A gas phase, where the molecules are not interacting and are completely spread out on the surface of water. A liquid phase, where some interaction begins as the film begins too loosely associate. And a solid phase where the molecules pack tightly into a well-ordered film after undergoing self-assembly. Molecules will have a certain isotherm shape.[120,127] The classical, “three section” isotherm is typically recorded using relatively small fatty acid molecules such as stearic acid and deviations from this are caused by differences in intermolecular forces.

2.3.5 Collapse pressure

At a certain point, the film will collapse if the surface pressure is continually increased. Molecular area can change depending on the history of the film, for instance film annealing can take place with repeated compressions. The standard mode of collapse is the formation of micelles on the surface of water by fatty acids, this occurs near the edges of the film initially. Other structures present include ridges or clusters of aggregated molecules if they are able to aggregate. The structure formed depends on the film in question. Other factors include the film stability, the subphase, the rate of compression and how well the molecules can orient themselves and how closely they are able to pack.[53,120,127,128]

2.4 Conclusion

This chapter shows some equations which were directly performed in the work carried out in this thesis, the most directly relevant is the calculation of energy transfer efficiency using donor fluorescence. Additionally, the theory behind interpreting Langmuir isotherms is used throughout this work.

It also shows some equations which were indirectly used, i.e., these calculations were carried out automatically by pieces of equipment like the fitting of the fluorescence lifetimes. For example the fluorescence lifetimes were handled by the fluofit software provided by picoquant and the trough measures surface pressure automatically an the calculations are carried out by the software using known parameters. It is prudent to have it here as an explainer of how this works.

It also shows some equations which were not directly or indirectly used but can be used to explain the things being studied in this thesis.

The theories behind fluorescence, energy transfer with respect to distance and quenching mechanisms are examples of explanatory theory, relevant, as they show what is involved in the fluorescence and phosphorescence of the samples and go some way to explaining some of the things seen in this thesis but were not required to be calculated.

Similarly the explanations of what happens with regards to electrons during the fluorescence and phosphorescence processes with regard to organic and organometallic are not directly used during the experimentation but are useful in understanding the processes occurring.

3. Experimental

3.1 Substrate preparation and cleaning methods

3.1.1 Substrate cleaning method

Silicon and glass preparation must remove as much contamination from the surface as possible. Chromic acid has been used in some procedures as well as piranha solution and hydrofluoric acid.[129] Immersion for 15-30 minutes in such a strongly acidic solutions has been used for substrates used in optical research to produce ultraclean surfaces.[50,87,130]

Initially, the slides and silicon wafers were washed in a hot solution of Decon 90 detergent, using abrasion with gloved fingers to clean the surfaces. They were then sonicated for 10 minutes in a new hot solution of Decon 90, then sonicated for 10 minutes in deionised water, then sonicated for a further 10 minutes in ethanol. Decon 90 is a laboratory detergent and the effectiveness of which is stated to range from cleaning up biological contamination to radiological hazards making it ideal for particulate contamination and some ionic contamination. The subsequent steps of sonication in ethanol and acetone were carried out in order to remove traces of the Decon 90.

Slides were then dried off under a stream of nitrogen and exposed to UV light in a Novascan PSD Pro Series, Digital UV Ozone system for approximately 5 minutes on both sides as shown in Figure 3.1. This final step was used to eliminate any organic contamination remaining on the substrate surface.

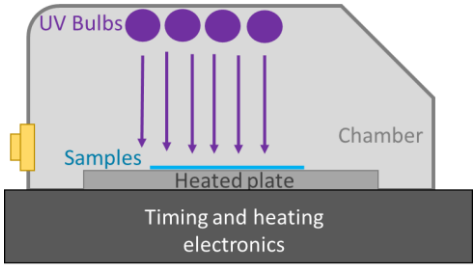

Figure 3.1: Schematic of the UV ozone system used to remove organics, the time and heat of the chamber are set and the samples are exposed directly on both sides to ultraviolet light from a bank of 4 mercury bulbs.

This method was used in some initial work with satisfactory results. However, work by Dr Punarja Kevin in our group using atomic force microscopy revealed microscopic particulates present on the surfaces and found contamination remained on the surface. This could be attributed to residual lipids from the Decon 90 due to insufficient cleaning. As a result, experiments with improvements including acidic etching solutions were tested similar to Danos et al (2008).[73]

3.1.2 Cleaning method development

The Decon 90 and solvent steps were kept for removing dust and dirt, propanol was used instead of ethanol and high purity solvents were purchased for cleaning. Additional steps using piranha solution (3 parts H_2SO_4 to 1 part H_2O_2 at 40ºC) and Radio Company of America (RCA) solutions (H_2O_2 and NH_4OH at 75-85ºC)[129,131] were added in order to remove anything left behind after the soap and solvent, combinations of these solutions were experimented with. After research on the methodology, a sufficiently effective method for cleaning in terms of time and convenience was found to be an initial cleaning with Decon 90 followed by cleaning with water and solvents in a sonicator bath as above. This was followed by immersion in piranha solution for 30 minutes and 40ºC followed by rinsing in deionised water (water that had been filtered to a resistivity of 18.2MOhm) and then exposure to the vapours of propanol vapours to dry the surface and a final stream of nitrogen to remove any dust. The final cleaning steps are shown in Table 3.1.

Step	Process
1	Wafer immersed in a solution of Decon 90 then in 99.8% Pure Acetone, Sonicate in the acetone 10 min
2	Wafer immersed in CHROMASOLV Propan-2-ol, Sonicate in the propanol10 min
3	UV, hot plate at 60˚C, 5 min on each side
4	Piranha solution, 40˚C, 30 min, sonicate in 18.2MOhm DI water at 40 ˚C for 10 min
5	Expose to Propan-2-ol and dry Under nitrogen stream.

Table 3.1: A table showing the five cleaning steps, including materials and conditions used to remove all contamination from silicon wafers and glass slides prior to exposure to HMDS.

3.1.3 Use of AFM and microscopy to confirm cleanliness

A Zeiss Axiolab 5 light microscope, capable of 5 to 20 times magnification was used to study the silicon surfaces before and after cleaning. The samples were illuminated from above and studied at 10- and 20-times magnification before and after cleaning. Removal of gross and microscopic contamination was found, and improvements were made by the addition of piranha steps. Examples are shown in Figure 3.2.

An Agilent technologies, Agilent 5500 atomic force microscope operating in alternating contact atomic force microscopy (ACAFM) was used for AFM. Nanosensors PPP-SEIHR-SPL tips and Budget sensors Tap 150 and Tap 300 tips were used, as described in section 3.3.6. An example is shown in Figure 3.3. showing analysis of the silicon surface. AFM is described in full detail in Section 3.7.

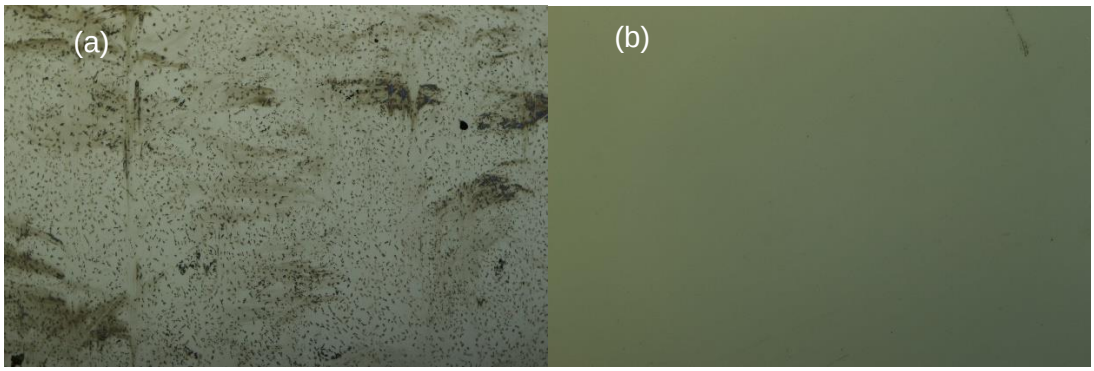

Figure 3.2: Images taken using a Zeiss light microscope at 10x magnification. (a) shows a piece of silicon before cleaning, the silicon shows significant contamination. (b) shows a piece of silicon after the complete cleaning stages.

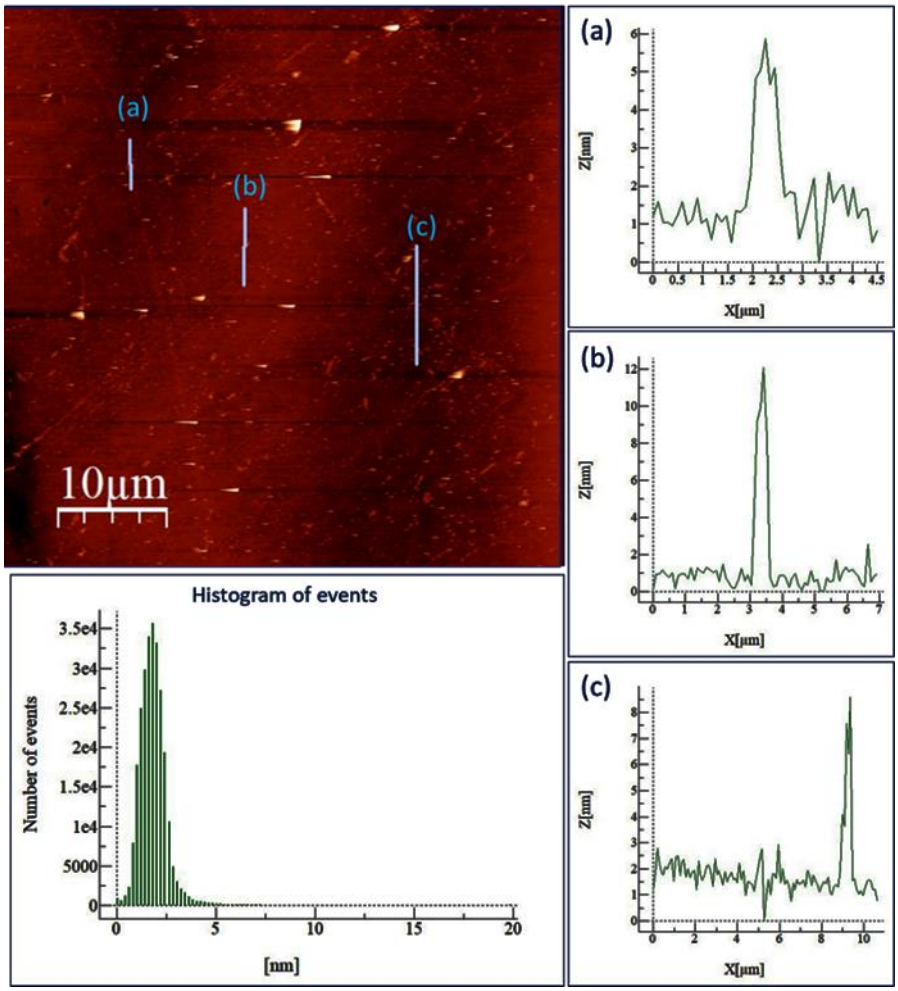

Figure 3.3: AFM of silicon wafer reveals some microscopic peaks and scratches however much of the surface is flat. This shows the low levels of contamination left over.

3.1.4 Substrate surface treatment

The cleaned surfaces from the glass and silicon substrates are hydroxyl (-OH) terminated. The top layer must be made hydrophobic in order to promote good adherence of the Langmuir Blodgett layers to the silicon/glass surface.

Hexamethyldisilazane (HMDS) (Electronics grade) supplied by Fisher Scientific will react with silicon wafer or glass surfaces by removing the hydrogen from two of the hydroxyl groups, leaving behind a molecule of ammonia. The silanes ($Si(CH_3)_2$) will then attach to the exposed oxide layer, creating a surface effectively passivated and hydrophobic as shown in Figure 3.4.

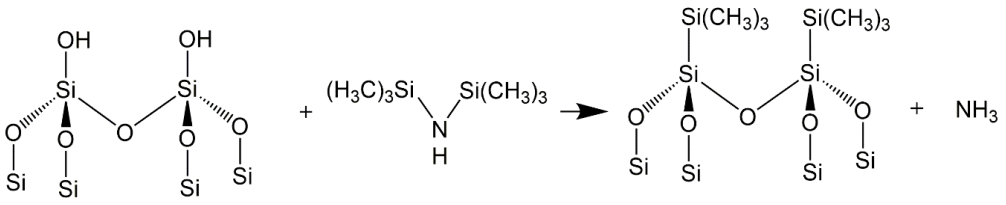

Figure 3.4: Balanced reaction of the surface of a silicon oxide with HMDS leaving a hydrophobic surface.

HMDS vapour treatment is used to reduce the exposure of the glass to organics and solvent post cleaning to avoid further contamination. The wafers and glass slides were stood upright in a lidded glass staining jar in a fume hood. Once the slides had been cleaned, they were exposed to HMDS vapours overnight (approximately 18 to 20 hours) by dripping HMDS into the bottom of the jar and closing it. Initially up to 1ml was used but was found to cause stains and microscopic imperfections to appear on the otherwise clean slides and wafers. Different amounts per cm^2 of glass slide area were experimented with and 10µl HMDS per cm^2 of glass was eventually applied, this was further refined to approximately 300µl for each container with 4-5 glass slides/silicon wafers. This was found to give good hydrophobic adhesion to the surface of the glass and silicon.

3.2 Experimental parameters for Langmuir monolayer formation

This section details the experimental parameters used for the preparations of the solutions and spreading of the monolayers to record the Langmuir isotherms from carbocyanine dyes, organometallic complexes and various porphyrins used in this study.

3.2.1 LB trough cleaning setup

The trough was thoroughly cleaned with chloroform with Kimtech Science tissues (75512) from Kimberly-Clark. It was placed inside a clean Perspex box with a door to keep dust off and prevent airflow from interfering with surface pressure measurements. No temperature controls or atmospheric controls were implemented routinely during this work however during particularly hot weather cooling was applied to a temperature of 15 ^{o}C. Otherwise, the trough water would be around room temperature, ranging from 18 ^{o}C to 22 ^{o}C. The temperature could vary throughout the day but would not change appreciably during individual experiments. Ultrapure water from a Milli-Q Reference system from Millipore and later a Sartorius Arium pro Water purification system was used with a resistivity of 18.2 MOhm/cm^2 and a pH between 6-7. After the clean water was added to the trough it was given at least 30 minutes to come up to room temperature and for the Wilhelmy paper plates to equilibrate.

3.2.2 Stock solutions

Pure spectroscopic grade 3,3'-Dioctadecyloxacarbocyanine Perchlorate (DiO) and 1,1'-Dioctadecyl-3,3,3',3'-Tetramethylindocarbocyanine Perchlorate (DiI) were purchased from Thermo Fisher, HPLC grade stearic acid (SA) was purchased from Sigma Aldrich and both the Rhenium bipyridine tricarbonyl pyridine-2-methylhexadecoate (ReC16) and Ruthenium bipy 2,7 bi Octadecanylamine bis Bipy (Ru C18) complexes were synthesised in house, reagents were purchased from Sigma Aldrich at reagent grade. For rhenium C16 Rhenium Tricarbonyl halide starters were reacted with Bipyridine inducing the replacement of the halide groups with a bipyridine to create a Rhenium tricarbonyl bipyridine with a single halide. This was the prepared for further reaction by replacing the halide with acetonitrile by reacting the components with Triflic acid in DCM.

The long chain pyridine group was synthesised by the coupling of hexadecenoic acid to3-hydroxymethylpyridine using 1-(3-Dimethylaminopropyl)-3-ethylcarbodiimide

hydrochloride dissolved in DMF/DCM. This ligand was then added to the preprepared Rhenium tricarbonyl bipyridine acetonitrile complex, replacing the Acetonitrile.
For the ruthenium complex Bis(2,2′-bipyridine)dichlororuthenium(II) was acquired from sigma Aldrich reacted with a pre-prepared ligand consisting of the pyridine with C18 tails. The ligand was created by linking of 2,2'-Bipyridine-4,4'-dicarboxylic acid and octadecylamine. The ligand and Bis(2,2′-bipyridine)dichlororuthenium(II) were then heated under reflux in ethanol replacing the chlorine ligands with the C18 tailed bipyridine ligand.
Stock solutions were made up to an approximate concentration of 1 mg/ml in spectroscopic or HPLC grade chloroform purchased from Sigma Aldrich. Three porphyrins were chosen for study in relation to silicon. Tetraphenylporphyrin (TPP), 5,10,15,20-Tetrakis-(N-methyl-4-pyridyl) porphine (TMPyP4), and Tetrasulphophenylporphyrin (TSPP). Tetraphenyl porphyrin was dissolved successfully in chloroform to a concentration of approximately 1 mg per ml along with stearic acid to a concentration of 1 mg per ml. TMPyP4 and TSPP were both dissolved in methanol and later a 3-1 (v-v) mix of chloroform to methanol.

For the carbocyanine study, six ratios of DiO (Donor) to DiI (Acceptor) were chosen from 1:1, 10:1, 25:1, 50:1, 75:1 and 100:1. High donor to low acceptor ratios were chosen in order to study the effect of light harvesting. Porphyrins were studied in molecular ratios with stearic acid 1:1, 10:1, 50:1 and 100:1. The mixed molar ratios were made up in chloroform from stock solutions to a final concentration of 1×10^{-4} M.

3.2.3 Langmuir isotherm measurements

A Nima 301D trough with 2 independent troughs was used. The trough was controlled using Nima tr7.1 software which recorded isotherms and controlled dipping speed and applied constant pressure on films. A newer version, Nima tr8.1, capable of automated repeating compression-release cycles was also tested and used for some isotherms. Solutions were deposited on the trough water in 10-25µl aliquots for the cyanine dyes and stearic acid, 15µl for the organometallic complexes and up to 50µl for the porphyrins with the PTFE barriers fully open before isotherm measurements. The addition of the aliquots was carried out using a glass syringe cleaned using chloroform and rinsed with the solution to be deposited. The maximum amount of each solution which could be deposited on the water of the trough was found through experimentation by keeping the surface pressure of the trough with the barriers fully

open at 0mN/m both before and after deposition of material. If the surface pressure increased after the deposition of material this indicated that too much had been deposited.

In all cases 15 minutes was allowed for the chloroform to evaporate. For isotherm studies, 10 to 13 compressions, including a final compression which recorded collapse pressure, were performed on a monolayer to study changes in the isotherm because of repeated compressions. The monolayers were compressed at a constant speed of 50 millimetres (mm) per minute. They would be released at a solid phase pressure before collapse occurred, usually at approximately 30mN/m. Repeated compressions would create changes in the isotherm over time which will affect the way the monolayer forms and how the molecules pack upon each compression. A reduction in of the molecular area shows the monolayer annealing and the molecules that form the monolayer packing closer together.

Stearic acid was recorded first and used after calibration was performed. The stearic acid isotherms were measured after to show whether the calibration was successful. Calibration was performed on the pressure sensors and trough area. [132,133]

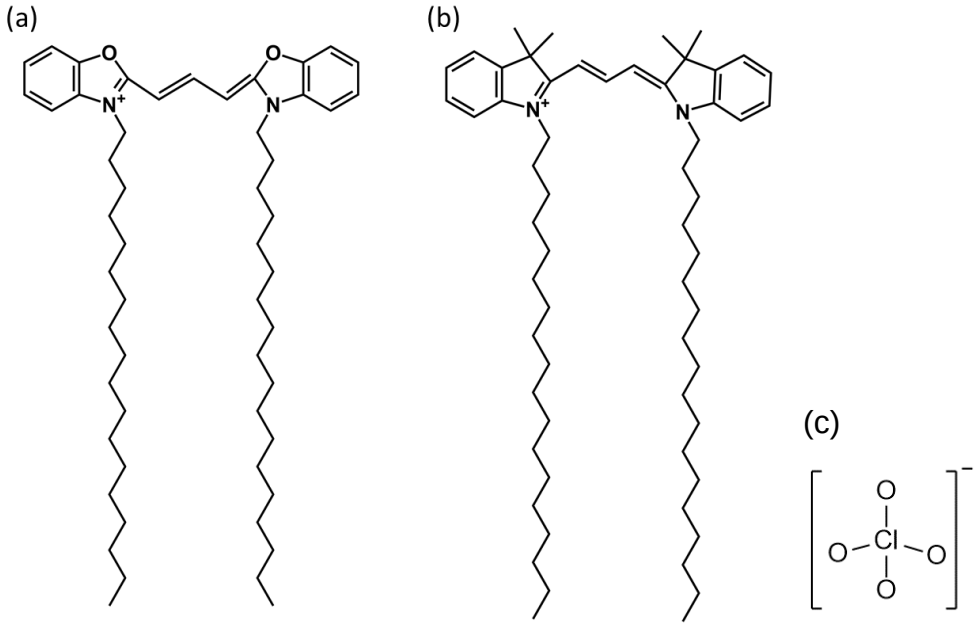

Figure 3.5: (a) 3,3'-Dioctadecyloxacarbocyanine Perchlorate (DiO) and (b) 1,1'-Dioctadecyl-3,3,3',3'-Tetramethylindocarbocyanine Perchlorate (DiI) the two dyes used in this study, the positively charged N on the head and lipophilic tails make them ideal candidates, both used (c) perchlorate as a counter ion.

The experimental procedures carried out are substantially the same for the cyanine dyes and for both organometallic complexes. The rhenium and ruthenium complexes used in this thesis are a rhenium bipyridine tricarbonyl pyridine-2-methylhexadecoate (Figure 3.6) and a ruthenium bipy 2,7 bi docdecanylamine bis bipy complex (Figure 3.7) synthesised by Dr Michael Coogan. Both complexes are in a 2+ oxidation state. Coupled with the long-saturated tails this gives the complexes the amphiphilic nature needed to use successfully with the Langmuir Blodgett technique.

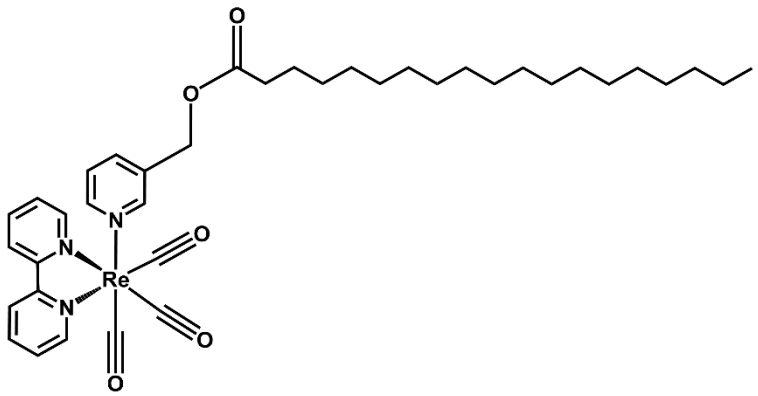

Figure 3.6: Rhenium bipyridine tricarbonyl pyridine-2-MethylHexadecoate (Re-C18) in its octahedral geometry. The long unsaturated chain added make this usable with the Langmuir Blodgett technique. The CO groups should interact with water making this amphiphilic. The counter ion was BF_4^-.

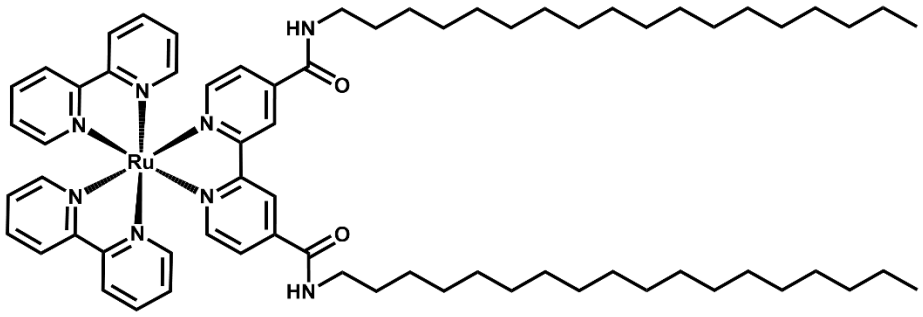

Figure 3.7: Ruthenium bipy 2,7 Bi Octadecanylamine bis Bipy (Ru-C18) in its octahedral geometry. featuring long unsaturated chains added make this usable with the Langmuir Blodgett technique. The length of the chains creates a sufficiently amphiphilic molecule to form thin films. The counter ions were $2Cl^-$

Three porphyrins were experimented with, and one was chosen for study in relation to silicon. Tetraphenylporphyrin (TPP), TMPyP4, and TSPP (shown in Figure 3.8). 1-1 10-1 50-1 and 100-1 were experimented with and TPP was chosen for quenching experiments. To measure the isotherms of TPP 50µl of solution was deposited on the surface of the trough. 15 minutes was given for evaporation of the chloroform. TPP films were compressed to record isotherms and spectra was recorded from the trough as described in the optical characterization section.

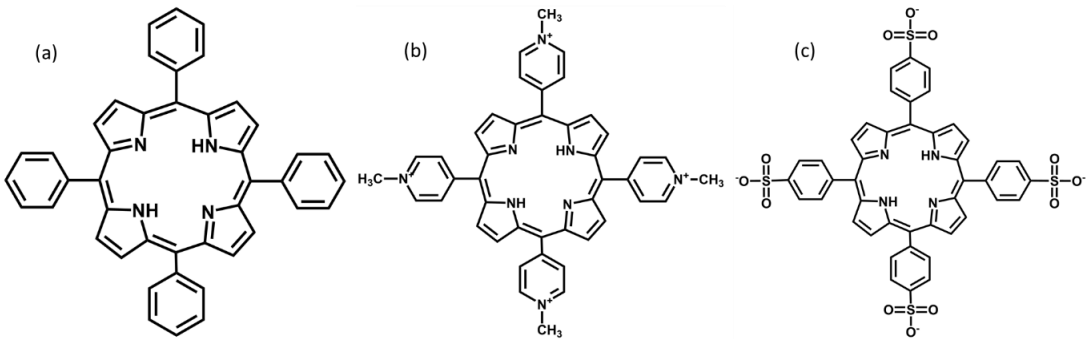

Figure 3.8: (a) Tetraphenylporphyrin (TPP) (b) 5,10,15,20-Tetrakis-(N-methyl-4-pyridyl) porphine (TmPYP4) (c) Tetrasulphophenylporphyrin (TSPP), the porphyrins experimented with in this study.

3.2.4 Carbocyanine dyes monolayer deposition parameters

Once the isotherm study was complete, monolayers of the films that had been studied were deposited on quartz glass slides. Slides were purchased from UQG optics and cut into 1cm by 5cm strips. These were then treated using the sample cleaning and treatment method outlined in sections 3.1.2 and 3.1.4. For glass samples six layers of stearic acid were deposited followed by a monolayer of the dye, complex or porphyrin to be tested. Stearic acid solutions were deposited in 20µl aliquots and dyes in 15µl aliquots using a glass syringe, more was added in 10 µl aliquots if more film was required.

The film was then compressed to the target pressure determined by the study of the isotherms. Three compressions to the target pressure were performed before any deposition to allow the film to organise prior to deposition. HPLC grade stearic acid was deposited at a pressure of 28mN/m, some experimentation was carried out with deposition at lower pressures (26mN/m) with a transfer ratio approaching unity. The dyes layers were compressed to and deposited at a constant pressure of 26mN/m on top of the six layers of stearic acid with a transfer ratio approaching unity. A two-layer stearic acid cap was then applied over the top. A schematic is shown in Figure 3.9 with the multilayer build up. Two separate trough wells were utilised to deposit the films in tandem. Films on the surface of water lasted long enough for two or more samples to be made.

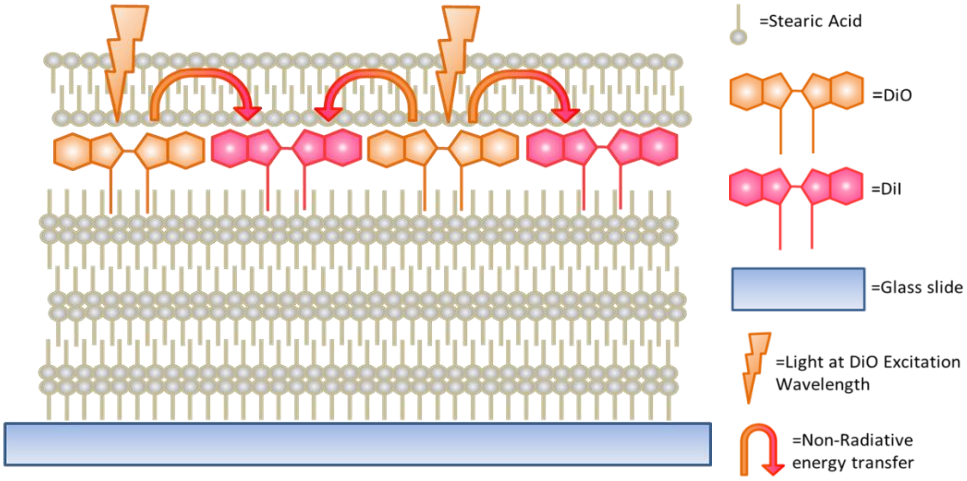

Figure 3.9: Schematic of the multilayer structure of the cyanine dye samples. Stearic acid is deposited on a cleaned prepared glass slide as a six-layer base, an experimental layer of cyanine dyes is added on top and then a cap of two layers of stearic acid is added after.

Slides were stored in polyethylene sample boxed purchased from Agar Scientific which had been cleaned with deionised water, Kimtech Science tissues (75512) from Kimberly-Clark and a nitrogen stream. These were stored in an airtight container.

3.2.5 Rhenium and Ruthenium monolayer complexes deposition parameters

The Re-C16 and the Ru-C18 complex were both studied on glass slides and silicon wafer as pure monolayers. Both complexes were studied for their energy transfer to silicon by varying the number of stearic acid layers deposited between the monolayer of complex and the silicon wafer. The phosphorescence quenching of these complexes by the silicon as a function of distance was studied. The sample structures are shown in Figure 3.10 and Figure 3.11.

For quenching experiments crystalline silicon substrates (N type, 111 orientation) with a 2nm oxide layer was used and were cleaned according to the cleaning and preparation steps outlined in section 3.3.6. Layers of stearic acid were deposited on silicon substrates at 26mN/m with each sample deposited a different number of layers. A monolayer of rhenium was then deposited on top of the stearic acid multilayers at 28mN/m followed by a two-layer stearic acid cap. An example is shown in Figure 3.10.

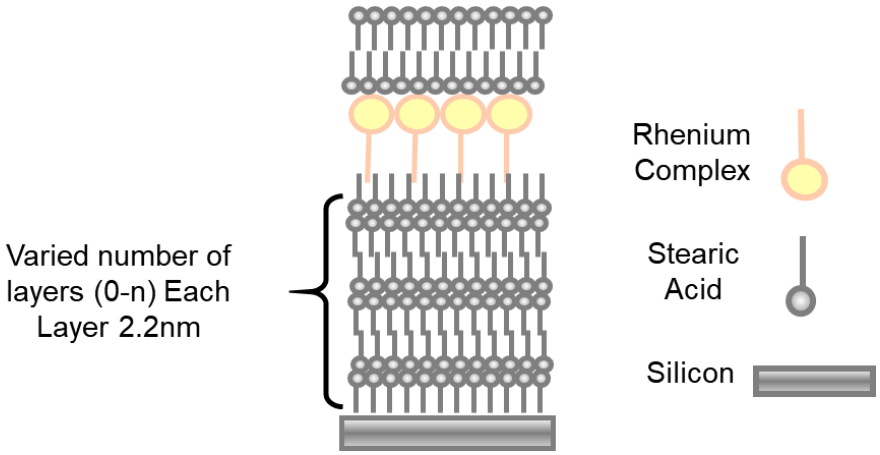

Figure 3.10: Schematic diagram showing the structure of a sample with six layers of stearic acid spacer. The spacer can be varied giving a distance of 2.2nm per layer from the surface of the silicon. The stearic acid spacer is deposited first then a single layer of rhenium complex is deposited on the spacers. Two layers of stearic acid are deposited on top.

Ruthenium samples were fabricated by depositing 15µl of Ruthenium solution on one trough and 15µl stearic acid solution. The trough conditions were the same as in the isotherms. Films were compressed to the pressure used for deposition 3 times before deposition was performed at 26mN/m. Stearic acid was deposited at a constant pressure of 26mN/m. Spacer layers were built up on the silicon in varying thicknesses in the same manner as described for rhenium. Ruthenium Complex monolayer was deposited at a constant pressure of 28mN/m. A cap layer was deposited on top. An example is shown in Figure 3.11.

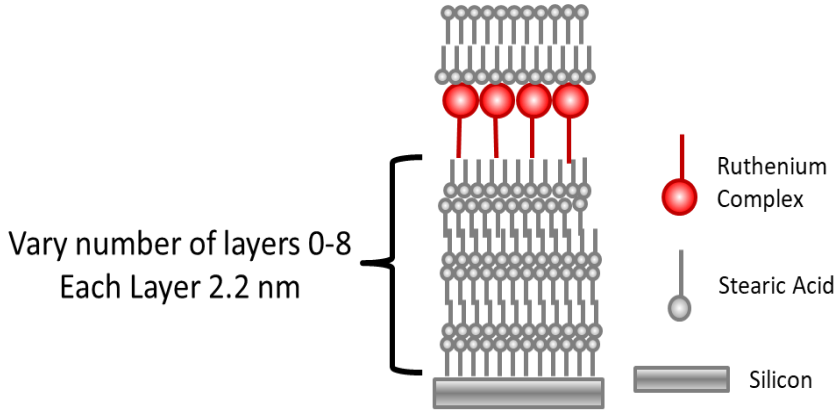

Figure 3.11: Schematic diagram showing the structure of a sample with six layers of stearic acid spacer. The spacer can be varied giving a distance of 2.2nm per layer from the surface of the silicon. The stearic acid spacer is deposited first then a single layer of ruthenium complex is deposited on the spacers. Two layers of stearic acid are deposited on top.

3.2.6 Tetraphenyl porphyrin monolayer deposition parameters.

All of the porphyrins used in this study were mixed with stearic acid for deposition into films. The ratio used was the lowest most stable ratio determined from the isotherm

study which was 1 to 1. The solutions of stearic acid and mixed stearic acid and porphyrin were deposited on the surface of the trough in 15µl aliquots. 15 minutes was given for the chloroform to evaporate. The films were then compressed to 30mN/m three times and then deposited at 30mN/m at a speed of 10mm/minute.

For the control samples deposited on glass, six layers of stearic acid were laid down first on a quartz glass slide that was treated in the way described above to yield a hydrophobic surface. A single layer of the porphyrin mixture was then deposited on top of that, and the sample was then capped with 3 layers of stearic acid.

For the silicon samples, porphyrin was deposited directly on the silicon substrate which was passivated with aluminium oxide (AlOx). The substrates were prepared using the methods described in sections 3.1.2 and 3.1.4. These samples were capped with three layers of stearic acid. This is shown in Figure 3.12.

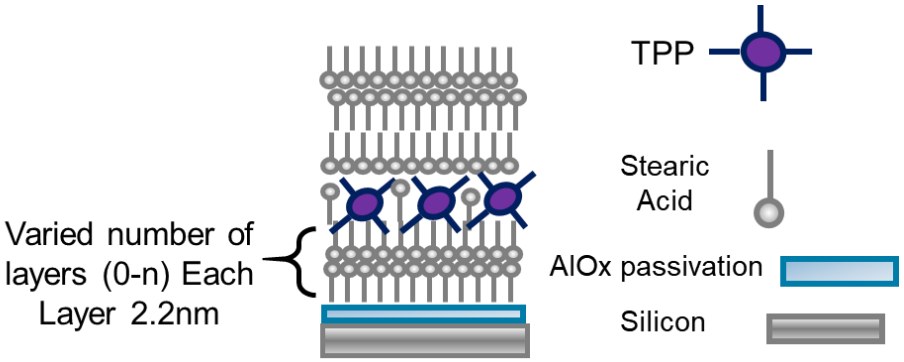

Figure 3.12: Schematic of the multilayer structure of the porphyrin samples. The silicon wafer is passivated with aluminium oxide. These wafers were coated with stearic acid layers, a layer of TPP mixed in a 1-1 ratio with stearic acid and a three-layer cap.

3.3 Optical Characterization of films.

3.3.1 Ellipsometry

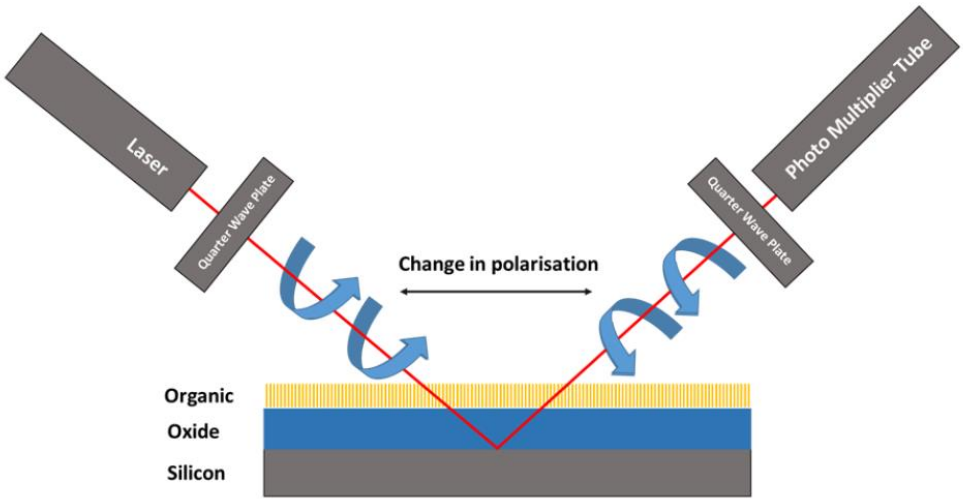

Figure 3.13: Diagram showing the function of an ellipsometer, a helium neon laser is reflected from the surface of a sample into a detctor, changes in polarization of a laser are used to measure the height of oxide and organic films.

The ellipsometer used in this study was a Rudolph auto EL 3 series ellipsometer with a thickness measurement range of 0.001 µm to 3.0 µm (+/-0.0005). The laser source was a helium neon 632 nm laser. The laser would be given at least 15 minutes and up to 30 minutes to warm up before use. The ellipsometer was then calibrated using the built-in calibration program and a known piece of silicon wafer with a 100 nm thick oxide. The oxide thickness would be measured to confirm the calibration. The program selected used a provided refractive index of 3.9 at a wavelength of 632 nm, this value was confirmed using a calibration sample of silicon with a known oxide thickness of 100 nm measured with a 632 nm laser and is consistent with the known optical properties of silicon.[134]

Three to five measurements were taken from each sample at different positions on the sample. These measurements were taken from the side of the wafer which was coated with film. This measures the thickness of both the film and the oxide layer of the silicon wafer. In order to determine the thickness of the film alone a second measurement of the bare wafer oxide thickness was taken from the uncoated side of the sample. This was then subtracted from the sample to give the total thickness of the film.

To account for the capping layer a set of samples were made consisting of stearic acid layers on treated silicon wafers. This gave the thickness of each layer of stearic acid deposited at 28mN/m which was 2nm, which could be subtracted from the thickness of each sample to account for the capping layers

3.3.2 In situ spectroscopy

A reflectance probe was used in conjunction with an Avantes AvaSpec-2048 spectrometer using a detector with a 2048-pixel CCD detector array spectrophotometer measuring from 200 to 800nm and a Thorlabs tungsten lamp which provided light from 250-800nm. The probe type used was a fibre optic housed in flexible metal cable covering. The probe consists of an input to be attached to the light source, an output to be attached to the spectrometer and the probe head itself. Six bundles of fibre optic in the probe head transmit light and correspond to the input end. Six bundles correspond to the output and take all reflected light back to the spectrometer. The software uses comparison with the environment being studied in the absence of sample as a blank. In the case of the trough the light can be reflected both from the trough surface itself and the surface of the water. The processes involved are shown in Figure 3.14.

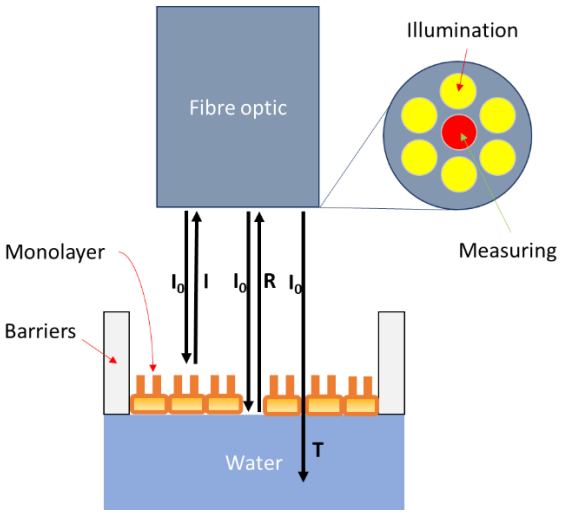

Figure 3.14: The Avantes probe setup sends light to the sample through six fibre optic bundles labelled illumination and receives light through one labelled measuring. Incident light (I_0) from the illumination bundles hits the film and is reflected from the film (I), reflected off the surface of the water (R), or diffused from the water and trough bed (T). The light reflected from the water and film is measured through the single measuring bundle.

Langmuir films of pure and mixed cyanine dyes and a mixture of Tetraphenylporphyrin and stearic acid were studied on the trough during compression using the fibre optic probe. The probe was secured in place above the trough using a 3D printed holder, printed on a Creality Ender 2 in ABS plastic, which fit into the dipping arm motor of the LB trough. The software was “zeroed” using a trough containing water and no dye as a blank and dark reference. The trough was covered on 4 out of 5 sides with aluminium foil to block ambient light. Constant pressure mode was then used to sequentially compress the film to higher surface pressures, adding 5mN/m up to 35mN/m. At each pressure a reflectance measurement was taken using the probe.

3.3.3 UV-Visible absorption, fluorescence and excitation spectroscopy

The absorption spectra were recorded using an Agilent technologies Cary 60 UV-Visible absorption spectrometer in the spectral range of 200-800nm. Samples in solution were recorded using 1cm path length quartz cuvettes and dissolved in spectroscopy grade chloroform purchased from Sigma-Aldrich. Deposited film samples on glass were held up on the sample holder using a metal clip. A blank slide was used to provide a baseline for the spectrometer. Excitation was performed with an 80Hz xenon flash lamp, capable of exciting from 190nm to 1100nm, which was built into the spectrometer.

Steady state fluorescence measurements involved recording both excitation and emission spectra. Emission spectroscopy involves exciting the sample at a wavelength where it absorbs and monitoring the emission of photons from the sample as a function of wavelength. Excitation spectra involves monitoring the emission wavelength of the sample and exciting it at all wavelengths before the emission wavelength to create a plot of photon counts (excited states) at the monitored wavelength vs excitation wavelength in nm.

The Agilent technologies Cary Eclipse Spectrofluorometer was used for both emission and excitation spectroscopy. Excitation was performed with an 80Hz xenon flash lamp, automatic bandpass filters from 200nm up to 900nm were selected automatically based on the type measurement being taken. Excitation and detection slits to restrict the size of the excitation beam and resulting fluorescence were set at 5nm. Additional glass

band pass and long pass filters were added to the sample chamber if required. To measure emission spectra, samples were excited at the shortest absorbing wavelength of a sample. Scans for emission were taken from the excitation wavelength+10nm up to 900nm. To measure excitation spectra sample light emission was monitored at the highest emitting wavelength, and the sample was then excited at every wavelength up to the monitored wavelength, and emission at each excitation wavelength was recorded.

Samples in solution in HPLC/spectroscopic grade chloroform were measured in a 1cm-by-1cm quartz cuvette. Solid samples were held in place on a steel mounting plate by retaining bolts, the height and angle of the plate were adjusted for optimum emission signal levels. Every sample was measured twice and the average of this was taken to eliminate anomalies in the spectrum. A blank of either a cuvette full of pure chloroform for solution samples or a blank piece of quartz glass for film samples was then measured twice using the same conditions. This gave an average background which was then subtracted from the sample spectra to find the true spectra.

3.3.4 Time correlated single photon counting (TCSPC)

Time correlated single photon counting (TCSPC) is the preferred method used in this study to measure the lifetime of excited states of molecules. A constant fraction discriminator (CFD) is triggered by the laser pulse hitting the sample which triggers the timing electronics known as a time to amplitude converter (TAC) to generate a voltage ramp. A photon from the sample then strikes the photomultiplier tube (PMT) which sends a pulse to a second CFD which stops the voltage ramp. The total voltage is proportional to the change in time and is converted into a number. The signal is amplified through a Programmable Gain Amplifier and then converted to data using an analogue to digital converter. The whole process is shown in Figure 3.15.

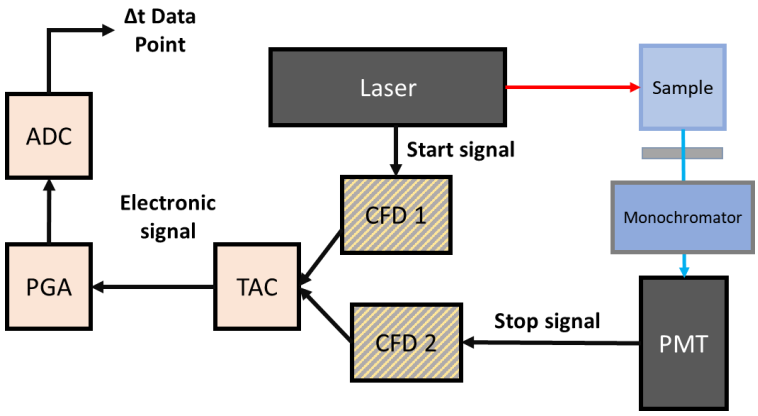

Figure 3.15: A diagram of a time resolved spectrometer showing the signal from the laser and PMT tube being converted into a data point by the timing electronics.

The time difference gives a lifetime, and this is added to the histogram as shown in Figure 3.15. The process is repeated at least 10,000 times to build a complete lifetime decay.

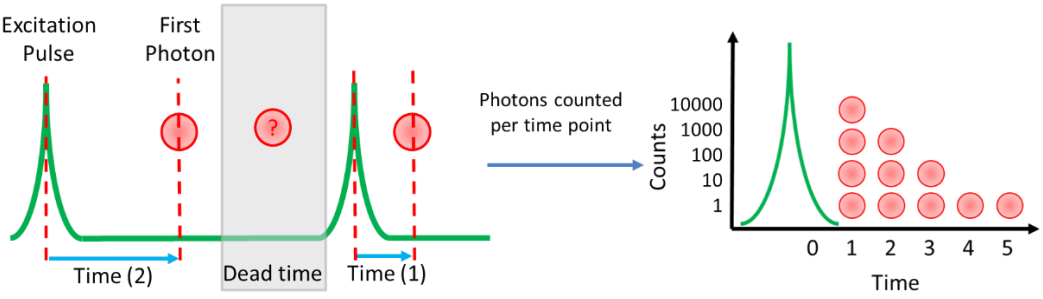

Figure 3.16: Diagram showing the sequence of events involved in recording TCSPC data. An excitation pulse hits the sample. The time between this pulse and the first photon striking the photomultiplier tube is measured. This datapoint is then added to the histogram and the cycle is repeated after the dead time.

Photon lifetimes cannot be measured during the dead time shown in Figure 3.16. Therefore, the excitation duration and laser intensity are limited to minimise emission of photons from the sample during the dead time as much as possible so that the result is not biased in favour of faster lifetimes. Photons detected during this time are measured as “pile up” and the lowest possible pile up should be achieved.[135]

A PicoQuant Fluotime 300 Time resolved spectrometer was used. Detection was performed using a photomultiplier tube (PMA-185 and PMA-C 192-M, PicoQuant). Long pass and band pass filters were used to block laser scatter from reaching the detector and detection wavelengths were selected using a Czerny-Turner style monochromator. Long pass laser filters from Shemrock and Chroma were used, the most commonly used one was a 488nm long pass filter. For solution measurements dyes and complexes were dissolved in HPLC and/or spectroscopic grade chloroform contained in quartz glass cuvettes. Cuvettes were cleaned using ethanol and acetone before measurements and were given periodic cleans using decon 90 and piranha solution.

For excitation different PicoQuant pulsed diode lasers were used. These lasers operated at the wavelengths 375nm with a 90ps pulse, 405nm with a 50ps pulse, 445nm with a 100ps pulse and 485nm with a 100ps pulse, both had a maximum repetition rate of 40mHz. These lasers were used as they correspond to the highest absorption wavelengths required to excite DiO, Re C16, Ru C18 and TPP, which were used in this study. Laser parameters are shown in Table 3.2. Burst mode was used for samples with low signals. This describes a mode where the sample is excited with multiple short pulses before detection to create more signal for the detection electronics. Instrument response function (IRF) was recorded using Ludox beads suspended in water in a quartz cuvette after removal of the filter and setting the monochromator to the wavelength of the laser.

Wavelength (± 10) [nm]	Pulse[1] (FWHM)[ps]	Max rep.rate [MHz]	High avg.power[2] [mW]	Low avg.power[3] [mW]	CW power [mW]
375	<90	40	10.0	2.5	50
405	< 50	40	3.0	1.0	50
450	<80	40	4.0	0.8	50
485	<100	40	5.0	0.7	50

Table 3.2: A table of the lasers used in this study and their parameters from PicoQuant.

3.3.5 Fluorescence lifetime imaging microscopy (FLIM)

Fluorescence lifetime imaging microscopy (FLIM) has similar characteristics to TCSPC. First the laser from a combining unit is passed through the microscope lens and

illuminates the sample. Emitted light from the sample then passes back through the microscope lens, through a dicroic mirror and pinhole into one or more PMT tubes which are restricted using band pass and long-pass laser cut-off filters. A full diagram is shown in Figure 3.17.

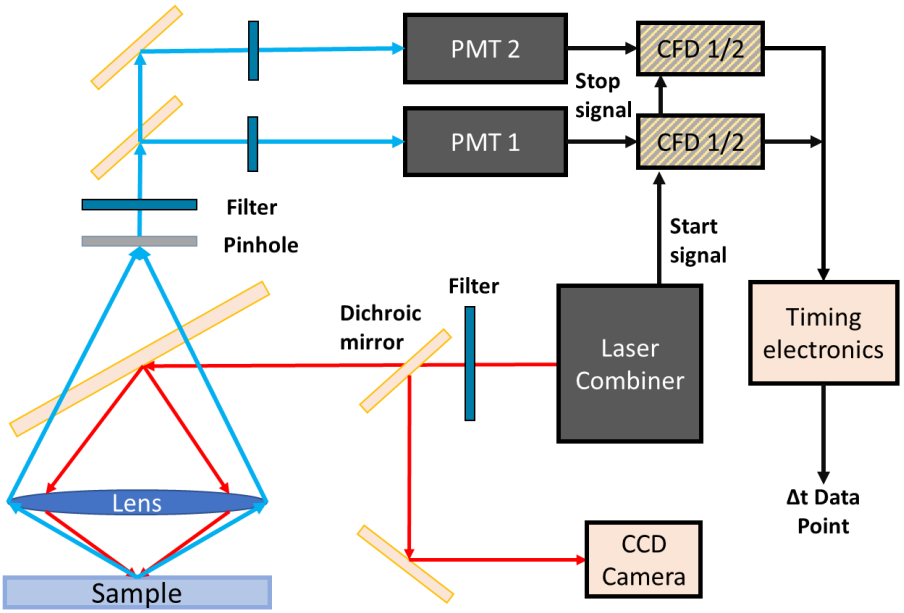

Figure 3.17: Confocal microscope set up for FLIM. A laser from a laser combining unit is split by a dichroic mirror into a CCD camera used to align the microscope. Another mirror reflects it down through a lens onto the sample. Light coming back from the sample is focussed through the lens, though a pinhole and filter and split into two PMT tubes which can each discriminate one wavelength by using more filters. (Figure has been adapted from material by PicoQuant and can be found at www.picoquant.com).[136]

During data acquisition the objective lens is moved over the sample, each position of the microscope lens corresponds to a pixel on the final image, the laser illumination will "dwell" on a spot to measure a lifetime. Data is recorded as the X and Y axis location of each pixel and the average lifetime of each pixel. The combined total of all photon counts from each pixel should be at least 10,000.

A PicoQuant MicroTime 200 Time-resolved confocal microscope was used. The system is comprised of an inverted Olympus IX73 confocal microscope equipped with

piezo scanning table to move the objective lens over the stationary sample with 1nm of positioning accuracy. A 405nm and 485nm laser in a laser combining unit was used as the excitation source, their parameters are shown in Table 3.2: A table of the lasers used in this study and their parameters from PicoQuant.. The lasers are connected to the microscope using a fibre optic cable. An air objective 100 X zoom lens manufactured by Olympus was used for all measurements. The microscope was equipped with 2 detectors, a PicoQuant SPAD-100 photon counting diode and a PicoQuant Hybrid detector alongside the PicoQuant Time harp 260 PCI card to record lifetimes. The detectors were used with long pass cut-off filters, a 75µm pinhole and dichroic mirrors. The filter was a 488nm long pass filter which let the entire spectrum in from all samples meaning the lifetimes represented in FLIM measurements are for the entire emission of the complexes in question as opposed to a single wavelength. For the triplet complexes burst mode was used to produce enough counts for an accurate measurement. Scans were performed in 80µm-by-80µm areas with a resolution of between 256 by 256 pixels to 580 by 580 pixels. Fitting was performed using Sympho time 64 software by PicoQuant and the quality of the measurement and fit was assessed by number of counts the closeness of the χ^2 value to 1.

3.3.6 Atomic force microscopy

Atomic Force Microscopy (AFM) is a member of the scanning probe microscopy family of characterisation methods, which utilise a sharp probe to measure the relative height of features on a sample surface as shown in Figure 3.18. Physical contact with the surface or interaction between the tip of a cantilever and the surface via intermolecular force is used to produce movement in cantilever by moving the tip up and down. The change in the up and down motion of the probe is measured using a laser which is reflected directly from the tip of the probe onto a detector. This movement is translated into data which forms an image of the surface.[137]

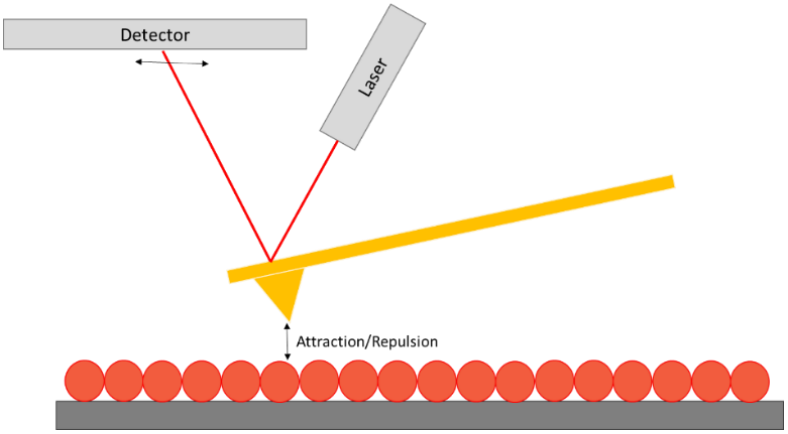

Figure 3.18: Basic schematic diagram of AFM operation. Shown here is the movement of the cantilever causing a shift in the angle of the laser on the detector allowing measurement of the surface topography.

In contact mode the tip of the cantilever makes contact with the surface of the sample, the movement of the tip over the sample surface is measured. The position of the cantilever is maintained with a constant level of force. This method gives the highest resolution images and is used most often.

The method used for this study was a variation of constant force known as alternating contact mode (AC), colloquially known as tapping mode as the tip makes rhythmic contact with the surface of the sample. The purpose is to generate an image which may be difficult to image in constant contact mode such as samples with soft surfaces. AFM was performed by the authour on an Agilent technologies 5100 AFM/SPM system in the Lancaster university chemistry department. Nanosensors PPP-SIEHR-SPL tips with a 1µm radius silicon nitride tips and a tapping frequency of 130kHz were used for measuring Langmuir Blodgett films on silicon wafers. Budget sensors Tap 150 with a 10µm aluminium coated silicon nitride tip and a tapping frequency of 150kHz were used for bare silicon measurements.

4. Intra layer energy transfer using carbocyanine dyes.

4.1 Aims and objectives

The aim of this chapter is to develop a light harvesting structure using readily available dyes within Langmuir Blodgett monolayers, with efficient energy transfer within the monolayer using multiple donors and an acceptor.

The objectives were therefore to create pure and mixed Langmuir monolayers of two carbocyanine dyes. To deposit these monolayers onto pre-prepared glass slides and to study the optical properties of the monolayers using steady state and time resolved fluorescence methods in order to determine the lateral energy transfer between the donors and acceptors within the monolayer.

4.2 Experimental overview

Figure 4.1: Donor (DiO) and acceptor (DiI) behaviour studied between two carbocyanine dyes at various molecular ratios deposited as Langmuir Blodgett films on glass slides supported by layers of stearic acid.

Two carbocyanine dyes shown in Figure 4.1 were combined at molecular ratios from 1-1 to 100-1 Donors to Acceptor. The Langmuir films were characterized and deposited on quartz glass slides as LB monolayers. These samples were analysed using time resolved techniques in order to determine if energy transfer occurred within the monolayer and the efficiency of energy transfer within the monolayer.

4.3 Results and discussion

4.3.1 Spectroscopy of pure Carbocyanine dyes in solution

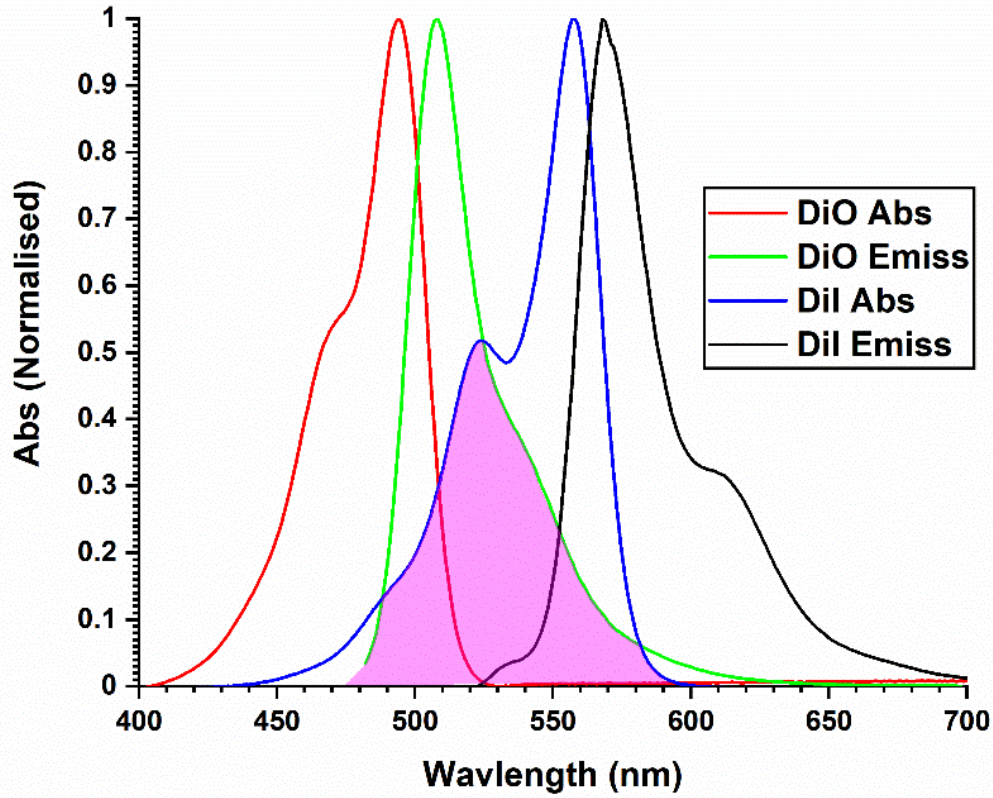

Figure 4.2: Comparison between the solution absorbance and fluorescence of DiO and DiI. The overlap between the DiO fluorescence emission and DiI absorbance is highlighted in magenta. The solutions were made up in chloroform from the stock solutions to concentrations of 3.7 x 10^{-5} M (DiO) and 3.5 x 10^{-5} M (DiI).

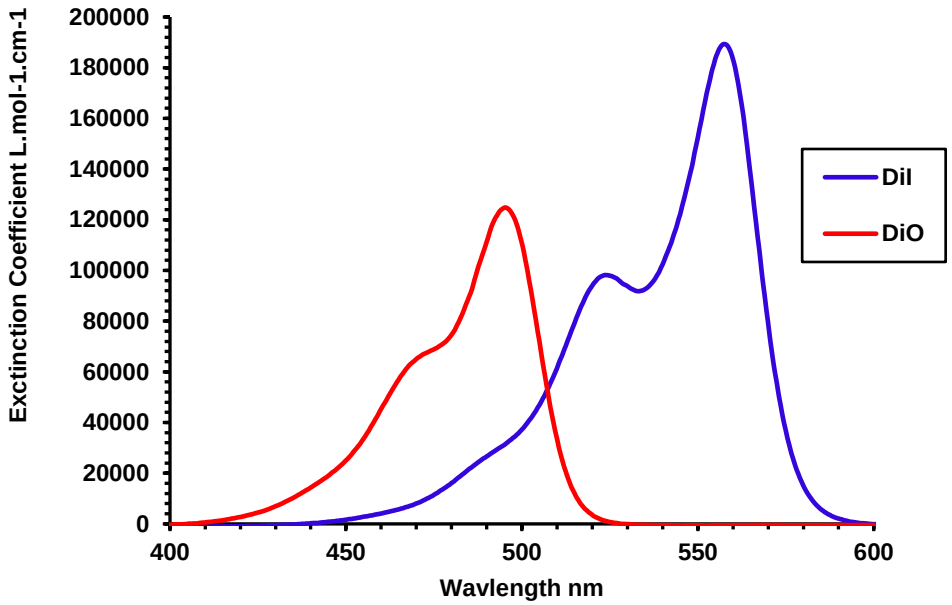

Figure 4.3: The molar absorption coefficient of DiO and DiI plotted as a function of wavelength, Coefficients at absorption maxima are shown below. Solutions were made up from stock in chloroform.

Both carbocyanine dyes, DiO and DiI, were dissolved into chloroform and the absorbance and fluorescence spectra of each dye was taken separately, this is shown in Figure 4.2. A clear overlap is shown between the DiO fluorescence and the DiI absorbance showing energy transfer between the two dyes is theoretically possible. The absorption coefficient was calculated based on Beer-Lambert line plots for both DiO and DiI in chloroform and was found to be similar to the manufacturer's value reported for dyes in methanol (DiO:154,000 L mol^{-1} cm^{-1}, DiI: 145,000 L mol^{-1} cm^{-1}).[79]

Molar absorption coefficients L.mol^{-1}.cm^{-1} (In $CHCl_3$)			
DiO	**470nm**	**495nm**	**484nm**
	64958.2	124600.1	86667.2
DiI	**525nm**	**560nm**	**550nm**
	97939.0	183313.5	152543.7

Table 4.1: The recorded molar absorption coefficients of DiO and DiI in chloroform

Both dyes used in this study show two absorption peaks and two emission peaks, 3,3'-Dioctadecyloxacarbocyanine Perchlorate (DiO) shows a band maximum at 480nm and a smaller shoulder at 465nm. A similar absorption band structure is present in 1,1'-Dioctadecyl-3,3,3',3'-Tetramethylindocarbocyanine Perchlorate (DiI) at a lower energy, the primary peak being at 560nm and the shoulder being at 520nm. The reason for this is that the level of conjugation increases between DiO and DiI as the structure of double bonds is extended. DiO and DiI are the focus of a lot of previous work on this class of dyes.[82]

4.3.2 Spectroscopy of mixed Carbocyanine dyes in solution

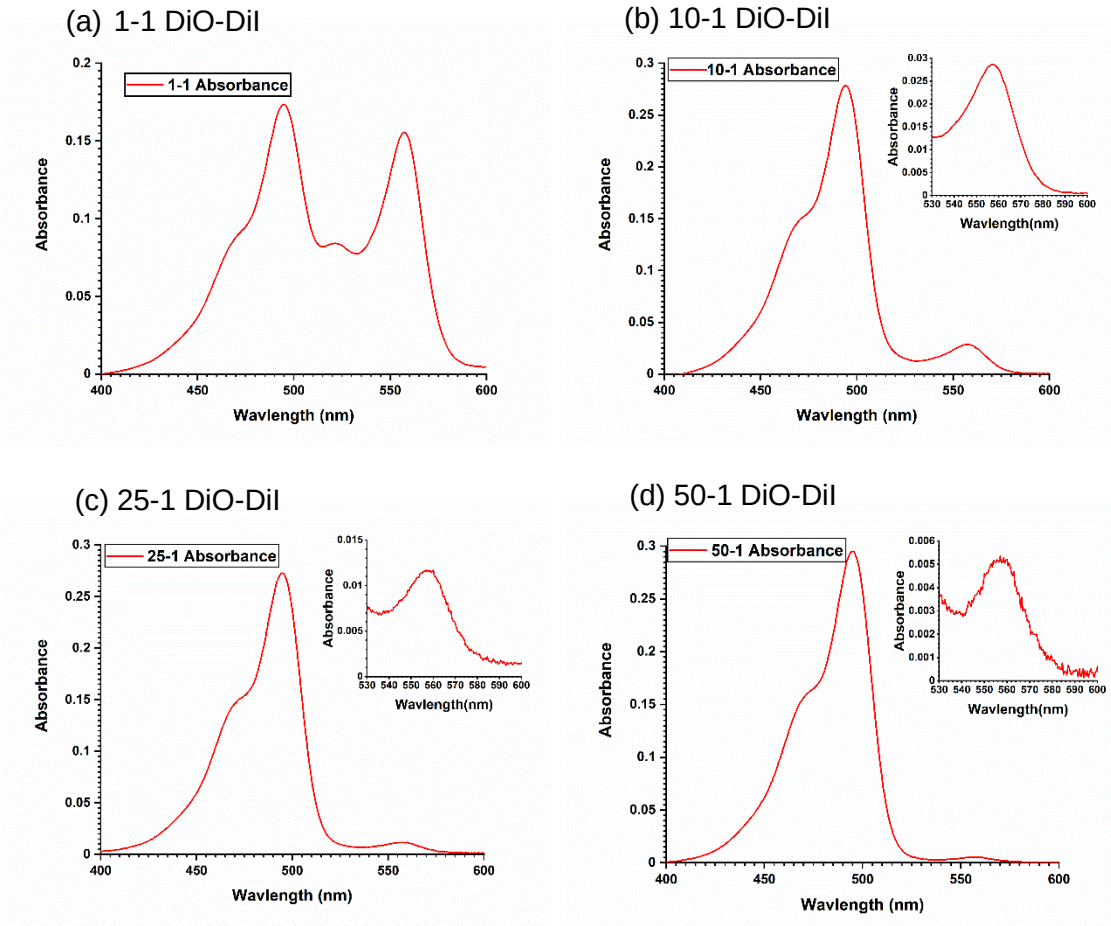

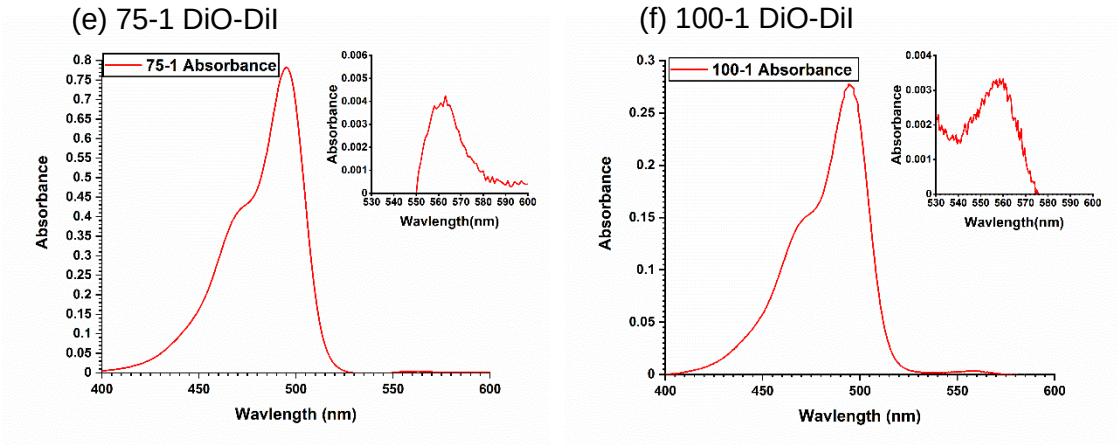

Figure 4.4: Absorbances for all the mixtures in solution at a concentration of this shows roughly what would be expected for mixed samples. Ratios of DiO-DiI shown are A) 1-1, B) 10-1, C) 25-1, D) 50-1, E) 75-1, F) 100-1. Solutions were made up from stock solutions in chloroform to a concentration of 3.2 x 10^{-6} M

Figure 4.4 shows the ratios of carbocyanine dyes in solution that were used for deposition into monolayers on glass substrates. The relative absorbance of each dye in each solution can be seen. The donor-acceptor ratio of 1-1 shows a relatively equal absorption spectra for each dye. However, the increased ratio of DiO to DiI shows a far higher absorption of DiO than DiI in each case.

4.3.3 Langmuir isotherms of pure and mixed films

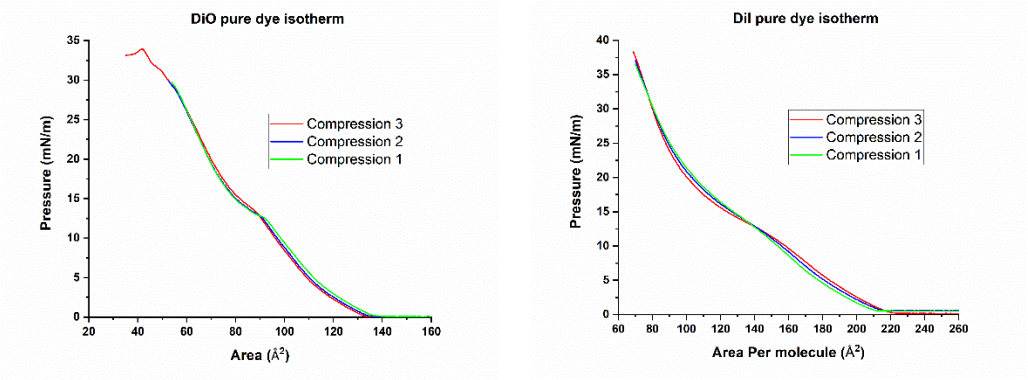

Figure 4.5: The isotherms for each pure molecule. Each one shows how the isotherm changes with repeated compressions until there is little to no change. Films were fabricated from stock solutions of a 1 x 10^{-3} M and deposited on room temperature water (~20 ^{o}C) and compressed at 50mm/min.

Figure 4.5 shows the measured isotherms for DiO, DiI and stearic acid (SA). The changes shown in the liquid phase is taken as evidence of the film annealing with repeated compressions. Doing this makes the films much more stable. Figure 4.5a shows SA with a regression line showing the molecular area to be around 21Å^2, the shape of the isotherms undergoes little change. Figure 4.5b shows pure DiO isotherm. Less shifting of the isotherm itself is notable here however the shape itself does undergo a significant change. The molecular area estimated is about 97Å^2 when the solid phase is extrapolated down to a pressure of 0 mN/m. The collapse pressure shown by the looping down region at the top of the final compression measured is around 34mN/m. Figure 4.5c shows pure DiI isotherms, again there is significant change between the first and last compression. The molecular area measured is close to 120Å^2 and the collapse pressure around 35mN/m.

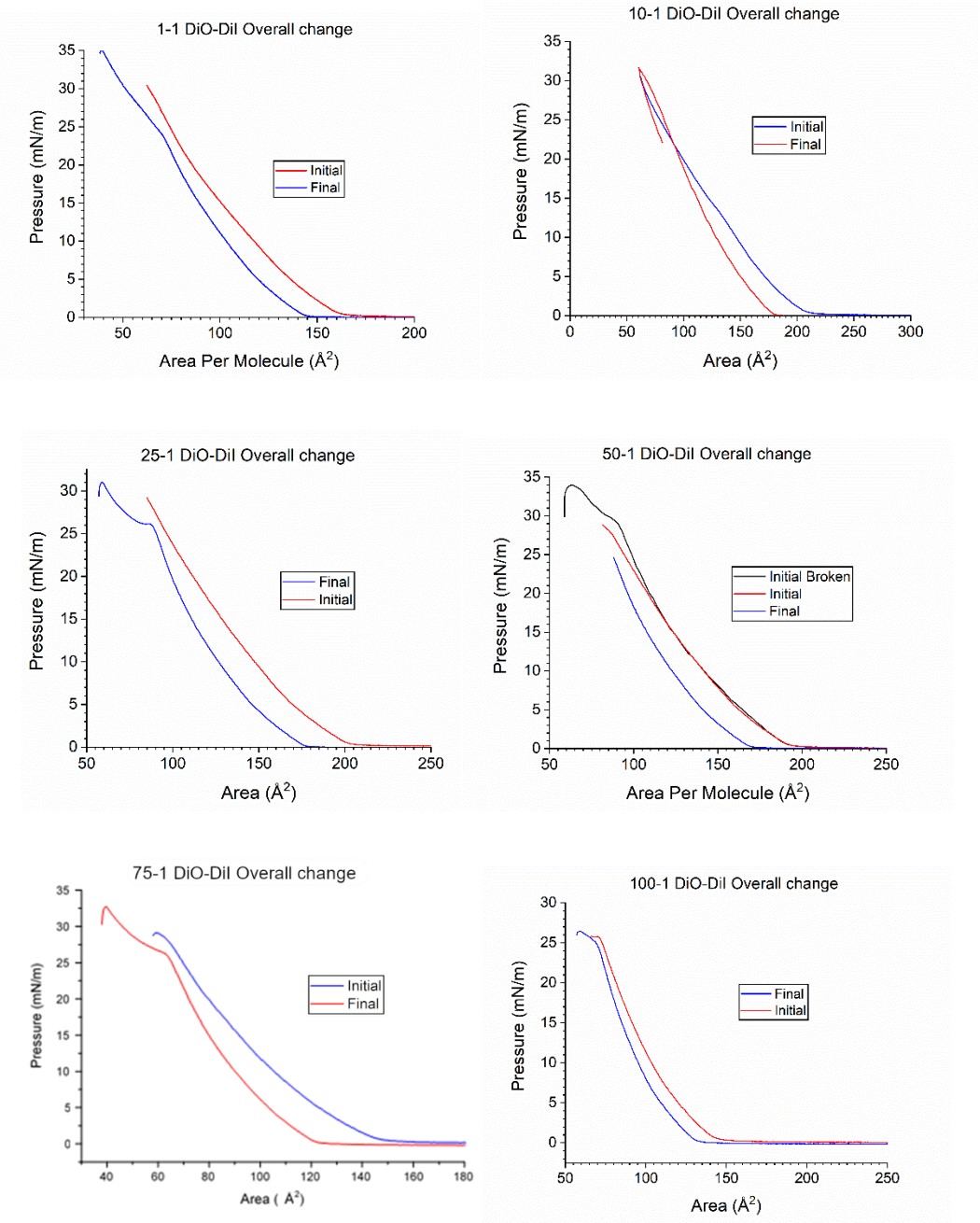

Figure 4.6: Langmuir isotherms from the first and last compression for each of the DiO-DiI solution dye ratios, the graphs show the first and last of ten compressions as well as a collapse pressure. The small loops at the end of the compressions show the collapse of the film, signifying the pressure. Monolayers were deposited from stock solutions with a concentration of 1 x 10^{-4} M at room temperature 20 ^{o}C and compressed at 50mm/min.

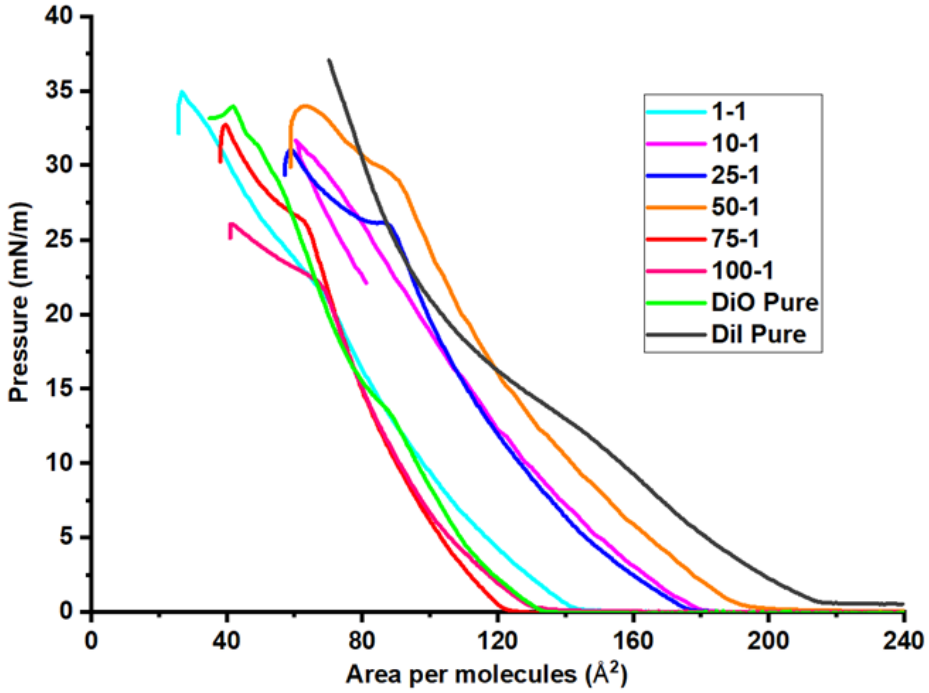

Figure 4.7: Langmuir isotherms of pure dye contrasted with isotherms of mixed dyes, the ratios shown here are DiO to DiI

Figure 4.6 shows the first and last recorded isotherm for each dye ratio. These graphs show the pliability of these films. In almost every case the final isotherm is a different shape and at a lower area per molecule than the first. It is interesting to note that some isotherms change more than others, this indicates changes in the conformation of the films with repeated compression. The Langmuir isotherms are also shown to be significantly different in shape to “classic” Langmuir isotherms as they do not show the distinct gas-liquid-solid transition demonstrated by the stearic acid isotherm in Figure 4.5. They show a gas and liquid phase that is similar to the classical shape, however the rate of increase in the surface pressure is not linear resulting in a curved liquid phase. The curve eventually reaches a gradient which could be described as a solid phase, in all cases this is at approximately 25Mn/m as shown in Figure 4.6 and Figure 4.7.

In all cases the rate of increase in surface pressure drops when the surface pressure goes above approximately 25 Mn/m. The rate of pressure increases then returns to that of a solid phase. This occurred for both pure DiO and DiI, the isotherms of DiO and DiI mixtures retained this shape. Figure 4.7 also shows Langmuir films of mixed DiO and

DiI increased the area per molecule relative to films of pure DiO. This occurred up to a ratio of 50-1, which is almost in line with the molecular area of DiI. It then decreased again as the ratio is made up of more of the smaller DiO.

The head groups of DiO and DiI were created and optimised in Avogadro.[138] The estimated bond lengths were input into the model. The models are shown in Figure 4.8 and Figure 4.9.

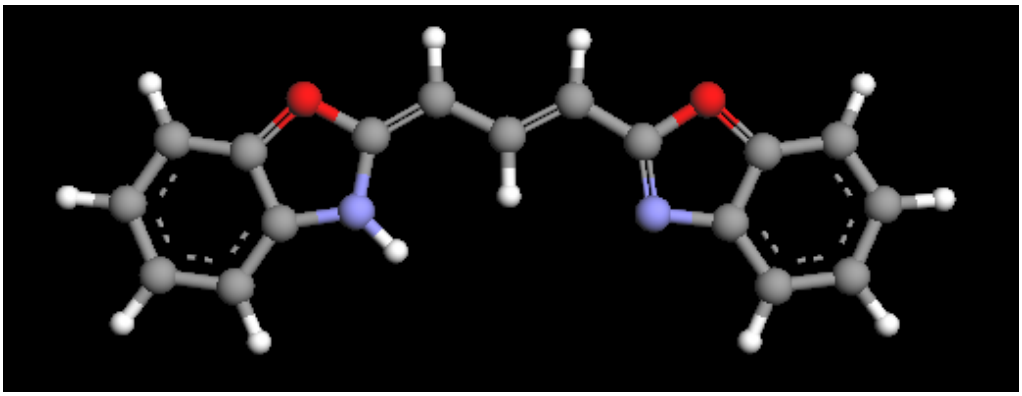

Figure 4.8: DiO head group only. First structure optimization gives a flat area of 5.07 x 16.08 angstroms, giving a total area of approximately 80 $Å^2$.

This model produces an estimation of the 2-dimensional size of the head group. The head group is the part of the molecule which is compressed and therefore contributes to the molecular area much more than the tail groups. The molecular area of pure DiO produced experimentally agrees with the molecular area of 90 angstroms found by the model in Figure 4.8. The same modelling was applied to a model of DiI and is shown in Figure 4.9.

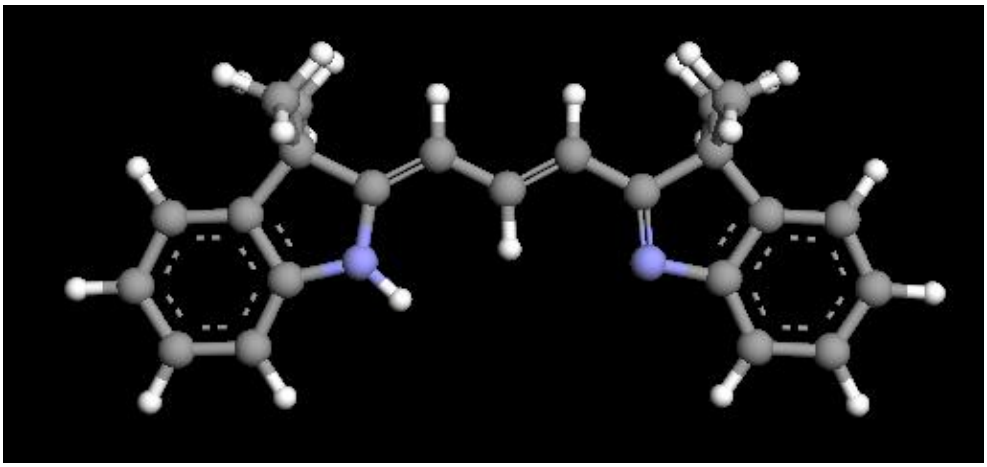

Figure 4.9 : DiI head group optimised once gives lengths and width of 6.5 And 16.5 angstroms. Giving a total area of 107.25 angstroms squared. This shows how the size of the molecule is increased by the presence of two methyl groups.

The model of DiI shown in Figure 4.9 creates a smaller area than what has been measured in the experimental isotherms and in the literature.[78]

The mixed films were analysed to determine changes in the molecular area as a function of the mixing ratio. In this case the known quantities are the average molecular area of the mixed isotherm gained from extrapolation of the solid phase of the isotherm at zero pressure, the number of molecules deposited on the trough and the mole fraction of the components of each mixture and therefore the amount of each molecule deposited.

The contribution of each component to a mixed monolayer is defined by the following equation.[100]

$$A_{Avg} = F_{DiO}A_{DiO} + F_{DiI}A_{DiI}$$

Equation 4.1: The contribution of each component of a monolayer to the average molecular area

Where A_{Avg} is the experimentally determined average area per molecule. A_{DiO} and A_{DiI} are the experimentally determined molecular areas of DiO and DiI and F_{DiO} and F_{DiI} are the mole fractions of the dyes.

This equation does require the assumption that one component of the mixed film is occupying the same molecular area as it would in a pure film. However, comparisons to expected molecular area can be made using this equation. The calculated molecular areas are shown in Table 4.2: Table showing the calculated molecular areas from the experimentally determined values and equation 1. The molecular area of pure DiO was 97Å2, pure DiI was 120Å2.

Ratio	Calculated molecular area	Experimental A_{AVG} Last
1 to 1	108.50	120
10 to 1	99.09	155
25 to 1	97.88	170
50 to 1	97.45	145
75 to 1	97.30	110
100 to 1	97.23	108

Table 4.2: Table showing the calculated molecular areas from the experimentally determined values and equation 1. The molecular area of pure DiO was 97$Å^2$, pure DiI was 120$Å^2$

The calculated molecular areas show that as the ratio of DiO to DiI increases the average molecular area decreases to account for the much higher number of the smaller DiO dye molecules. The predicted molecular area for 1-1 is an average of the molecular area for each dye, making it higher than that of DiO but lower than that of DiI. As more DiO is added the molecular area decreases. The experimentally measured molecular area actually increases with increased ratios of DiO to DiI up to 50-1 and then decreased again to an area similar to DiO. Differences in the shapes of the isotherms give results that vary from that of the experimentally determined values. However, it agrees with the molecular area being lower than that of DiI but higher than that of DiO. This suggests that mixing DiO and DiI interrupts the interaction of the dyes with one another.

In comparison to Sakomura et al[94,95] a similar phenomenon is shown whereby there is no clear correlation between the mixing ratio and the changes in the isotherm but there

are alterations to the collapse pressure and the molecular areas. They use a similar methodology to us of comparing the theoretical size of the molecules with the measured size and suggest a head-to-head arrangement of the dyes.

4.3.4 In situ using spectroscopic study.

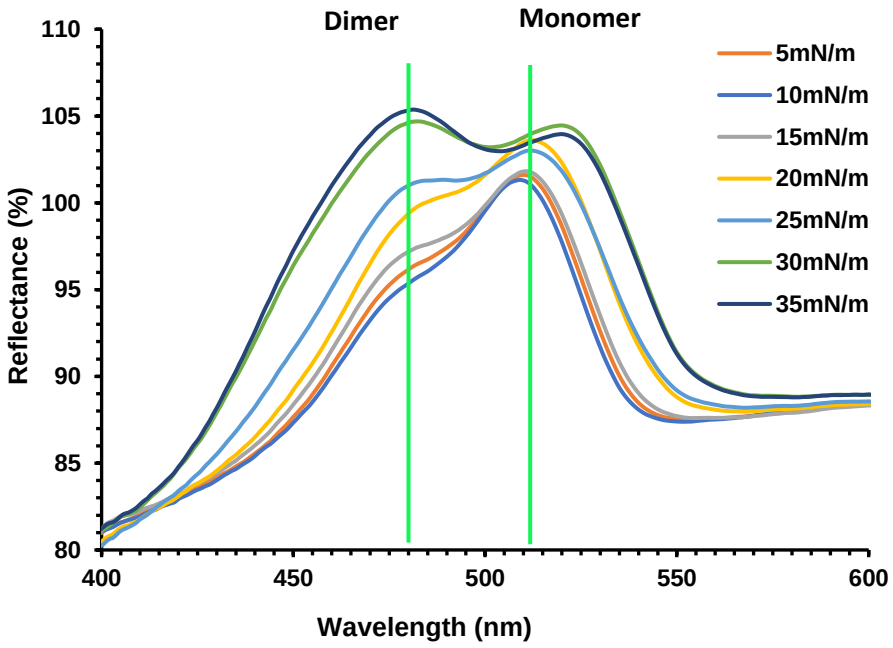

Figure 4.10: Reflectance absorbance spectra of DiO from the surface of water in a Langmuir trough as a function of surface pressure.

Figure 4.10 shows that at pressures of 5, 10 and 15mN/m the shape of the spectra was similar to the spectra from dyes in solution. The spectra show higher intensity peaks at 510nm and lower intensity peaks at 480nm. During compression these peaks undergo changes in intensity with respect to one another. The 480nm peak became more intense with respect to the 510nm peak as the surface pressure increased. In addition, the overall intensity of the spectrum increases. The peak at 510nm shifts to 525nm whilst the peak at 480nm stays in the same position. These peaks have been assigned to dimers and monomers in previous works and suggests the formation of dimers and/or aggregates at surface pressures of around 25-35mN/m.[84] DiI did not show the same change and only increased in intensity, further suggesting that it does not aggregate in a pure monolayer as DiO does. This also shows that the aggregation is caused during the formation of the Langmuir film on the surface of water and not as a result of the deposition of the film into an LB monolayer on a solid sample.

4.3.5 Pure Langmuir Blodgett films of carbocyanine dyes, spectroscopic characterization.

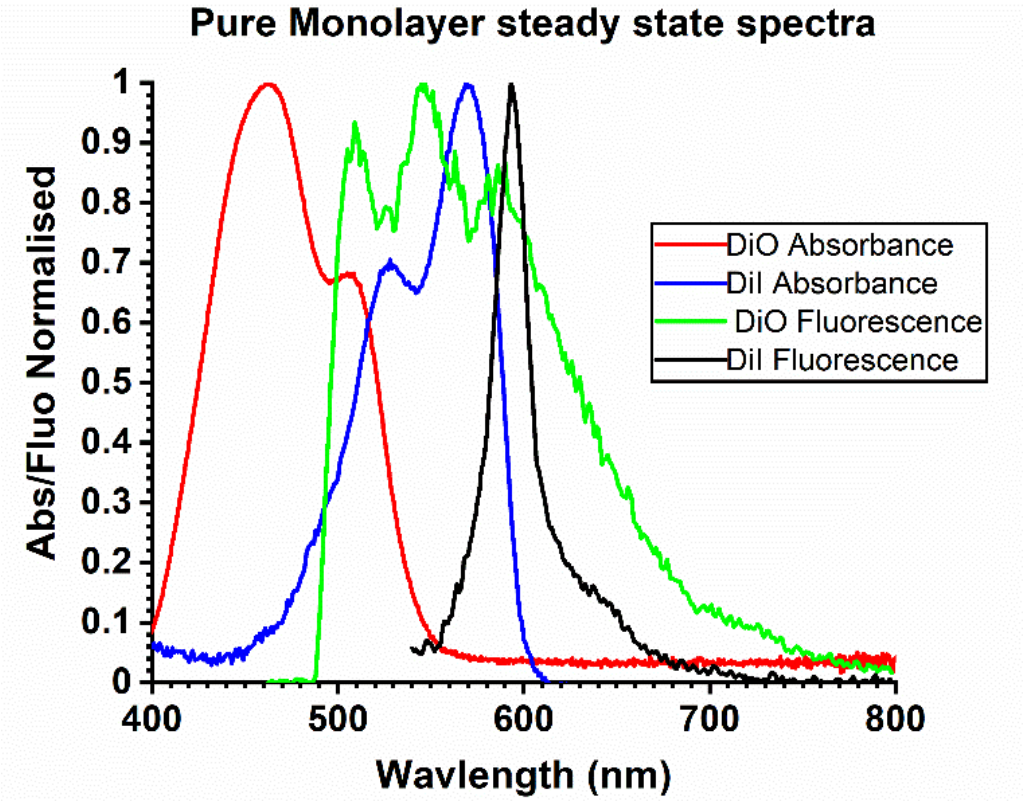

Figure 4.11: Steady State absorption spectroscopy of Pure DiO and DiI deposited as a monolayer on quartz glass and stearic acid supports. Films were fabricated from monolayers deposited using 1 x 10^{-3} M stock and the spectra recorded at room temperature (~20 ^{o}C).

The absorbance of the deposited LB films of pure DiO and Pure DiI on glass is shown in Figure 4.11. The absorbance of DiO shows a significant change when compared to the solution spectra shown in Figure 4.2. The peak at 520nm has diminished massively in comparison to the solution spectra. This peak has been assigned to monomers of DiO and suggests a reduction in the number of monomers. The peak at 460nm has increased massively compared to the solution spectrum. This peak has been assigned to dimers and higher aggregates. This suggests that the deposition of the DiO as a pure LB monolayer causes aggregation between the dyes. The absorption spectrum of DiO also shows a peak shift from 490nm to 460nm. The same change was not observed in the absorption spectrum of DiI indicating no change in the amount of one species over the other, the absorption spectrum of DiI in a pure LB monolayer did not

show any shifts when compared to the absorption of DiI in solution however the peak at 520nm shows a higher intensity relative to the peak at 570nm than in the solution spectrum.

The fluorescence spectrum of LB monolayers of DiO also shown in Figure 4.11 shows massive changes in comparison to the solution spectrum. Instead of two peaks mirroring the absorption, three peaks are shown, one at 500nm, one at 550nm and one at 660nm. In addition, the fluorescence spectrum of DiO also showed a significant broadening which increased the overlap with the absorbance of DiI, this is highly advantageous as increased overlap from the donor to the acceptor increases the rate of energy transfer. The fluorescence spectrum of LB monolayers of pure DiI did not change significantly, this reflects upon the lack of changes in the absorption spectrum, however there was some sharpening of the peak at 600nm. This peak is assigned to dimer/aggregate emission, suggesting that there is some aggregation occurring, however not to the same degree as with pure DiO.

Danos et al[73] showed a very similar spectrum when DiO was deposited in a 10-1 molar ratio with stearic acid on glass slides. They show similar peaks at 550nm and 580nm. This agrees with the results shown here, they attribute the peak at 550nm to the monomer and 580nm to the dimer. An example of pure DiI deposited as ten pure layers shows similar fluorescence to DiI fluorescence in Figure 4.11 in terms of shape and the sharpening of the peak in comparison to the solution spectrum. However, it shows a much stronger shift of the peak, in this case to 700nm as opposed to 600nm shown in Figure 4.11 suggesting that the deposition of multiple layers may be causing some shifting in comparison to a monolayer.[78]

4.3.6 Mixed films of carbocyanine dyes steady state spectroscopic characterization.

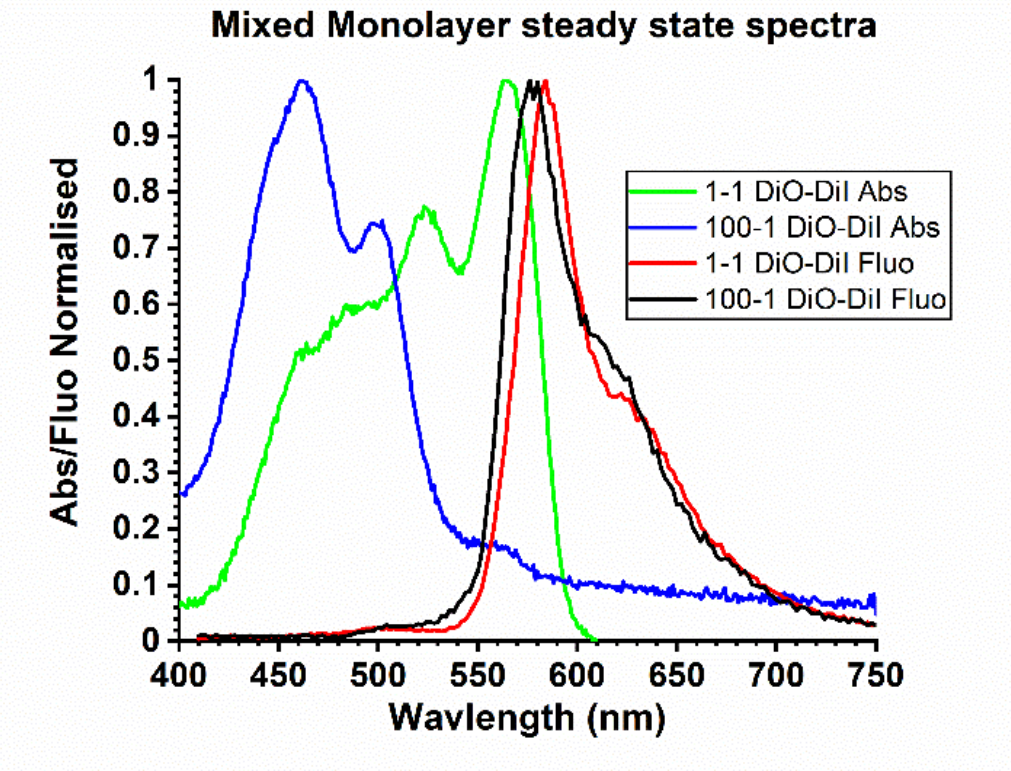

Figure 4.12: Absorbance and fluorescence spectra of the DiO-DiI 1-1 and 100-1 ratio samples deposited on quartz glass. Films were fabricated from monolayers deposited using 1 x 10^{-4} M stock and the spectra recorded at room temperature (~20 ^{o}C).

Figure 4.12 shows the mixed absorption spectra for 1-1 and 100-1 monolayer films of DiO and DiI deposited on glass. The absorption spectra for 1-1 is the combination of the pure absorption spectra of DiO and DiI. The region assigned to DiO, from 400 to 550nm, shows a peak at approximately 460nm and one around 500nm. The ratio of these two peaks (460nm and 500nm) appear less sharp and in different proportion than the one observed for the pure DiO monolayer. This might suggest that the degree of aggregation occurring in the pure DiO monolayer sample is not occurring in the case of the 1-1 sample. In the 100-1 sample however the DiO absorption region appears largely as it does in the pure sample, suggesting the smaller amount of DiI relative to DiO does not interfere with the aggregation state as it does in the 1-1.

In the 1-1 sample DiI, which is present from 500 to 600nm, appears largely unchanged from the pure DiI sample shown in Figure 4 . 11, suggesting the aggregation state does not change significantly when co deposited with DiO. The DiI absorbs more intensely than the DiO despite both dyes being present in equal amounts which is to be expected owing to the much higher absorption coefficient of DiI.

Both 1-1 and 100-1 monolayer fluorescence spectra showed a massive reduction in the intensity of DiO fluorescence. Fluorescence occurred from the DiI portion of the spectrum even when DiO alone was excited at 405nm. This suggests that significant energy transfer is occurring from the DiO to the DiI in place of fluorescence from the DiO.

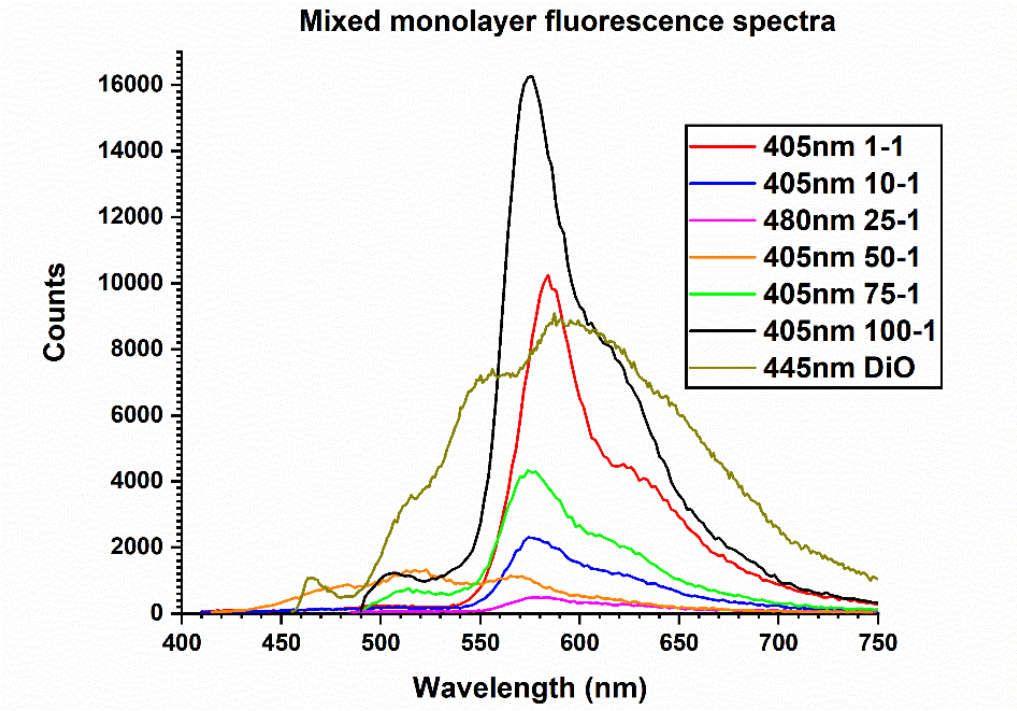

Figure 4.13: Fluorescence emission of an LB monolayer of each mixture of DiO-DiI compared with Pure DiO, excitation wavelength is included in the legend. Films were fabricated from monolayers deposited using 1 x 10^{-4} M stock and the spectra recorded at room temperature (~20 ^{o}C).

Figure 4.13 shows the steady state fluorescence emission spectrum for each dye ratio deposited as a monolayer on a stearic acid coated glass slide. There are two indicators of energy transfer occurring. The absence of DiO fluorescence and the presence of DiI

fluorescence even when the excitation wavelength should not be exciting DiI. This indicates that DiO is acting as a donor and donating the absorbed energy from the light to DiI. Every sample shows a highly diminished DiO fluorescence (from 500 to 550nm) in comparison to the Pure DiO monolayer sample and the DiI Sample. The DiO Fluorescence does not increase to the number of counts displayed by the DiI in any of the samples, despite the fact that there is a much higher amount of DiO present than DiI. Using the fluorescence at 515nm an approximate estimation of the energy transfer was calculated and is displayed in Table 4.3.

Ratio DiO-DiI	Energy transfer (%) (515nm)
Pure DiO	0
1 to 1	94
10 to 1	95
25 to 1	97
50 to 1	64
75 to 1	78
100 to 1	68

Table 4.3: Energy transfer for each mixed monolayer sample calculated using the reduction in the fluorescence intensity of DiO (donor), these values are based on a set of 1 sample each and should be regarded accordingly.

The reduction in fluorescence intensity in DiO is taken to be the product of energy transfer and shows energy transfer occurring in each case. The 1-1, 10-1 and 25-1 ratios show over 90% energy transfer. 50-1, 75-1, and 100-1 show over 60% energy transfer. The fact that lower energy transfer rates occur at higher ratios indicates that the energy transfer is less efficient when there is a greater distance between the donor and the acceptor, as will be the case in the higher ratio samples. However likely owing to the aggregation effects enabling better energy transfer from dimers and aggregates the amount of energy transfer still exceeds 60%.

4.3.7 Films of carbocyanine dyes, imaging with FLIM and AFM.

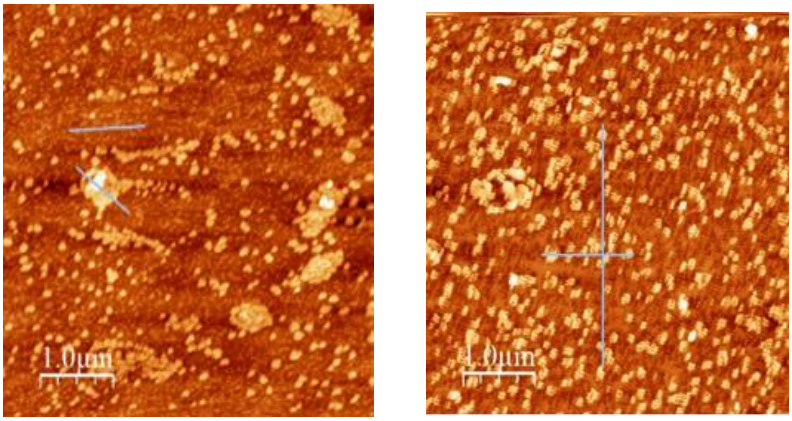

Figure 4.14: AFM image of DiO (Left) and DiI (Right) deposited on stearic acid layers on an Si wafer with no cap.

Figure 4.14 shows the surface topography of the dye layers by DiO and DiI measured by AFM. Both samples show small circular protrusions. DiO shows groups of protrusions clustered together whereas DiI shows the domains spread out evenly. Both scans also show a homogenous surface behind the highest domains in the foreground. Previous research does suggest that aggregates can be observed using AFM however they display well defined rectangular shapes, this suggests that these domains are not highly organised aggregates but rather amorphous dimers and excimers.[91]

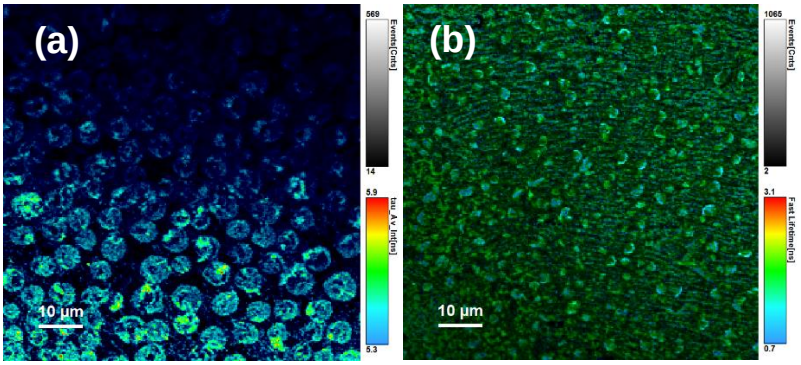

Figure 4.15: Fluorescence lifetime imaging microscopy of monolayer samples of DiO (a) and DiI (b). The absorption of the samples are shown in Figure 4.11.

When compared with the AFM images in Figure 4.14 the FLIM images in Figure 4.15 show different shapes on the surface of the samples. The DiO sample showed most of the fluorescence coming from circular domains. The DiI sample showed smaller evenly spread domains. More fluorescence was observed originating from behind the domains as well.

This potentially shows that clustered masses of dye form on the surface of the water before spreading or transferring the dyes to the solid slides results in the formation of these clusters. Alternately this may be the way unsupported Langmuir Blodgett films of carbocyanine dyes form when deposited on a solid substrate. Previous studies on Langmuir Blodgett films of carbocyanine dyes have utilised films stabilised with stearic acid mixed into solution with the dyes and/or have not studied such films under a microscope to reveal the topography. Without direct observation, one cannot be confirmed over the other. However, in this study the changes in the spectra on the surface of water may indicate that these domains formed prior to deposition onto a glass slide.

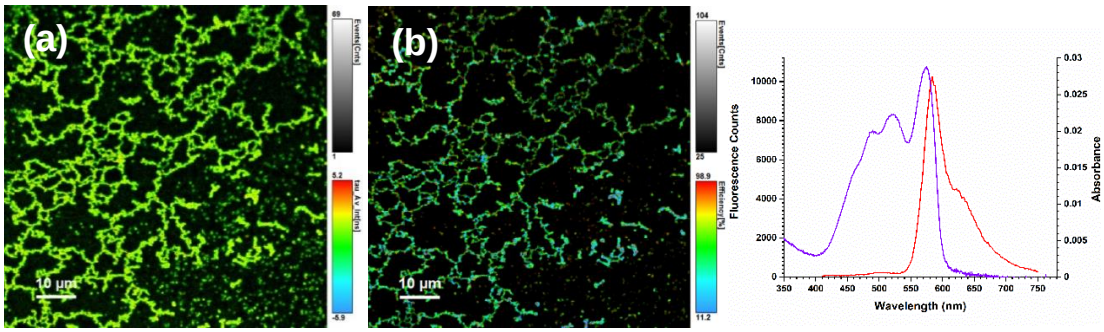

Figure 4.16 A FLIM image (a) and a FRET image (b) of a 1-1 sample recorded with a 485nm laser. The absorption (blue) and fluorescence (red) of the sample is shown.

The FRET images take the lifetime of the DiO as measured by the microscope and use it to calculate the efficiency of energy transfer by observing the difference in the donor channel between the quenched and unquenched lifetime. A higher number of photon counts is observed in the lines shown in the film by Figure 4.16 (a). When analysed for energy transfer these regions show a strong 50% energy transfer suggesting that DiI may be present in these regions and therefore energy transfer is occurring in the

regions near to DiI. The darker regions show similar efficiency. This could suggest that these regions are mostly DiO and the energy is being transferred away from these regions instead of emitted as photons.

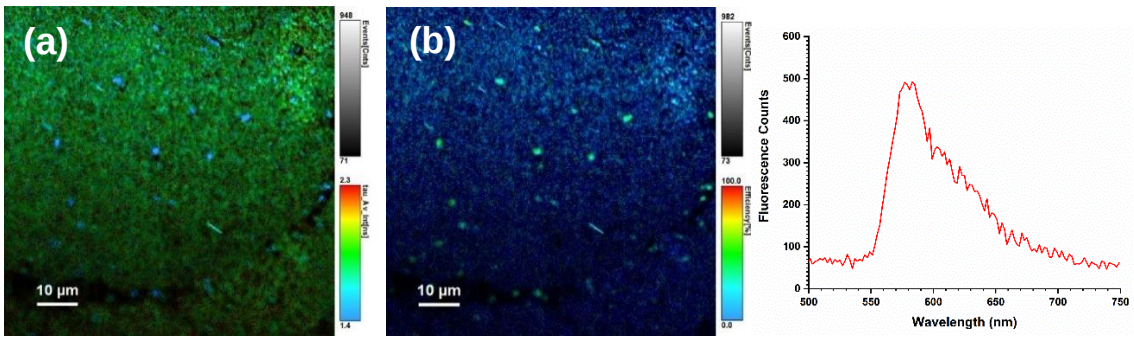

Figure 4.17: A FLIM image (a) and a FRET image (b) of a 25-1 sample recorded with a 480nm excitation laser. The fluorescence (red) of the sample is shown.

The FLIM image in Figure 4.17 (a) shows a homogeneous surface, showing good film deposition across the sample. Specks of blue (indicating a faster lifetime) show areas where energy transfer may be taking place as a faster lifetime is indicative of lifetime reduction through fluorescence quenching. The percentage energy transfer is shown in (b) and the flecks appear to be transferring energy.

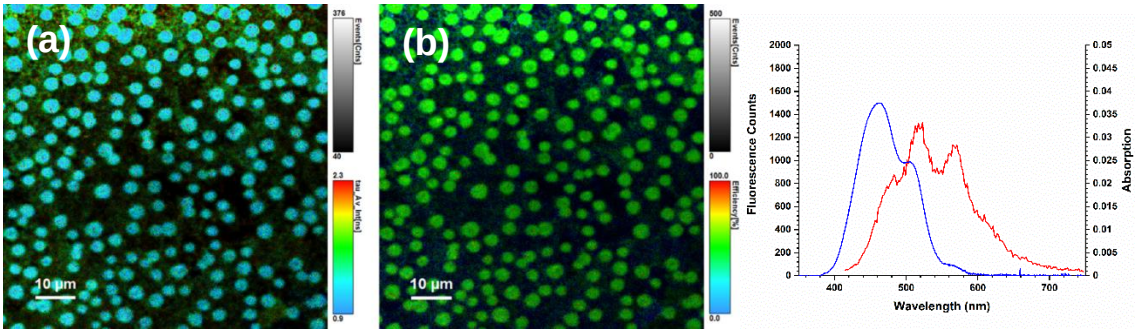

Figure 4.18: A FLIM image (a) of one of the 50-1 samples as well as a FRET image (b) recorded with a 480nm laser. The absorption (blue) and fluorescence (red) of the sample is shown.

Figure 4.18 (a) and (b) shows a number of domains where energy transfer is particularly active as they show a higher number of events owing to a higher emission rate of photons. They also show approximately 50% energy transfer in these regions whereas the darker regions with fewer counts show lower efficiency energy transfer. The interpretation of this is that energy transfer is occurring only where DiI is present in the film. Additionally, this result does agree with the overall energy transfer measurement of the film measured with the FT300 suggesting 50% energy transfer.

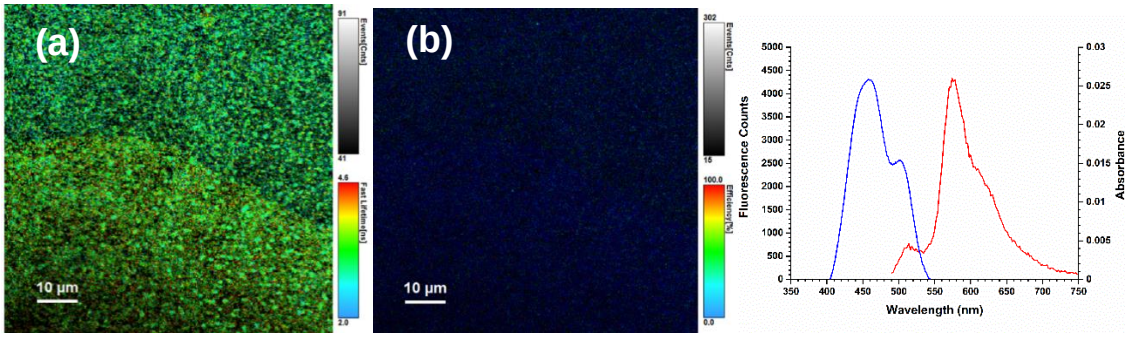

Figure 4.19: A FLIM image (a) of one of the 75-1 samples as well as a FRET image (b) recorded with a 480nm laser. The absorption (blue) and fluorescence (red) of the sample is shown.

The FLIM image in Figure 4.19 shows a relatively constant lifetime across the entire film surface. Also, the entire surface now has a structure approaching that of the DiI from Figure 4.19 (b). It should be noted however that this sample is a ratio of 75-1 and therefore is mostly DiO. As this is the case the image should appear similar to the structure shown in Figure 4.15 (a). However, the structure appears similar to DiI suggesting a different organization of the film to the pure DiO. It also suggests the formation of a film which does not include the protrusions seen before. The difference is that in previous studies they have taken on well-defined shapes which reflect the stacking of the complexes. The lack of protrusions and well-defined shapes may be the effect of DiI on the film formation properties of DiO. Using the decay from each image, average lifetimes were calculated and plotted on bar charts as shown in Figure 4.20.

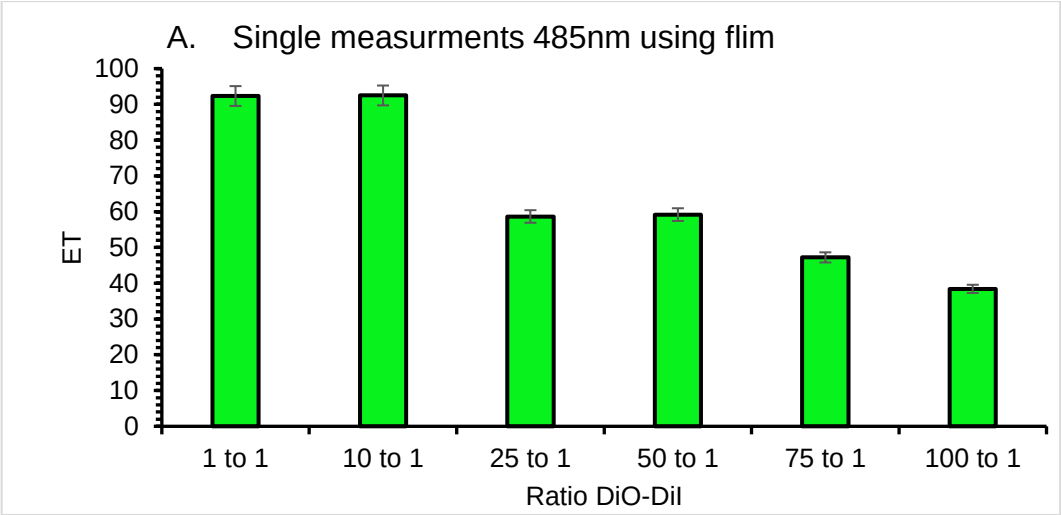

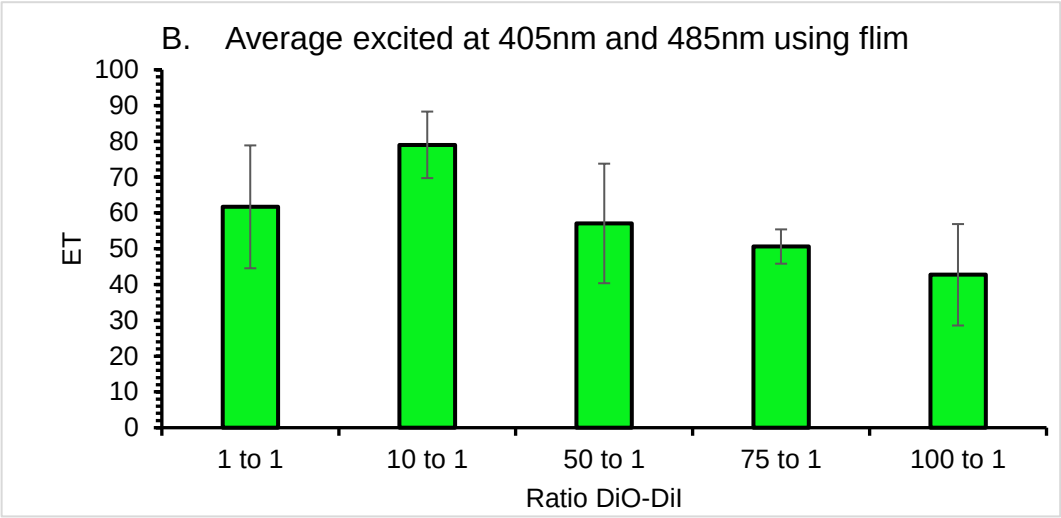

Figure 4.20: Bar charts showing the calculated energy transfer using single examples with 3% error applied (A) and the averages (B) from Lifetimes of microscopy image. Lifetimes of the pure DiO and mixed samples were recorded using a fluorescence lifetime imaging microscope. The total average energy transfer and standard deviation is shown in B. A 405/480nm laser and a 488nm long pass filter was used to record these lifetimes. Two samples of each were created except for 25-1 which had only one.

Figure 4.20 shows the transfer efficiency of samples measured by the FLIM method indicating that there is a divergence from the values of energy transfer measured by the Fluotime 300. The same general trend is followed of high percentage energy transfer at low ratios of donor to acceptor, averaging around 60% with the highest values being around 90%, which then decreases to around 50% energy transfer as the ratio of donor to acceptor is increased to 100-1. The single measurements have a low

error of 1-3%, there was a high degree of deviation in the averages. However this could be attributed to the very small area that the FLIM focusses on compared to the FT300. This may be indicative of some variation depending on the point of a sample being measured.

There are differences between the FT300 and FLIM measurements. The differences between the two methods likely causes a disparity in the measured values. Specifically, the FILM microscope does not record the lifetime of a specific wavelength but all lifetime of the fluorescence emission past 480nm owing to the emission only being restricted by an 480nm edge pass filter the means that other lifetimes are present and may be interfering with the result. However, the evidence does show energy transfer occurring and does agree with the steady state and FT300 results in that the efficiency of energy transfer reduces as the ratio of donor to acceptor increases.

A reduction in the lifetime of DiO is consistently observed. The 1-1 and 100-1 sample became the focus of this work as they show the most interesting results. The 1-1 showing a high efficiency energy transfer and the 100-1 showing some evidence of exciton diffusion.

4.3.8 Energy transfer calculated using TCSPC values (FT300).

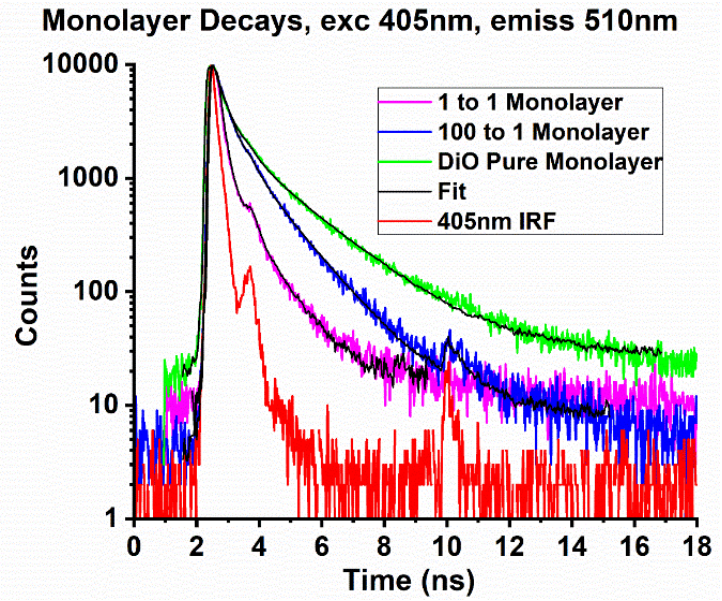

Figure 4.21: The 1-1 and 100-1 monolayer lifetimes compared to the pure DiO dye monolayer. The IRF is shown in red. The fits are shown in black; these were fit using Pico quant's FluoFit Software. A 480nm laser and a 488nm long pass filter was used to record these lifetimes.

The results from the FT300 time resolved fluorescence spectrometer showed the mixed monolayer samples exhibiting a faster lifetime than the pure DiO samples when measured at the emission wavelengths of DiO, examples are shown in Table 4.4. The model used to fit the decays was exponential reconvolution using two lifetimes. Tables of average recorded lifetimes and calculated energy transfer are shown in Table 4.4.

table of percentage energy transfer							
	Excitation-Detection wavelength (nm)						
Sample	445-510	445-540	445-580+590	480-510	405-510	480-580+595	Average
1 to 1	43%	32%	70%	39%	67%	71%	54%
10 to 1	39%	--	54%	--	12%	45%	38%
25 to 1	--	--	--	39%	--	25%	32%
50 to 1	47%	26%	26%	16%	--	--	19%
75 to 1	6 %	5%	--	13%	--	26%	10%
100 to 1	7%	--	25%	--	--	55%	17%
table of lifetimes in nanoseconds, **errors are within 1-3%**							
Sample	445-510	445-540	445-580+590	480-510	405-510	480-580+595	Average
DiO	0.79	0.7	1.02	0.97	0.55	1.15	0.86 ± 0.03
1 to 1	0.45	0.48	0.29	0.59	0.19	0.32	0.38 ± 0.01
10 to 1	0.48	x	0.44	x	x	0.63	0.52 ± 0.02
25 to 1	x	x	x	0.59	0.60	0.86	0.72 ± 0.02
50 to 1	0.41	0.52	0.73	0.86	0.74	1.33	0.76 ± 0.02
75 to 1	0.74	0.67	1.06	0.81	x	1.51	0.96 ± 0.03
100 to 1	0.73	0.70	0.73	x	0.56	0.52	0.65 ± 0.02

Table 4.4: Table showing the energy transfer and fluorescence lifetime of each ratio showing the excitation and detection wavelength.

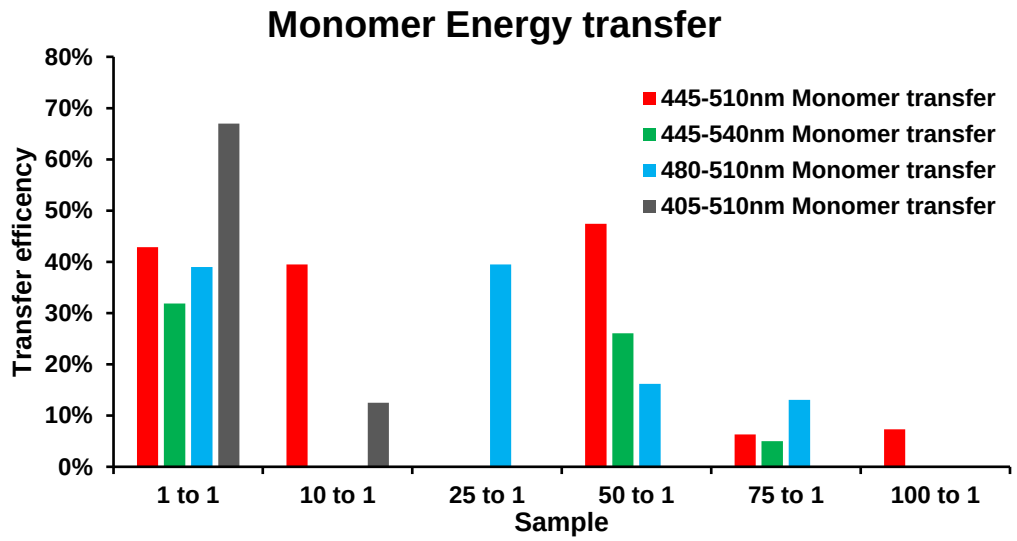

Figure 4.22: Bar chart representing the energy transfer recorded using the PicoQuant FT 300. The Lifetimes recorded at these wavelengths represent monomer decay. A 488nm bandpass filter was used to record the lifetimes. The results are from two samples (except for 25-1) each bar represents the average measurements performed with the stated set of parameters.

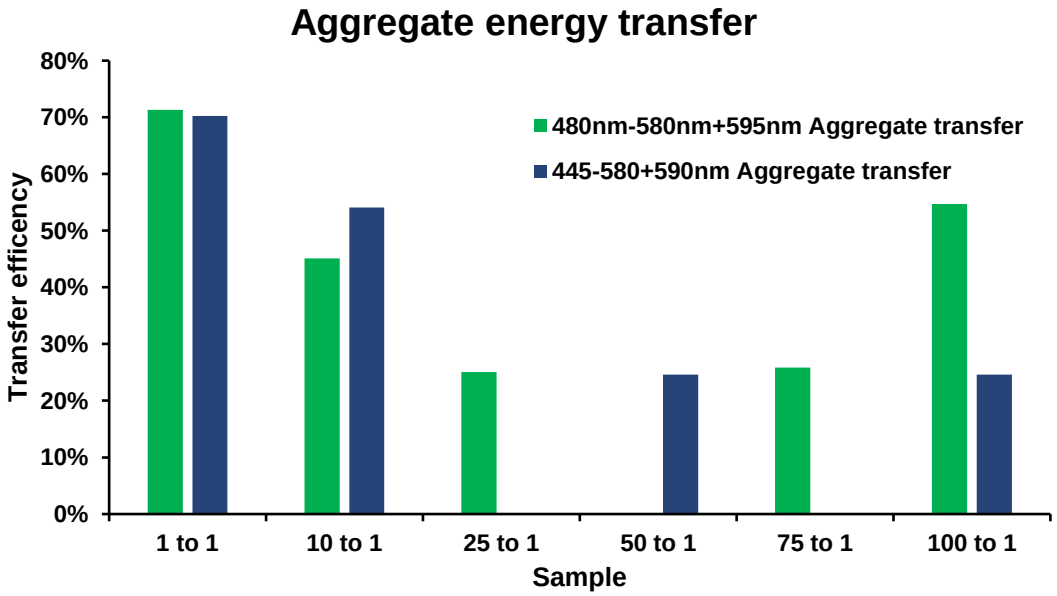

Figure 4.23: Bar chart showing the energy transfer calculated using data from the FT300. The wavelengths at which the lifetimes are measured are representative of Aggregates. A 488nm bandpass filter was used to record the lifetimes. The results are from two samples (except for 25-1) each bar represents the average measurements performed with the stated set of parameters.

The bar charts for each excitation wavelength in Figure 4.22 and Figure 4.23 show the percentage energy transfer for the given excitation and detection wavelength. An absent bar means no quenching occurred. The data is organized into two charts to represent the two states of the donor formed during the deposition of the DiO into a film, which has been shown to occur through the steady state spectroscopy as shown in Figure 4.10 and Figure 4.12. The percentage transfer in Figure 4.22 was calculated from decays from the monomers of DiO. Figure 4.23 was calculated from decays from the aggregates of DiO.

From this it can be determined what effect the aggregation may have had on the energy transfer. Owing to the broadening of the fluorescence of DiO shown in Figure 4.11 the formation of aggregates of DiO increases the area of DiI absorption covered by the fluorescence of DiO. This increases the rate of energy transfer. In the case of 1-1 samples, comparing the aggregate to the monomer shows both are capable of up to 70% energy transfer efficiency however excitation with a 445nm and 480nm laser produces poorer monomer energy transfer showing 43% 33% and 39% energy transfer, a reduction of around 30% in efficiency. This suggests that there is a transfer of energy from the monomer to the aggregates and then to the DiI. DiI was shown to interfere with the aggregation so there is less aggregate relative to monomer than in the case of the pure DiO samples suggesting that the aggregation is beneficial to the energy transfer as it outperforms the monomer even when there is far less of it.

10-1 aggregate also shows a higher energy transfer rate of 54% than the monomer at 39%, with around a 15% increase, albeit with a smaller improvement than the 1-1. In the case of 25-1 and 50-1, these show a higher level of energy transfer than in the monomer (40%) than the aggregate (25%). However, the 75-1 and 100-1 aggregates (26% and 55% respectively) are higher in efficiency than the monomer (13% and 8%) this reflects the increasing amount of aggregate in these samples in comparison to the monomer. This enables lateral energy transfer through the aggregates of DiO towards the DiI acceptors as a result of the close proximity of the DiO molecules and the overlap DiO has with its own absorption spectrum.

Previous studies of energy transfer observe the transfer using a reduction in the steady state fluorescence show a similar phenomenon to this study. In the case of the high ratio samples aggregate formation is occurring in the donor and behaving as an antenna for the acceptors, ratios as high as 250-1 and 1000-1 were studied. This agrees with the fact that the aggregate data shows a much higher level of energy transfer than the monomer as the higher ratio samples may have allowed for the formation of aggregates in the donors.

However, in the case of the 1-1 and 10-1 energy transfer where there is far less aggregation, but the donors are extremely close to the acceptors thus making high efficiency energy transfer possible without aggregation. In previous studies very high ratios of donor to acceptor were studied in order to encourage aggregation. However, the aim of this project is to create a system informed by photosynthesis and in photosynthesis the ratio of donors to acceptors is 100-1 which is why lower ratios were studied and the highest ratio studied in this thesis was 100-1. Additionally, the acceptor molecule is supposed to be the final trap which transfers energy to the, therefore a significant concentration of the acceptor is required in the film in order to promote final transfer of energy to the silicon by the acceptors.[94,95]

This then raises the question of how to promote aggregation in the acceptor in the high ratio films, or if the low ratio films are good enough to be used alone, this raises the need into study into aggregation control in mixed films of these cyanine dyes and for photocurrent studies into silicon samples of these films.

Energy transfer behaviour was observed repeatedly, however the exact same value of energy transfer efficiency proves difficult to ascertain as shown by the variation in values recorded and more work is needed in making the structure of the films consistent. Adding simpler fluorescence microscopy techniques for faster sample characterization may be advantageous.

4.3.9 Energy transfer maps using FLIM FRET fitting.

The software Symphotime 64 was used to calculate energy transfer within a FLIM image using the expected lifetime of the donors and acceptors and the actual lifetimes recorded in the sample. This allows mapping of the energy transfer on the image and recording for the number of energy transfer events by efficiency as shown in Figure 4.24.

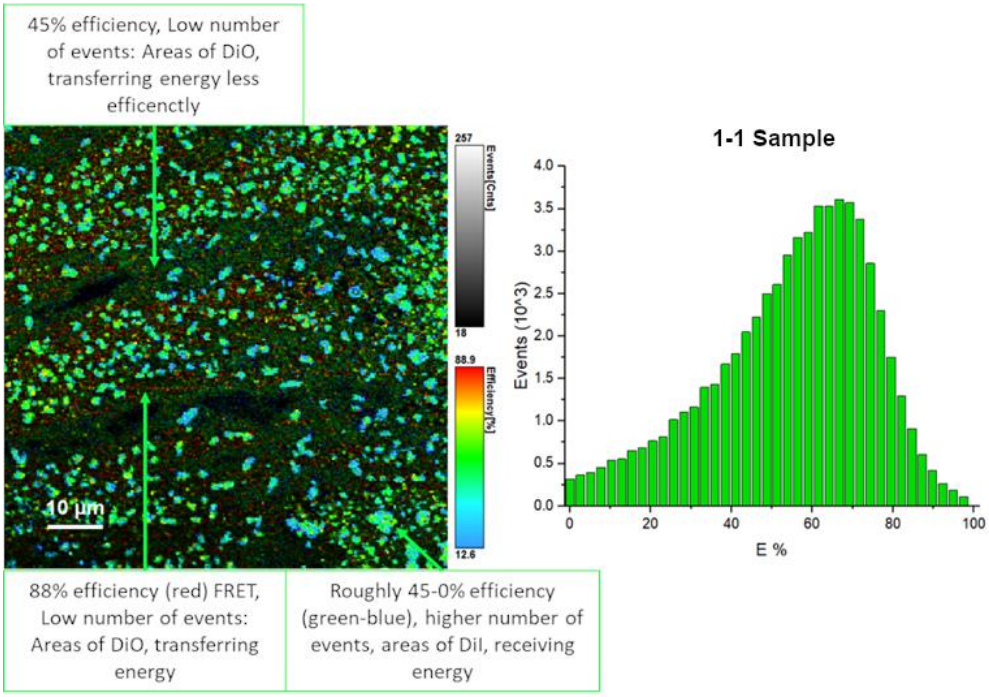

Figure 4.24: A Förster resonance energy transfer fitting of a FLIM image of a 1-1 sample showing the numbers of lifetime events energy transfer events as a function of their efficiency (E%) and mapping the events to an image of the sample.

Figure 4.24 shows an image of a 1-1 sample. The efficiency is shown by different colours, higher efficiency energy transfer shown in red is dispersed throughout the sample. These are interpreted to be where energy transfer is occurring from DiO. When plotted on a histogram as the number of events versus the transfer efficiency the data for the 1-1 sample agrees with the calculated energy transfer. The majority of the energy transfer is 75% efficiency. It then shows a significant number of events above 75%, however a significant drop off and a slow build-up of events to 75%. This shows a skew towards high energy transfer consistent with the measure energy transfer of the 1-1 sample.

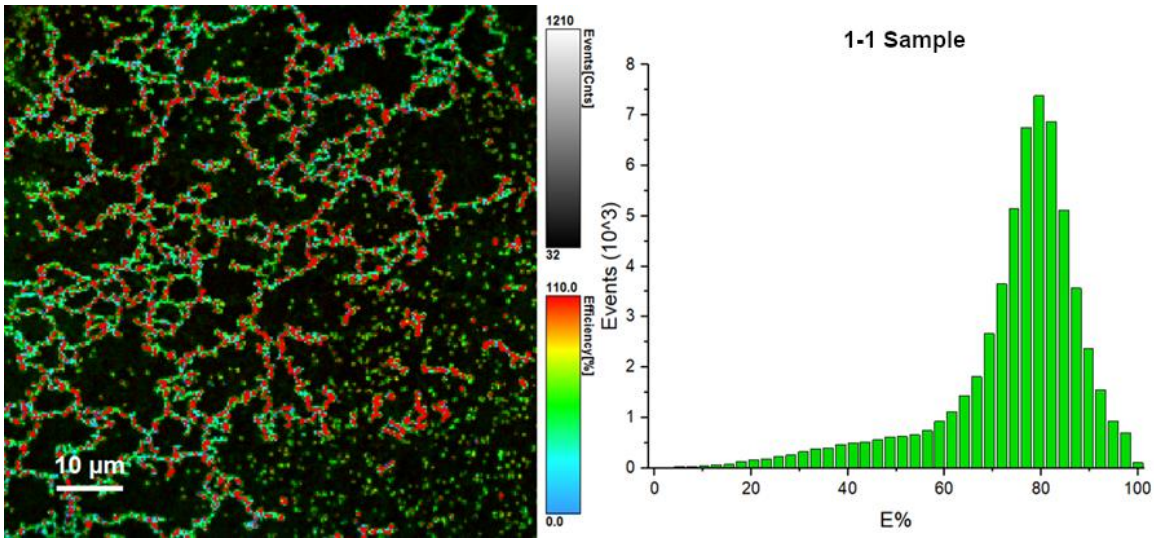

Figure 4.25: A Förster resonance energy transfer fitting and number of energy transfer events as a function of their efficiency (E%) of a different 1-1 sample.

Figure 4.25 shows a different 1-1 sample recorded sometime after it's deposition. The percentage transfer efficiency is skewed further towards higher energy transfer efficiencies. However, the structure appears different, showing a structure akin to a network of veins. There are still spots of higher and lower energy transfer distributed throughout the image.

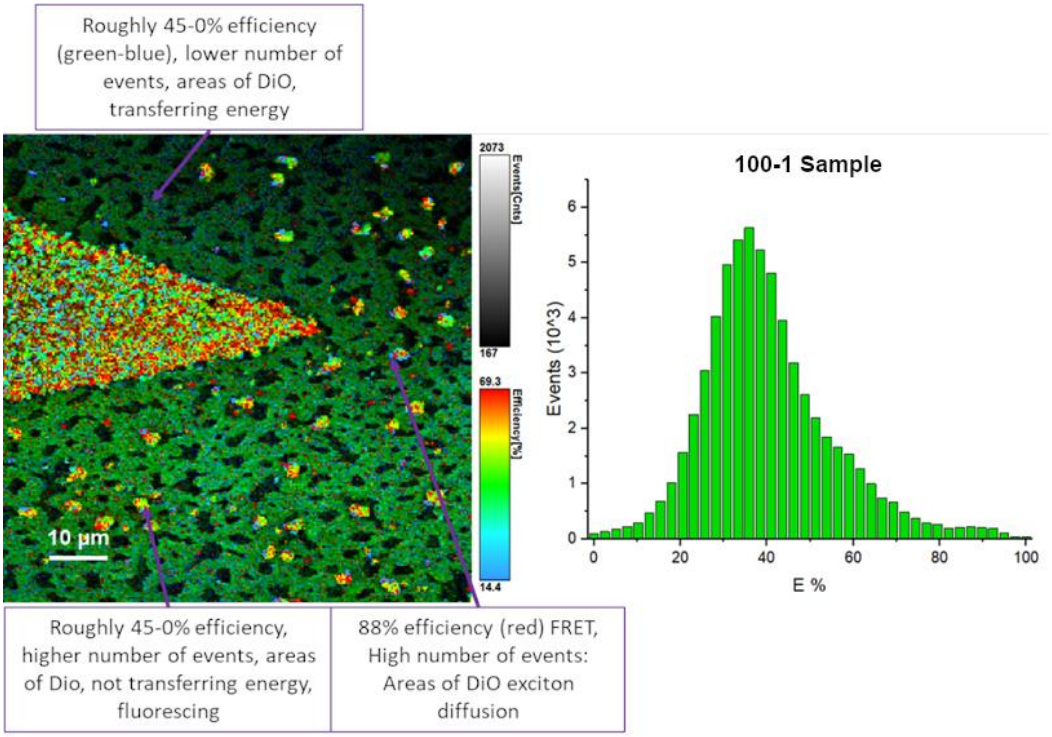

Figure 4.26: A FLIM-FRET image of a 100-1 sample with the percentage energy transfer versus the number of events plotted on a histogram.

Figure 4.26 shows a FRET fitting of a FLIM image of a 100-1 sample. This is again in agreement with much lower efficiency energy transfer shown by the FT300 measurements. This sample shows most events happening at around 30% efficiency with some of lower efficiency happening on either side. The film shows a different morphology to the 1-1 but still mostly shows isolated spots of high efficiency energy transfer. The large spike shape shown is taken to be a large excimer of DiO with a different lifetime which reads as faster.

Older images recorded sometime after their fabrication show a different appearance.

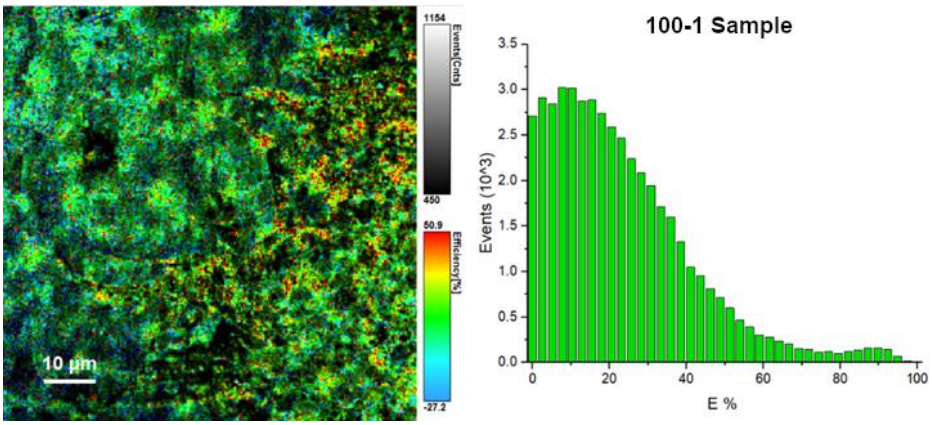

Figure 4.27: A FRET fitting of a FLIM image and number of energy transfer events as a function of their efficiency (E%) of a 100-1 sample recorded several months after deposition.

Figure 4.27 shows a representative image of what happens in the 100-1 samples over time. The films have become amorphous and there are no longer well-defined globular domains. Energy transfer is still visible however it is far more dispersed, suggesting that the distance between some of the donors and acceptors has increased due to the films relaxing and shifting over time. This is represented by a shift in the efficiency of energy transfer to a lower 0-20% range than the 40% range shown in newer samples.

4.4 Conclusions

Langmuir monolayers of DiO and DiI were studied using in situ spectroscopy, which led to the fabrication of Langmuir Blodgett films on quartz glass slides. These films produced Langmuir isotherms with shapes and molecular areas similar to those which have been recorded in prior research.[78,139] The isotherms generated by the dyes showed less distinct gas to liquid phase transitions and a small hump in the liquid phase suggesting some changes during compression. The occurrence of the changes was supported by the in-situ spectroscopy of DiO which showed aggregation in the DiO but not in the DiI. Changes to the ratio of donor to acceptor resulted in changes to the molecular area and changes in the way the DiO in the film aggregates which was confirmed by the spectroscopy of the samples.

The films showed regular surface structures across the samples in the single dye films as shown in the FLIM images. These are also shown in the AFM images, both of which

further confirm the presence of aggregation in the samples which occurred during the formation of the film on the Langmuir trough. They show the films to be repeating patterns of shapes and that there are some effects on the steady state and the fluorescence lifetimes of the DiO but less so of the DiI.

The mixed films were studied with time resolved spectroscopic methods and steady state fluorescence spectroscopy. Introduction of acceptor into films with multi donor dyes caused reduction in the lifetime and fluorescence intensity of DiO which is taken as evidence of energy transfer. The occurrence of this at high donor-acceptor ratios is evidence of exciton diffusion, the ability for the excitonic diffusion to take place is attributed to the formation of higher aggregates which allows greater coverage of the DiI absorption by the DiO fluorescence. Additionally, the steady state spectra showed an absence of donor fluorescence. This is strong evidence of energy transfer, showing between 65 to 95% reduction in fluorescence.

Energy transfer was also calculated using time resolved methods. The highest efficiency recorded was 94% for 1-1 and 95% for 10-1, this was found when the decrease in donor fluorescence was measured. Increasing the ratio of donor to acceptor would increase the distance from most of the individual donors to acceptors. In these samples energy transfer still occurred with up to 50% efficiency which suggest the significance of donor exciton diffusion. It must be kept in mind that these values were shown to be variable however the overall trend of high energy transfer efficiency at low ratios and low efficiency energy transfer at high ratios still occurs.

The trend of the highest percentage energy transfer occurring in the 1-1 ratio, which then decreased as the ratio of donor to acceptor was increased until the lowest percentage energy transfer occurring at the 100-1 ratio was repeated across the different methods of measurement suggesting that there being higher distances between a donor and an acceptor negatively effects the energy transfer, however when controlled for aggregation the aggregates who a higher level of energy transfer suggesting the aggregation of DiO positively impacts energy transfer.

In comparison to the intra layer research of Sakomura they do not comment of the transfer efficiency values but find a ratio of 250-1 exhibits donor acceptor behaviour. This shows that further work of pushing the limits of light harvesting behaviour should be carried out on DiO and DiI with higher ratios of donor to acceptor. Additionally, the fact that they do not mention specific energy transfer efficiency is problematic.[94,95]

5. Energy transfer from triplet emitting monolayers to silicon wafers

5.1 Aims and objectives

The second half of this project involved the fabrication and characterisation of Langmuir Blodgett (LB) films prepared with organometallic complexes in order to study their Förster Resonance Energy Transfer (FRET) to silicon wafers. The aim of this study was to investigate the quenching of phosphorescence from an organometallic complex by bulk silicon and study the distance dependence.

To achieve this the objectives were to fabricate the LB films based on a Rhenium complex designated as ReC18 and a Ruthenium complex designated as RuC18. Monolayers of both ReC18 and RuC18 were deposited on quartz glass slides and silicon wafers. The samples were characterised spectroscopically with steady state and time resolved spectroscopy, fluorescence lifetime imaging microscopy (FLIM) in order to observe triplet emission quenching to bulk silicon.

5.2 Experimental Overview

The Rhenium complex (ReC18) and Ruthenium complex (RuC18) shown in Figure 5.1 were synthesised by Dr Mike Coogan, ReC16 was originally synthesised as a membrane stain and RuC18 is a well-known complex.[61,71] Addition of the bipyridine ligand to rhenium and ruthenium allows light absorbance to facilitate triplet phosphorescence.

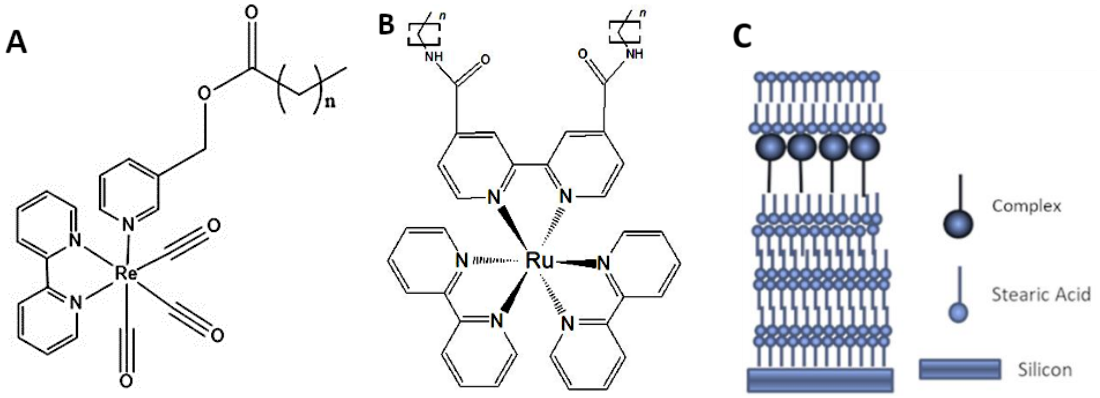

Figure 5.1: Chemical Structures of (A) the Rhenium complex (ReC18) and (B) the Ruthenium complex (RuC18) used in this study. (C) The sample structure shows a variable number of monolayers of stearic acid used as a spacer between the layer of ReC18 and RuC18 complexes and the silicon.

Both ReC18 and RuC18 were then deposited as a monolayer and multilayers on quartz glass slides using the Langmuir Blodgett technique. These complexes were picked for their triplet emission and the fact of their being transition metal ion centred complexes. These samples were then studied using steady state and time resolved spectroscopy in order to find changes between the solution and LB film configuration.

Monolayers were then deposited on silicon wafers. Stearic acid multilayers were applied to the top of the samples. The distance from the silicon wafer was altered using spacer layers made from stearic acid as shown in Figure 5.1. The emission lifetimes of ReC18 and RuC18 monolayers were measured as a function of the distance from the surface of silicon wafers. Fluorescence lifetime microscopy and atomic force microscopy were used to study the appearance of the films. The structures of the samples were determined through the monitoring of successful deposition of the films in the correct order and confirmed using ellipsometry to measure the thickness of the films.

5.3 Results and discussion

5.3.1 Langmuir films of the ReC18 complex

Langmuir monolayers of ReC18 were compressed and annealed up to ten times in order to improve the organisation stability in the monolayer, as showing in Figure 5.2.The films were compressed slowly up to a surface pressure of 30mN/m to prevent damage or collapse of the monolayer. It can be seen that repeated isotherm compressions introduce a shift of about 5Å^2 in the estimated molecular area towards a lower molecular area and an increase in the rate of rise in the surface pressure in the liquid phase.

The observed decrease in the molecular area is caused by solvent evaporation from the monolayer and better organization of the Langmuir film into a tighter packed structure creating a slightly steeper rate of pressure increase each compression. The ReC18 isotherm shows a phase change around 7mN/m.

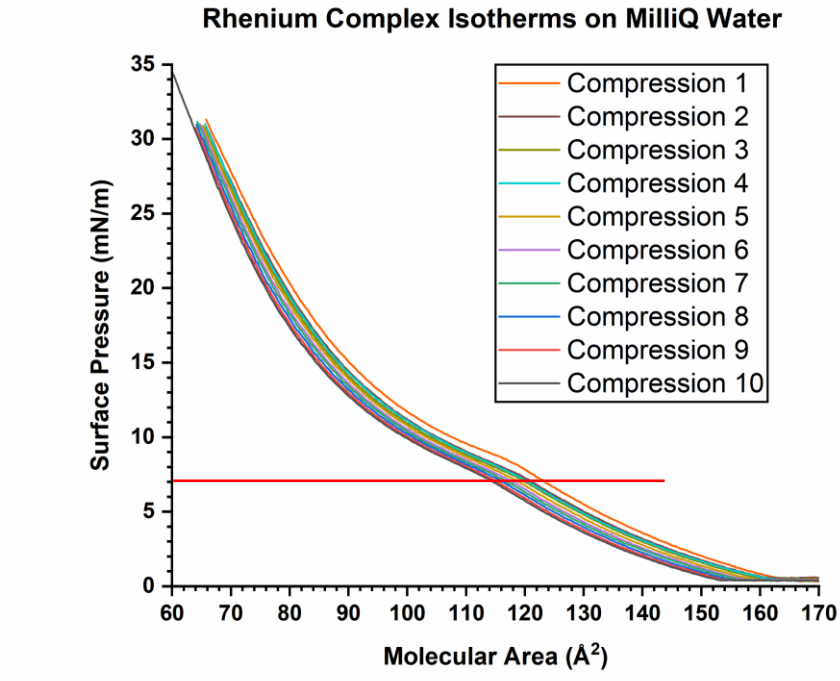

Figure 5.2: ReC18 isotherms recorded over the course of ten compressions of the same film on ~15^{o}C ultrapure water at 50mm/min barrier speed, the film was deposited from the 1 x 10^{-3} M stock solution. The 7mN/m transition is marked with a red line.

The isotherms from Figure 5.2 show the three principal components of solid, liquid and gas phases and the hump representing a secondary liquid phase, this shape is common to isotherms of similar complexes. The gas phase of the complex proceeds to a molecular area of 160Å^2 to 154Å^2. An increase in the surface pressure is then shown to a liquid phase which is present up to approximately 122Å^2 to 116Å^2. A hump is then shown which corresponds to a reduction in surface pressure, this is believed to indicate a shift in the arrangement of the complexes on the surface of the trough. From there until the end of the isotherm the rate of increase in pressure climbs up rapidly between 90 and 80, this is the monolayer entering the solid phase.

The tenth isotherm of ReC18 is shown in Figure 5.3. Extrapolation to zero surface pressure showed the molecular area to be 95Å^2 per molecule. The collapse pressure of the monolayer is shown to be 40mN/m. The second liquid phase represents a change in position or change in organization of the complexes on the surface of the water in such a way that the rate of increase in surface pressure drops momentarily.

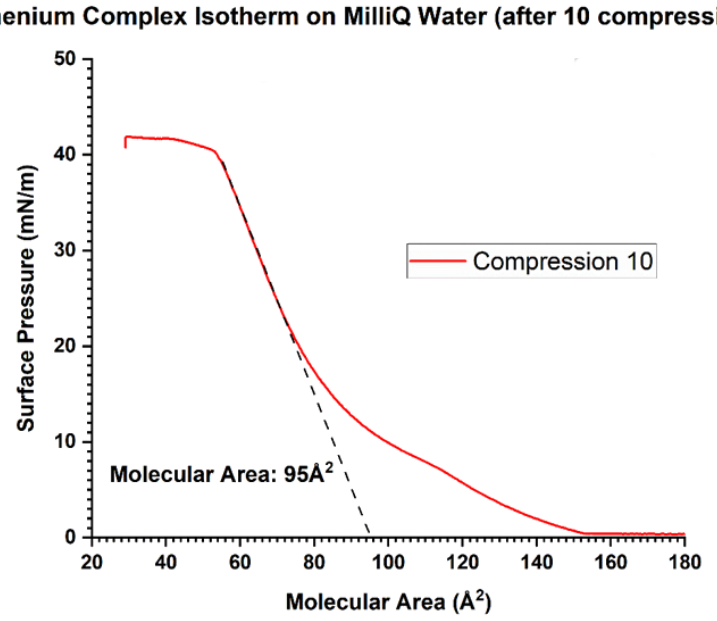

Figure 5.3: A single isotherm of ReC18 recorded after ten compressions, shown in Figure 5.2 recorded on ~15°C ultrapure water at 50mm/min.

The shape of the isotherm agrees with literature on similar complexes, Yam et al[140] shows every complex tested to have an expanded liquid phase which is very pronounced to the point that they could be interpreted as the film collapsing and layers

sliding over and under each other additionally the isotherms run from around 80Å to 20Å showing a much smaller molecular area and overall isotherm showing a very dissimilar isotherm to the one presented here. However, the isotherms show similarity in the shape of their liquid and solid phases.[140]

Li[37] and Zhang[39] both show isotherms with a similar initial liquid phase and the overall smaller molecular area with isotherms running from around 80Å to 20Å, they also show an expanded liquid phase in one of their isotherms but with no subsequent recovery into a second solid phase.[49,51] Other studies show a more classical isotherm structure, with a gas to liquid to solid phase transition, albeit less well defined than that of smaller molecules such as stearic acid, however these papers have a radically different ruthenium complex structure. But a similar smaller molecular area.[53,141]

The molecular area of the complex was shown to be 95Å per molecule which is larger than the molecular areas recorded in previous work, suggesting a key difference which gives ReC18 a greater molecular area. Literature shows a high variation in the molecular area, from 20Å^2 to 62Å^2, modifications to the ligands and changes of the ligands created huge variation in the molecular area showing that direct comparison between different rhenium complexes is difficult. In all the previous studies smaller molecular areas of 20-30 were collected from complexes which were rhenium bipyridine tricarbonyl with a chlorine ion creating a neutral change. Addition of ligands created higher molecular areas.[49,140]

Modelling of ReC18 was carried out using the software package Spartan shown in Figure 5.4. The model was created using a combination of crystallographic data of a rhenium bipyridine tricarbonyl complex obtained from previous research[142] with the tail group optimised and then added in Avogadro.

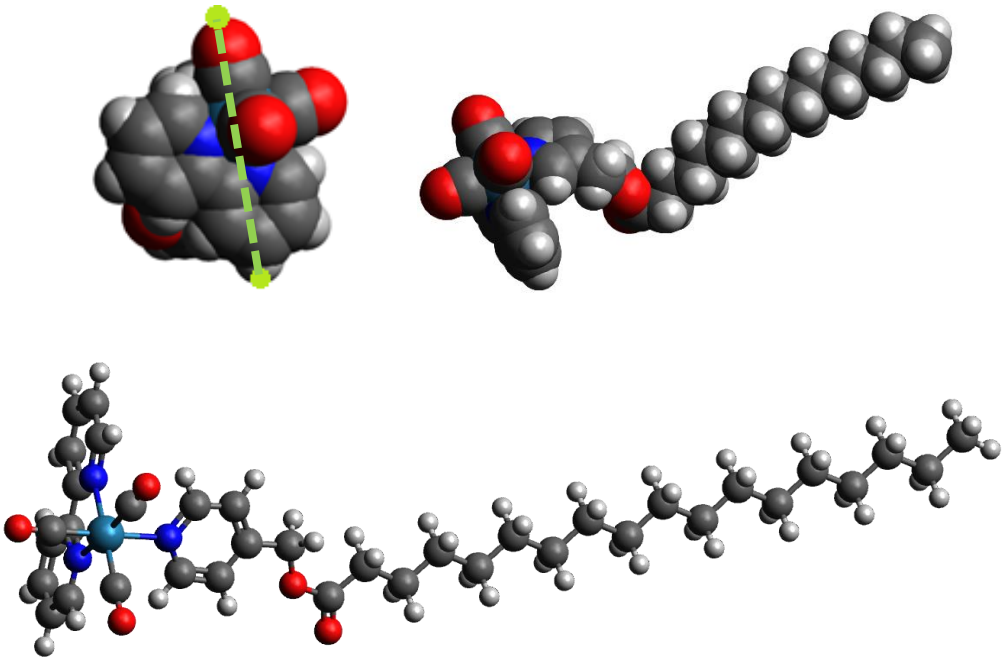

Figure 5.4: Shows a model of the Rhenium complex used in this study. This model was created by using the head group of crystallographic data from Moore et al[142], the tail was added and optimised using spartan.[142] Measurement points are highlighted in green. The tail is flexible and is likely not straight all the time in reality. This figure is showing the maximum size the complex could occupy.

For estimation of size measurements were taken of the model from the outer edge of the bipyridine to the edge outer of the carbonyl group, highlighted in green in Figure 5.4. This is taken as the diameter of a circle which represents a rough cross section of the head group. The formula for calculating the area of a circle (πr^2), was used to calculate the area of a circle representing a cross section of the head group. Adding the van der walls shells gives a radius of 11.7Å gives a 2-dimensional area of the head group of 108Å^2. This model agrees with the molecular area gained using the isotherms.

5.3.2 Langmuir films of RuC18 complex

Isotherms taken at 15^{0}C give a molecular area of 47Å^2 when extrapolated down to a pressure of zero, this is shown in Figure 5.5.

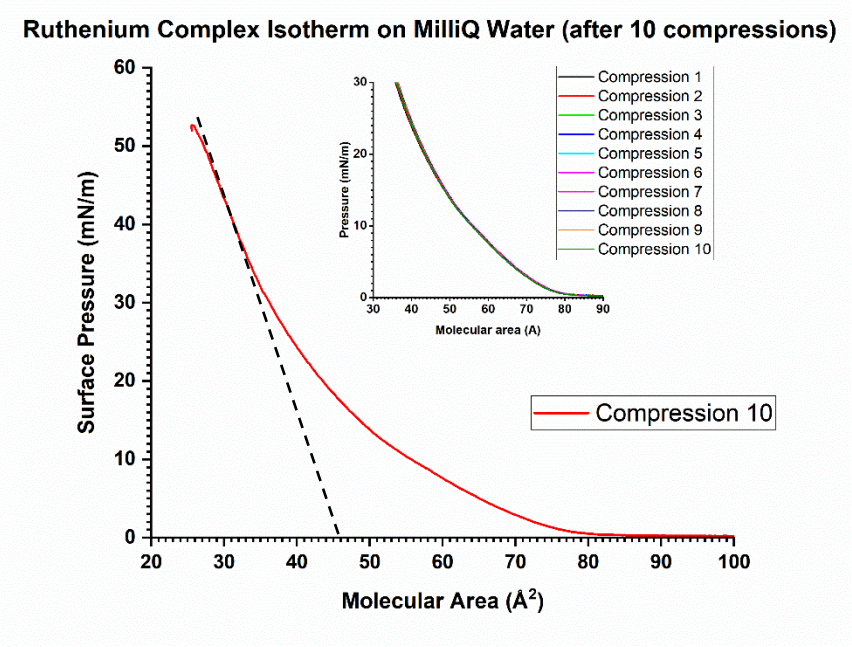

Figure 5.5: Isotherm showing the final isotherm of ruthenium after ten compressions, shown on the insert graph, on ~15^{o}C ultrapure water at a compression speed of 50mm/min deposited from a stock solution of 1 x 10^{-3} M.

The shape of the isotherm did not change throughout the course of the experiments. This suggests the film was stable and resistant to changes in organization from the initial formation. A collapse pressure of 50mN/m is shown Figure 5.5. The recorded isotherms depicted in the insert of Figure 5.5 exhibit little change over the course of the compression-annealing, with only a small shift of around 2-3Å observed in the change of the molecular area.

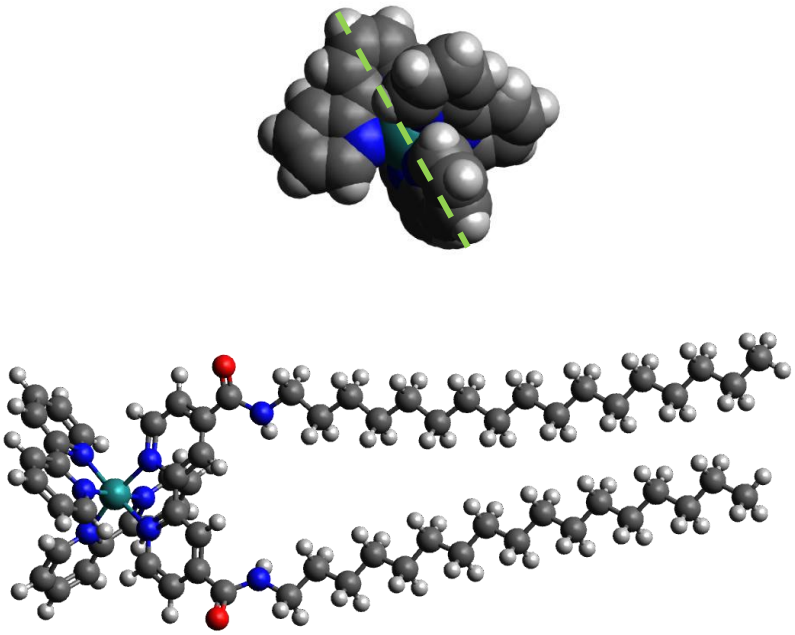

Figure 5.6: A model of a ruthenium tris bipyridine complex created using crystallographic data from Tamura et al[143] to represent the head group of the Ruthenium complex.[143] The cross section taken is shown in green.

Modelling of a tris bipyridine head group was used to calculate the area of a circle as in section 5.3.1. Using the area of a circle gives a head group area of 122.72Å^2. This model coupled with data recorded with the same complex by Yamada et al[71] is in some agreement, however again as conditions are different direct comparison is difficult.[71] They state a molecular area of 95Å^2 is achieved and that it is in good agreement with a CPK model used by them which gave a cross section of between 80-100Å^2. However other literature shows wide variance even with similar complexes, for instance, in a comparison of two studies on a similar ruthenium complex J. Kawamata et al[53] and K. Okamoto et al [63] both show differences in molecular area and diversions in the shape of the isotherm between two laboratories.[66,144] Studies of similar sized complexes such as K. Wohnrath et al[56] and much larger complexes such as B. Sandrino[57] et al have yielded of around 20mN/m and 40mN/m respectively.[69,70]

This suggests either errors in the fabrication of the films or a difference in the way that these different ruthenium complexes interact with each other. This suggests that further work looking at the specific interactions between the complexes using IR spectroscopy

would be valuable to see what causes the variation in collapse pressure and molecular area.

The collapse pressures recorded are in good agreement however, therefore the likely issues are either the differences in temperature or mistakes during spreading and solution preparation which led to a smaller molecular area. The shape of the isotherm is also in good agreement, suggesting a similar origination to a traditional film with less definition between the phases.

Finally, it is worth noting that the molecular area gained at room temperature initially was around 70Å^2 and shrank to 45Å^2 upon the introduction of cooling, whilst this is still smaller and in poor agreement with the modelling performed in this study. this suggests a role being played in the vibration of the complexes at room temperature pushing one another apart, as once the temperature is lowered the area per molecule reduces. This suggests a contribution of temperature and further work should be performed in this regard to establish if the deposition temperature has a meaningful on the organization of the complexes in the films.

5.3.3 ReC18 in solution, Steady state spectra

The ReC18 complex shows an absorbance consistent with the absorbance characteristics of rhenium complexes studied in the literature (Figure 5.7). [57,58,60,145]

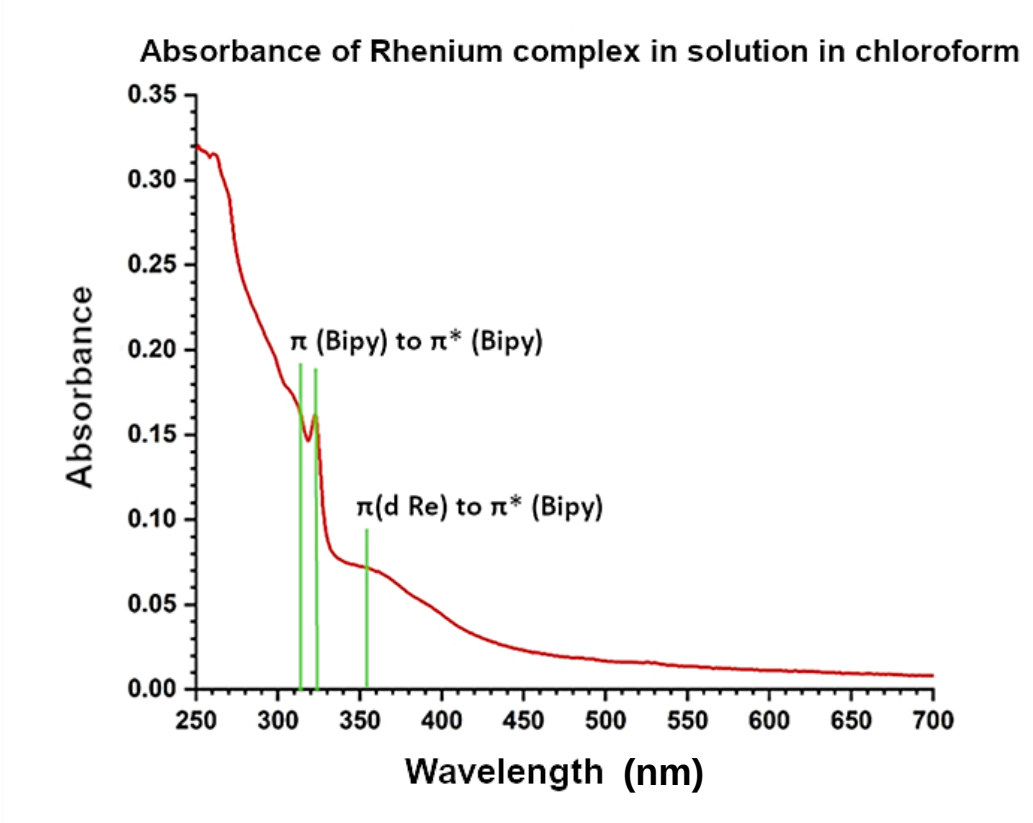

Figure 5.7: Absorbance of the ReC18 complex in chloroform recorded at a concentration of 3.2 x 10^{-5} M. Peaks are shown at 270nm, 322nm and 355nm..

According to previous research on similar complexes containing a rhenium Bipyridine tricarbonyl head group and a variable tail section the high energy bands around 250 to 322nm can be assigned to the transition within the bipyridine ligands, *π (bipyridine)* to *π* (Bipyridine)* and *n* to *π**. Lower energy absorbance beyond 322nm and 355nm can be assigned to the Metal to ligand charge transfer occurring between the metal and the ligands, *π(d Re)* to *π* (Bipyridine)* transitions.[57,58,60,145]

ReC18 shows a broad phosphorescence emission from 450 to just over 700nm as shown in Figure 5.8. The phosphorescence maximum occurs at 550nm..[57,60,61,146]

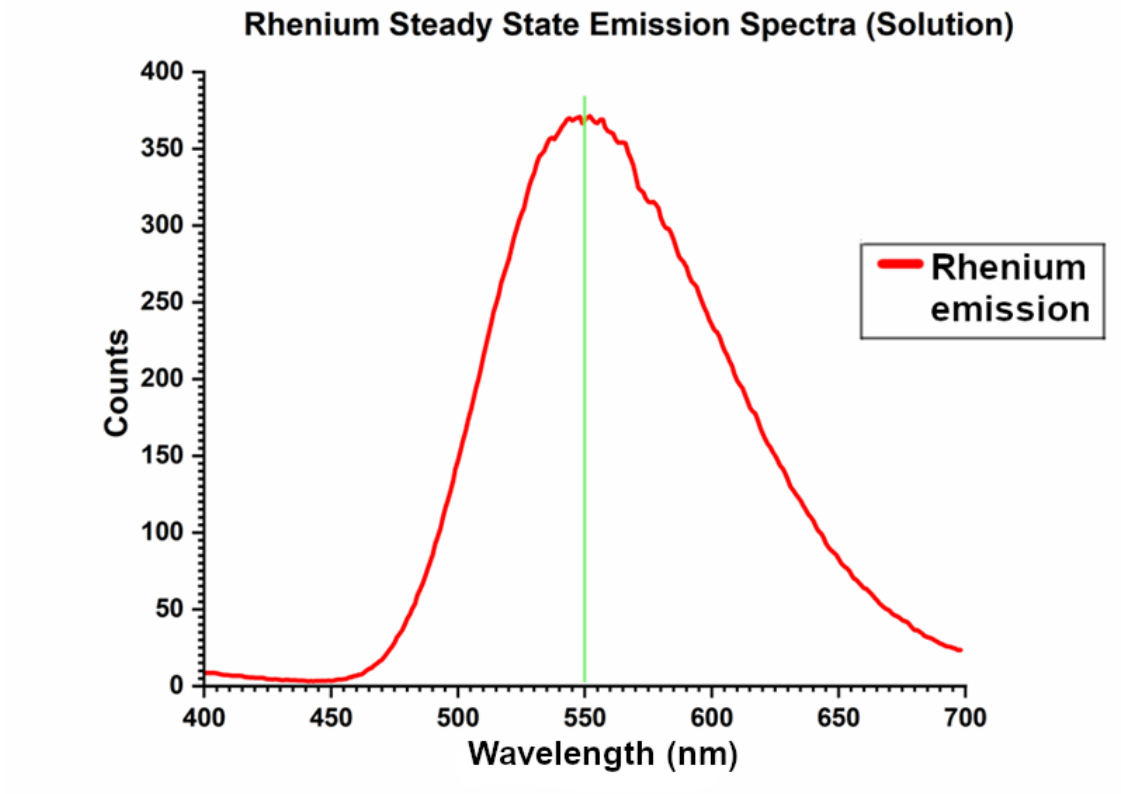

Figure 5.8: Steady state phosphorescence emission of the ReC18 complex in chloroform recorded at a concentration of 3.2 x 10^{-5} M excited at 405nm. The spectrum shows a single broad emission peak at 550nm.

5.3.4 RuC18 in solution, Steady state spectra

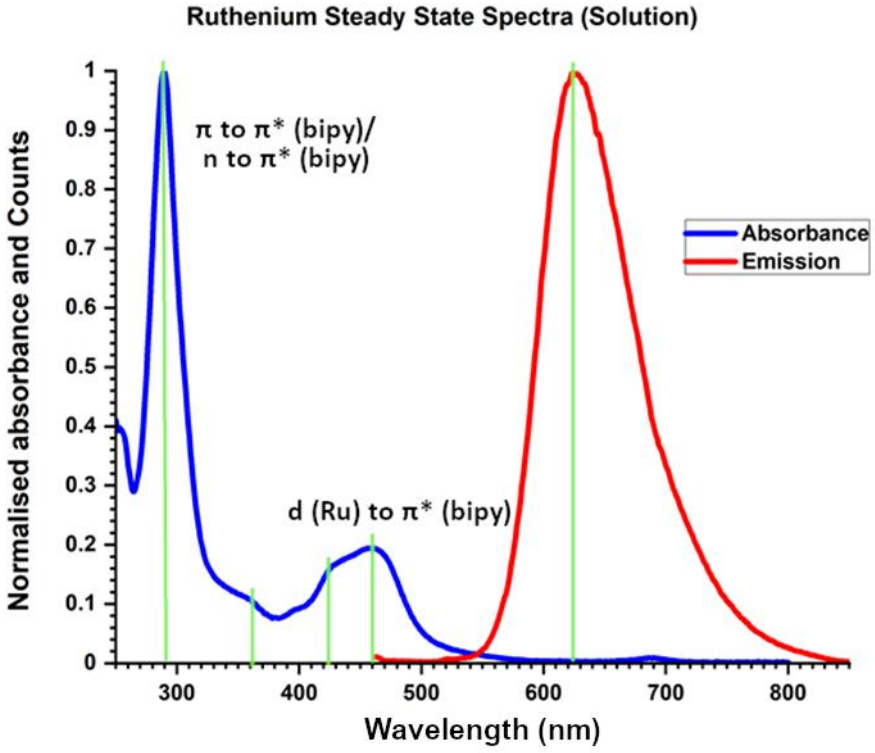

Figure 5.9: Shows Ru18 in chloroform recorded at a concentration of 3.2 x 10^{-5} M. Phosphorescent emission at 625nm and absorption from 300-500nm. Broad absorption peaks are shown at 425nm and 460nm and one very sharp peak is shown at 290nm.

The ruthenium complex shows a strong absorbance peak at 290nm, a very small shoulder at 360nm and a broad peak at 460nm with a smaller shoulder at 425nm. The spectra are shown in Figure 5.9. In previous research the bands around 450nm have been ascribed to the MLCT between the ruthenium d orbitals and the ligands π^* orbitals. The higher energy absorption from 200-350nm can be ascribed to ligand absorption the transitions being π to π^* (bipyridine)/ *n* to π^* (bipyridine) transitions.[147–150]

The phosphorescence spectrum remains the same with different excitation wavelengths. The phosphorescence shows a maximum at 625nm (Figure 5.9) in good agreement with literature. [147,150,151] The addition of chains does not influence the absorption and phosphorescence of ruthenium tri s-bipyridine.

5.3.5 Phosphorescence decay study of the ReC18 Complex in solution

The phosphorescence decays of ReC18 in chloroform were recorded using two excitation wavelengths, 375nm and 405nm, as shown in Figure 5.10, the decay curves show no meaningful difference between the two excitation wavelengths. The excited state phosphorescence lifetime of ReC18 estimated from a single exponential fit is approximately 0.3 µs. In comparison to similar complexes measured in similarly polar solvents like water this is a slightly longer than expected lifetime but when averaged is similar showing either an increase of 0.2µs or a decrease of around 1µs.[55,61] This shows the effect on the emission properties of the change in solvent environment.

The decay curve shows a good fit with the χ^2 value being very close to 1. The ReC18 was measured using burst mode to reach the required number of counts as the low quantum yield results in too few counts for the spectrometer to be used on single pulse mode.

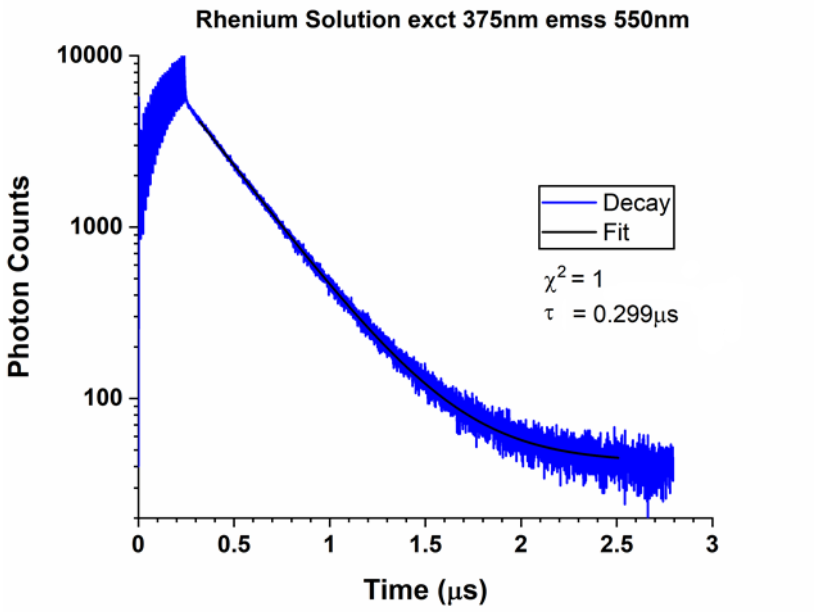

Figure 5.10: Lifetime of ReC18 in solution of chloroform recorded at an excitation wavelength of 375nm and emission wavelength of 550nm using a 488nm bandpass filter fitted with a single exponential tailfit. ± 3% error gives ±0.009 µs.

5.3.6 Phosphorescence decay study of the RuC18 complex in solution

The time resolved decay curve of the RuC18 complex in chloroform solution is shown in Figure 5.11. Excitation was carried out with a 485nm laser and fitted lifetime was approximately 725ns fitted with a single exponential. This is similar but slightly shorter to previously recorded lifetimes at room temperature.[152] This indicates only one lifetime present and thus one species or radiative pathway present, this agrees with the spectral data showing one decay characteristic of the ruthenium. The χ^2 of each decay is close to one showing good fits.

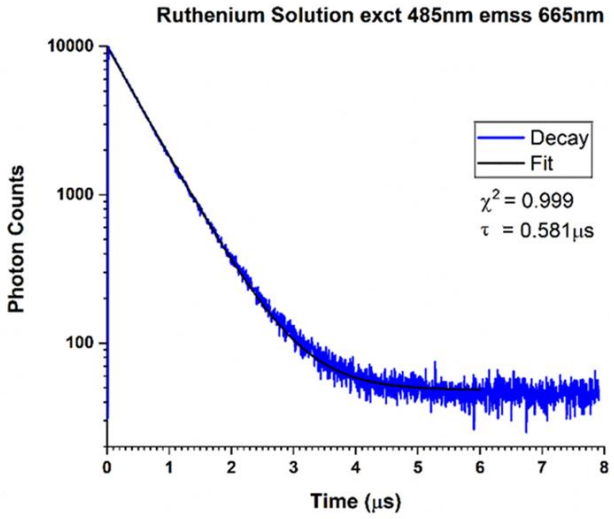

Figure 5.11: Shows the lifetime of RuC18 recorded in chloroform, the same excitation wavelength used, and the lifetimes are shown. Samples are excited at 485nm and recorded at 665nm using a 488nm bandpass filter, lifetime was fitted with a single exponential tailfit. ± 3% error gives ±0.017 μs.

5.3.7 ReC18 complex freeze pump and thaw

Three freeze-pump-thaw cycles were performed on ReC18 in chloroform to remove dissolved oxygen from the solution and observe the unquenched and increased phosphorescence lifetime. The unquenched phosphorescence lifetime was shown to be approximately 0.455μs when excited at 375nm and recorded at 550nm emission wavelength.

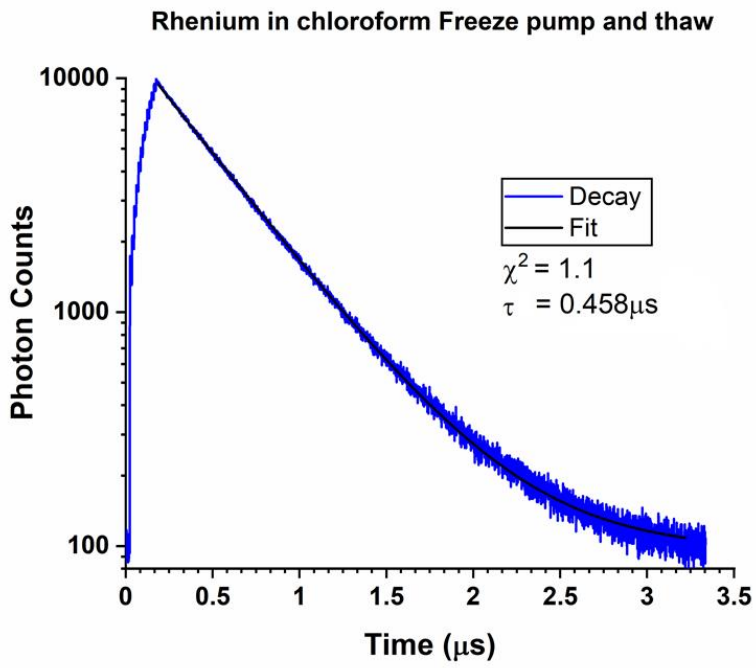

Figure 5.12: 'Freeze pump and thaw' measurements taken for the ReC18 complex in chloroform showing the phosphorescence lifetime in the absence of oxygen. The lifetime was fitted with a single exponential tailfit. The sample was excited at 375nm and detected at 550nm using a 488nm bandpass filter. ± 3% error gives ±0.014 μs.

This is an increase of approximately 155ns from the previously recorded lifetime. The decay curve was fitted with a single exponential indicating only one radiative species present in the solution.

5.3.8 RuC18 complex freeze pump and thaw

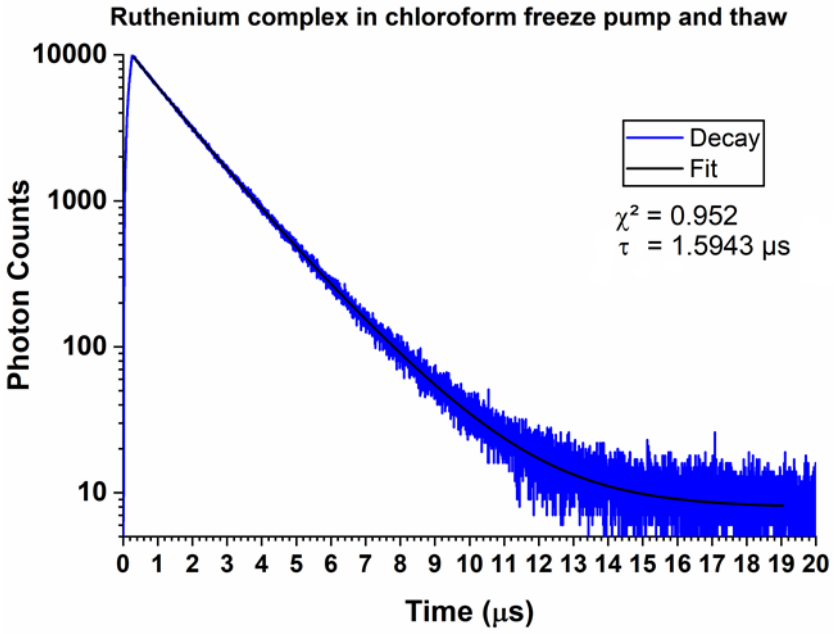

Figure 5.13: A time resolved decay showing the RuC18 in chloroform phosphorescence lifetime in the absence of oxygen. Sample was excited at 485nm and recorded at 665nm using a 488nm bandpass filter. ± 3% error gives ±0.048 µs.

Three freeze-pump-thaw cycles were performed on RuC18 in chloroform. The unquenched phosphorescence lifetime was shown to be approximately 1.594µs when excited at 485nm and detected at 665nm, an increase of over 1µs. This shows that in the absence of gasses in solution the lifetime is far longer which indicates that the RuC18 complex is quenched strongly by oxygen present in the air.

5.3.9 Spectroscopy of ReC18 Langmuir Blodgett monolayer and multilayer on glass

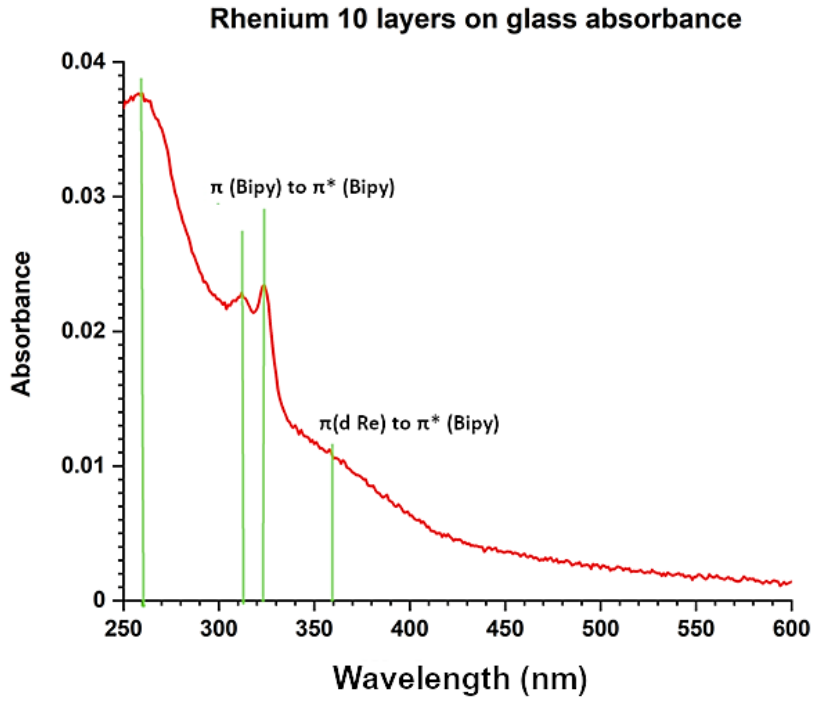

Figure 5.14: Absorbance of ten layers of rhenium complex deposited on a quartz glass slide and stearic acid base using the conditions described in the experimental, scanned from 200nm to 700nm. Peaks and the associated transitions are shown.

The absorption spectrum of the ReC18 LB film is shown in Figure 5.14. The absorption peak shown at 258nm in this spectrum appears red-shifted by approximately 8nm when compared to the solution. The absorbance spectra from 10 layers of ReC18 show similar absorption profile to the one recorded in solution. The most prominent features of the solution spectra are clear in the 10-layer absorption spectrum. The peaks at 250nm and 315-322nm from the solution spectra appear red-shifted at 258nm and 319 and 324nm. The hump at 355nm has disappeared into a broad band ending at 400nm. The spectral shifts are caused by change in environment, from a liquid to a solid phase. This is due to the sensitivity of such complexes to the change in polarity of their environment, shifting to a lower energy absorption peak indicates a lower degree of splitting of the d orbitals, causing a slightly smaller transition in rigid media than in solution.

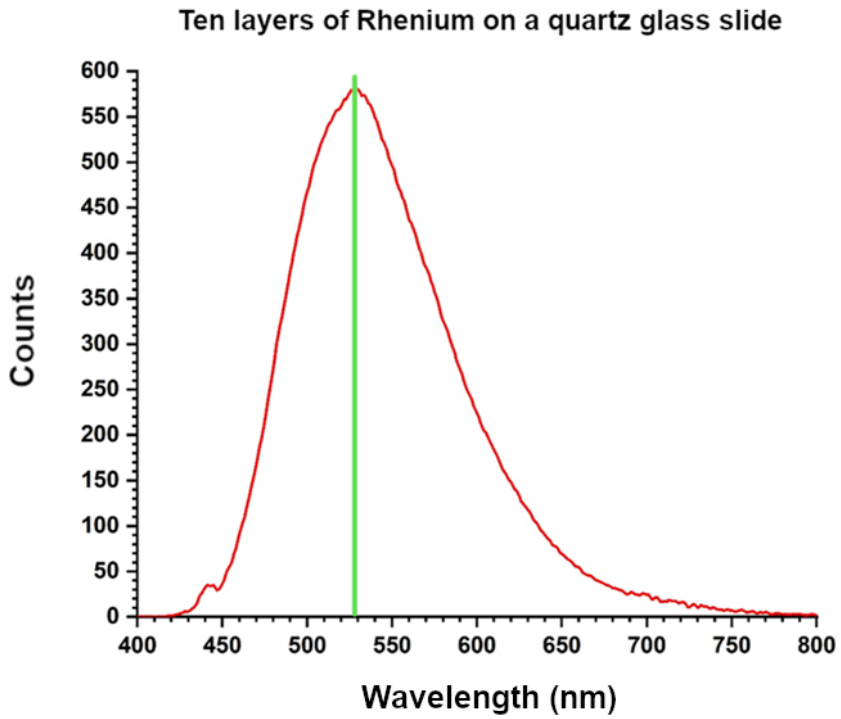

Figure 5.15: Phosphorescence spectrum obtain from 10 layers of ReC18 deposited on a quartz glass slide and stearic acid base, excited at 375nm and scanned from 400nm to 800nm, a peak at 528nm is shown.

The recorded phosphorescence from ten layers of ReC18 is shown in Figure 5.15. The phosphorescence peak appears blue shifted by approximately 20nm from 550nm to approximately 530nm. The shape and half-width of the band does not change significantly. This is explained by the change in environment and consequently a change in the intermolecular forces acting on the complex, in this case the complex has been removed from a polar environment of chloroform and added to a less polar environment where it is either in contact with stearic acid or other complexes, however a strong shift does not take place in the same way it might have in the case of the absorption spectrum, as shown in previous work on the subject the emission is not effected in the same way as the absorption spectrum.[55]

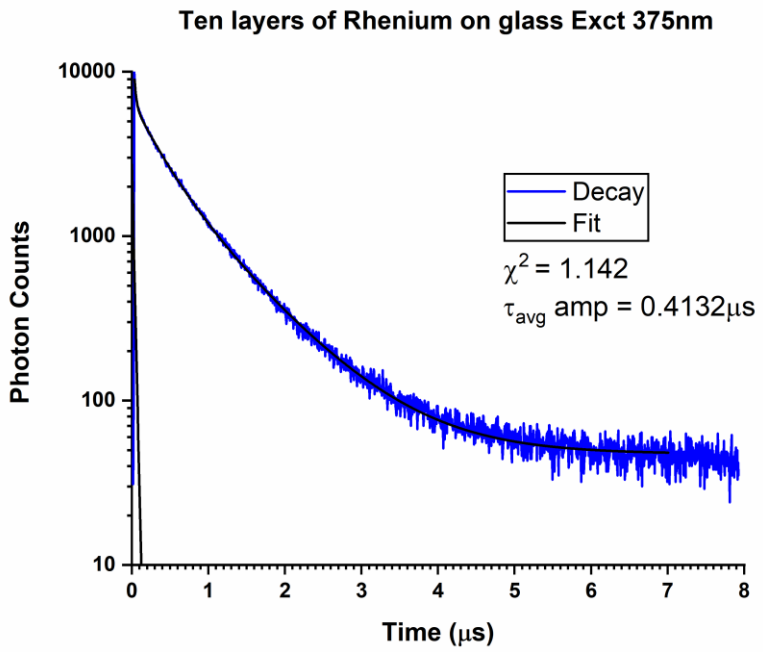

Figure 5.16: Lifetime of ten layers of Rhenium complex deposited on a quartz glass slide, excited at 375nm and detected at 550nm, fitted with a two exponential tailfit. ± 3% error gives ±0.012 μs.

The phosphorescence lifetime recorded at an emission wavelength of 550nm using 375nm or 405nm excitation shown in Figure 5.16. The lifetimes were all recorded at similar wavelengths. The lifetime shows an increase with respect to the one recorded in solution. This is consistent with the general trends seen throughout this study, removal from solution increases lifetime due to the absence of quenching avenues as molecules have fewer vibrational routes and collisional quenching routes. There is a noticeable fast component at the very beginning of the decay. This suggests a fast emission not present in solution and that the immobilization into a film created this fast-emitting species or can signify a fast energy transfer step within the ten layers.

The ReC18 complex was also measured from monolayer samples. Since these samples did not produce enough photon counts to be measured in single pulse mode, they were measured in burst mode.

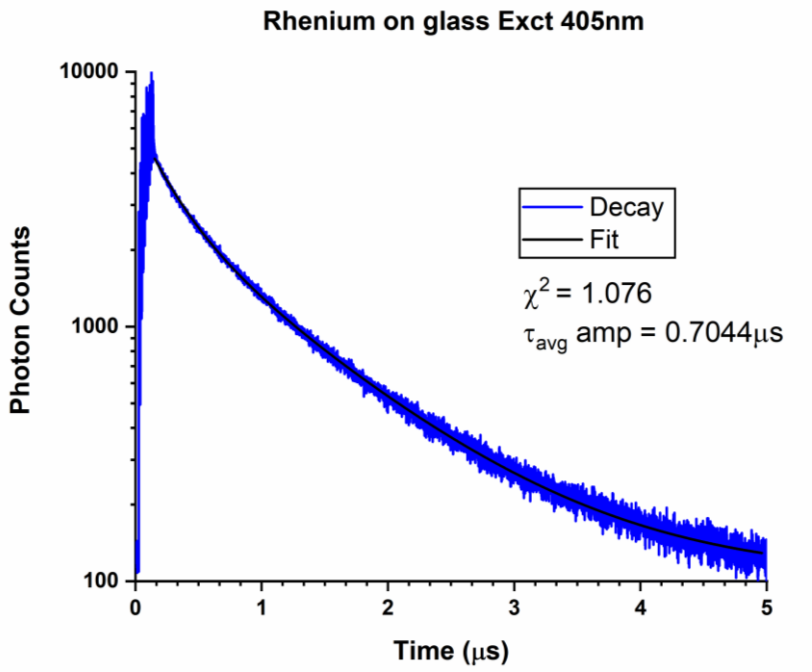

Figure 5.17: Lifetime of Rhenium monolayer deposited on a quartz glass slide and stearic acid, excited at 405nm and detected at 550nm using a 488nm bandpass filter, fitted with a two exponential tailfit. ± 3% error gives ±0.021 μs.

The fast-emitting species is no longer present in these samples. The effect of this is shown by the increased lifetime compared to the ten-layer sample. Interactions between the rhenium layers is the likely cause, specifically energy transfer from complex to complex, specifically some small amounts of reabsorption occurring. This is made possible by the close proximity of the complexes.

5.3.10 Spectroscopy of ReC18 Langmuir Blodgett monolayers on silicon wafer

ReC18 was deposited as Langmuir Blodgett monolayers on both glass and silicon wafer that had been cleaned, treated to create a hydrophobic surface and coated with stearic acid monolayers. Glass samples were studied spectroscopically to provide the unquenched spectrum and lifetime of the ReC18 complex in the deposited Langmuir Blodgett film state against which the silicon samples will be compared. ReC18 monolayers deposited on silicon wafer were then measured spectroscopically. These were compared against the glass samples in order to study the degree of quenching occurring. Once quenching was established the number of stearic acid monolayers was

varied in order to vary the distance from the ReC18 monolayer to the surface of the silicon wafer.

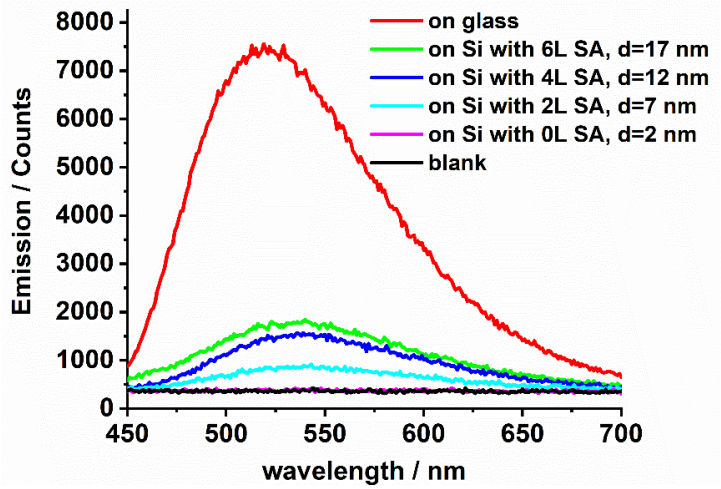

Figure 5.18: Steady state phosphorescence of deposited films of Rhenium complex at 4 different distances from silicon wafer. The emission spectrum from blank silicon and a Rhenium monolayer on a quartz glass slide shown for comparison.

The reduction in phosphorescence intensity of the ReC18 monolayer deposited on silicon wafer, when compared with the glass slides, shows that at very close distances to the silicon surface (17nm and below) strong phosphorescence quenching takes place. Within this close distance the likely cause is resonance energy transfer as the theoretical maximum limit to resonance energy transfer is 50nm. The quenching shown in the steady state spectra reaches as high as 90% when the ReC18 monolayer is only 7nm away from the surface. Closer than this and the phosphorescence appears fully quenched indicating close to 100% energy transfer and the phosphorescence intensity of the monolayer reaches the spectrometer's sensitivity of detection. To gain a more accurate measurement of the degree of energy transfer the fluorescence lifetime of the films have been measured using time resolved phosphorescence microscopy (FLIM) which allows greater sensitivity in signal detection.

5.3.11 Spectroscopy of RuC18 Langmuir Blodgett monolayers and multilayers on glass

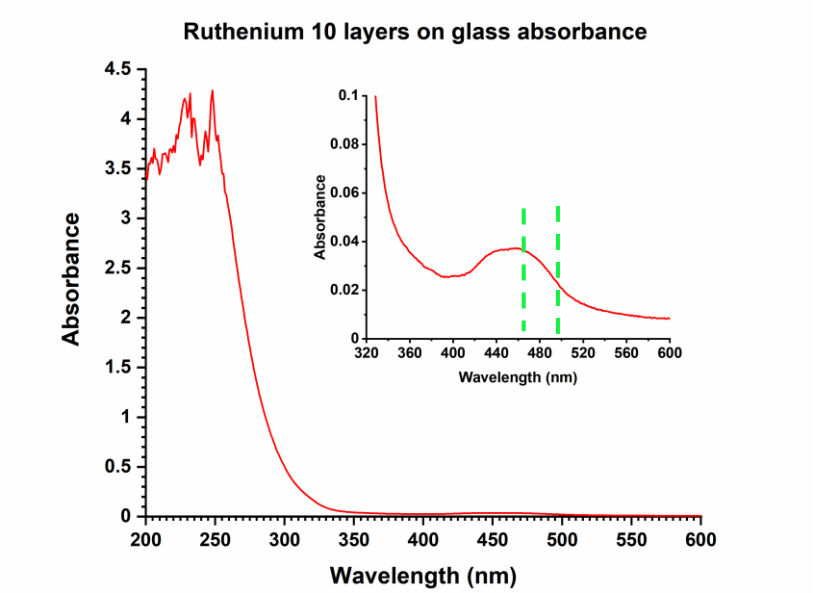

Figure 5.19: Absorption spectrum of ten layers of RuC18 deposited on quartz glass. A smaller broad absorption band can be seen at 460nm with a small shoulder at 435nm.

The absorption spectrum shown in Figure 5.19 is similar to the absorption spectrum shown in Figure 5.9. Changes in the spectrum are attributed to the change in environment from the deposition of the complex from solution to Langmuir Blodgett film. The absorption before 300nm can be attributed to the π to π^* and n to π^*. The absorption from 420 to 500nm is attributed to MLCT from the d(Ru) orbital to the π^*(bipyridine) orbital.

The spectra is in complete agreement with ruthenium tris bipyridine spectra recorded in previous research, for example Leung et al shows a very similar complex with the similar absorption spectrum.[153] Research papers involving the deposition of ruthenium tris bipyridine by attaching it to polymer chains show a consistent absorption spectrum, Taniguchi[148] and Fushimi[150] attached ruthenium tris bipyridine to copolymers with spacers, both saw the same absorption spectra and ascribed the 400-500nm region to MLCT and the 290nm peak to ligand centred π to π^* absorption.[148,150] This research did not report any peak shifts when the solution was transferred to the solid state.

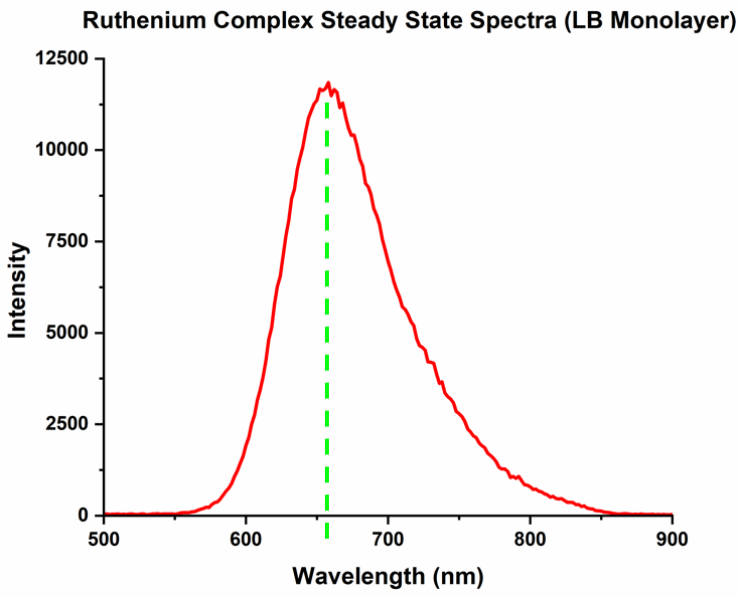

Figure 5.20: The phosphorescence emission spectrum excited at 405nm and scanned from 500nm to 900nm of the RuC18 complex deposited into a Langmuir Blodgett monolayer on quartz glass and shows a peak at 655nm.

The emission spectrum shows a blue shift of approximately 25nm with respect to the phosphorescence spectrum recorded from the RuC18 in solution shown in, the shift is attributed to the change in environment.

Comparison to previous literature suggests that emission of a ruthenium complex is responsive to modifications to the bipyridine groups, with emission peak ranging from 600 to 700nm. Examples include a ruthenium emission at 600nm which was shown in both Chen et al[66] and in Fukuda et al[70]. Using the bipyridine as an attachment point, both studies incorporated ruthenium tris bipyridine into an alternating copolymer and both show a phosphorescence peak around 600nm.[147,151] This shows a higher similarity to the solution spectra shown Figure 5.9 which had a peak at 625nm rather than the solid sample spectra shown in Figure 5.20 which had a peak at 650nm. The deposition of ruthenium as a polymer may then not have the same effect as the Langmuir films as the peak at 600nm shows a shift of 25nm from the solution spectra in Figure 5.9.

5.3.12 Fluorescence lifetime imaging of ReC18 monolayers on glass and silicon

Fluorescence lifetime imaging microscopy (FLIM) was used to study the lifetimes of the films due to the increased sensitivity of the microscope compared to the lifetime spectrometer. The samples shown in Figure 5.21 show holes in the film. The film around the holes is uniformly smooth. It is possible the holes were caused by the action of surface tension on the film (from adjacent stearic acid) and the formation of round micelles.

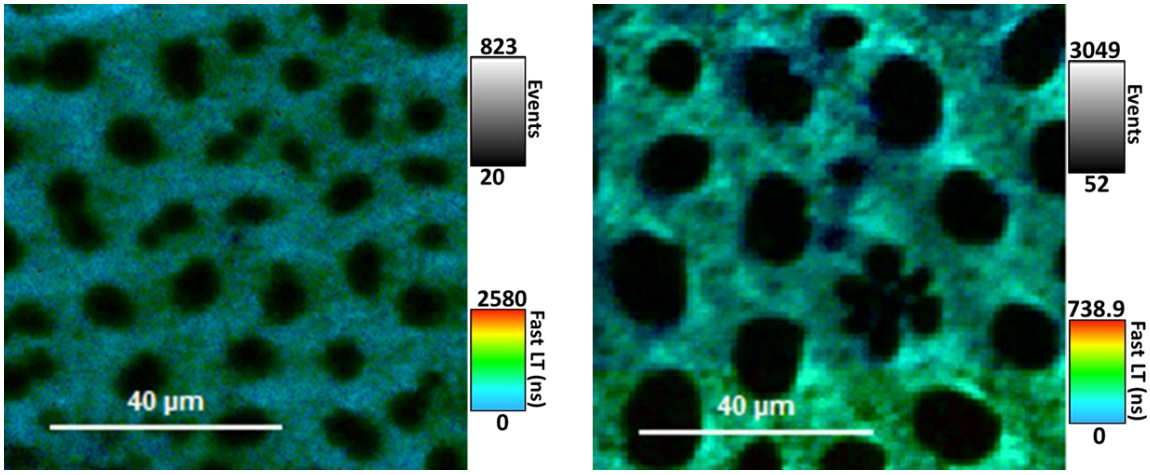

Figure 5.21: FLIM microscope images of a monolayer of Rhenium complex on a glass slide with a capping layer on the top. Excited at 485nm and detected using a 485nm long pass filter. Holes measuring approximately 10 to 20µm are visible.

AFM found large crystalline structures within the holes; these samples had been created with silicon which was cleaned using the old cleaning technique. Piranha solution and new solvent combinations were introduced, this was found to remove the crystallites and leave a clean surface however the holes were still present and were thus attributed to the action of surface tension. Figure 5.22 shows the pure monolayer deposited on glass film after cleaning. Small globular domains are present with more intense emission compared to the rest of the structure. Similarly, there are also darker domains.

However, deposition on silicon creates large globular domains and a much darker background. The sample shown in Figure 5.22 has no separating layers of stearic acid between the silicon and the rhenium monolayer (S0) and shows the reverse of what was found in the previous glass samples in Figure 5.21. Globular domains appear to have formed, and this is the only part of the film which is fluorescing. Emission is occurring from the other parts of the film however, but only very dimly. The globular domains have very fast lifetimes compared to the rest of the film.

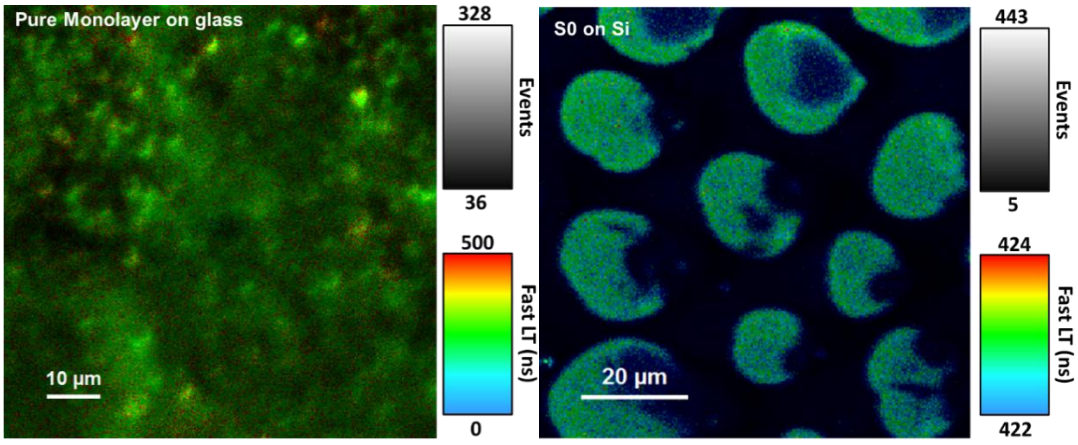

Figure 5.22: FLIM microscope image of a monolayer of Rhenium complex on a glass slide and a monolayer of Rhenium complex deposited directly onto a silicon wafer with a capping layer on the top.

Figure 5.23 shows a monolayer of Rhenium complex deposited on top of one spacer layer of stearic acid in a hydrophilic orientation (S1a) which shows some fluorescence detected within holes and a Monolayer of Rhenium complex in a hydrophobic orientation with one layer of stearic acid spacer. It also shows which (S1b) displays 2 distinct regions, the fast region is shown in blue around the circular domains which are shown in green. These are two samples which have been deposited in two different orientations. S1a was deposited in a hydrophilic fashion whereas S1b was deposited in a hydrophobic fashion. An explanation of this behaviour is that the orientation of the complexes in the globular domains caused by interaction with the stearic acid results in differences in fluorescence intensity, lifetime and mount of quenching from the surroundings.

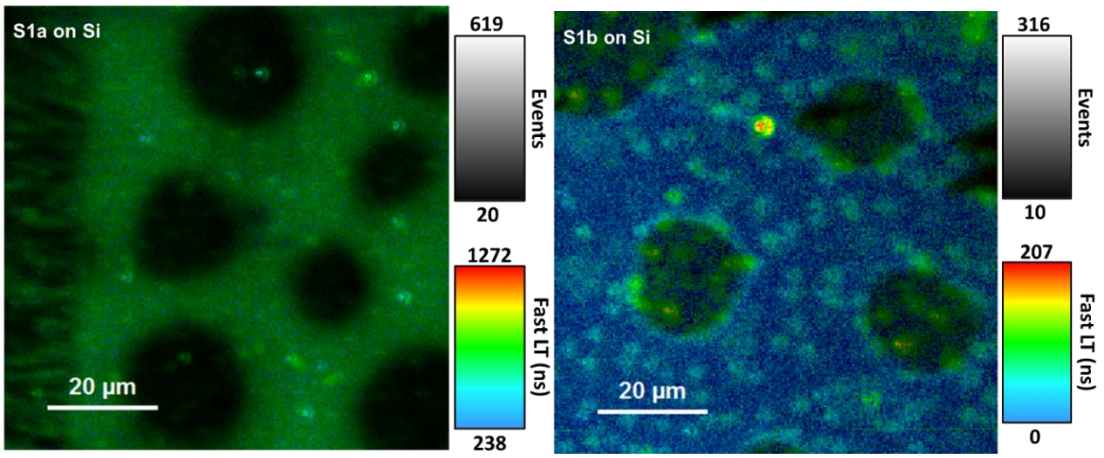

Figure 5.23: FLIM microscope images of a monolayer of Rhenium complex deposited on top of one layer of stearic acid in a hydrophilic orientation (S1a) and a Monolayer of Rhenium complex deposited directly onto silicon in a hydrophobic orientation (S1b). Both were deposited with a 2-layer stearic acid cap.

Figure 5.24 shows a similar phenomenon in the S2 (2 layers of spacer) and the S0(no spacer) configuration, despite the fact the S2 is deposited in a hydrophobic fashion indicating the addition of further lays of stearic acid have different effects to the complexes.

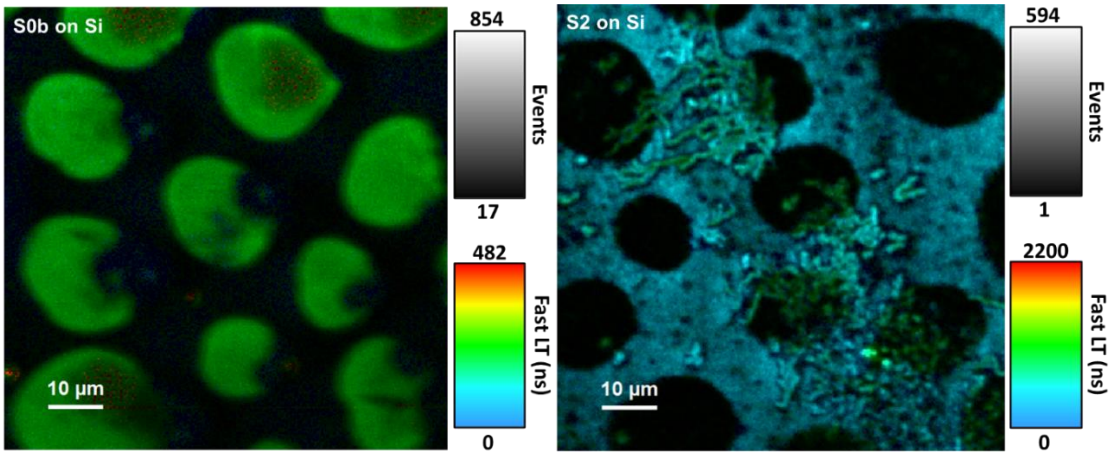

Figure 5.24: A monolayer of Rhenium complex deposited without spacer on silicon wafer in the hydrophobic configuration (S0b) and a Rhenium monolayer deposited on 2 layers stearic acid on silicon (S2) imaged with FLIM.

The samples were further investigated with AFM. The difference between the hydrophobic and hydrophilic deposition types shows a difference in the films appearance when imaged using AFM. The S1a hydrophilic deposition created a much flatter surface compared to the hydrophobically deposited S1b which showed formation of large globular domains. as shown in Figure 5.25.

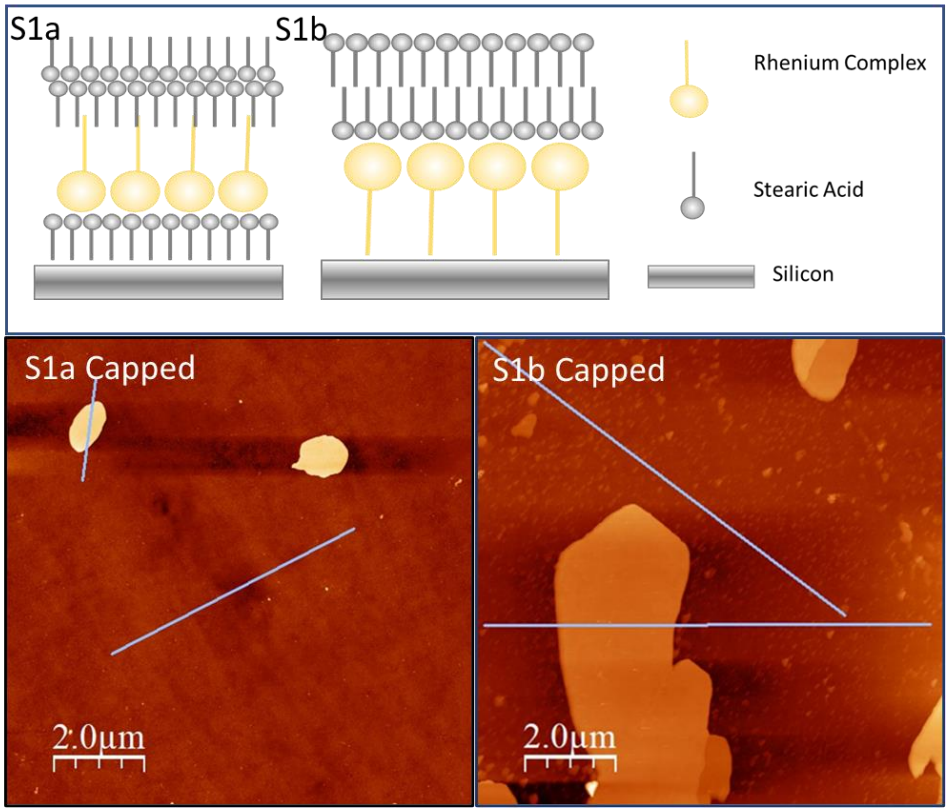

Figure 5.25: Comparison of the S1 A and S1 B sample and the sample structures.

5.3.13 ReC18 quenching and energy transfer to silicon wafer

The lifetimes recorded during FLIM imaging were used to calculate the quenching and therefore the amount of energy transfer occurring when Rhenium monolayers were deposited at varying distances from the surface of silicon wafer.

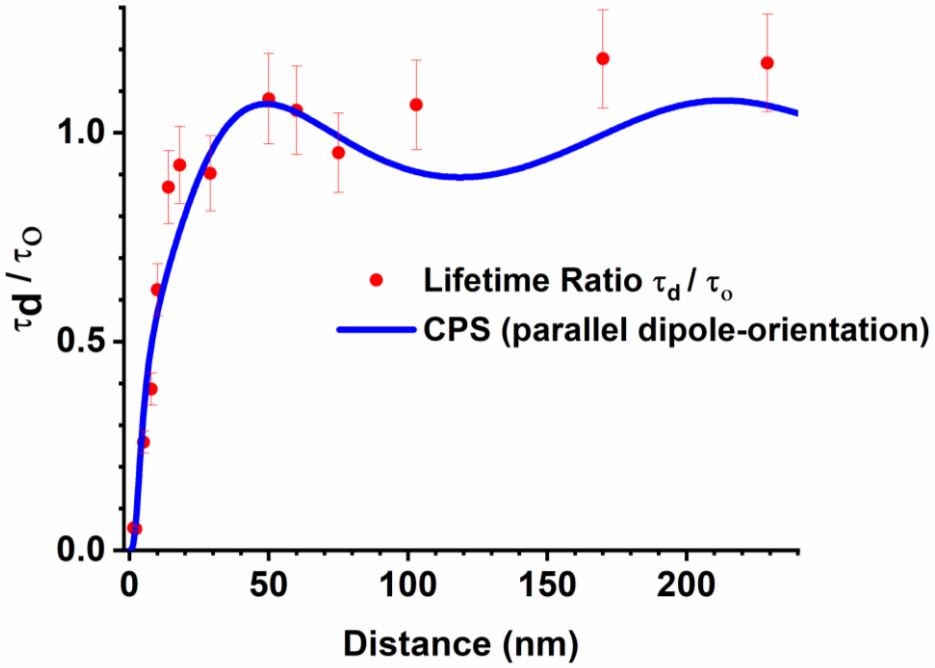

Figure 5.26: The lifetime versus unquenched lifetime ratios of rhenium recorded as a function of distance for this study and the theoretical calculated values for parallel dipole orientation. Each data point represents two samples.

The phosphorescence lifetimes of quenched samples and the lifetime of unquenched samples was used to calculate the degree of quenching as represented by the ratio of the quenched to unquenched lifetime (τ_d / τ_0). The lower the value of the ratio of τ_d / τ_0 the higher the degree of quenching occurring. This is plotted compared to the theoretical value of τ_d / τ_0 calculated for a parallel dipole orientation according to CPS theory. Quenching begins to occur at distances below 40nm from the surface of the silicon with a quenching rate of approximately 10%. This is consistent with the theoretical maximum distance of Förster resonance energy transfer and the research described on metal mirrors where non-radiative energy transfer can only take place within 50nm.

The degree of quenching increased as the monolayer was deposited closer to the surface of silicon wafers below 50nm. The amount of quenching shows a linear relationship to the distance from the silicon wafer and closely follows the expected theoretical value. At distances below 10nm the lifetimes calculate ratios of τ_d / τ_0 of 0.4 and 0.26 which indicates approximately 60% and 74% quenching efficiency.

The highest amount of quenching was shown when the ReC18 monolayer was deposited directly onto the silicon wafer's oxide layer which separated it from the bulk silicon by only 2nm. The 2nm separation showed a ratio of τ_d / τ_0 of 0.05, which corresponds to 95% phosphorescence quenching which is extremely high. The amount of quenching shown is attributed to energy transfer, as the theory does not say that there is any destructive interference at this point.

The calculated pattern of fluorescence amplification and quenching at distances greater than 50mm follows the recorded results within the margin of error. This suggests a pattern of constructive and destructive interference due to reflection of light from the Rhenium film causing the appearance of enhancement and quenching of luminescence. This means that the pattern of enhancement and reduction of the lifetime can be attributed to parallel dipoles interacting with one another between the surface of silicon and the ruthenium monolayer confirming the presence of nonradiative energy transfer.

5.3.14 Fluorescence lifetime imaging of RuC18 monolayers on glass and silicon

Ruthenium films were imaged using a fluorescence lifetime imaging microscope. Figure 5.27 shows a single layer of RuC18 deposited on glass resulting in a uniform surface. There are some small domains visible with a slightly brighter emission.

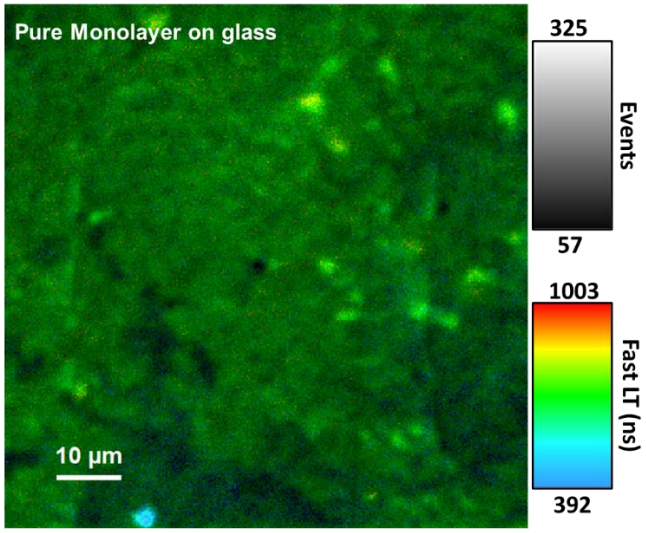

Figure 5.27: A FLIM image Showing a single layer of ruthenium deposited on glass.

In comparison deposition onto the silicon wafer as shown in Figure 5.28 shows a higher number of brighter domains, as well a s a generally much lower signal. This shows that more quenching may be taking place in small domains. It shows no significant difference compared to the glass samples and with no apparent holes in the film.

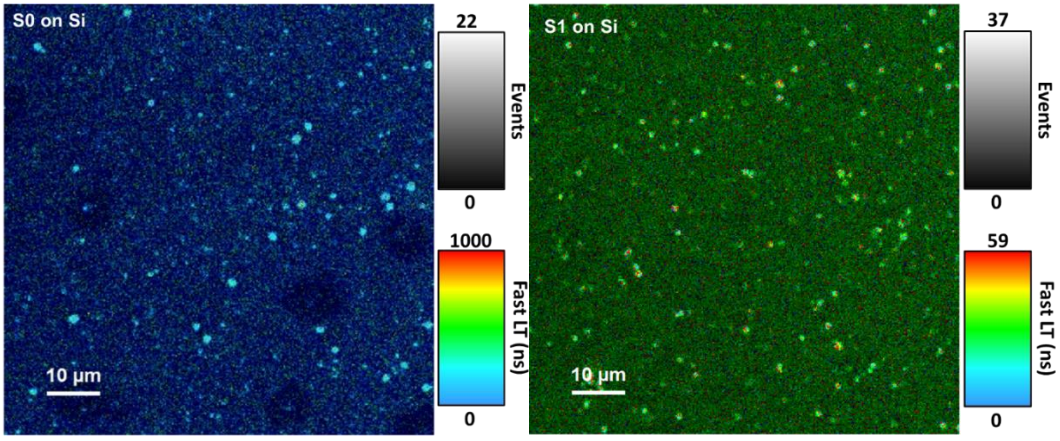

Figure 5.28: FLIM images of Ruthenium complex monolayers with no spacer (S0) and one layer of spacer (S1) deposited on silicon wafers

In comparison Figure 5.29 shows a monolayer of RuC18 deposited onto a two layer of stearic acid on top of a silicon wafer, this forms a smaller number of slightly larger domains in comparison to glass, also shown in Figure 5.29.

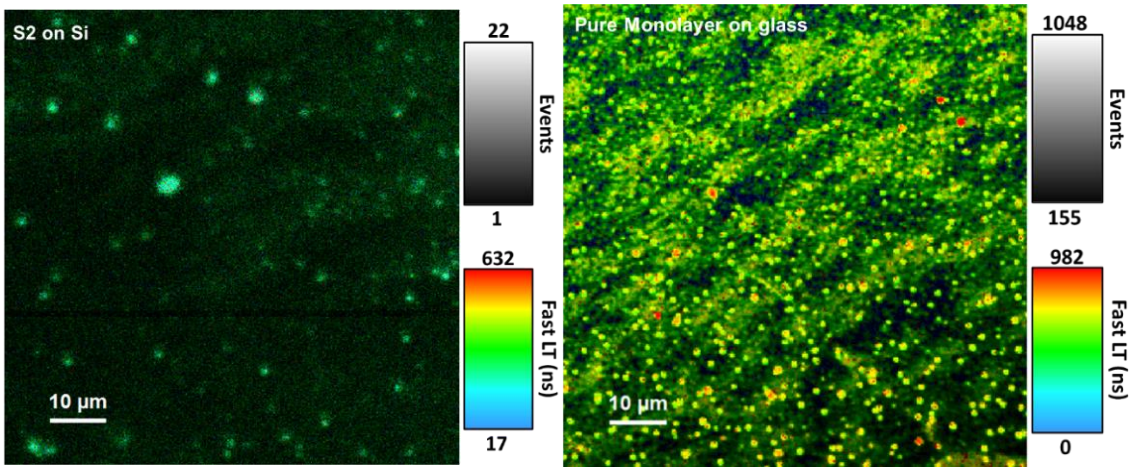

Figure 5.29: FLIM images of a Ruthenium sample with 2 layers of spacer (S2) deposited on Silicon wafer and a Hydrophilic orientation Monolayer of Ruthenium Deposited on Glass.

The AFM of the ruthenium complex in Figure 5.30 showed similar globular domains. The height is an error as a result of the cantilever getting stuck in the sample, this is known as the recorded heights are not possible. However, the domains are there, and their appearance is consistent with the FLIM images.

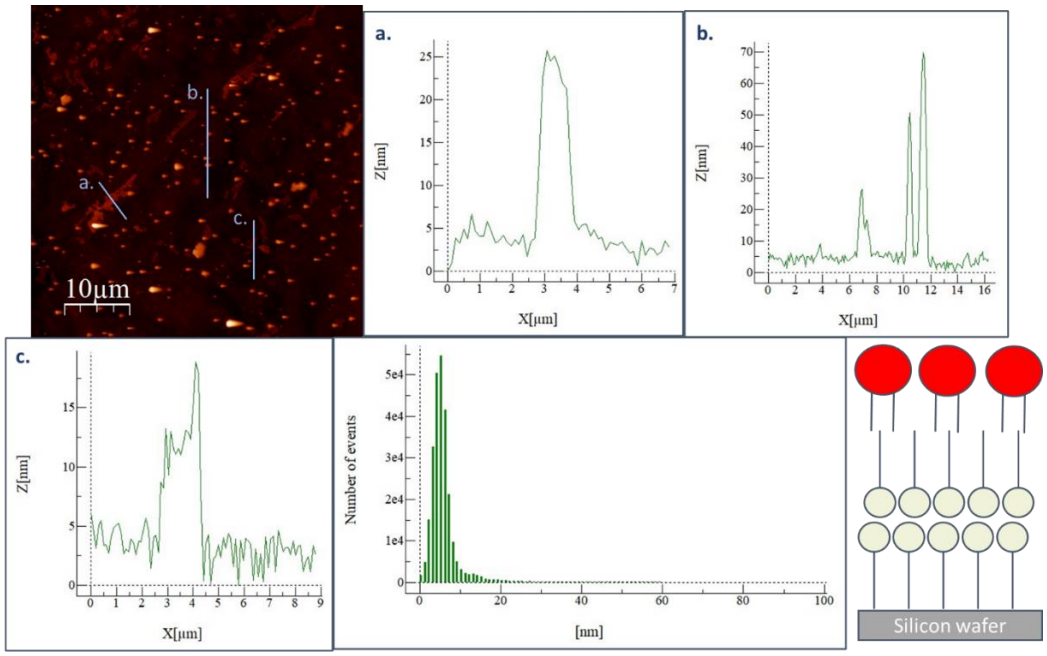

Figure 5.30: AFM of a sample of a Ruthenium monolayer deposited with no stearic acid cap on top of a two layers of stearic acid.

1.1.4. RuC18 quenching and energy transfer to silicon

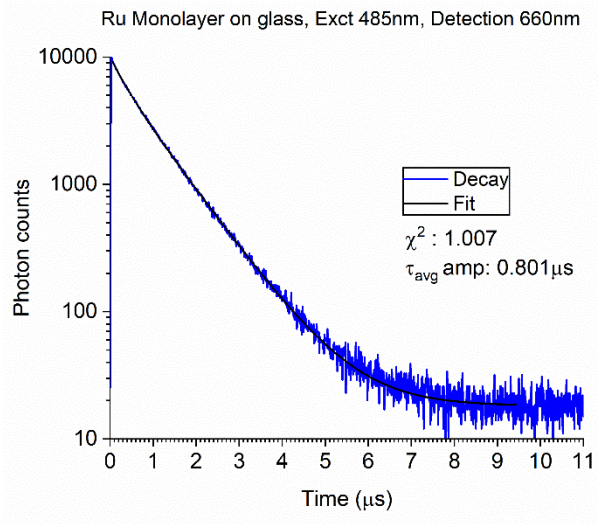

Figure 5.31: Phosphorescence decay curve and estimated lifetime of a RuC18 monolayer deposited on quartz glass slides, excited at 485nm and detected at 660nm, fitted with a two exponential tailfit. ± 3% error gives ±0.024 µs.

Figure 5.31 shows the full decay with a small slow component around 0.8µs. The average lifetime is shown to be approximately 801ns. The shape of the lifetime suggests both fast and slow emitting species. This is confirmed by the fractional amplitudes of the decay. With 24% the average made up by a 333ns component (the fast lifetime) and 76% made up by a 944ns component (the slow lifetime). The solution lifetime shown in Figure 5.13 has been fitted to a single exponential fit, suggesting there is only one species present in the solution. This means the effect of removal from solution causes interaction between the ruthenium complexes which alters the lifetime of some, likely energy transfer between the ruthenium complexes in extremely close proximity. The average lifetime taken from samples deposited on glass was compared to samples deposited on silicon wafers.

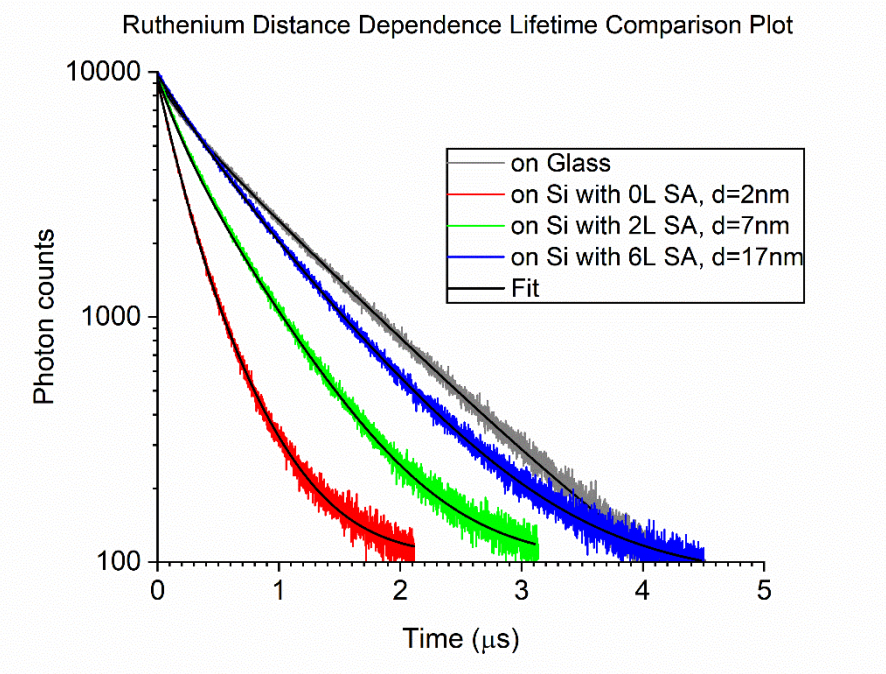

Figure 5.32: Phosphorescence Decay curves from monolayers of RuC18 on glass and deposited close to the surface of silicon wafers. Excited at 485nm and measured at 660nm using a 488nm bandpass filter.

Figure 5.32 shows that when RuC18 is deposited close to the surface of the silicon the phosphorescence emission is quenched which signifies energy transfer to the silicon wafer. The emission intensity from these samples was also significantly weaker. The

results from the MT 200 show a distance dependence of the reduction in lifetime on the distance of the ruthenium monolayer from the sample.

Further characterization was performed using the Microtime 200 FLIM microscope. Lifetimes for each sample were recorded and used to characterise the energy transfer of RuC18 as a function of distance from the surface of silicon. The distance was measured with ellipsometry.

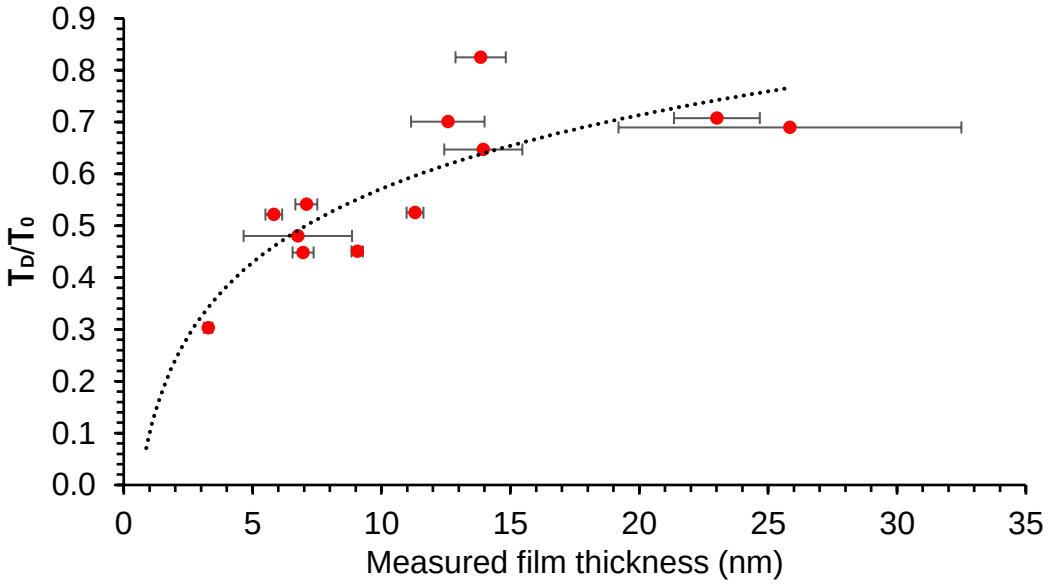

Figure 5.33: Phosphorescence quenching of the Ruthenium monolayers on silicon wafers vs the measured spacer thickness using ellipsometry, the data points show individual samples, each spacer thickness was repeated. The error shows the standard deviation of the spacer thickness measured with ellipsometry.

As both Figure 5.32 and Figure 5.33 show, there is a distance dependence relationship between the quenching occurring and the distance of the RuC18 from the surface of the silicon. The primary focus in this set of samples was to study the energy transfer energy transfer for distances up to 30 nm. So, the study of the constructive and destructive interference past 25nm was not undertaken. This is well established in metal mirror research.[81] A simple best fit curve is shown in Figure 5.33. The error bars represent standard deviation of the measured film thickness using ellipsometry. As they show some samples had a very high standard deviation. Besides some outliers there

seems to be a relationship between the distance from the surface and the lifetime of the films.

Looking at percentage quenching below a distance from the surface of 1nm as shown in Figure 5.33 shows a clear relational decrease in the lifetime of the film as the distance decreases. The highest percentage quenching recorded was approximately 63% with no spacer layers from the film. Taking the oxide layer into account this is 2.4nm from the bulk silicon.

5.4 Conclusions

The rhenium and ruthenium complexes show absorbances comparable to similar complexes from previous studies indicating to the expected metal-ligand charge transfer. Changes in the excitation wavelength does not change the ReC18 wavelength of emission at 550nm and the RuC18 emission at 650nm is blue shifted slightly when the complex is deposited into a monolayer. This is also in line with previous research on both complexes and is characteristic of emission from both metals regardless of ligands, indicating MLCT is taking place in both cases. The time resolved results indicate a long phosphorescence lifetime, approximately 0.3µs for ReC18 and 0.6µs for RuC18. Removal of oxygen in both cases results in an increased lifetime which indicates the triplet state dependent lifetimes, 0.45µs for ReC18 and 1.6µs for RuC18.

Deposition of both complexes into a film on a Langmuir Blodgett trough was shown to be successful and isotherms were recorded and repeated showing the molecular areas to be 95Å^2 per molecule for Rhenium and 65Å^2 per molecule for Ruthenium. The films showed shifting with repeated compressions, which might suggest some loss of material with each compression and may indicate instability. However, the more likely reason is to indicate re-organization of the film into a more organized form. The molecular area of ReC18 was also shown to be significantly larger than the majority of previous research which showed values between 40 to 70Å^2, a difference of 55 to 25Å^2, suggesting a different arrangement of complexes compared to previous studies whilst the molecular area of RuC18 was shown to be smaller than previous research, which showed molecular areas around 90Å^{2,} a difference of around 25Å^2.[58,71] However, Previous studies showed an inconsistent molecular area measurement for various Rhenium and Ruthenium complexes. It is difficult to make direct comparison between

examples of previous research and the current work as differences in experimental procedure and the complexes being tested contribute to differences in measured molecular area.

The complexes were successfully deposited into films, which were characterised using spectroscopy and microscopy. The spectroscopic characterization of the samples showed small spectroscopic shifts in the absorption and fluorescence spectra occurred as a result of deposition and the environment change. The shifts are common when deposition of a fluorophore takes place, and the blue shifted fluorescence peaks of both complexes suggest this same effect of removal from solution on the spectra. The increase in the measured phosphorescent lifetime shown in the freeze pump and thaw experiments is consistent with the lifetime increases from deposition into a film reducing the opportunity for collisional quenching by oxygen, an increase of approximately +50% for the ReC18 and 150% for the RuC18.

The results of ReC18 monolayers deposited on silicon wafer showed quenching which followed a pattern similar to that of metal mirror research on Eu^{3+} complexes, with 95% phosphorescence quenching with respect to a glass sample used as a control shown for the ReC18 2nm from the surface and patterns of constructive and destructive interference shown above 20nm from the surface suggesting the silicon acts in a similar manner as a metal mirror and that there is energy transfer to the silicon wafer, when fitted with the CPS dipole theory, the pattern of quenching roughly follows it.

For RuC18 monolayers the distance was not increased to the point where constructive and destructive interference was shown however a relationship between distance from the surface and quenching was shown. RuC18 showed 63% phosphorescence quenching 2nm from the surface with respect to the lifetime of RuC18 deposited on glass used as a control. The quenching is taken as energy transfer to the silicon wafer, this means the ruthenium showed a reasonably high level of energy transfer to the silicon wafer. Microscopy of the films showed some discrepancies which were ameliorated by repeats showing areas of the film which were thought to be holes interreacting differently with the silicon, possibly due to formation of structures which have different emissive properties, this was the case for both films. The results clearly show quenching taking place close to the silicon and still occurring as far away as

20nm in both cases, this is consistent with quenching which can be attributed to energy transfer and is consistent with theoretical maximum distance of Förster resonance energy transfer.[135,154] The behaviour after of Rhenium films after 20nm fits with behaviour attributed to far field effects from constructive and destructive interference from the mirrored silicon surface showing that silicon is acting as a mirror and providing constructive and destructive interference.[48,81]

The results therefore show that as a final trap molecule and have great potential to be used in conjunction with a light harvesting system, as described by Dexter in the literature review.[2] This is a first in the use of this ReC18 complex and RuC18 complex in a Langmuir Blodgett film used as a sensitiser of a silicon wafer with minimal modifications, the silicon was not etched, and the complexes where not attached suggesting a simple coating process requiring minimal modifications could be developed from this data. The Rhenium complex was shown to be particularly effective even at 6nm distance from the surface of the silicon. This shows a potentially highly effective sensitizer to be used as the final step in a light harvesting process. However, some problems arise, namely that it only absorbs light in a very high energy region of the spectrum and misses out the majority of visible light available to a solar panel, therefore looking into different complexes in now required. In addition, the creation of light harvesting systems using this as a final acceptor in order to absorb light much more efficiently and from more of the spectrum should be investigated.

RuC18 was also shown to form a film on silicon which transferred energy to the silicon wafer at distances below 20nm, since this is the only region of interest for this study no further investigations were deemed relevant. The degree of energy transfer was shown to be lower than that of ReC18 however it still gave approximately 60% energy transfer around 2nm away from the surface of the silicon from a monolayer of complex. This shows both complexes which cover 200-500nm of light absorption could be used as components of a light harvesting system, there is a small degree of overlap meaning that there is a theoretical possibility of a light harvesting system based on these complexes, however this may prove expensive and industrial scaling up of the film fabrication would also need to be considered, therefore using it as the final layer to a cheaper system would be simpler.

6. Silicon photosensitisation using tetraphenyl porphyrin layers detected using silicon emission

6.1 Aims and objectives

Porphyrins have been selected for the final chapter of the thesis. In this chapter the use of passivated silicon wafers and a new method of detecting sensitization of silicon are used to study the monolayers of tetraphenyl porphyrin on silicon wafer. Despite being singlet emitters porphyrins were chosen for their fluorescence near to the infra-red end of the visible spectrum and for the fact that they can be modified by the insertion of metals allowing for selection of additional fluorescence decay wavelengths.

Porphyrins have been shown to transfer energy between one another and are an integral part of the photosynthetic light harvesting process which has been identified as a natural process which could be exploited as a potential green energy source.[11,12] This shows porphyrins as a great candidate for light harvesting films.

The aim of this chapter was to investigate the energy transfer of porphyrin (tetraphenyl porphyrin) LB films to silicon wafer which had surface modification with aluminium oxide in order to improve the passivation.

To achieve this the objectives were to fabricate Langmuir films of a tetraphenyl porphyrin (TPP). To use LB to deposit TPP as monolayer onto silicon wafers that have been chemically modified by etching and passivation as well as non-etched cleaned silicon wafers with an oxide layer. To study the steady state fluorescence and fluorescence lifetimes of both the TPP films and the silicon wafer photoluminescence emission. The aim of this being to detect fluorescence quenching of the porphyrin layers by the silicon which could be attributed to energy transfer to the silicon. In addition, enhanced emission from silicon wafers can be an indication of sensitization of the silicon caused by the layers of porphyrin.

6.2 Experimental overview

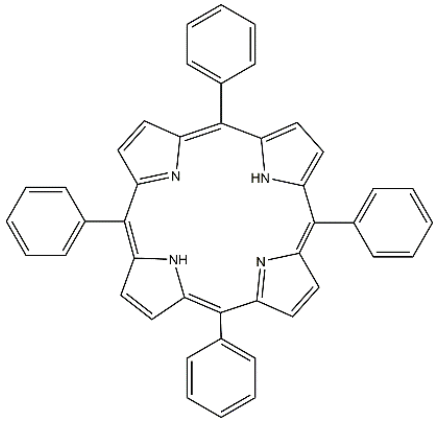

Figure 6.1: Chemical structure of 5,10,15,20-Tetraphenylporphin (TPP), the porphyrin selected for study in this chapter.

Tetraphenyl porphyrin was purchased from Sigma-Aldrich and mixed with stearic acid in a molar ratio of 1-1 which was tested spectroscopically on the LB trough to determine if a stable film had formed. The stable film was then deposited on quartz glass slides, unmodified oxide coated silicon wafer and etched silicon wafers passivated with Aluminium Oxide. The steady state fluorescence emission and fluorescence decays of the TPP layers and the silicon wafer itself was investigated to determine if non-radiative energy transfer was occurring.

6.3 Results and discussion

6.3.1 Solution Steady State

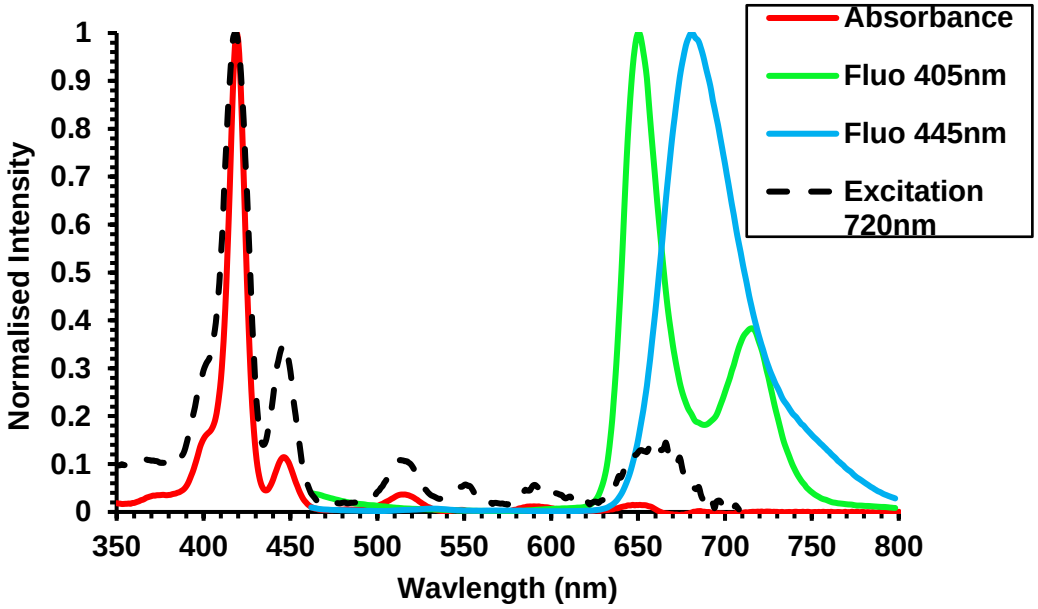

Figure 6.2: Normalised absorption, fluorescence, and excitation spectra of 5,10,15,20-Tetraphenylporphin dissolved in $CHCl_3$. The Fluorescence shows two different excitation wavelengths, 405nm and 445nm. The excitation spectrum is recorded by monitoring the fluorescence at 720nm and exciting from 300 to 800nm.

Figure 6.2 shows the recorded steady state absorption and fluorescence spectra of the TPP in solution. The absorption spectra show a strong peak at 415nm, attributed to S_0 to S_2, π to π^* transitions. The band is thin and sharp. There are multiple additional smaller peaks and shoulders at 400nm and 450nm which are also assigned to S_0 to S_2, π to π^*. Additional peaks at 515nm, 590nm and 650nm are assigned to S_0 to S_1, also π to π^* transitions. The excitation spectra follow the absorption spectra however it shows the smaller peaks as much stronger. The fluorescence spectra show two different spectra depending on where absorption occurs. Excitation at 405nm gave two peaks, one at 650 and one at 720nm whilst excitation at 445nm yields one peak at 690nm. The spectra shown here agrees with literature on the subject.[100,104,155] The dual nature of the fluorescence spectrum is attributed to Gouterman's four orbital model of porphyrin absorption and fluorescence where two sets of overlapping HOMO and LUMO orbitals allow transition from either LUMO to either HOMO. Thus, this allows for more than one excitation and deexcitation pathway.

6.3.2 Porphyrins pure and mixed with stearic acid isotherms.

Figure 6.3: Pure TPP deposited in $CHCl_3$ on a pure deionised water at room (~20 ^oC) temperature on a Langmuir trough, compressed ten times at 50mm/min.

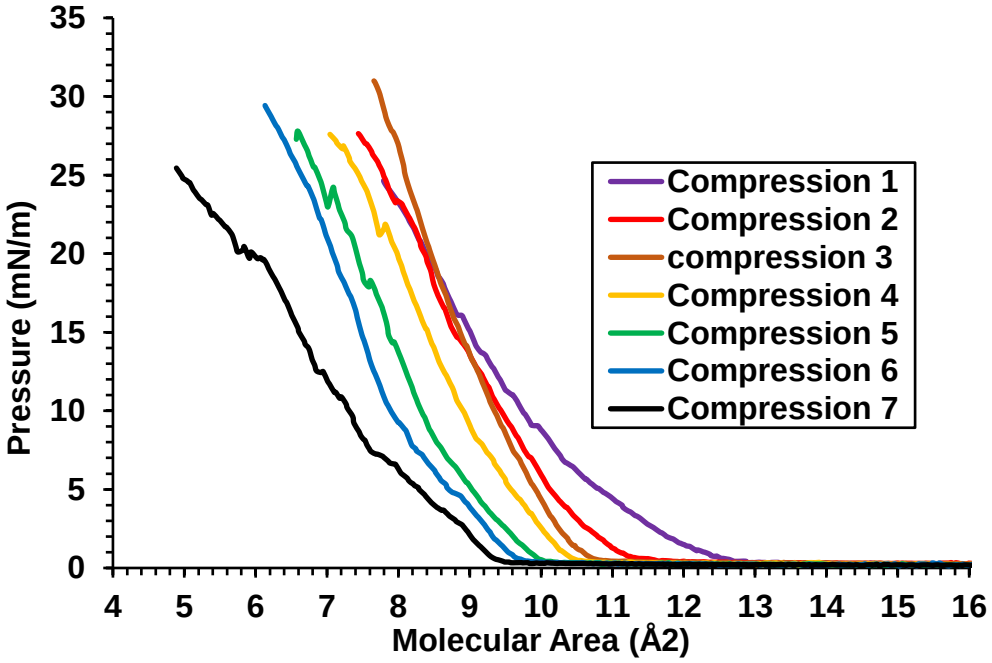

The Langmuir isotherm of pure porphyrin shown in: Pure TPP deposited in CHCl3 on a pure deionised water at room (~20 ^{oC}) temperature on a Langmuir trough, compressed ten times at 50mm/min.indicates the film is collapsing as it is compressed, collapse is shown by the ragged, uneven lines showing drops in the surface pressure as the compression occurs and the movement of each curve towards a much lower molecular area showing loss of material into the subphase. This shows that the method used here was not sufficient to deposit films of TPP. There are several reasons for this. For one the deposition method was very simple. As Mansur et al[101] does show, there is an effect of deposition on the quality of the porphyrin films. The deposition method used here is roughly two to three drops per second but was not quantified in any meaningful way. Additionally, there were no

modifications made to the TPP to improve its film forming abilities nor were buffers added to the trough. This resulted in the porphyrin dissolving into the subphase as a result of the compression.

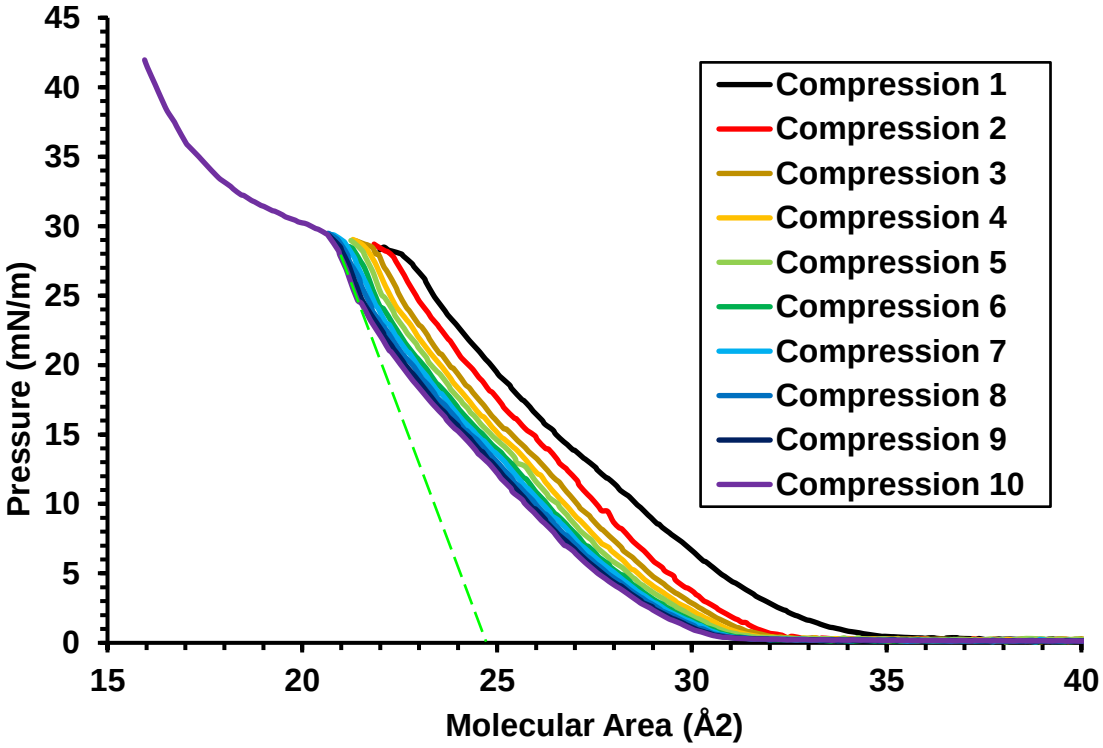

Figure 6.4: TPP mixed in a 1-1 ratio with stearic acid deposited in $CHCl_3$ on a pure deionised water at room temperature (~20 ^{o}C) subphase on a Langmuir trough, compressed ten times at 50mm/min.

In order to form stable films, several ratios of stearic acid to porphyrin were created and tested. 1-1, 10-1, 25-1, 50-1 and 100-1 were all tested. 1-1 was chosen to give the highest coverage possible and because the lower ratios did not give a high enough signal. As shown in literature, mixing with stearic acid provided a very stable film which has the appearance of a mix between a large molecule and stearic acid, showing a smooth curve with no defined solid liquid or gas phase.[100–102] The final molecular area extrapolated to zero surface pressure from the solid phase of the final compression was estimated to be around 25Å^2 per molecule. Repeated compression and release cycles showed the films to reach a lower level of change after five compressions and there was little change after eight compressions. The estimated molecular area agrees with some previous research. However other examples exist of larger molecular areas, no consistent molecular area is reported.[100,101,156] As in previous chapters a

computational model of porphyrin was made, and the molecular area calculated to compare to the experimentally determined values.

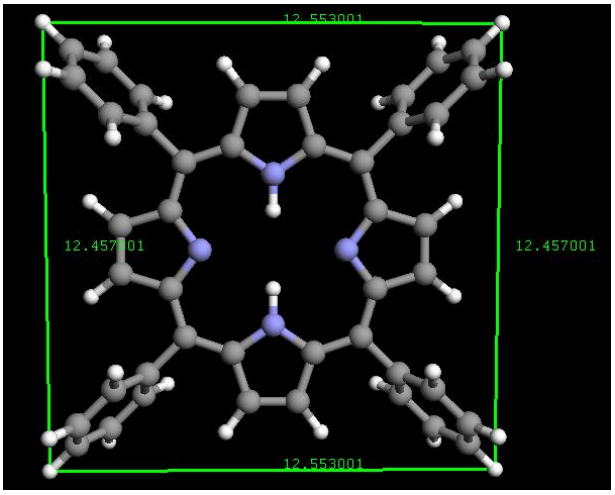

Figure 6.5: A computational model of TPP with the area measured as a square from the tip of each phenyl group.

Figure 6.5 shows a model of porphyrin used to measure the theoretical area of the molecule. Treating the porphyrin as a square gives an area of 156.37Å^2.

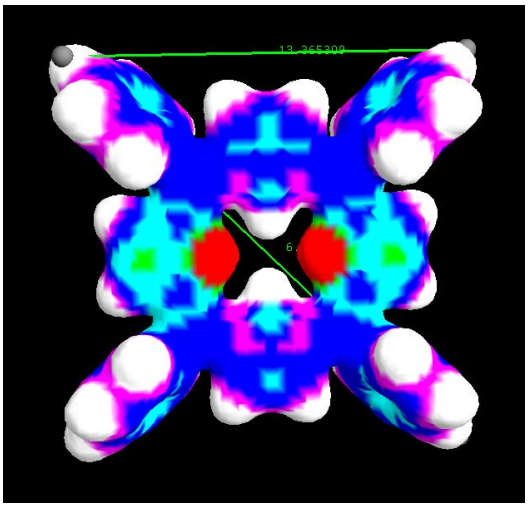

Figure 6.6: TPP model with the van der walls shells generated in Argus lab and measured from the exterior of the shells for the maximum theoretical size of TPP.

Figure 6.6 shows a van der walls model of TPP with atoms around the outside of the van der walls shells to provide attachment points for a rough measurement of the surface. This gives 13.36Å of distance. Taking this as the length for all sides gives an area of 178.49Å^2. Increasing this to 13.5 Å to give a “max possible” distance estimation gives an area of 182.25Å^2. However, measuring the side profile (3-7Å depending on the rotation of the phenyl groups) of the molecule gives a far smaller area of 40-94Å^2. this agrees with previous research estimates. Of particular interest was the fact that the measured molecular area differed significantly from the predicted molecular area in previous studies.[101,156]

This is larger than the experimentally determined molecular area. The molecular area is instead similar to the molecular area of stearic acid but marginally bigger. Using the molecular area of stearic acid which is usually between 19Å^2 and 21Å^2 (depending on various factors such as pH and temperature. The contribution of the porphyrin can be calculated using Equation 6.1.[100]

$$A_{TPP} = \frac{A_{Avg} - (F_{SA}A_{SA})}{F_{TPP}}$$

Equation 6.1: Calculation the contribution of TPP to the mixed monolayer average molecular area

Where A_{TPP} is the calculated molecular area of TPP. A_{Avg} is the measured molecular area of the mixed monolayer. A_{SA} is the molecular area of stearic acid and F_{SA} is the fraction of stearic acid. Using the experimental value of 25Å^2 for the mixed monolayer and 21Å^2 for molecular area of stearic acid the contribution of the porphyrin is calculated to be 29Å^2, this is reasonably close to the smallest possible estimated value and suggests the TPP is not lying flat in the film. This is somewhat in agreement with some similar work[157]. However, in most cases with which it can be compared the addition of carboxylic acid groups, long chain hydrocarbons or metalation, a direct comparison is difficult.[158]

6.3.3 Porphyrins pure and mixed with stearic acid in situ spectra.

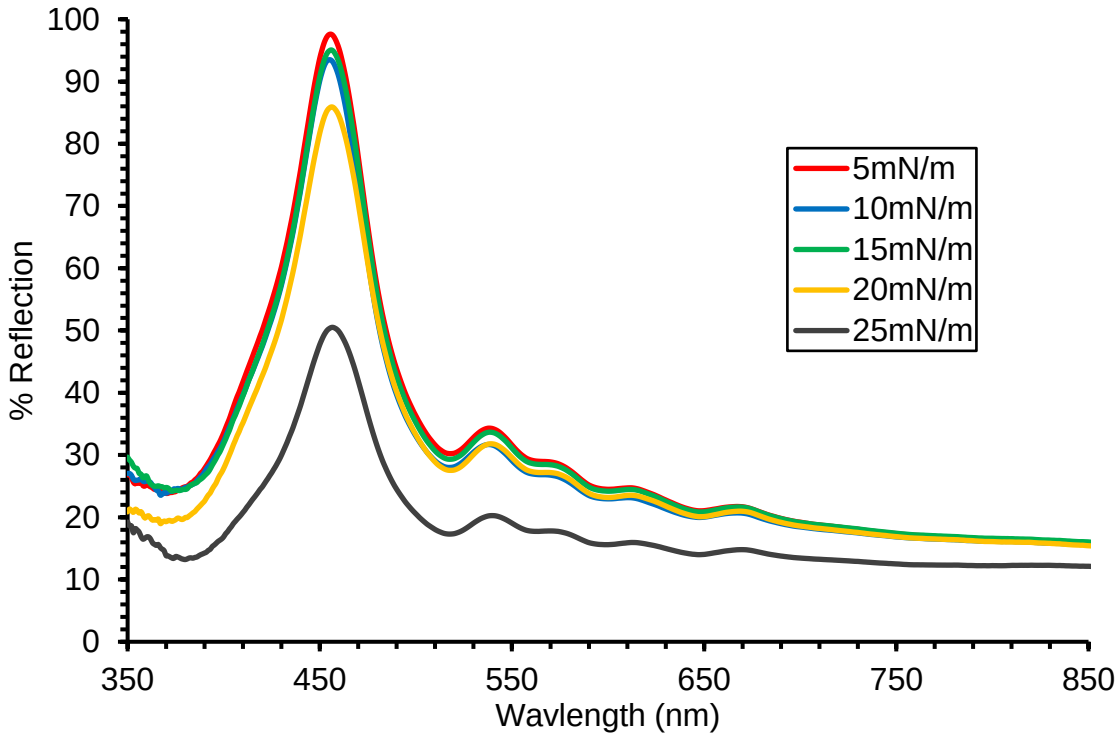

Figure 6.7: Absorption measured by reflection of pure TPP deposited in $CHCl_3$ on a pure deionised water subphase at room temperature (~20 ^oC) on a Langmuir trough, compressed to and measured at five different surface pressures.

In order to assess the quality of the films on the surface of the trough a reflectance spectrum was taken. Figure 6.7 shows the spectra of pure porphyrin on the surface of the trough. This shows largely the same spectra as the solution except the peak at 420nm has disappeared and peak at 450nm has shifted to around 455nm and become the dominant peak. The pure films are detectable using this method despite collapsing, however there is a decrease in the intensity as the pressure increases. This may be indicative of some level of collapse. Additionally, if film formation was occurring a level of aggregation should be occurring. This would result in significant band shifting of the peaks. The shift and changes that have occurred is attributed to the change in environment from solution to monolayer.

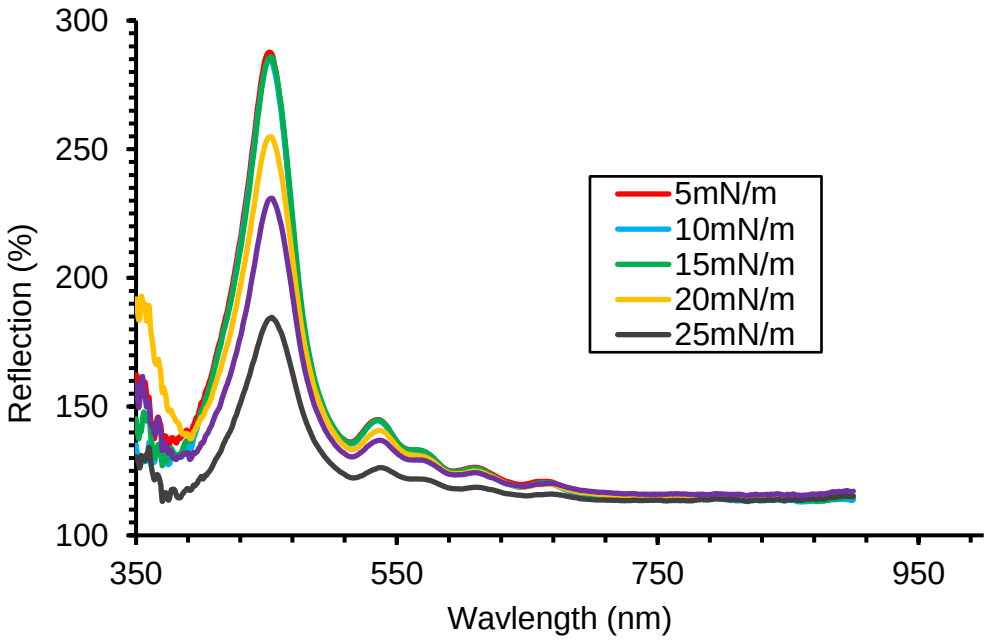

Figure 6.8: Absorption measured by reflection of TPP mixed with stearic acid in a 1-1 ratio deposited in $CHCl_3$ on a pure deionised water subphase at room temperature (~20 ^{o}C) on a Langmuir trough compressed to and measured at five different surface pressures

Figure 6.8 shows the reflectance spectra of the 1-1 ratio of porphyrin to stearic acid. The shape of the spectrum agrees with Figure 6.7 which suggests that the same effect of being removed from solution is occurring, and that the stearic acid does not have an appreciable effect on the spectrum. The intensity of reflection from the trough has changed which suggest more porphyrins have been made available. This coupled with the mixed nature of isotherm is evidence of the stabilizing effect of the stearic acid allowing a successful film formation.

6.3.4 Spectroscopic characterization of mixed LB films of porphyrins on glass.

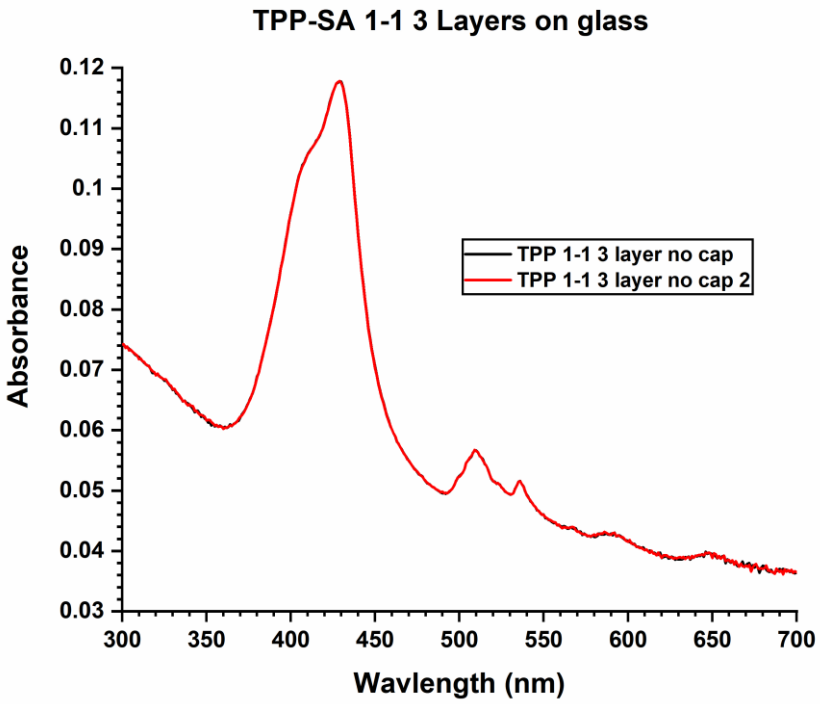

Figure 6.9: Absorption measured by reflection of TPP mixed with stearic acid in a 1-1 ratio deposited in $CHCl_3$ on a pure deionised water subphase on a Langmuir trough compressed to and measured at five different surface pressures

LB films deposited on glass substrates were fabricated by depositing six layers of stearic acid on cleaned glass substrates that have been modified using HMDS, then depositing one to three layers of 1-1 TPP layer, finishing with three cap layers added to the top. An absorption spectrum was taken using an Agilent Cary 60 UV-VIS spectrometer, the result of which is shown in Figure 6.9. The shoulder on the blue side of the maximal peak is much stronger than in the solution spectrum. The maximal peak is no longer at 450nm but it is blue shifted slightly to around 440nm. Shifting in the minor peaks has also occurred to lower wavelengths. This is attributed to further changes in the environment around the porphyrins.

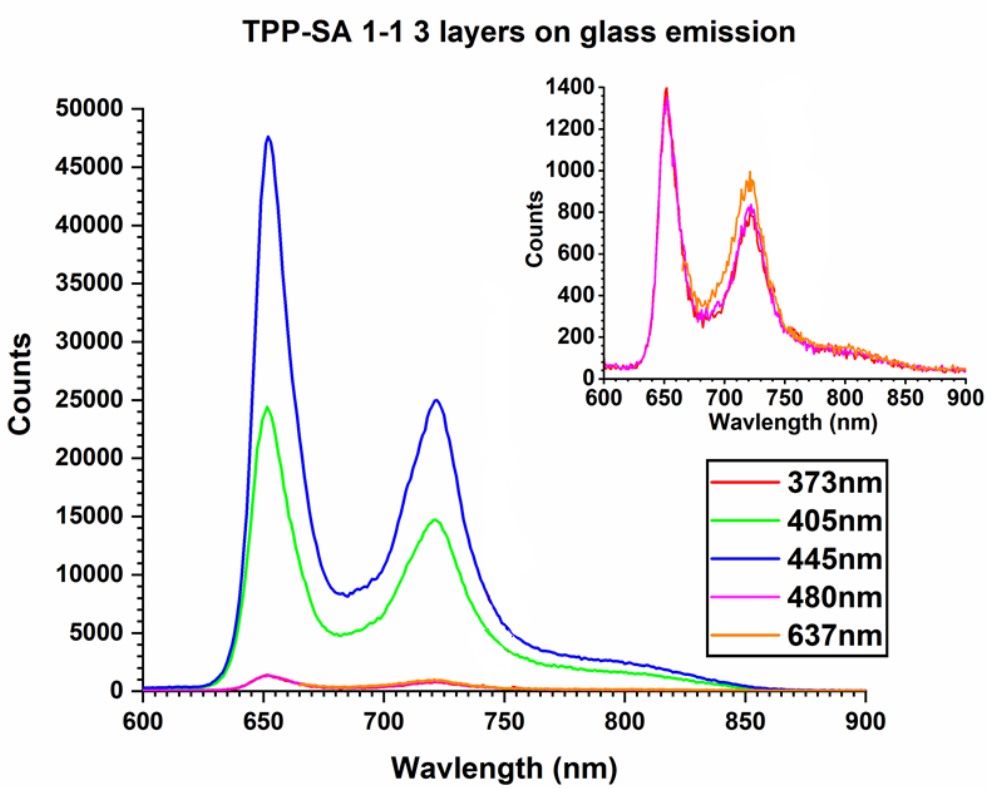

Figure 6.10: Fluorescence spectrum of 3 LB monolayers of TPP mixed in a 1-1 ratio with stearic acid deposited on a stearic acid coated glass slide, excited with five different wavelengths of light and measured from 600 to 900nm.

Figure 6.10 shows the fluorescence spectra of the glass sample. The sample is excited at every wavelength which lasers were available. The highest intensity was gained by excitation at 405nm and 445nm. This is hitting either side of the maximal absorption peak. However, the same fluorescence spectrum, albeit at far lower intensities was recorded. The fluorescence spectrum is the same two peak format as shown in the solution spectrum in Figure 6.2. This shows the occurrence of fluorescence from two HOMO orbitals to two LUMO orbitals according to Gouterman's four orbital model.

Single layer samples were also investigated on glass as shown in Figure 6.11. The fluorescence lifetimes measured at various wavelengths are shown in Figure 12-14. The lifetime is shown to be around 1ns.

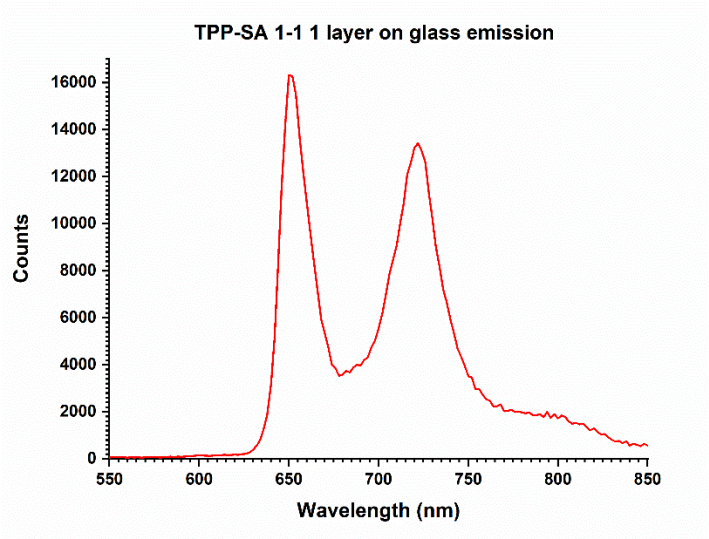

Figure 6.11: Fluorescence spectrum of a single LB monolayer of TPP mixed in a 1-1 ratio with stearic acid deposited on stearic acid coated glass. The sample was excited at 405nm and measured from 550-850nm.

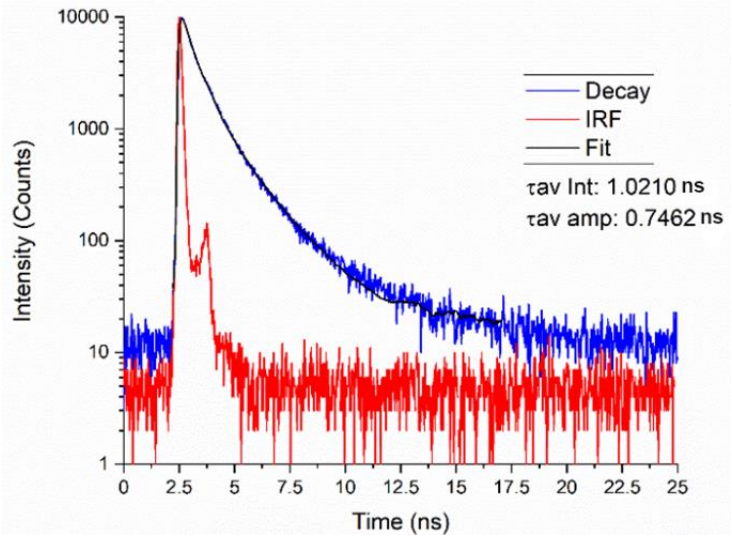

Figure 6.12: Fluorescence decay of a monolayer of 1-1 TPP-SA deposited on a quartz glass slide and coated with a 1-1 TPP-SA monolayer excited at 405nm and detected at 720nm,.± 3% error gives ±0.0224 ns.

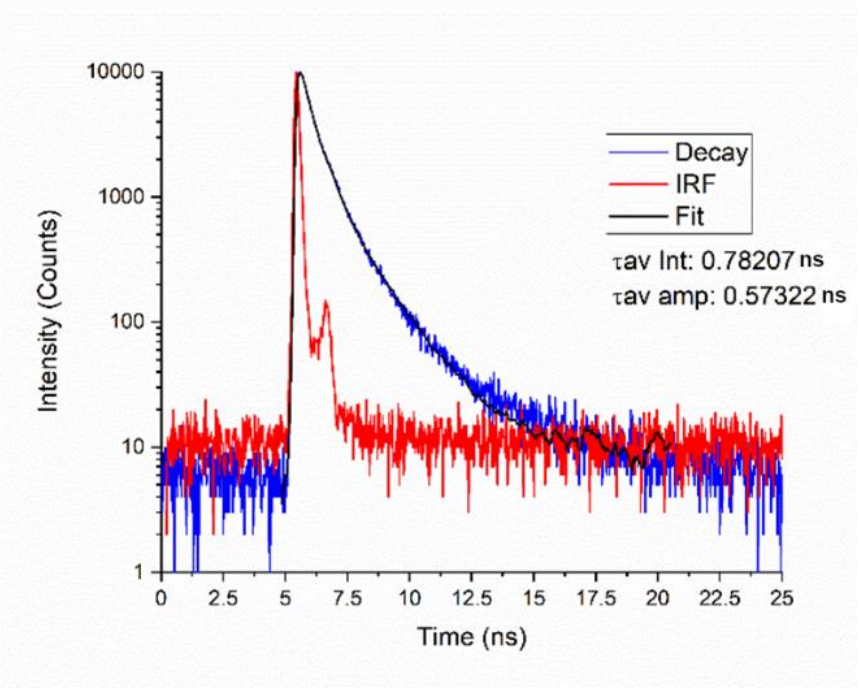

Figure 6.13: Fluorescence decay of a monolayer of 1-1 TPP-SA deposited on a quartz glass slide excited at 445nm and detected at 720nm. ± 3% error gives ±0.01720 ns.

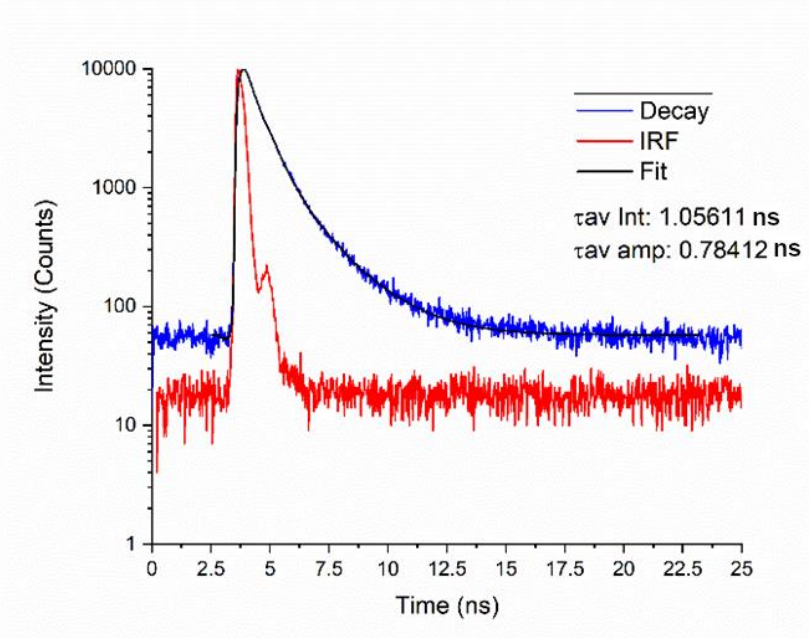

Figure 6.14: Fluorescence decay of a monolayer of 1-1 TPP-SA deposited on a quartz glass slide and coated with a 1-1 TPP-SA monolayer excited at 480nm and detected at 720nm. ± 3% error gives ±0.02352 ns.

6.3.5 Monolayers of 1-1 TPP-SA deposited on silicon wafers

The steady state fluorescence emission and fluorescence decay from the TPP 1-1 film on the silicon was recorded. If no energy transfer was occurring a slight reduction in the fluorescence intensity of the silicon wafer and no significant change in the TPP layer fluorescence intensity or lifetime would be expected relative to the glass control samples. This is because the TPP layer would still absorb some of the incident light leading to reduced emission intensity from the wafer.

If energy transfer from the TPP was occurring a reduction in the fluorescence lifetime and intensity of the TPP layer relative to the glass control samples and an enhancement of the fluorescence emission of the silicon wafer relative to the bare silicon control samples would be observed.

In this case the time resolved emission decays can be used, a reduction in the lifetime of the TPP film and/or an increase in the lifetime of the silicon wafer may be indicative of energy transfer. 1-1 TPP monolayers were deposited on passivated silicon wafer, the results are shown below.

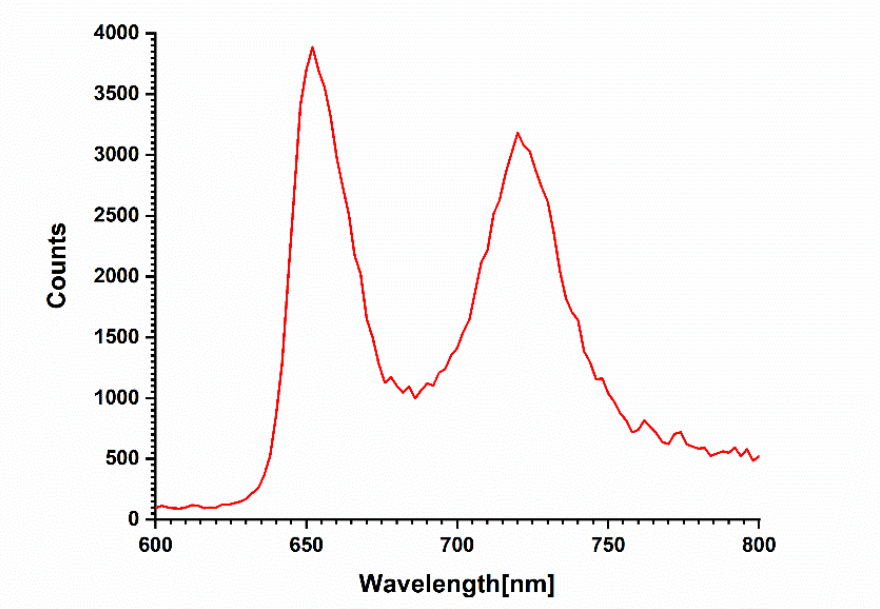

Figure 6.15: Fluorescence spectrum of one LB monolayer of TPP mixed in a 1-1 ratio with stearic acid deposited on silicon wafer. The sample was excited at 405nm and measured from 600-800nm.

Comparing the spectrum on glass shown in Figure 6.10 with the spectrum on silicon wafer shown in Figure 6.15 there is a decrease of around four times, this suggests some energy transfer occurring from a single layer to the silicon. Further investigation was performed on single layer samples using time resolved spectroscopy on the porphyrin fluorescence from the TPP-silicon samples used un-passivated silicon. Samples of TPP were fabricated on silicon wafers that were passivated. A single layer was deposited. The samples where characterised using time resolved spectroscopy shown in Figure 6.16.

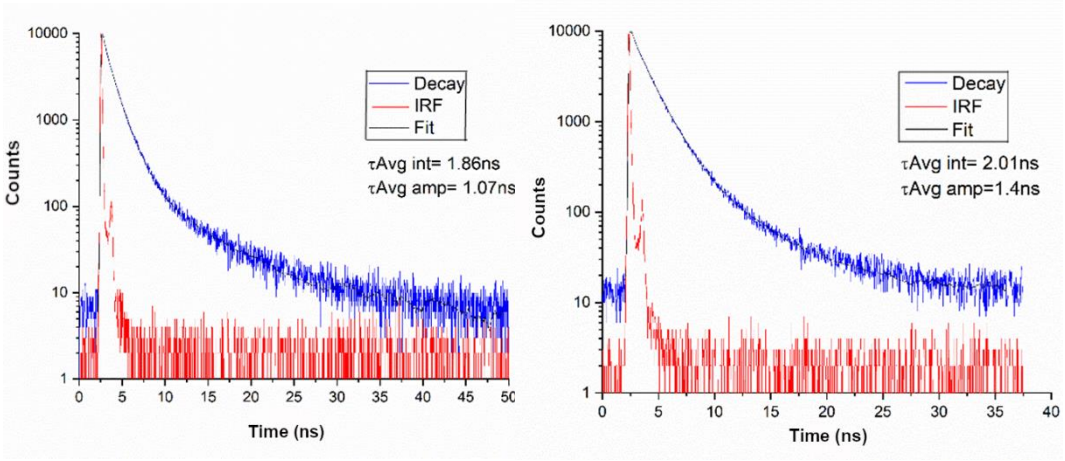

Figure 6.16: Fluorescence decay of a single layer of 1-1 TPP-SA on a silicon wafer excited at 405nm and detected at 650nm (Left) and 720nm (Right) ± 3% error gives ±0.03ns and ±0.04ns respectively. .

Contrary to the expected result the fluorescence lifetime of the TPP measured at 720nm has increased. This indicates that this method of passivation and deposition of a thin layer of TPP was insufficient for sensitization.

6.3.6 Fluorescence of Multilayer TPP on silicon wafers

Silicon wafer was then used as a substrate for deposition of up to three LB monolayers of TPP mixed with stearic acid as a stabilizer in a molecular ratio of 1-1.

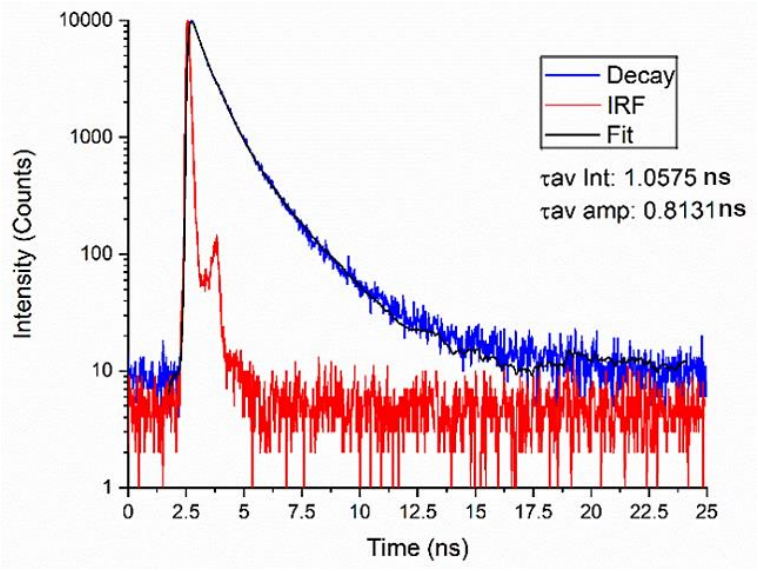

Figure 6.17: Fluorescence decay of a 3 layer sample of 1-1 TPP-SA deposited on a silicon wafer excited at 405nm and detected at 720nm to measure the change in TPP lifetime. ± 3% error gives ±0.0244ns

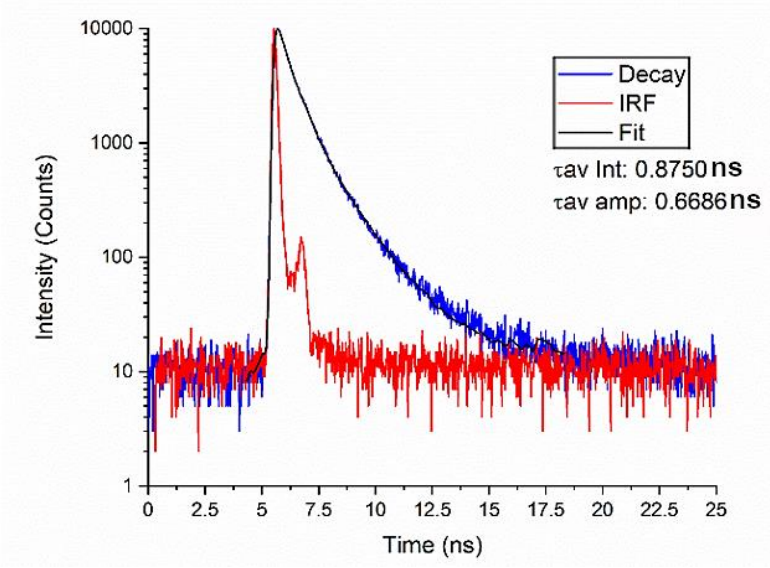

Figure 6.18: Fluorescence decay of a 3-layer sample of 1-1 TPP-SA deposited on a silicon wafer excited at 445nm and detected at 720nm to measure the change in TPP lifetime. ± 3% error gives ±0.0200ns

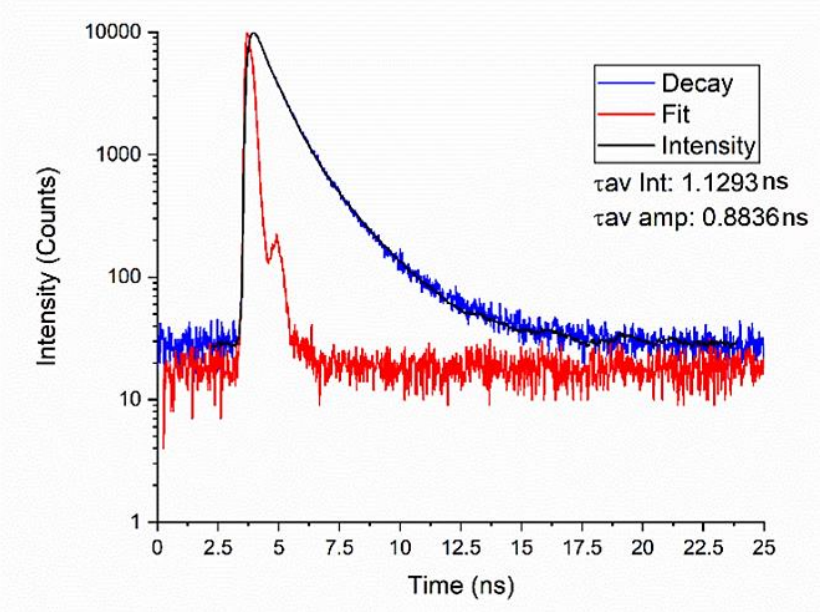

Figure 6.19: Fluorescence decay of a 3 layer sample 1-1 TPP-SA deposited on a silicon wafer excited at 480nm and detected at 720nm to measure the change in TPP lifetime. ± 3% error gives ±0.0265ns

The results shown in Figure 6.17, Figure 6.18 and Figure 6.19 use the fluorescence of the TPP itself to determine whether or not energy transfer is occurring, the expected result in the case of energy transfer occurring would be a reduction in the fluorescence lifetime. However, this does not occur, there is no significant reduction in the lifetime and in every case, there is a slight increase in the fluorescence lifetime when compared to the glass samples shown in Figure 6.12, Figure 6.13 and Figure 6.14, this may be explained by reflections from the surface of the silicon causing light to travel from the film, towards the silicon and then back towards the detector, thus adding some longer-lived photons to the count and artificially pushing the fluorescence lifetime up. It is also possible that this is constructive interference from the silicon acting in a similar manner to a metal mirror.[47]

The results from the 3-layer steady state measurements shown earlier can be fairly described as indicating that energy transfer is occurring, however when observing the time resolved results there is either a small enhancement or a no enhancement, this then suggests that there is a small amount of energy transfer happening however it seems to be unreliable. On top of this there is no evidence that the TPP film is actually transferring energy to the silicon wafer. This would then require another explanation

for the observed increase in acceptor fluorescence occurring from silicon when the TPP is applied despite the fact that some of the exciting light is absorbed by the film and for the fact that the energy is seeming not coming from the TPP film. A possible explanation is that the fluorescence of TPP only appears uninterrupted as only the closest layers are being quenched whilst the layer furthest away is left to fluoresce.

6.3.7 Bare silicon emission

Silicon wafers can be studied in terms of their fluorescence emission. The emission of light occurs from silicon when pairs of electrons and holes recombine. It therefore stands to reason that an increase in the number of electron hole pairs generated from light absorbed should lead to an increase in the fluorescence intensity relative to an unmodified sample. Such an increase would be brought about if, for example, a sensitizer was applied to the surface. Likewise, if radiative recombination was prevented, especially at the surface where fluorescence is most visible, a lower fluorescence would be observed.

A bare piece of silicon shows a broad spectrum with a peak at 1130nm, the spectrum is wider on the blue side than it is on the red side. Excitation with multiple wavelengths reveals no difference in the shape of the spectra. This is shown in Figure 6.20.

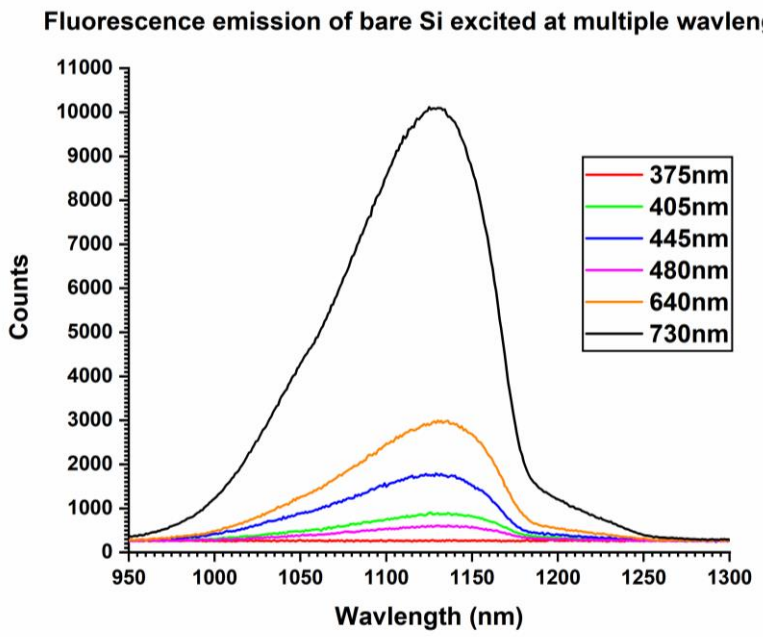

Figure 6.20: Fluorescence spectrum of silicon excited with multiple wavelengths of light measured from 900-1300nm.

As the wavelengths are increased the intensity of fluorescence also increases. There is no difference in the shape of the spectra.

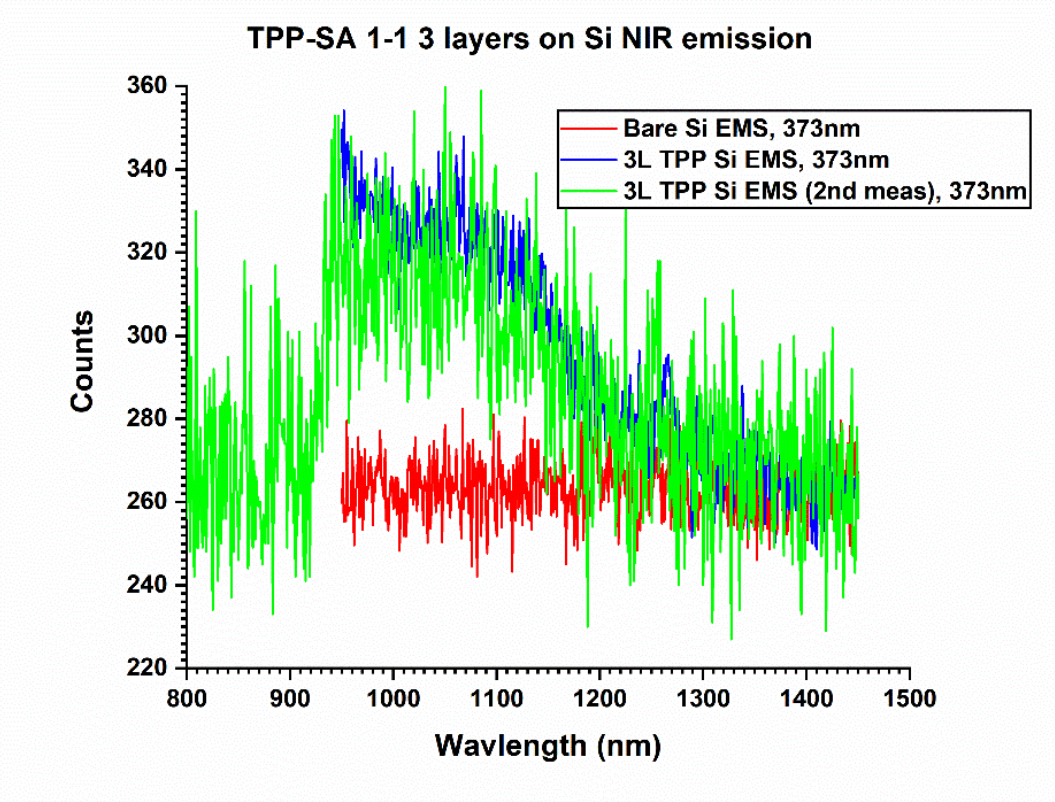

Figure 6.21: Fluorescence of a silicon wafer coated with three LB monolayers of 1-TPP-Stearic acid excited at 375nm and fluorescence from a bare un-coated silicon sample.

Excitation of the silicon at 375nm shows a low number of counts, with the TPP added some fluorescence is visible in both samples showing the enhancement of silicon fluorescence.

The lifetimes were also investigated and fitted. Bare silicon wafer and AlOx coated silicon wafer is shown first in Figure 6.22 and Figure 6.23.

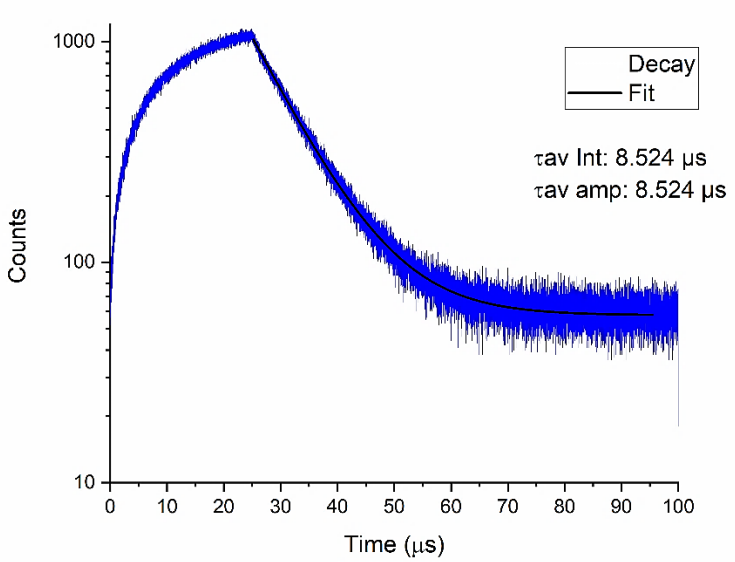

Figure 6.22: Single exponential decay of AlOx passivated silicon wafer excited at 635nm and detected at 1135nm, ± 3% error gives ±0.256 µs

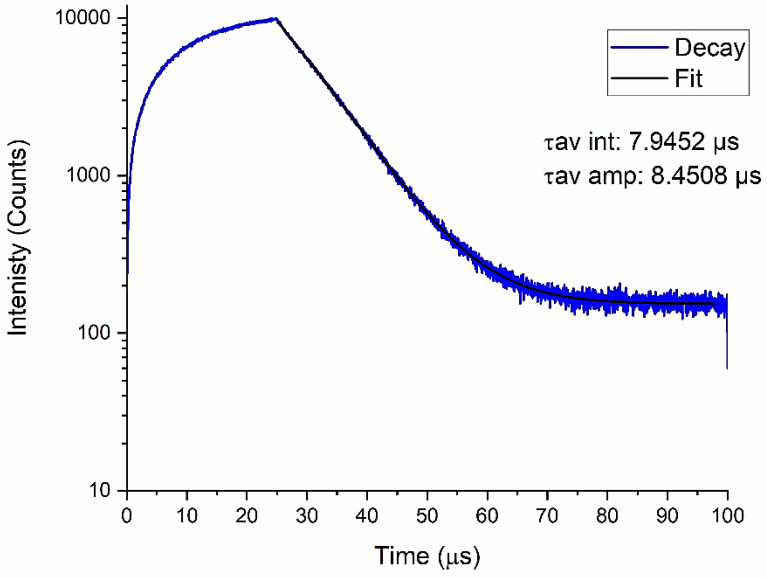

Figure 6.23: AlOx Coated silicon wafer excited at 730nm and measured at 1135nm. ± 3% error gives ±0.2535 µs

Regular fitting with an exponential tailfit gives the silicon wafer and silicon wafer coated with aluminium oxide a lifetime of around 8 nanoseconds.

6.3.8 TPP on silicon steady state characterization using Si Fluorescence.

A piece of silicon was prepared for us by a collaborator using a passivation method of etching the silicon oxide from the surface and adding a coating of aluminium oxide. This prevents recombination at the surface of the silicon sample.[159]

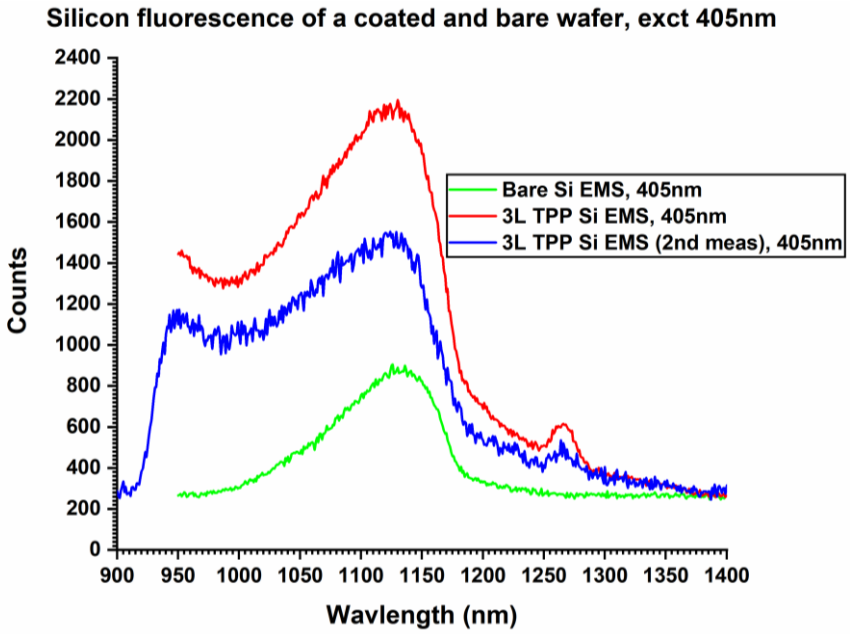

Figure 6.24: Fluorescence from Silicon excited at 405nm, A bare silicon sample and a sample of silicon coated with three 1-1 TPP-SA monolayers measured from 900-1400nm are shown.

This graph in Figure 6.24 shows an increase in the fluorescence at 1150nm in comparison to the bare silicon, this fluorescence is coming from the silicon. This is taken as evidence that there is some sensitization of the passivated silicon occurring.

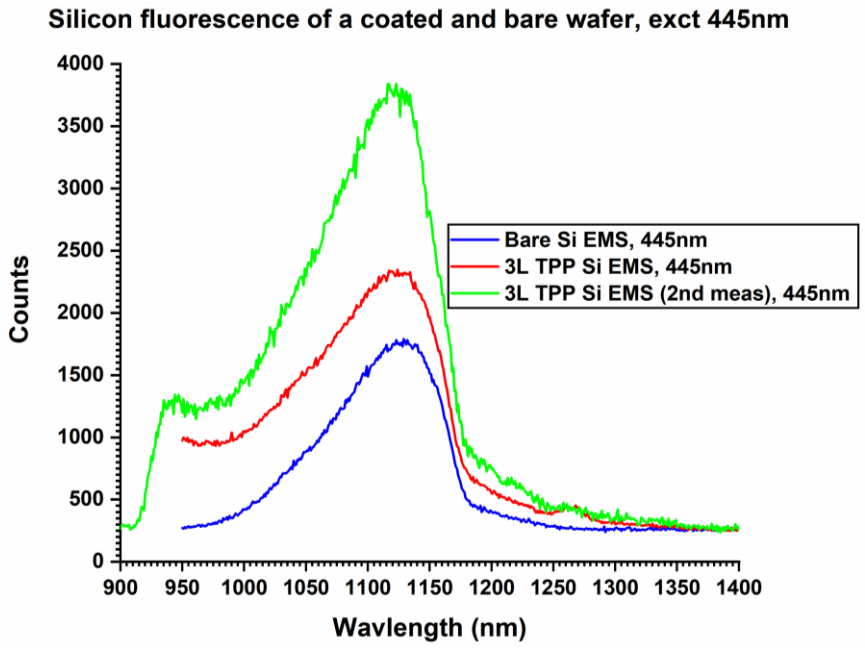

Figure 6.25: Fluorescence from silicon excited at 445nm. A bare silicon sample and a sample of silicon coated with three 1-1 TPP-SA monolayers measured from 900-1400nm are shown.

Figure 6.25 shows the fluorescence of the silicon has been enhanced, however measuring the same sample twice has produced two dramatically different results. This suggests that there is some change in the film between the measurements, it is possible that the film has bleached as a result of the measurement or that in shifting to a new area a less populous part of the film was analysed. This suggests that whilst there has been some energy transfer, there was enough energy left over in the film for fluorescence as well meaning there was likely not much.

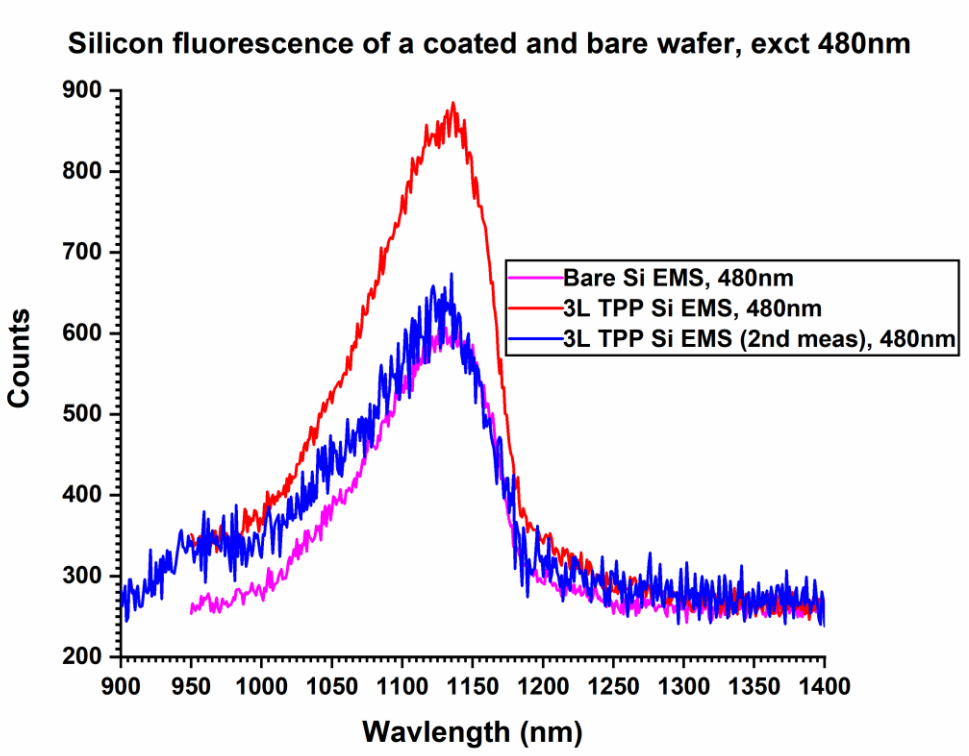

Figure 6.26: Fluorescence from silicon excited at 480nm. A bare silicon sample and a sample of silicon coated with three 1-1 TPP-SA monolayers measured from 900-1400nm are shown.

Figure 6.26 shows different results, there is no increase in the fluorescence in the second measurement compared to the bare silicon, however there was a significant increase in the first measurement, this throws the results into doubt, there are a few possible explanations. The film may have deposited unevenly, and the laser may be hitting a spot with a higher quality film and therefore with more TPP.

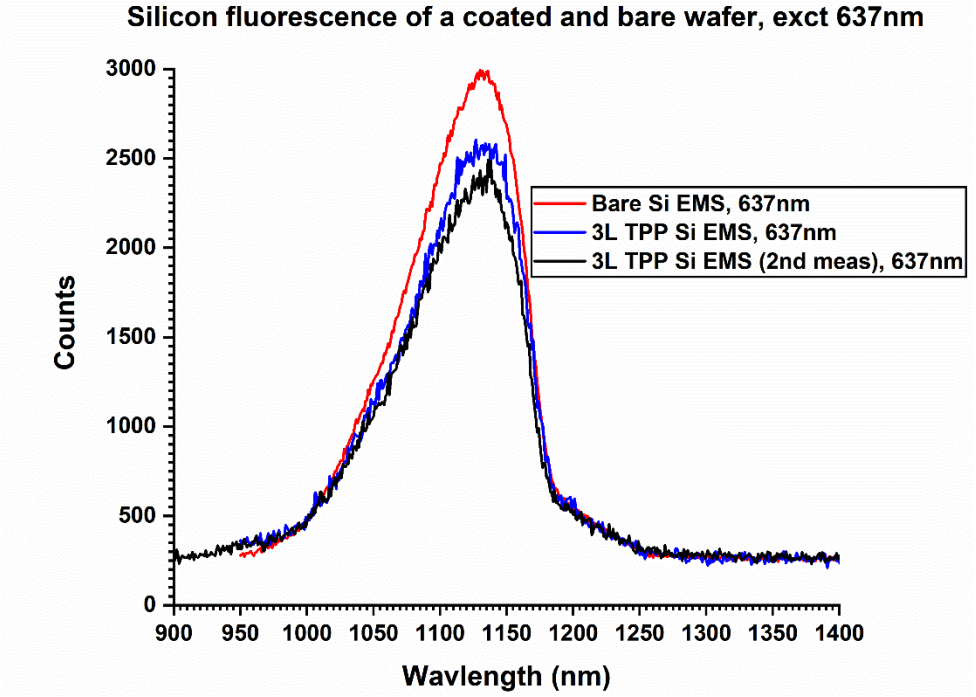

Figure 6.27: Fluorescence from silicon excited at 635nm. A bare silicon sample and a sample of silicon coated with three 1-1 TPP-SA monolayers measured from 900-1400nm are shown.

Figure 6.27 the film excited at 635nm now shows no discernible increase and in fact shows a marked decrease in the fluorescence of the silicon. When excited at this wavelength TPP samples will produce fluorescence but will fluoresce at a much lower intensity when excited at this wavelength. The film is absorbing, which is shown by a lower fluorescence from the silicon as excitation light has been absorbed by the film as opposed to the silicon.

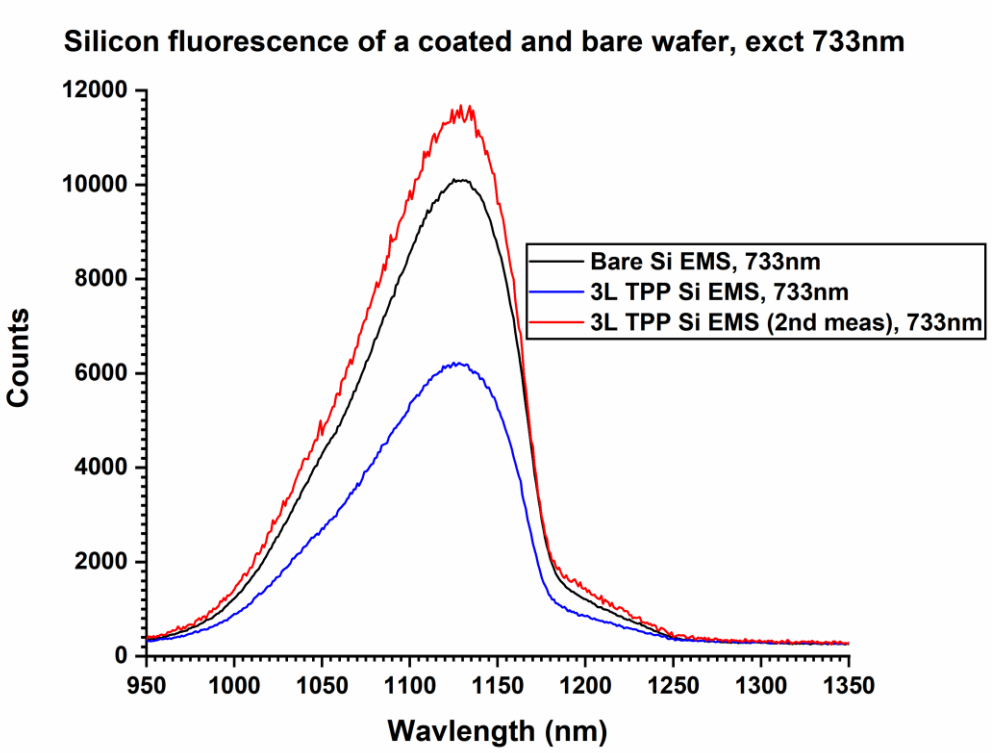

Figure 6.28: Fluorescence from silicon excited at 735nm. A bare silicon sample and a sample of silicon coated with three 1-1 TPP-SA monolayers measured from 900-1400nm are shown.

Figure 6.28 shows the same sample excited at 735nm, a similar phenomenon is shown to Figure 6.27 whereby no enhancement is shown. This suggests that whilst TPP fluorescence is not dependent on the excitation wavelength, exciting the samples at a lower wavelength than the 405nm and 445 excites the regions of the absorption spectrum where TPP is most highly absorptive. This therefore produces a much stronger fluorescence response and much more energy that can be transferred to the silicon wafer. Whereas at higher wavelengths there is far less energy to transfer, and it therefore does not create an improvement in the fluorescence of silicon.

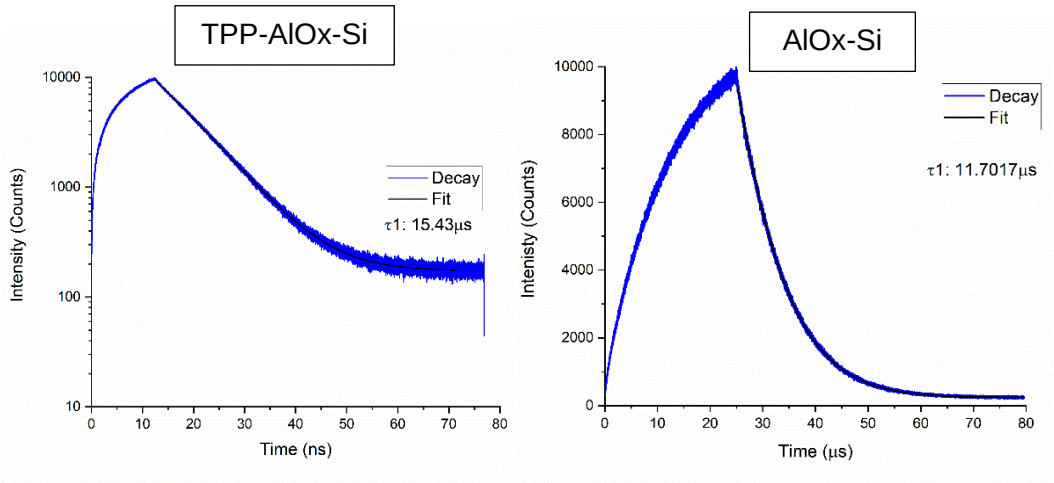

Figure 6.29: Fluorescence decay of the Silicon from a blank silicon sample with aluminium oxide passivation (right) and a sample of silicon coated with 3-layer TPP monolayer LB films (left) excited at 735nm and detected at 1135nm. ± 3% error gives ±0.46 μs and ±0.3511 μs

Figure 6.29 shows the increase in lifetime of the silicon wafer when it is coated with TPP showing further evidence of sensitization.

6.4 Conclusions

The porphyrin solution showed a fluorescence and absorption spectra that is consistent with porphyrins in solution. Absorption was shown to have a single sharp peak at 420nm and several smaller peaks at higher wavelengths. The solution exhibited fluorescence dependent upon the excitation wavelength. With excitation at 405nm producing a single peak of fluorescence and excitation at 445nm producing two peaks. The tetraphenyl porphyrin did not form a Langmuir film on it's own. Factors including the spreading method chosen and the fact the TPP was unmodified played a role in the poor film forming. TPP was mixed with stearic acid in numerus ratios. The ratio of 1-1 was chosen. It was shown that there was little difference between the ratio and the pure film indicating that there was formation of aggregates occurring both with and without the addition of stearic acid. The addition of stearic acid is known to cause aggregation.

The objective was to measure quenching in terms of the fluorescence of the donor and the acceptor. Quenching of the donor signified by the reduction of the steady state fluorescence intensity and reduction of the fluorescence lifetime. Enhancement of the acceptor was signified by the opposite, an increase in the fluorescence intensity and lifetime.

When deposited onto glass the porphyrin showed an absorption spectra that was an similar to the solution spectra. This shows that there is a shift in the state of the porphyrins during deposition, showing they are highly state-dependent. The fluorescence spectra of the solid samples show only the two-peak state no matter the excitation wavelengths showing the excitation. It shows good agreement with literature absorption spectra of the 1-1 Langmuir films of TPP.[100]

The porphyrin on silicon showed some evidence of energy transfer and some contradictory evidence. The steady state spectra showed some reduction in the porphyrin fluorescence in comparison to the glass sample, and the fluorescence of the silicon wafer was enhanced relative to blank silicon which is indicative of energy transfer to the silicon wafer, additionally the silicon showed an increase in lifetime relative to the un-sensitized silicon wafer which is again indicative of energy transfer to the silicon wafer. However, the lifetime of the Tetraphenylporphyrin fluorescence did not show a decrease and even increased compared to the glass samples indicating that there was no energy transfer. This indicates that it may be a different mode of energy transfer. Non-radiative energy transfer causes a reduction in fluorescence because occurs instead of fluorescence. Alternately the TPP may have fluoresced first, and the silicon absorbed the light from the TPP. This is an overall positive result however it is not as conclusive as the evidence shown for silicon sensitization in previous chapters and therefore requires further work.

7. Conclusions

7.1 Light harvesting using cyanine dyes

This work is intended to demonstrate light harvesting behaviour within an organic monolayer using two off the shelf carbocyanine dyes and a donor-acceptor pair one of which has been shown to transfer energy to silicon wafer.[73] Ratios of donor to acceptor varied from 1-1 to 100-1 were tested. Energy transfer was shown at every ratio and the efficiency of the energy transfer was calculated primarily using the observed reduction in the donor lifetime decay. The ratio of 100-1 showed higher energy transfer in comparison to the ratios at 50-1 and 75-1. The importance of this should be stated as it means an excited state could travel through up to 100 donor molecules before reaching an acceptor. This shows a strong basis for use of these dyes in a light harvesting system.

There are two more dyes from the same series as DiO and DiI. DiD and DiR. Preliminary results show that these dyes will from Langmuir films as well. This opens up possibilities to cover much more of the visible spectrum with dyes which will act in a donor acceptor quartet, funnelling energy towards the surface of silicon. Further tests on the efficiency of energy transfer parings and silicon sensitization of these dyes should be investigated. Additionally, the survivability of these dyes in real world conditions should be determined.

7.2 Ruthenium and Rhenium sensitization of silicon wafers

In order to demonstrate highly efficient sensitization of silicon wafers, rhenium and ruthenium complexes (ReC18 and RuC18) were synthesized and deposited as pure monolayers on silicon wafers, the distance from the silicon wafer was controlled by the addition of stearic acid layers underneath the ReC18 and RuC18 complexes. Energy transfer to the silicon wafer is evidenced by the reduction in the triplet excited state lifetime of the complexes. Bringing the complexes closer to the silicon shows a higher energy transfer efficiency. This shows these complexes to be good candidates for being final energy trap molecules in a light harvesting structure.

Further avenues of investigation are opened up. Experimenting with other transition metal complexes for the purposes of sensitization using the same method in order to cover more of the spectrum and potentially find a better sensitizer should be undertaken, additionally mixed films of sensitizer could be experimented with.

Additionally, a move away from quenching experiments should be made towards direct characterization of the silicon wafer with applied layer in order to observe the effect on the generation of electron hole pairs. Silicon passivation in conjunction with sensitizers in order to directly study the silicon emission and therefore quantify the level of sensitization may achieve this. In addition, moving from the research stage to the practical stage is important to consider and therefore research into direct attachment of sensitizers onto silicon with these organometallic complexes should be undertaken.

7.3 Porphyrin silicon sensitization

Silicon was prepared in the same way as the previous chapter and by etching and passivation with aluminium oxide. Films of Tetraphenylporphyrin in a molecular ratio of 1-1 with stearic acid were deposited on the silicon. The silicon fluorescence was studied in conjunction with the fluorescence from the Tetraphenyl porphyrin film in order to determine if any reductions in fluorescence from the film were due to the transfer of energy. Increases in the emission intensity of the silicon showed some indication of energy transfer. However, this was offset by the lack of a decrease in excited state lifetime from the porphyrin film.

Future work would expand this to more porphyrins as well as looking at insertions of metals into the porphyrins that make up these films

7.4 Summation

In summary this thesis attempted to demonstrate potential improvements that could be made to silicon wafers in order to greatly enhance their light absorbing capability and reduce the amount of silicon needed to effectively absorb light to create a solar cell. These improvements are informed by the light harvesting occurring in photosynthesis and the theory they have inspired. To summarize these achievements the figure of a sensitized solar cell from chapter 1 is shown.

Carbocyanine Dye Research

- Energy transfer between a donor and acceptor.
- Diffusion to reach an acceptor.

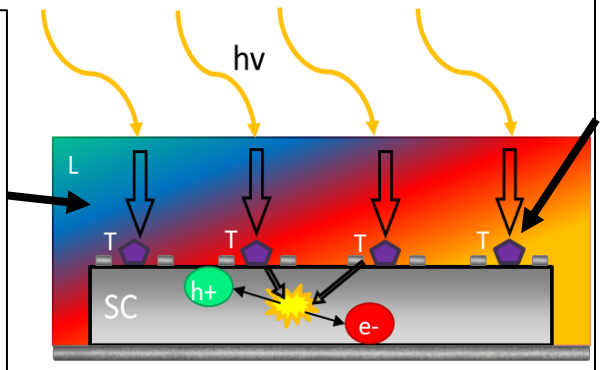

Organometallic and Porphyrin Research

- Energy transfer of triplet rhenium complex to semiconductor.
- Energy transfer of ruthenium complex to semiconductor.
- Potential energy transfer of TPP, a known light harvester.

Figure 7.1: A thin silicon solar cell with an organic absorbing layer and trap molecules applied.

The cyanine dyes showed energy transfer from a donor to an acceptor and diffusion through a collection of donors to reach an acceptor, this fulfils the organic light harvesting component. The efficient energy transfer from the rhenium complex fulfils the role of an efficient trap molecule to pass energy to the silicon non-radiatively. Rhenium and Ruthenium also showed energy transfer up to 90% and 60% efficiency showing that this metal may be used as a sensitiser in a different manner which increases efficiency, additionally there was evidence that a TPP monolayer stabilized with stearic acid sensitizes silicon wafer when paired with aluminium oxide passivation. The TPP work additionally elucidated a secondary method of detecting sensitization.

7.5 Future work

In order to carry on this work, the next stages would be to continue what was experimented with during the porphyrin work. Additions of dyes to a light harvesting layer to expand it to the entire spectrum and finding the optimal distance of the layer to the silicon should also be undertaken. Additionally, the use of ultrathin silicon and silicon on insulator and characterization of the silicon fluorescence using steady state emission spectra and time resolved spectroscopy should be undertaken in order to prove the concept of thin film silicon wafer.

An additional method of detecting sensitization could be excitation spectroscopy of the sensitized silicon wafer. This would confirm the sensitization of silicon by showing the absorption of the dyes through the fluorescence of the silicon. Finally finding a link

between the light harvesting layer and the trap molecules in order to make a fully functional light harvesting structure.

8. Bibliography

1 IEA, *Global Energy Review 2021*, 2021.

2 D. L. Dexter, *J Lumin*, 1979, **18–19**, 779–784.

3 IPCC, *Climate change widespread, rapid, and intensifying*, 2022.

4 C. Honsberg and S. Bowden, PV Education, http://pveducation.org.

5 T. Markvart, *Solar Electricity*, Wiley, Chichester, 2nd edn., 2000.

6 M. V. Dambhare, B. Butey and S. V. Moharil, *J Phys Conf Ser*, 2021, **1913**, 1–16.

7 J. Peng, L. Lu and H. Yang, *Renewable and Sustainable Energy Reviews*, 2013, **19**, 255–274.

8 M. A. Green, Y. Hishikawa, E. D. Dunlop, D. H. Levi, J. Hohl-Ebinger, M. Yoshita and A. W. Y. Ho-Baillie, *Progress in Photovoltaics: Research and Applications*, 2019, **27**, 3–12.

9 M. A. Green, *Third generation photovoltaics: solar cells for 2020 and beyond*, 2002, vol. 14.

10 A. Borisov, *Photosynth Res*, 1989, **58**, 35–58.

11 J. Barber, *Chem Soc Rev*, 2009, **38**, 185–96.

12 R. Blakenship, *Molecular mechanisms of photosynthesis*, Chichester, 2nd edn., 2001.

13 S. I. Allakhverdiev, V. Thavasi, V. D. Kreslavski, S. K. Zharmukhamedov, V. V. Klimov, S. Ramakrishna, D. a. Los, M. Mimuro, H. Nishihara and R. Carpentier, *Journal of Photochemistry and Photobiology C: Photochemistry Reviews*, 2010, **11**, 101–113.

14 X. Li and M. L. Tang, *Chem. Commun.*, 2017, **53**, 4429–4440.

15 V. M. Agranovich, Y. N. Gartstein and M. Litinskaya, *Chem Rev*, 2011, **111**, 5179–5214.

16 B. J. Walker, A. J. Musser, D. Beljonne and R. H. Friend, *Nat Chem*, 2013, **5**, 1019–24.

17 X. Li, A. Fast, Z. Huang, D. A. Fishman and M. L. Tang, 2017, 5598–5602.

18 H. Kouno, T. Ogawa, S. Amemori, P. Mahato, N. Yanai and N. Kimizuka, *Chem. Sci.*, 2016, **7**, 5224–5229.

19 V. Gray, P. Xia, Z. Huang, E. Moses, A. Fast, D. A. Fishman, V. I. Vullev, M. Abrahamsson and K. Moth-, *Chem Sci*, 2017, **8**, 5488–5496.

20 Z. You, C. Hsu, G. R. Fleming, Z. You and G. R. Fleming, *J Chem Phys*, , DOI:10.1063/1.2155433.

21 D. Dexter, R. Knox and M. Stavola, *Phys Rev B*, 1985, **31**, 2277–2289.

22 Y. Y. Cheng, B. Fückel, T. Schulze, R. W. MacQueen, M. J. Y. Tayebjee, A. Danos, T. Khoury, R. G. C. R. Clady, N. J. Ekins-Daukes, M. J. Crossley, B. Stannowski, K. Lips and T. W. Schmidt, in *Organic Photovoltaics XIII*, 2012, vol. 8477, p. 84770X.

23 A. Nattestad, Y. Y. Cheng, R. W. Macqueen, T. F. Schulze, F. W. Thompson, A. J. Mozer, B. Fückel, T. Khoury, M. J. Crossley, K. Lips, G. G. Wallace and T. W. Schmidt, *Journal of Physical Chemistry Letters*, 2013, **4**, 2073–2078.

24 T. Schulze, K. Lips and T. W. Schmidt, *SPIE Newsroom*, 2014, 10–12.

25 R. W. Macqueen, M. Liebhaber, J. Niederhausen, M. Mews, C. Gersmann, S. Jäckle, K. Jäger, M. J. Y. Tayebjee, T. W. Schmidt, B. Rech and K. Lips, *Mater Horiz*, 2018, **5**, 1065–1075.

26 J. Niederhausen, R. W. MacQueen, E. Özkol, C. Gersmann, M. H. Futscher, M. Liebhaber, D. Friedrich, M. Borgwardt, K. A. Mazzio, P. Amsalem, M. H. Nguyen, B. Daiber, M. Mews, J. Rappich, F. Ruske, R. Eichberger and K. Lips, *Journal of Physical Chemistry C*, 2020, **124**, 27867–27881.

27 J. C. Phys, B. Naydenov, K. Lips, E. Unger and W. Rowan, , DOI:10.1063/5.0026564.

28 T. Hayashi, T. G. Castner and R. W. Boyd, *Chem Phys Lett*, 1983, **94**, 461–466.

29 P. M. Whitmore, A. P. Alivisatos and C. B. Harris, *Phys Rev Lett*, 1983, **50**, 1092–1094.

30 A. P. Alivisatos, M. F. Arndt, S. Efrima, D. H. Waldeck and C. B. Harris, *J Chem Phys*, 1987, **86**, 6540–6549.

31 M. I. Sluch, A. G. Vitukhnovsky and M. C. Petty, *Phys Lett A*, 1995, **200**, 61–64.

32 R. J. Moerland and J. P. Hoogenboom, *Optica*, 2016, **3**, 112–117.

33 W. L. Barnes, *J Mod Opt*, 1998, **45**, 661–699.

34 V. Balzani, A. Credi and M. Venturi, *ChemSusChem*, 2008, **1**, 26–58.

35 W. Peng, S. M. Rupich, N. Shafiq, Y. N. Gartstein and A. V Malko, *Chem Rev*, 2015, **115**, 12764–12796.

36 W. Peng, S. M. Rupich, N. Shafiq, Y. N. Gartstein, A. V. Malko and Y. J. Chabal, *Chem Rev*, 2015, **115**, 12764–12796.

37 A. Yeltik, B. Guzelturk, P. L. Hernandez-Martinez, A. O. Govorov and H. V. Demir, *ACS Nano*, 2013, **7**, 10492–10501.

38 A. Yeltik, B. Guzelturk, P. Ludwig Hernandez-Martinez, S. Akhavan and H. Volkan Demir, *Appl Phys Lett*, 2013, **103**, 261103.

39 M. T. Nimmo, L. M. Caillard, W. De Benedetti, H. M. Nguyen, O. Seitz, Y. N. Gartstein, Y. J. Chabal and A. V Malko, 2013, 3236–3245.

40 H. M. Nguyen, O. Seitz, Yu. N. Gartstein, Y. J. Chabal and A. V. Malko, *Journal of the Optical Society of America B*, 2013, **30**, 2401.

41 H. M. Nguyen, O. Seitz, W. Peng, Y. N. Gartstein, Y. J. Chabal and A. V. Malko, *ACS Nano*, 2012, **6**, 5574–5582.

42 J.-C. G. Bünzli and S. V. Eliseeva, *Journal of Rare Earths*, 2010, **28**, 824–842.

43 K. H. Drexhage, *J Lumin*, 1970, **1–2**, 693–701.

44 H. Morawitz, *Physical Review*, 1969, **187**, 1792–1796.

45 W. H. Weber and C. F. Eagen, *Opt Lett*, 1979, **4**, 236–238.

46 Y. Ishibashi, S. Ohshima and T. Kajiwara, *Surf Sci*, 1988, **201**, 311–320.

47 R. R. Chance, A. Prock and R. Silbey, *J Chem Phys*, 1974, **60**, 2184–2185.

48 R. R. Chance, A. Prock and R. Silbey, *J Chem Phys*, 1974, **60**, 2744–2748.

49 D. Li, X. Hou, W. Bu, L. Wua, J. Gao, X. Zhang and J. Shen, *Materials Science and Engineering C*, 2001, **18**, 205–209.

50 V. W.-W. Yam, K.-Z. Wang, C.-R. Wang, Y. Yang and K.-K. Cheung, *Organometallics*, 1998, **17**, 2440–2446.

51 J. Zhang, B. W. Chu, N. Zhu and V. W. Yam, *Organometallics*, 2007, **26**, 5423–5429.

52 D. L. Hwi, K. O. Sang, S. C. Chan and K. Y. Kay, *Eur J Inorg Chem*, 2007, 503–508.

53 Y. Joo, J. W. Spalenka, K. M. McElhinny, S. K. Schmitt, P. G. Evans and P. Gopalan, *Langmuir*, 2014, **30**, 6104–6113.

54 V. Fernández-Moreira, F. L. Thorp-Greenwood, A. J. Amoroso, J. Cable, J. B. Court, V. Gray, A. J. Hayes, R. L. Jenkins, B. M. Kariuki, D. Lloyd, C. O. Millet, C. Ff. Williams and M. P. Coogan, *Org Biomol Chem*, 2010, **8**, 3888.

55 M. Wrighton and D. L. Morse, *J Am Chem Soc*, 1974, **96**, 998–1003.

56 J. Zhang, B. W. K. Chu, N. Zhu and V. W. W. Yam, *Organometallics*, 2007, **26**, 5423–5429.

57 M. J. Li, X. Liu, M. J. Nie, Z. Z. Wu, C. Q. Yi, G. N. Chen and V. W. W. Yam, *Organometallics*, 2012, **31**, 4459–4466.

58 V. W. Yam, Y. Yang, H. Yang and K. Cheung, *Organometallics*, 1999, **18**, 5252–5258.

59 B. J. Coe, S. P. Foxon, R. A. Pilkington, S. Sánchez, D. Whittaker, K. Clays, N. Van Steerteghem and B. S. Brunschwig, *Organometallics*, 2016, **35**, 3014–3024.

60 M. Rajkumar, J. Bhuvaneswari, M. Velayudham, E. Rajkumar and S. Rajagopal, *J Fluoresc*, 2011, **21**, 1729–1737.

61 M. P. Coogan, V. Fernández-Moreira, J. B. Hess, S. J. A. Pope and C. Williams, *New Journal of Chemistry*, 2009, **33**, 1094.

62 J. Pazinato, D. M. Hoffmeister, K. P. Naidek, E. Westphal, H. Gallardo and H. Winnischofer, *Electrochim Acta*, 2015, **153**, 574–582.

63 B. O'Regan and M. Grätzel, *Nature*, 1991, **353**, 737–740.

64 A. Lanzilotto, L. a. Büldt, H. C. Schmidt, A. Prescimone, O. S. Wenger, E. C. Constable and C. E. Housecroft, *RSC Adv.*, 2016, **6**, 15370–15381.

65 F. Odobel, D. Massiot, B. S. Harrison and K. S. Schanze, *Langmuir*, 2003, **19**, 30–39.

66 K. Okamoto, M. Taniguchi, M. Takahashi and A. Yamagishi, *Langmuir*, 2001, **17**, 195–201.

67 K. Okamoto, M. Taniguchi, M. Takahashi and A. Yamagishi, 2001, 195–201.

68 L. M. Moretto, T. Kohls, D. Badocco, P. Pastore, N. Sojic and P. Ugo, *Journal of Electroanalytical Chemistry*, 2010, **640**, 35–41.

69 K. Wohnrath, C. J. L. Constantino, P. A. Antunes, P. M. Dos Santos, A. A. Batista, R. F. Aroca and O. N. Oliveira, *Journal of Physical Chemistry B*, 2005, **109**, 4959–4964.

70 B. Sandrino, E. C. Wrobel, T. M. Nobre, L. Caseli, S. R. Lazaro, A. C. Júnior, J. R. Garcia, O. N. Oliveira and K. Wohnrath, *Chem Phys Lett*, 2016, **649**, 29–36.

71 S. Yamada, T. Nakano and T. Matsuo, *Thin Solid Films*, 1994, **245**, 196–201.

72 H. Berneth, in *Ullmann's Encyclopedia of Industrial Chemistry*, Wiley, Berlin, 6th edn., 2008, pp. 49–53.

73 L. Danos, R. Greef and T. Markvart, *Thin Solid Films*, 2008, **516**, 7251–7255.

74 G. Biesmans, M. Van Der Auweraer and F. C. De Schryver, *Langmuir*, 1990, **6**, 277–285.

75 L. Fang, N. Alderman, L. Danos and T. Markvart, *Materials Research Innovations*, 2014, **18**, 494–499.

76 S. Chakraborty, P. Debnath, D. Dey, D. Bhattacharjee and S. A. Hussain, *J Photochem Photobiol A Chem*, 2014, **293**, 57–64.

77 S. Chakraborty, D. Bhattacharjee, H. Soda, M. Tominaga, Y. Suzuki, J. Kawamata and S. A. Hussain, *Appl Clay Sci*, 2015, **104**, 245–251.

78 P. Debnath, S. Chakraborty, S. Deb, J. Nath, D. Bhattacharjee and S. A. Hussain, *Journal of Physical Chemistry C*, 2015, **119**, 9429–9441.

79 Fisher scientific, Invitrogen™ Lipophilic Tracer Sampler Kit, Invitrogen™ Lipophilic Tracer Sampler Kit, (accessed 6 February 2022).

80 H. Kuhn, *Pure and Applied Chemistry*, 1965, **11**, 345–358.

81 H. Kuhn, *J Chem Phys*, 1970, **53**, 101–108.

82 H. Kuhn and D. Möbius, *Angewandte Chemie International Edition in English*, 1971, **10**, 620–637.

83 T. Markvart, *Prog Quantum Electron*, 2000, **24**, 107–186.

84 L. Danos and T. Markvart, *Chem Phys Lett*, 2010, **490**, 194–199.

85 F. Meng, K. Chen, H. Tian, L. Zuppiroli and F. Nuesch, *Appl Phys Lett*, 2003, **82**, 3788–3790.

86 N. Sinin, M. Ibrihim, M. Teridi, N. Ludin, S. Sepeai and K. Sopian, *MALAYSIAN JOURNAL OF ANALYTICAL SCIENCES*, 2015, **19**, 1256–1263.

87 H. Grüniger, D. Möbius and H. Meyer, *J Chem Phys*, 1983, **79**, 3701–3710.

88 G. Ma and H. C. Allen, *Langmuir*, 2006, **22**, 5341–5349.

89 R. Mendelsohn and C. R. Flach, *Handbook of Vibrational Spectroscopy*, 2002, 1028–1041.

90 T. Y. Kim and D. J. Ahn, *Materials Science and Engineering C*, 2004, **24**, 205–208.

91 V. V. Prokhorov, S. I. Pozin, D. A. Lypenko, O. M. Perelygina, E. I. Mal'Tsev and A. V. Vannikov, *Chem Phys Lett*, 2012, **535**, 94–99.

92 M. G. Petrova, V. V. Prokhorov, S. I. Pozin, N. N. Kovaleva and E. I. Demikhov, *Bulletin of the Russian Academy of Sciences: Physics*, 2014, **78**, 1362–1366.

93 S. N. Magonov and N. A. Yerina, *Langmuir*, 2003, **19**, 500–504.

94 M. Sakomura, T. Takagi, H. Nakayama, R. Sawada and M. Fujihira, *Colloids Surf A Physicochem Eng Asp*, 2002, **198–200**, 769–775.

95 M. Sakomura, K. Hirabayashi, K. Ueda and M. Fujihira, *Colloids Surf A Physicochem Eng Asp*, 2006, **284–285**, 599–602.

96 J. Hansen, F. Platten, D. Wagner and S. U. Egelhaaf, *Phys. Chem. Chem. Phys.*, 2016, **18**, 10270–10280.

97 Z. Zhang, K. Nakashima, A. L. Verma, M. Yoneyama, K. Iriyama and Y. Ozaki, *Langmuir*, 1998, **14**, 1177–1182.

98 D. M. Togashi, R. I. S. Romão, A. M. Gonçalves da Silva, A. J. F. N. Sobral and S. M. B. Costa, *Physical Chemistry Chemical Physics*, 2005, **7**, 3874.

99 S. Biswas, H. Y. Ahn, M. V. Bondar and K. D. Belfield, *Langmuir*, 2012, **28**, 1515–1522.

100 R. A. Bull and J. E. Bulkowski, *J Colloid Interface Sci*, 1983, **92**, 1–12.

101 H. S. Mansur, N. F. De Sales and A. A. P. Mansur, *Surface and Interface Analysis*, 2011, **43**, 1423–1429.

102 X. Li, W. Xu, T. Itoh, A. Ikehata, B. Zhao, B. Li and Y. Ozaki, *J Colloid Interface Sci*, 2005, **284**, 582–592.

103 S. H. Varghese, Y. Yoshida, T. Maekawa and D. Sakthikumar, *Sensors and Materials*, 2011, **23**, 335–345.

104 M. M. Makhlouf, A. El-Denglawey, H. M. Zeyada and M. M. El-Nahass, *J Lumin*, 2014, **147**, 202–208.

105 M. M. El-Nahass, H. A. Zayed, E. E. Elgarhy and A. M. Hassanien, *Opt Quantum Electron*, 2016, **48**, 1–13.

106 K. Tomita, N. Shioya, R. Kise, T. Shimoaka, H. Yoshida, T. Koganezawa, K. Eda and T. Hasegawa, *Thin Solid Films*, 2018, **665**, 85–90.

107 J. E. Kroeze, R. B. M. Koehorst and T. J. Savenije, *Adv Funct Mater*, 2004, **14**, 992–998.

108 N. Alderman, L. Danos, L. Fang, M. C. Grossel and T. Markvart, *Chemical Communications*, 2017, **53**, 12120–12123.

109 M. Fluorescence, B. Valeur and W. V. G. Isbns, *Molecular fluorescence: principles and applications*, 2001, **8**, 20–33.

110 J. Lakowicz, *Principles of flurescence spectroscopy*, Springer, London, 3rd edn., 2007.

111 N. J. Turro, V. Ramamurthy and J. C. Scaiano, *Principles of molecular Photochemistry: An introduction*, 2015.

112 P. Atkins and J. de Paula, *Physical Chemistry*, Oxford University press, 10th edn., 2018.

113 B. Valeur, in *Molecular Fluorescence: Principles and Applications*, 2001, vol. 8, pp. 20–33.

114 M. L. T. Cossio, L. F. Giesen, G. Araya, M. L. S. Pérez-Cotapos, R. L. VERGARA, M. Manca, R. A. Tohme, S. D. Holmberg, T. Bressmann, D. R. Lirio, J. S. Román, R. G. Solís, S. Thakur, S. N. Rao, E. L. Modelado, A. D. E. La, C. Durante, U. N. A. Tradición, M. En, E. L. Espejo, D. E. L. A. S. Fuentes, U. A. De Yucatán, C. M. Lenin, L. F. Cian, M. J. Douglas, L. Plata and F. Héritier, *Semiconductors : bonds and bands*, 2012, vol. XXXIII.

115 A. Eisfeld and J. S. Briggs, *Chem Phys*, 2006, **324**, 376–384.

116 N. Transitions, E. States, T. Perrin, B. Valeur and M. N. Berberan-Santos, *Characteristics of Fluorescence Emission*, 2012, vol. 0.

117 I. Langmuir, *Proc Natl Acad Sci U S A*, 1917, **3**, 251–257.

118 K. B. Blodgett, *J Am Chem Soc*, 1934, **56**, 495–495.

119 F. Benjamin, B. William and Farish, *Philosophical Transactions of the Royal Society*, 1774, **64**, 445–460.

120 NimaTechnology, *Langmuir Blodgett Troughs, Operating Manual Sixth Edition*, 2004.

121 A. Pockels, *Nature*, 1891, **43**, 437–439.

122 I. Langmuir, *J Am Chem Soc*, 1917, **39**, 1848–1906.

123 I. Langmuir, *Proc Natl Acad Sci U S A*, 1917, **3**, 251–257.

124 K. B. Blodgett, *J Am Chem Soc*, 1935, **57**, 1007–1022.

125 K. B. Blodgett, *J Am Chem Soc*, 1934, **56**, 495–495.

126 J. E. Greene, *Appl Phys Rev*, 2015, **2**, 011101.

127 M. C. Petty, *Langmuir Blodgett Films: An Introduction*, Cambridge University Press, Cambridge, 1st edn., 1996.

128 G. Roberts, *Langmuir-Blodgett Films*, Plenum Press, Ney York, 1990.

129 W. Kern, *J Electrochem Soc*, 1990, **137**, 1887–1892.

130 F. W. Vergeer, X. Chen, F. Lafolet, L. De Cola, H. Fuchs and L. Chi, *Adv Funct Mater*, 2006, **16**, 625–632.

131 W. Kern and D. Puotinen, *RCA Review*, 1970, **31**, 187–206.

132 NimaTechnology, *Langmuir Blodgett Troughs, Operating Manual Sixth Edition*, 2004.

133 M. C. Petty, *Langmuir Blodgett Films: An Introduction*, Cambridge University Press, Cambridge, 1st edn., 1996.

134 C. Honsberg and S. Bowden, Optical Properties of Silicon, https://www.pveducation.org/pvcdrom/materials/optical-properties-of-silicon, (accessed 3 December 2021).

135 J. R. Lakowicz, *Principles of fluorecence spectroscopy*, Springer US, New Jersey, Third., 2006.

136 Pico quant, Micro Time 200/Pico Quant, https://www.picoquant.com/products/category/fluorescence-microscopes/microtime-200-time-resolved-confocal-fluorescence-microscope-with-unique-single-molecule-sensitivity, (accessed 7 November 2021).

137 Keysight Technologies, *Keysight 5500 Scanning Probe Microscope, User's Guide*, Keysight Technologies, Santa Rosa, USA, 1st edn., 2014.

138 Avogadro, https://avogadro.cc/, (accessed 6 February 2022).

139 S. A. Hussain, D. Dey, S. Chakraborty and D. Bhattacharjee, *J Lumin*, 2011, **131**, 1655–1660.

140 Wing Wah Yam, Vivian Choryue Lau, Victor Wang, Kezhi Cheung, Kungkai Huang and Chunhui, *J Mater Chem*, 1998, **8**, 89–97.

141 V. W.-W. Yam, B. Li, Y. Yang, B. W.-K. Chu, K. M.-C. Wong and K.-K. Cheung, *Eur J Inorg Chem*, 2003, **2003**, 4035–4042.

142 A. L. Moore, B. Twamley, C. L. Barnes and P. D. Benny, 2011, 4686–4688.

143 H. Tamura, N. Ikeda, T. Iguro, T. Ohno and G.-E. Matsubayashi, *Acta Crystallographica Section C*, 1996, **52**, 1394–1399.

144 J. Kawamata, H. Yamaki, R. Ohshige, R. Seike, S. Tani, Y. Ogata and A. Yamagishi, *Colloids Surf A Physicochem Eng Asp*, 2008, **321**, 65–69.

145 C. W. Tse, L. S. M. Lam, K. Y. K. Man, W. T. Wong and W. K. Chan, *J Polym Sci A Polym Chem*, 2005, **43**, 1292–1308.

146 A. J. Amoroso, M. P. Coogan, J. E. Dunne, V. Fernández-Moreira, J. B. Hess, A. J. Hayes, D. Lloyd, C. Millet, S. J. A. Pope and C. Williams, *Chem. Commun.*, 2007, 3066–3068.

147 N. Fukuda, M. Mitsuishi, A. Aoki and T. Miyashita, *J Phys Chem B*, 2002, **106**, 7048–7052.

148 T. Taniguchi, Y. Fukasawa and T. Miyashita, *Journal of Physical Chemistry B*, 1999, **103**, 1920–1924.

149 H. Sakaguchi, T. Nagamura and T. Matsuo, *Jpn J Appl Phys*, 1991, **30**, 377–379.

150 T. Fushimi, A. Oda, H. Ohkita and S. Ito, *Journal of Physical Chemistry B*, 2004, **108**, 18897–18902.

151 J. Chen, M. Mitsuishi, A. Aoki and T. Miyashita, *Chem Commun (Camb)*, 2002, 2856–2857.

152 F. E. Lytle and D. M. Hercules, *J Am Chem Soc*, 1969, **91**, 253–257.

153 F. C. M. Leung, A. Y. Y. Tam, V. K. M. Au, M. J. Li and V. W. W. Yam, *ACS Appl Mater Interfaces*, 2014, **6**, 6644–6653.

154 B. Valeur, *Molecular Fluorescence: Principles and Applications*, 2001, **8**, 247–272.

155 M. M. El-Nahass, H. M. Zeyada, M. S. Aziz and M. M. Makhlouf, *Spectrochim Acta A Mol Biomol Spectrosc*, 2005, **62**, 11–15.

156 R. Paolesse, L. Valli, C. Goletti, C. Di Natale, A. Froiio, A. Macagnano, G. Bussetti, P. Chiaradia and A. D'Amico, *Materials Science and Engineering C*, 2002, **22**, 219–225.

157 Y. Rong, P. Chen, D. Wang and M. Liu, *Langmuir*, 2012, **28**, 6356–6363.

158 C. P. Ponce, H. Y. Araghi, N. K. Joshi, R. P. Steer and M. F. Paige, *Langmuir*, 2015, **31**, 13590–13599.

159 T. Markvart and L. Castañer, *Semiconductor Materials and Modeling*, Elsevier Ltd, 2018.

9. Appendix

Included here are some examples of work which may be relevant including extra microscopy images, examples of Langmuir Blodgett deposition and work which did not fit in to the final chapters.

9.1 Examples of deposition

9.1.1 Example of stearic acid deposition

Figure 9.1: 2 layers of stearic acid deposited as a capping layer. The transfer ratio shown was calculated to be 1, showing excellent deposition.

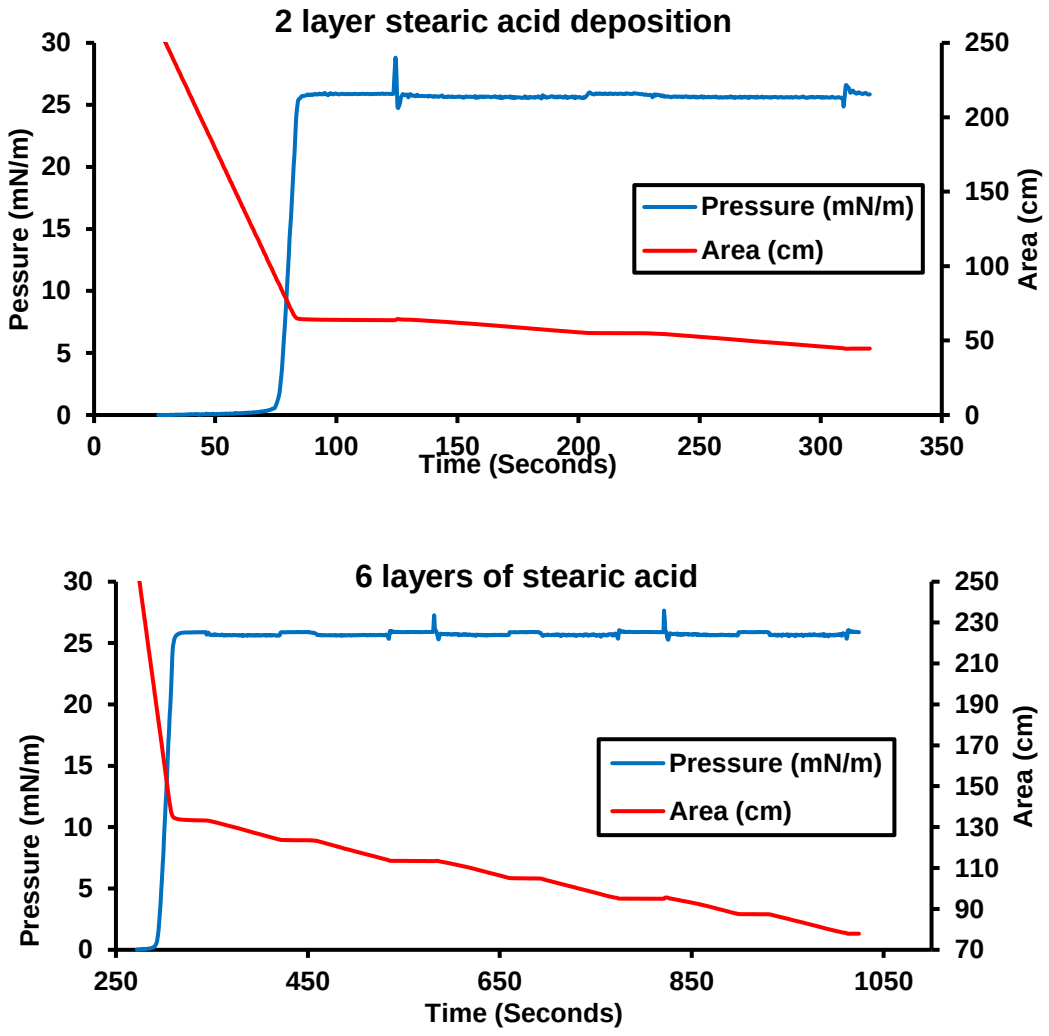

Figure 9.2: Six layers of stearic acid deposited on a glass slide one after the other, the average transfer ratio was calculated to be 1.

9.1.2 Examples of Cyanine dye deposition

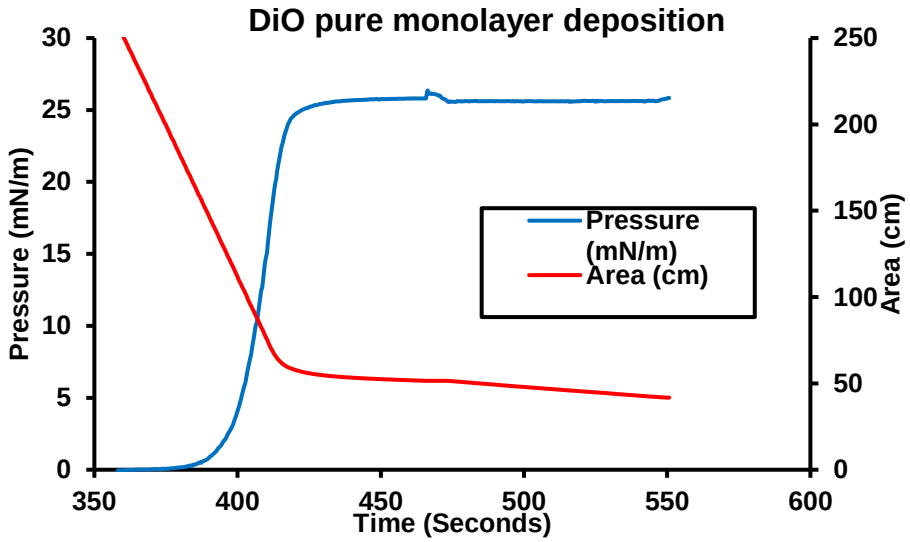

Figure 9.3: A single layer of pure DiO deposited on a glass slide with a calculated transfer ratio of 1 showing excellent deposition of the pure dye.

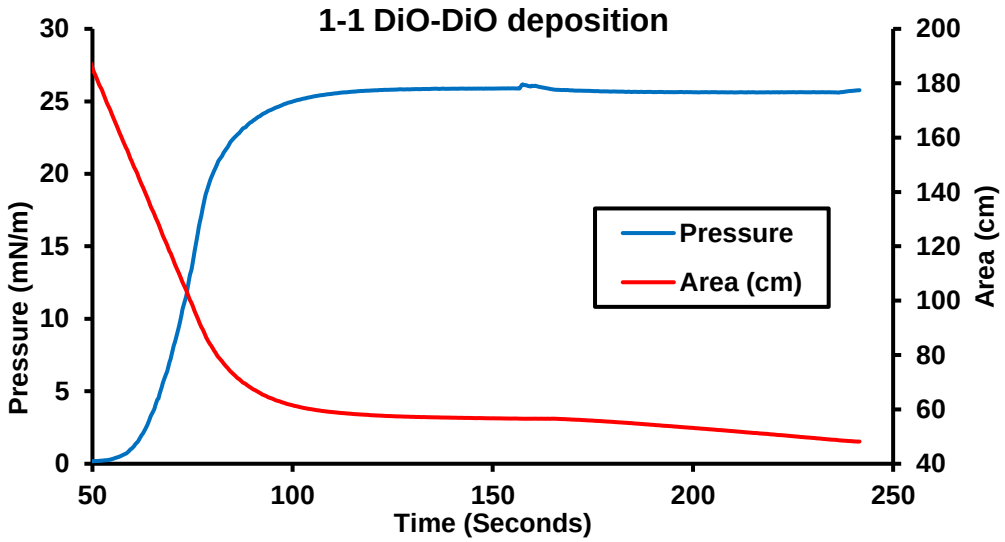

Figure 9.4: A single layer of Mixed DiO-DiI in a 1-1 ratio deposited on a glass slide with a calculated transfer ratio of 1 showing excellent deposition of the mixed dye.

9.1.3 Example of Ruthenium deposition

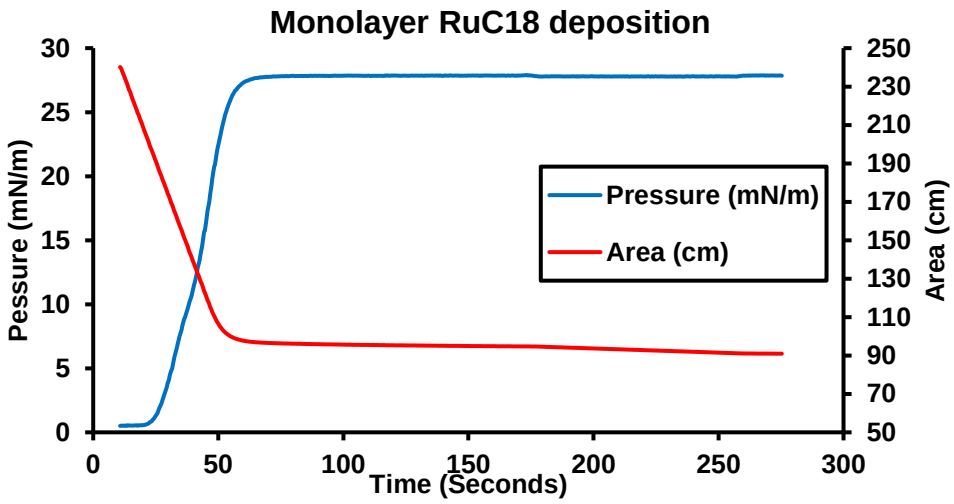

Figure 9.5: A single layer of RuC18 deposited on a glass slide as a pure monolayer with a calculated transfer ratio of 0.96, very close to 1, showing excellent deposition of the complex.

9.2 Cyanine dyes

9.2.1 FLIM-FRET images of mixed monolayer samples

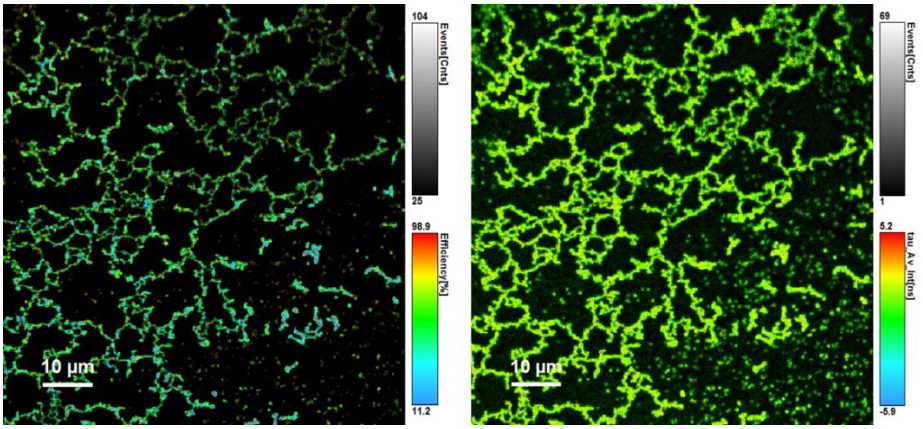

Figure 9.6: 1-1, 485nm, FLIM-FRET on quartz glass

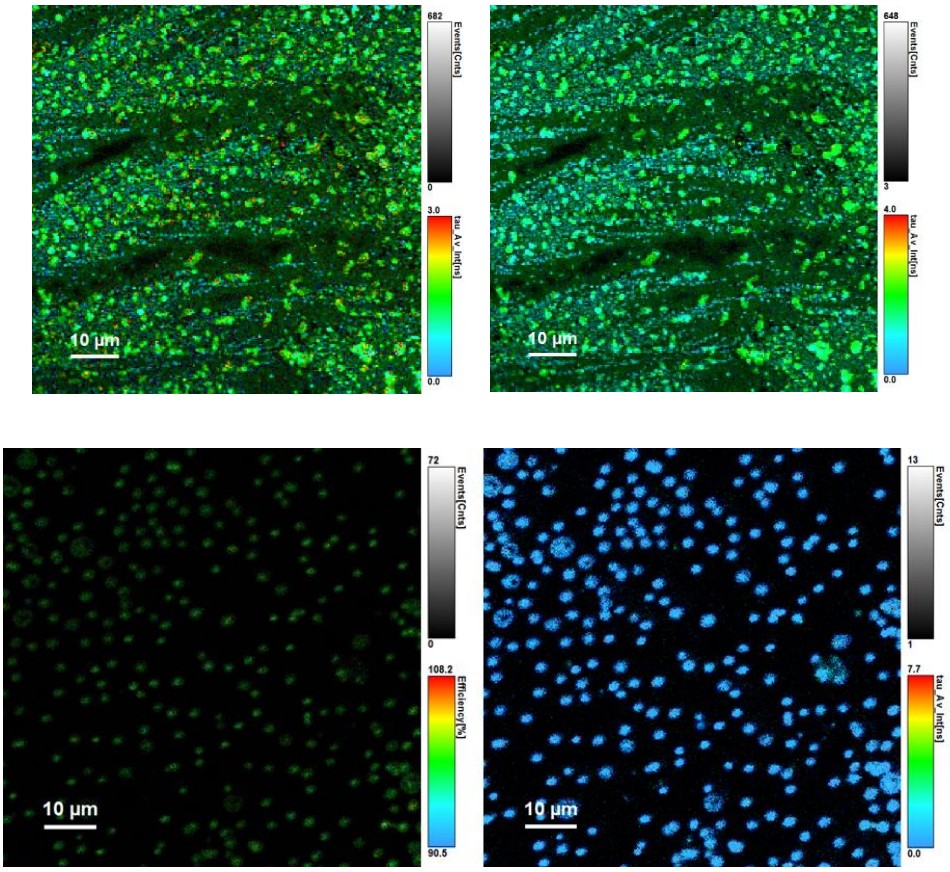

Figure 9.7: 1-1, 485nm FLIM on quartz glass

Figure 9.8: 10-1, 485nm, FLIM-FRET on quartz glass

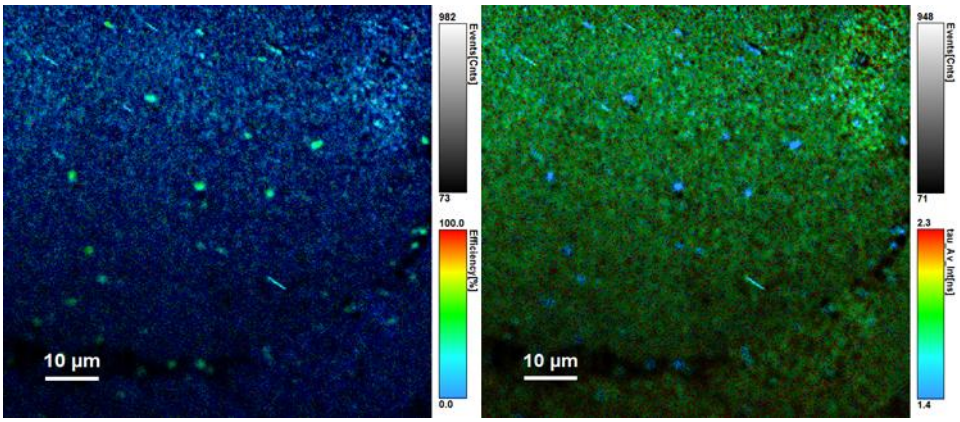

Figure 9.9: 25-1, 405nm, FLIM-FRET on quartz glass

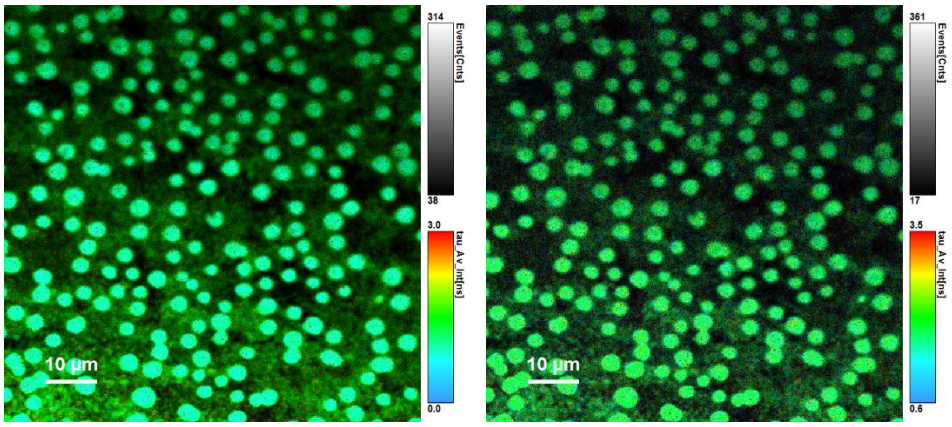

Figure 9.10: 50-1, 485nm FLIM on quartz glass

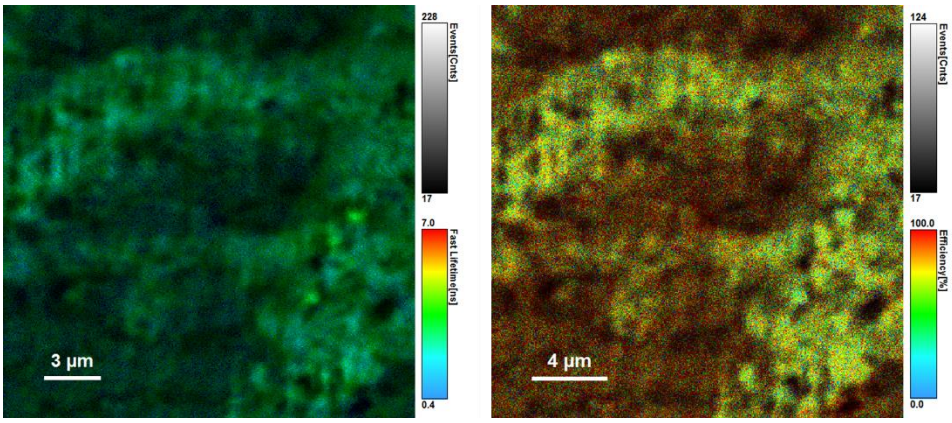

Figure 9.11: 50-1, 485nm, FLIM-FRET on quartz glass

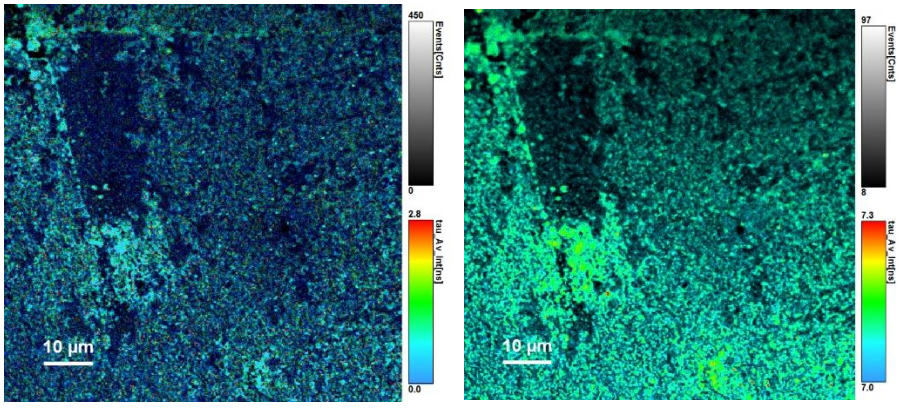

Figure 9.12: 75-1, 485nm on quartz glass

Figure 9.13: 75-1, 485nm, FLIM-FRET on quartz glass

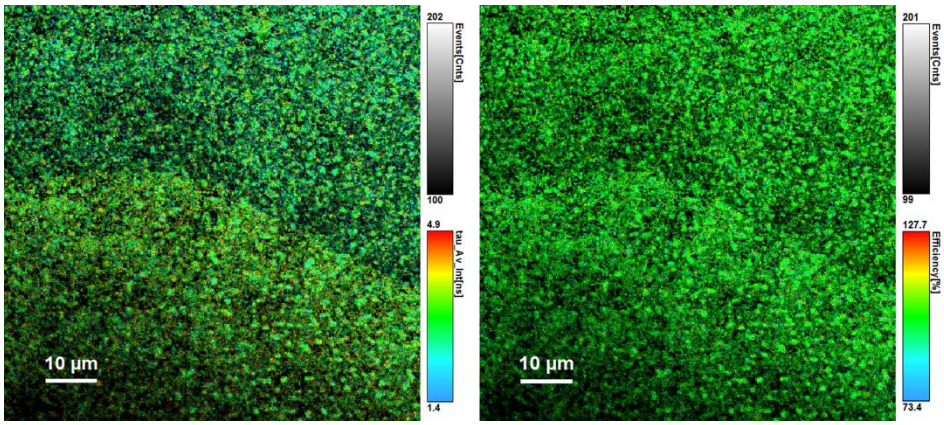

Figure 9.14: 100-1, 485nm FLIM on quartz glass

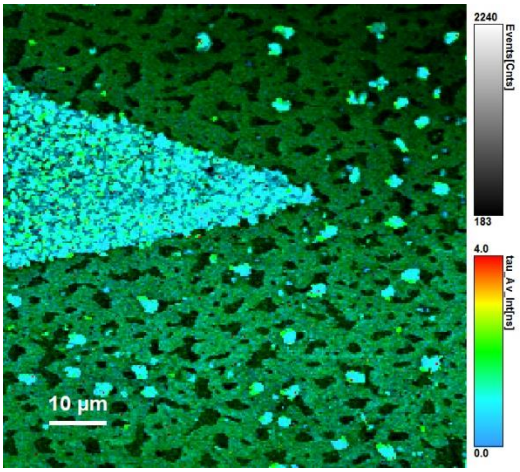

9.3 Rhenium- Ruthenium

9.3.1 Re to Ru energy transfer

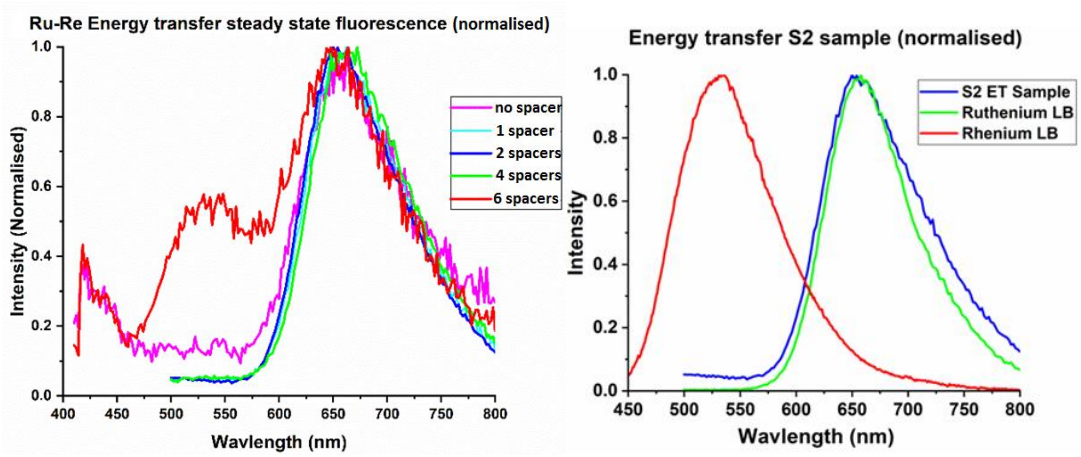

Figure 9.15: Evidence of energy transfer from monolayers of complexes of ReC18 to RuC18 deposited on quartz glass slides spaced apart using stearic acid.

9.3.2 Microscope images

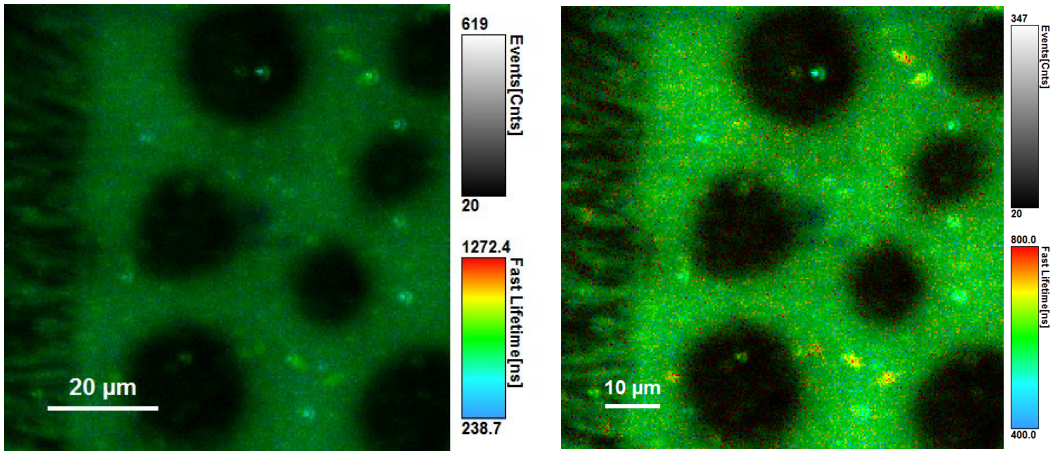

Figure 9.16: FLIM Microscope images of Rhenium monolayer on silicon wafer (S1a)

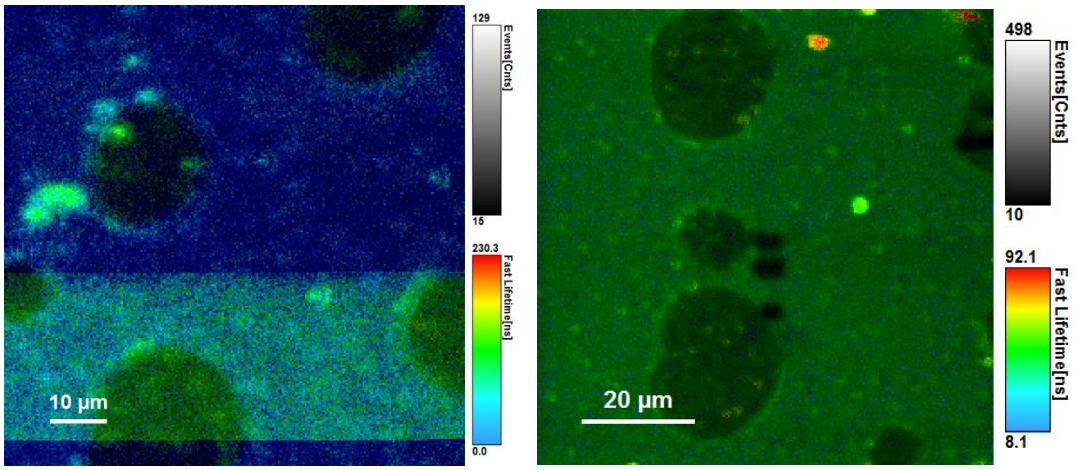

Figure 9.17: FLIM Microscope images of Rhenium monolayer on silicon wafer (S1b)

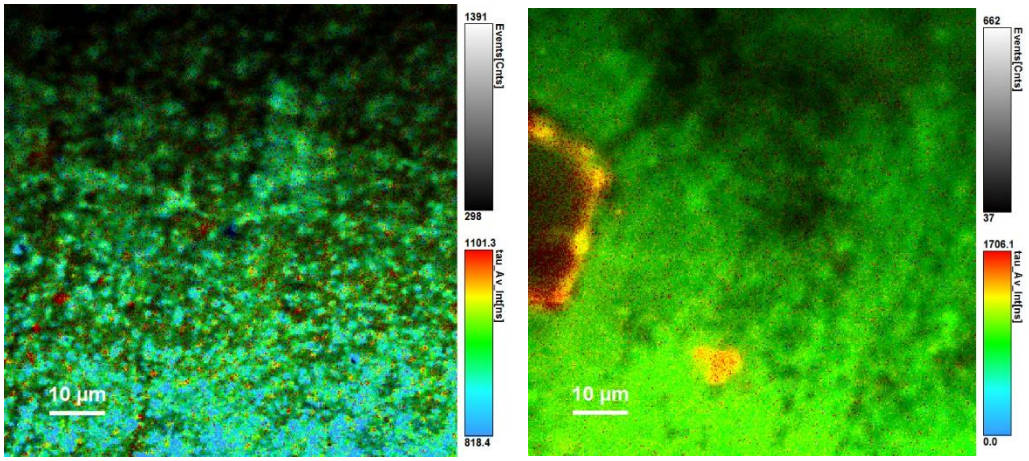

Figure 9.18: FLIM Microscope images of Ruthenium monolayer on glass

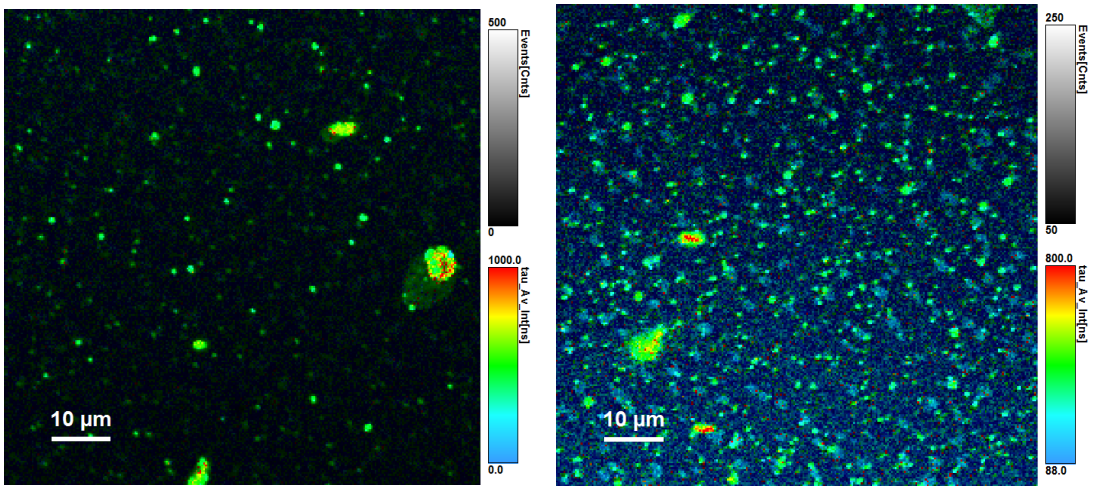

Figure 9.19: Ruthenium S0 monolayer on Silicon wafer

9.4 Porphyrins

9.4.1 Spectroscopy of additional porphyrins

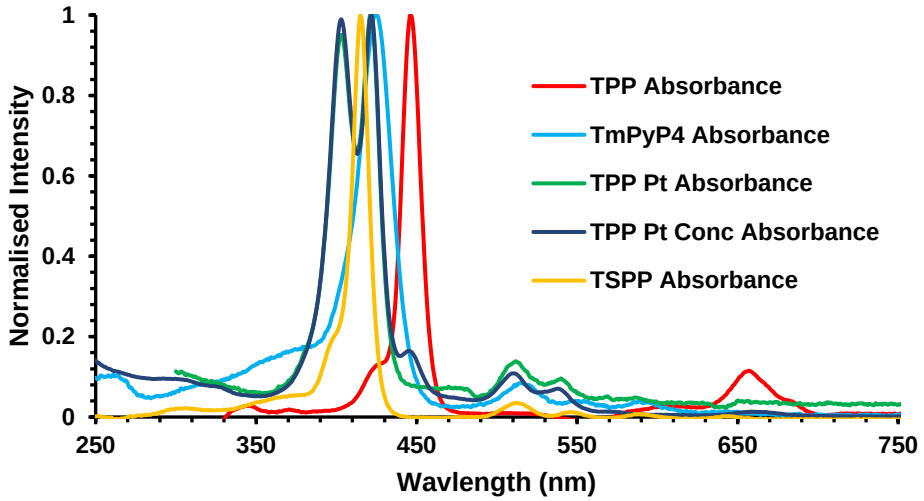

Figure 9.20: Absorption spectroscopy of TPP, TSPP, TmPyP4 and TPP Pt.

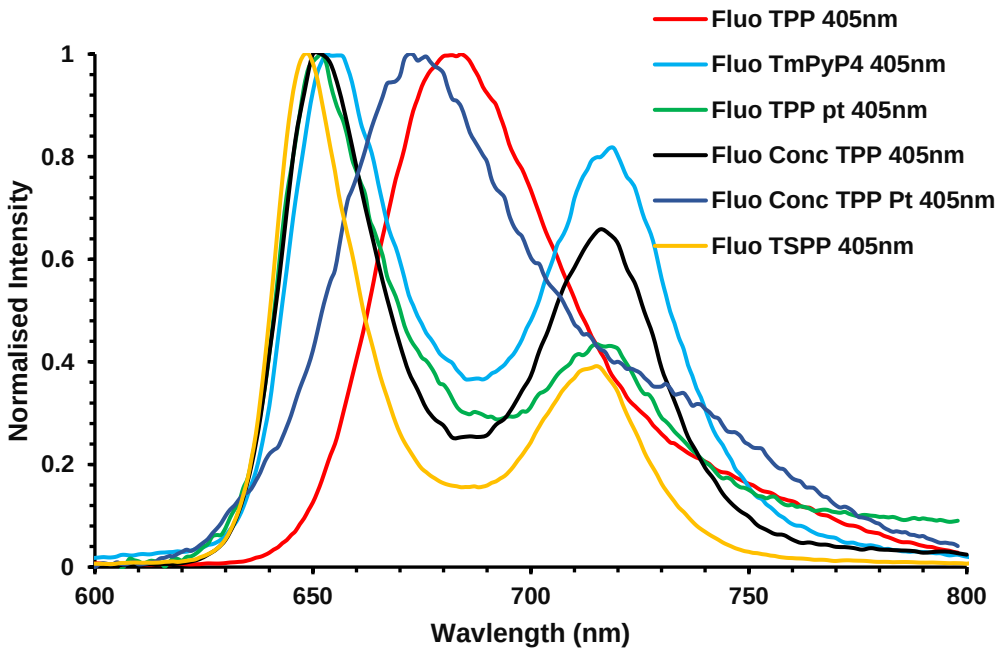

Figure 9.21: Fluorescence spectroscopy of TPP, TSPP, TmPyP4 and TPP Pt.

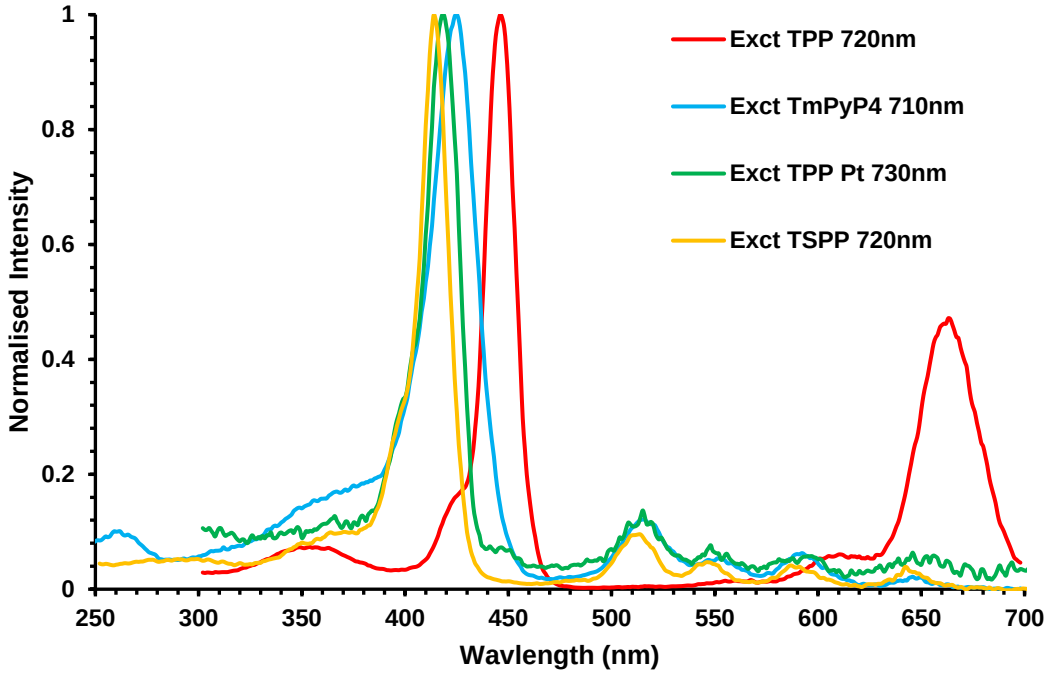

Figure 9.22: Excitation spectroscopy of TPP, TSPP and TmPyP4.

1.1.5. Examples of multiple SA-TPP ratios

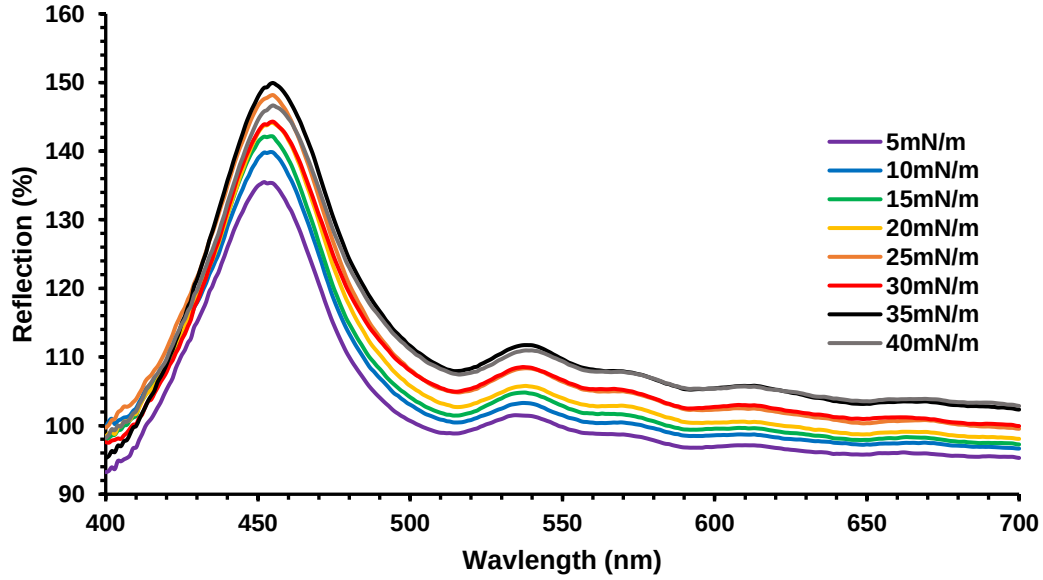

Figure 9.23: Reflection spectrum of 5-1 SA-TPP as a function of surface pressure.

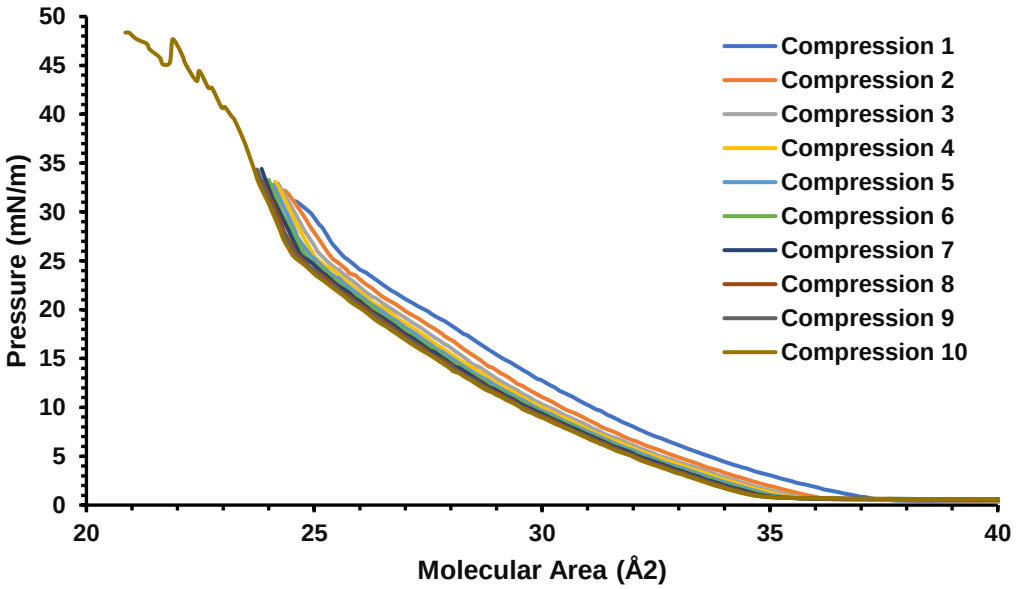

Figure 9.24: 5-1 SA-TPP isotherms

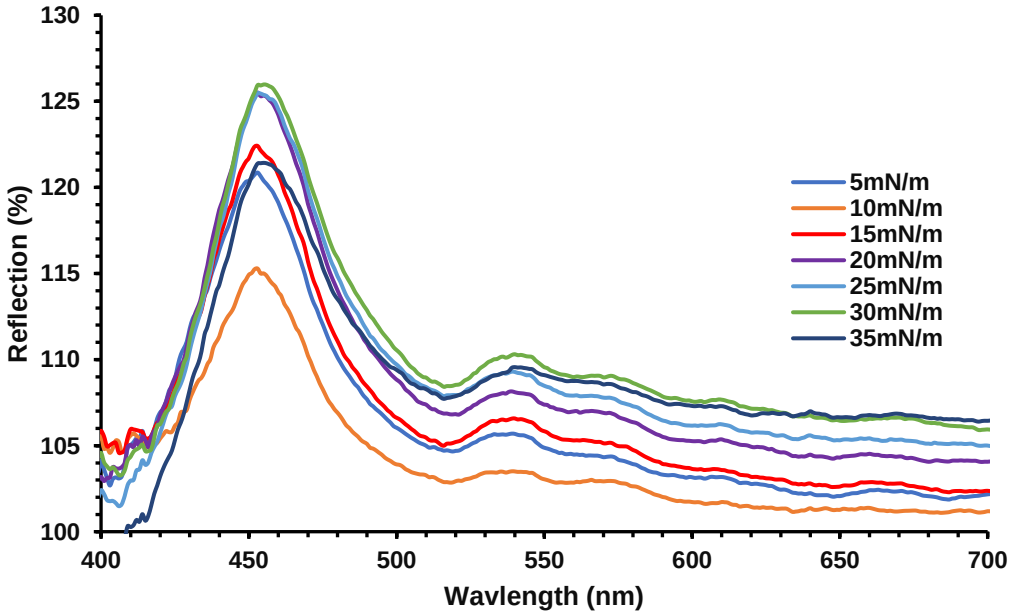

Figure 9.25: Reflection spectrum of 10-1 SA-TPP as a function of surface pressure.

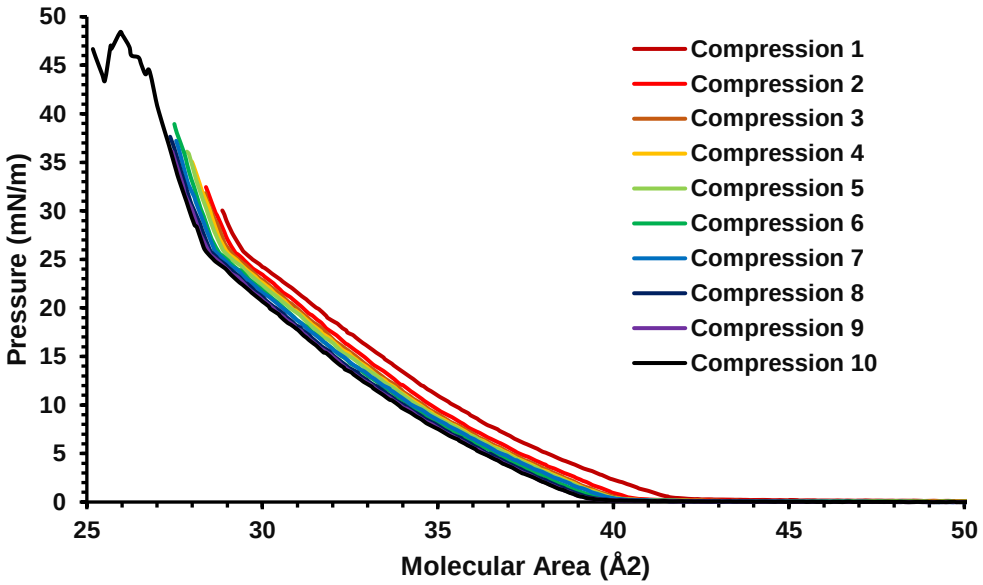

Figure 9.26: 10-1 SA-TPP isotherms

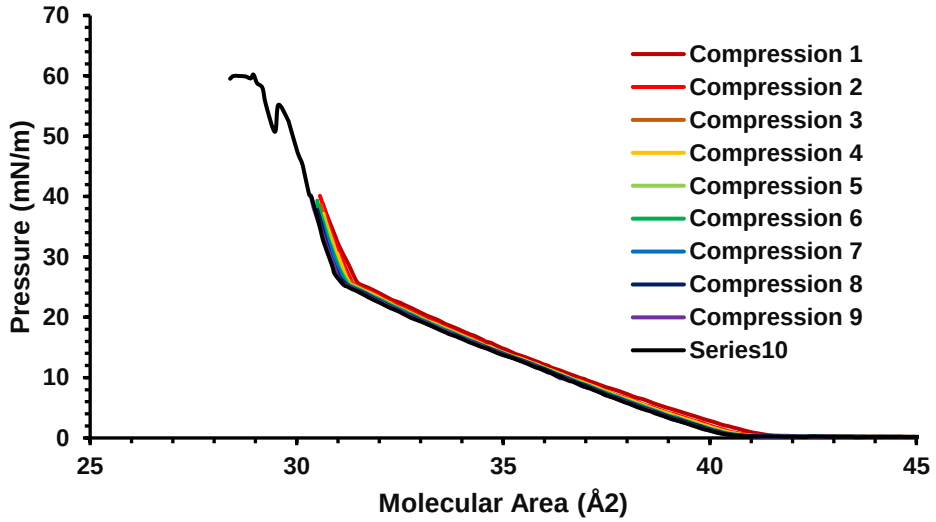

Figure 9.27: 50-1 SA-TPP isotherms